

# Dynamics of Quantized Vortices and Electron Bubbles in the Gross-Pitaevskii Model of a Superfluid



Alberto Villois  
School of Mathematics, UEA  
Norwich, NR4 7TJ, England.

A thesis submitted to the University of East Anglia for the degree of  
*Doctor of Philosophy*

May 16, 2018

© This copy of the thesis has been supplied on condition that anyone who consults it is understood to recognise that its copyright rests with the author and that use of any information derived there from must be in accordance with current UK Copyright Law. In addition, any quotation or extract must include full attribution.



# Abstract

In this thesis we present an extensive study on quantised vortex dynamics using the Gross-Pitaevskii model of a superfluid in the limit of zero temperature. We make use of an accurate and robust numerical method that we developed to detect topological defects present in the scalar order parameter characterising the superfluid. We begin by focusing on the scattering of vortex rings by a superfluid line vortex. Thereafter, we focus on the development and decay of a turbulent vortex tangle, measuring the Vinen's decay law for the total vortex length. Moreover, the temporal evolution of the Kelvin wave spectrum is obtained providing evidence of the development of a weak-wave turbulence cascade. The study of superfluid vortex reconnections is also carried out in order to identify what aspects of the reconnection process are universal.

Aside from the investigation on quantised vortex dynamics, in this thesis we also present a study on the motion of an electron bubble in a superfluid. The electron bubble dynamics is studied in the adiabatic approximation using the Gross-Pitaevskii equation to model the superfluid wavefunction and a Schrödinger equation to model the electron wavefunction. This model allows us to recover the key dynamics of the ion-vortex interactions that arise and the subsequent ion-vortex complexes that can form. We determine the vortex-nucleation limited mobility of the ion to recover values in reasonable agreement with measured data. Moreover, considering the scenario of an ion trapped on the core of a vortex line, we investigate how small and large amplitude Kelvin waves and solitary waves affect the drift velocity of the ion. In particular, we have identified that Hasimoto soliton-bubble complexes propagating along the vortex can arise.

# Contents

<b>1</b>	<b>Introduction</b>	<b>1</b>
1.1	Background on Superfluidity . . . . .	1
1.1.1	Landau Criterion . . . . .	1
1.1.2	Two Fluid Model . . . . .	4
1.1.3	Superfluid Vortices . . . . .	5
1.2	Superfluid Turbulence . . . . .	6
1.2.1	Zero Temperature Superfluid Turbulence . . . . .	7
1.2.2	Quasi-Classical Turbulent Regime . . . . .	8
1.2.3	Ultra-Quantum or Vinen Turbulent Regime . . . . .	9
1.3	Open Problems . . . . .	9
1.4	Aim of the Thesis . . . . .	10
1.5	Outline of the Thesis . . . . .	12
<b>2</b>	<b>Mathematical Models</b>	<b>16</b>
2.1	The Gross Pitaevskii Equation . . . . .	16
2.1.1	Conserved Quantities . . . . .	18
2.2	Elementary Excitations and Superfluidity . . . . .	19
2.2.1	Ground State . . . . .	19
2.2.2	Fluctuations on the Ground State . . . . .	20
2.2.3	Bogoliubov Dispersion Relation . . . . .	21
2.3	Hydrodynamics Interpretation . . . . .	21
2.4	Vortex Solutions . . . . .	23
2.4.1	Terminology . . . . .	23
2.4.2	Stationary Vortex Solution . . . . .	24
2.5	Vortex Motion . . . . .	26
2.5.1	Vortex Dynamics . . . . .	26
2.5.2	Kelvin Circulation Theorem . . . . .	27
2.6	Incompressibility Approximation and the Vortex Filament Model . . . . .	28
2.6.1	Biot-Savart Law . . . . .	28
2.7	Local Induction Approximation . . . . .	30
2.7.1	Singularity Regularisation . . . . .	30
2.7.2	Local Induction Equations . . . . .	32
2.8	Vortex Energy . . . . .	34

<b>3</b>	<b>Vortex Tracking Method</b>	<b>36</b>
3.1	Introduction . . . . .	36
3.2	Tracking Vortices in Two-Dimensional Complex Fields . . . . .	37
3.3	Tracking Vortex Filaments in Three-Dimensional Complex Fields . . . . .	40
3.4	Case Studies . . . . .	42
3.4.1	Vortex Ring and Torus Vortex Knot . . . . .	42
3.4.2	Kelvin Wave Spectra . . . . .	45
3.4.3	Several Rings . . . . .	47
3.4.4	Vortex Tangle . . . . .	48
3.5	Conclusions . . . . .	52
<b>4</b>	<b>Scattering of Line-Ring Vortices</b>	<b>53</b>
4.1	Introduction . . . . .	53
4.2	Numerical Method . . . . .	54
4.3	Results . . . . .	55
4.4	Conclusions . . . . .	61
<b>5</b>	<b>Turbulent Vortex Tangle</b>	<b>63</b>
5.1	Introduction . . . . .	63
5.2	Method . . . . .	64
5.3	Vinen's Law for the Decay of a Vortex Tangle . . . . .	64
5.4	Complexity Measures for a Vortex Tangle . . . . .	66
5.5	Kelvin Waves Cascade . . . . .	71
5.6	Conclusions . . . . .	73
<b>6</b>	<b>Vortex Reconnections</b>	<b>74</b>
6.1	Introduction . . . . .	74
6.2	The reconnection Case Studies . . . . .	76
6.3	Approach and Separation Rates . . . . .	76
6.4	Analytical Predictions Using a Linear Approximation . . . . .	79
6.5	Numerical Measurements of the Curvature and Torsion . . . . .	84
6.6	Conclusions . . . . .	86
<b>7</b>	<b>Dynamics of Electron Bubbles</b>	<b>90</b>
7.1	Introduction . . . . .	90
7.2	Mathematical Model . . . . .	91
7.2.1	The Gross-Clark Model . . . . .	91
7.2.2	A Simplified Mathematical Model of Electron Bubble . . . . .	92
7.3	Numerical scheme . . . . .	95
7.3.1	Non-dimensional Form of the Equations of Motion . . . . .	95
7.3.2	Adiabatic Approximation . . . . .	96
7.3.3	Initial Condition . . . . .	97
7.3.4	Dynamical Evolution . . . . .	98
7.3.5	Projected Gross-Pitaevskii Equation . . . . .	99
7.4	Result for the Motion of a Free Electron . . . . .	100

## CONTENTS

---

7.4.1	Numerical Results . . . . .	101
7.5	Motion of an Electron Trapped on a Vortex Line . . . . .	110
7.5.1	Excitations on a Vortex Line . . . . .	111
7.5.2	Numerical Results . . . . .	116
7.6	Conclusion . . . . .	125
<b>8</b>	<b>Conclusions and Future Perspectives</b>	<b>128</b>
<b>A</b>	<b>Taylor–Green Flow</b>	<b>131</b>
<b>B</b>	<b>Conserved Quantities in the GP Model</b>	<b>133</b>

# Acknowledgements

I would like to thank all the people who contributed to the work described in this thesis. First and foremost, I would like to thank both my academic advisors, Dr. Hayder Salman and Dr. Davide Proment, for their guidance, encouragement and help during my studies. Additionally, I would like to thank Dr. Giorgio Krstulovic, Prof. Miguel Onorato and Dr. Davide Maestrini for the valuable discussions, their interest in my work and for hosting me at the Laboratoire Lagrange, at the Università degli studi di Torino and at his place, respectively. I am also grateful for the funding provided to me by the University of East Anglia and the School of Mathematics that has allowed me to pursue my graduate studies. The computations presented in this thesis were carried out on the High Performance Computing Cluster supported by the Research and Specialist Computing Support service at the University of East Anglia.

# Chapter 1

## Introduction

### 1.1 Background on Superfluidity

The term superfluidity has been associated to either liquids or gases that in contrast to ordinary fluids, can flow without experiencing any energy dissipation that would give rise to a drag force with an obstacle or with the walls of a capillary. The first fluid exhibiting such behaviour was liquid helium when cooled down below a critical temperature  $T_\lambda = 2.17\text{K}$  [1, 2]. Such a phenomenon, that makes liquid helium different from any other liquid present in nature, is due to the microscopic properties characterising the atoms of helium. At very low temperatures liquid helium does not solidify because of the high quantum zero point energy of its constituents which prevents the formation of a rigid crystal structure. It follows that Quantum mechanical effects associated with the Bose–Einstein statistics, that the helium atoms obey, manifest themselves in the superfluid properties of the system. More specifically, liquid helium can be considered as a collection of bosons that below  $T_\lambda$  can macroscopically occupy the lowest available energy level behaving coherently as single a giant matter wave also called Bose Einstein condensate (BEC). The transition to superfluid liquid helium was historically named the  $\lambda$ -transition and liquid helium above and below  $T_\lambda$  called helium-I and helium-II, respectively. The link between the  $\lambda$ -transition and the Bose-Einstein phase transition was firstly pointed out by Fritz London in 1938. Thereafter, Onsager and Penrose estimated that roughly 8% of the atoms in superfluid liquid helium are in the condensate state [3]. The first experimental evidence of the superfluid nature of a weakly interacting Bose gas was given by Cornell and Winen [4] at JILA and by Ketterle [5] at MIT in 1995 when the first gaseous BEC was created in a laboratory.

#### 1.1.1 Landau Criterion

Having identified the properties of helium-II with the formation of a Bose–Einstein condensate, we will explain why a BEC can experience superfluidity. The reason can be found in the particular type of low energy (or elementary) excitation spectrum admitted by such systems. The relation between the energy spectrum and the absence of viscosity was first pointed out by Landau in what is known as the *Landau criterion for superfluidity*. This criterion can be explained by focusing on the motion of an

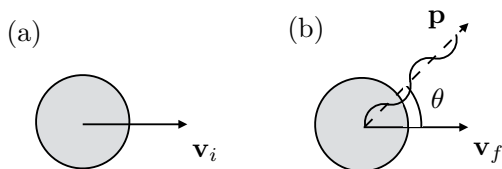


Figure 1.1: Illustration of the impurity interacting with the fluid and emitting a quasi particle excitation. a) Before the emission and b) after the emission.

impurity/object through the fluid. For an ordinary viscous fluid, the drag experienced by the impurity/object will lead to energy dissipation with the consequent generation of heat in the fluid. Landau reasoned that these dissipative processes could be modelled in terms of the generation of elementary excitations inside the fluid [6]. Since these collective phenomena can be mathematically expressed as excitations on the ground state of the superfluid, it is possible to associate to them a single quantum of energy  $\epsilon(\mathbf{p})$  and momentum  $\mathbf{p}$  and to treat them as quasi-particle excitations, as show in Fig. 1.1. By denoting the initial velocity of an impurity with mass  $M$  by  $\mathbf{v}_i$  and its final velocity by  $\mathbf{v}_f$ , the conservation of kinetic energy requires

$$\frac{1}{2}M|\mathbf{v}_i|^2 = \frac{1}{2}M|\mathbf{v}_f|^2 + \epsilon(\mathbf{p}), \quad (1.1)$$

while conservation of momentum gives

$$M\mathbf{v}_i = M\mathbf{v}_f + \mathbf{p}. \quad (1.2)$$

By substituting

$$\mathbf{v}_f = \mathbf{v}_i - \frac{\mathbf{p}}{M}, \quad (1.3)$$

into Eq. (1.1), one obtains

$$|\mathbf{v}_i||\mathbf{p}| \cos(\theta) = \frac{|\mathbf{p}|^2}{2M} + \epsilon(\mathbf{p}). \quad (1.4)$$

Since  $\cos(\theta) \leq 1$  it follows that

$$|\mathbf{v}_i||\mathbf{p}| \geq \frac{|\mathbf{p}|^2}{2M} + \epsilon(\mathbf{p}). \quad (1.5)$$

The above inequality sets a necessary condition to generate an excitation that satisfies both energy and momentum conservation. Hence, we can define a critical velocity given by

$$|\mathbf{v}_c| = \left( \frac{|\mathbf{p}|}{2M} + \frac{\epsilon(\mathbf{p})}{|\mathbf{p}|} \right)_{min} \quad (1.6)$$

below which is not possible to generate quasi-particle excitations. As discussed in [6], for heavy impurities characterised by high kinetic energy we can assume that

$$\frac{|\mathbf{p}|^2}{2M} \ll \epsilon(\mathbf{p}), \quad (1.7)$$

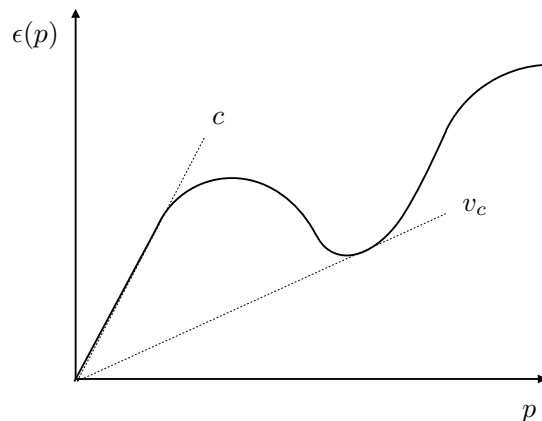


Figure 1.2: Excitation spectrum of liquid helium.

where we defined  $\mathbf{p} \equiv p$ . However, we notice that Eq. (1.7) is not true in general, especially when soft particle impurities are considered, such as for electron bubbles which will be object of investigation in chapter 7. Equation (1.7) leads us to the well know condition of Landau critical velocity

$$|\mathbf{v}_c| = \min \left( \frac{\epsilon(p)}{|p|} \right), \quad (1.8)$$

or equivalently

$$\frac{d}{dp} \left( \frac{\epsilon(p)}{p} \right) = 0, \quad (1.9)$$

which gives us

$$\frac{d\epsilon(p)}{dp} = \frac{\epsilon(p)}{p}. \quad (1.10)$$

According to Landau, a fluid can then exhibits superfluid behaviour depending on the existence of a critical velocity which differs from zero. This provides a criterion to establish when the fluid moving with velocity  $v < v_c$  can interact with an external body, such as an impurity or the wall of a capillary, without dissipating energy. From Landau's criterion given by Eq. (1.8) it is clear that the type of excitation spectrum plays a key role in establishing whether or not a fluid can exhibit superfluidity behaviour. For example, a system characterised by only free particle excitations having

$$\epsilon(p) = \frac{p^2}{2m}, \quad (1.11)$$

does not fulfil Landau's criterion since the critical velocity for such a system is zero. On the other hand, a system having an energy excitation spectrum linear in  $p$  represents a good candidate for supporting superfluidity. We recall that a typical system where the excitations follow the relation  $\epsilon(p) = cp$  is given by sound waves propagating with velocity  $c$  through a crystal. In analogy with such a system, the excitations present in a fluid having a linear energy-momentum relation are usually called phonons or simply sound waves. The excitation spectrum for a weakly interacting Bose gas is also linear for

small momenta but quadratic for an ideal gas. This spectrum can be formally derived by starting from first principles within a quantum mechanical description of the gas. This calculation will be presented in the following chapter. Hence, we can conclude that a weakly interacting Bose gas fulfils Landau's criterion where the critical velocity is set by the speed at which phonons propagate through the media.

In contrast to a Bose gas, the energy spectrum of liquid helium exhibits three different main trends: a phononic regime at small momenta, a quadratic (free particle) regime at large momenta and in the intermediate regime characterised by a minimum, called roton minimum, see Fig. 1.2. Using Eq. (1.10) which sets a condition to graphically estimate the critical velocity, we can find  $v_c$  in Fig. 1.2 by looking for a straight line passing from the origin of the axis which is also tangential to the energy spectrum. From the figure it is clear that two lines satisfy this requirement, one with the slope corresponding to the speed of sound  $c$  and another one very close to the velocity of roton excitations. Since the slope of the second one is smaller we can conclude that the Landau critical velocity for liquid helium-4 is to a good approximation given by the speed of rotons.

### 1.1.2 Two Fluid Model

According to Landau's criterion, the drag experienced by a fluid flowing through a thin capillary can be attributed to the interactions and the collisions between elementary excitations of the fluid and the walls of the capillary. As a result, Landau formulated the first phenomenological model to describe the dynamics of helium-II, the so called two fluid model [7]. This model is based on the idea that helium-II could be described as a mixture of two interpenetrating fluids consisting of a superfluid and a normal component. The superfluid component is a potential flow given by

$$\mathbf{v} = \nabla S, \tag{1.12}$$

characterised by the absence of viscosity. Prior the discovery of quantised superfluid vortices, the vorticity field

$$\boldsymbol{\omega} \equiv \nabla \times \mathbf{v} \tag{1.13}$$

was assumed to vanish everywhere. The normal component is composed of all the elementary excitations and behaves as an ordinary viscous fluid with velocity  $\mathbf{v}_n$ . If we denote the density of the superfluid component by  $\rho_s$ , and the density of the normal component by  $\rho_n$ , the total density of helium-II is given by  $\rho = \rho_s + \rho_n$ , where the ratio between the two component  $\rho_s/\rho_n$  depends on the temperature of the system. As shown by Adronikashvili [8], who measured the damping of oscillations of a disk immersed in liquid helium, the presence of the normal fluid is negligible with respect to the superfluid component for temperatures approaching absolute zero. On the other hand raising the temperature increases the density of thermal excitations within the liquid which consequently increases the amount of normal fluid component and diminishes the superfluid component (see Fig. 1.3).

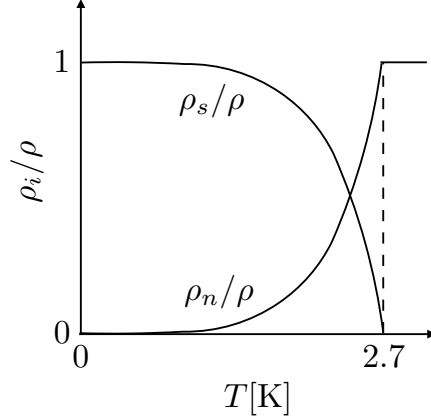


Figure 1.3: Plot illustrating the temperature dependence of the density of the normal and the superfluid component in liquid helium-4.

### 1.1.3 Superfluid Vortices

Despite being irrotational the superfluid component can, in fact, support hydrodynamical vortices characterised by a non-zero circulation

$$\Gamma = \oint_{\mathcal{C}} \mathbf{v} \cdot d\mathbf{l} \quad (1.14)$$

along a closed path  $\mathcal{C}$ . This result is well known in classical fluid dynamics. By substituting Eq. (1.12) into Eq. (1.14) and taking  $\mathcal{C}$  to correspond to a contour of radius  $R$  lying on a plane and centred at the origin of a polar coordinate system  $(r, \theta)$ , we obtain

$$\Gamma = \oint_{\mathcal{C}} \nabla S(r, \theta) \cdot d\mathbf{l} = \oint_{\mathcal{C}} \left( \frac{\partial S(r, \theta)}{\partial r}, \frac{1}{r} \frac{\partial S(r, \theta)}{\partial \theta} \right) \cdot (dr, r d\theta), \quad (1.15)$$

which reduces to

$$\Gamma = \int_0^{2\pi} \frac{\partial S(r, \theta)}{\partial \theta} d\theta = S(R, 2\pi) - S(R, 0). \quad (1.16)$$

Now considering a line vortex with axis aligned with the  $z$ -axis of a cylindrical polar coordinates  $(r, \theta, z)$ , it follows that the velocity field is given by

$$\mathbf{v} = \nabla S(r, \theta, z) = \alpha \nabla \theta = \frac{\alpha}{r} \hat{\mathbf{u}}_{\theta}, \quad (1.17)$$

with  $\hat{\mathbf{u}}_{\theta}$  being the unitary azimuthal vector and  $\alpha$  being an arbitrary constant. From Eq. (1.17) we have that

$$\Gamma = 2\pi\alpha \quad (1.18)$$

for each closed path  $\mathcal{C}$  encircling the  $z$ -axis of the cylinder. Recalling Stokes' theorem given by

$$\oint_{\mathcal{C}} \mathbf{v} \cdot d\mathbf{l} = \int_{\delta\mathcal{C}} \nabla \times \mathbf{v} \cdot \hat{\mathbf{n}} dA \quad (1.19)$$

where  $A$  is a surface delimited by  $\mathcal{C}$  and  $\hat{\mathbf{n}}$  is the unit vector normal to the surface, for a generic phase field well-defined everywhere in the fluid domain, the circulation  $\Gamma$  is indeed zero for each closed path that does not enclose a vortex since

$$\Gamma = \int_A \nabla \times \mathbf{v} \cdot \hat{\mathbf{n}} dA = \int_A \boldsymbol{\omega} \cdot \hat{\mathbf{n}} dA = 0. \quad (1.20)$$

Given that a potential flow can admit solutions with non-zero circulation for a non-simply connected domain, Onsager firstly suggested that a superfluid in a cylindrical annular container can support a rotating flow with  $\Gamma \neq 0$ . Moreover, from quantum mechanical considerations on the phase of the wave-function of liquid helium (which will be discussed in the next chapter), he concluded that  $\Gamma$  was not only constant but also quantised and equal to

$$\Gamma = \pm \frac{h}{m}, \quad (1.21)$$

where  $h/m$  is commonly called the *quantum of circulation*. Thereafter, Feynman suggested that vortices can also exist in bulk superfluid helium in the form of filamentary structures with a core of atomic dimensions where the superfluid must be excluded from it in order to satisfy the condition imposed by Onsager on the quantisation of the circulation. According to Feynman, a superfluid vortex can be described by a Dirac-delta distributions of vorticity (1.13)

$$\boldsymbol{\omega}(\mathbf{x}) = \Gamma \int \delta(\mathbf{x} - \mathbf{s}(\sigma)) d\sigma. \quad (1.22)$$

where  $\mathbf{s}(\sigma)$  is a curve denoting the location of the superfluid vortex, and  $\sigma$  is a generic parametrisation of such curve.

The first experimental evidence of a vortex with a single quantum of circulation was achieved in 1961 by Vinen [9] who studied the effect of the circulation on the vibrational mode of a wire extending along the center of a rotating vessel containing superfluid helium.

## 1.2 Superfluid Turbulence

The observation of superfluid vortex excitations, despite being a fundamental step in the understanding of superfluidity, opened a new entire field of research based on the study of turbulent flow in a superfluid, commonly known as superfluid or quantum turbulence. Such a topic has been mostly investigated in liquid helium-4 [10, 11] and helium-3 B [12, 13] and only recently extended to quantum Bose gases [14]. The ideas behind superfluid turbulence were first introduced by Feynman [15] in 1955 when he suggested that two vortices approaching each other could bend, reconnect and eventually cascade into smaller vortex structures, such as vortex rings, mimicking the Richardson cascade in classical turbulence [16]. Moreover, Feynman also proposed that turbulence could take place even in the zero temperature limit, when both phonons and rotons are

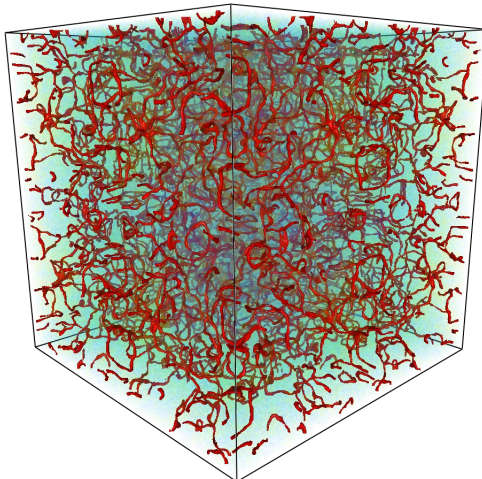


Figure 1.4: Image of a turbulent vortex tangle. Vortex excitations are shown in red while phonons are rendered in blue.

absent. He conjectured that a possible end of this cascade process could be the formation of vortex rings of atomic size able to excite helium atoms and hence providing a mechanism to transform kinetic energy of the fluid into heat.

The fascinating hypothesis formulated by Feynman and the idea that turbulence in a superfluid could be considered as the skeleton of classical turbulence, generated much interest in this field. However, it was soon recognised that superfluid turbulence can not be viewed as a simplified version of classical turbulence in an ordinary fluid. In fact, quantum turbulence, for example in liquid helium-4, can give rise to completely different types of turbulence depending on the temperatures and on the scales at which the phenomenon is being described. As a consequence, it turns out that different theoretical models and different experimental techniques are needed in order to study and describe all the different regimes that can emerge in superfluid turbulence. An attempt to classify these regimes can be found in [17, 18].

### 1.2.1 Zero Temperature Superfluid Turbulence

For the aim of the this thesis we will mainly focus on the study of superfluid turbulence in the zero temperature limit. We note that for liquid helium-4, such a limit corresponds to temperatures below 0.5 K where the effect of elementary excitations on quantum vortices can be neglected. For  $T > 0.5$  K, the scattering between vortices and phonons/rotons gives rise to mutual friction acting on the vortices. Hence, in the zero temperature limit, superfluid vortices can be considered as the only degree of freedom present in system.

Turbulence at zero temperature is in general characterised by a high density of vortex lines which interact generating topologically complex vortex tangles (see Fig. 1.4). The

discrete nature of quantised vortex lines allows for the measurement of the total vortex line density  $\mathcal{L}$ . A key quantity that characterises the density of the tangle is the mean inter-vortex distance given by

$$l \equiv \mathcal{L}^{-1/2}. \quad (1.23)$$

The existence of a characteristic length makes superfluid turbulence different from the turbulence in an ordinary fluid. In fact, the mechanisms responsible for the transfer of energy within the fluid vary according to the scale  $l_f$  at which the energy is injected into the system. In particular, we can distinguish two regimes: the quasi-classical regime when  $l_f \gg l$  and an ultra-quantum or Vinen regime when  $l_f \leq l$

### 1.2.2 Quasi-Classical Turbulent Regime

If the superfluid is forced at large scales such that it leads to regions consisting of polarised vortex lines, then at length scales much larger than  $l$ , one can neglect the discrete nature of superfluid vortices and treat the vorticity field (1.13) as a continuous field. Under this assumption superfluid turbulence exhibits a behaviour that is similar to classical turbulence and for that reason is commonly called quasi-classical turbulence. For instance, in the case of homogeneous and isotropic turbulence, superfluid turbulence shows an inertial regime where the energy spectrum follows the famous Kolmogorov scaling [16]

$$E(k) \sim k^{-5/3}. \quad (1.24)$$

We recall that the theory behind this power law is based on Richardson's idea where large energy containing eddies break into smaller structures transferring energy toward the smallest scales in a self-similar manner. This cascade process is believed to carry on until the smallest eddies reach a viscous scale where energy can be efficiently converted into heat. Even though direct measurements of the Kolmogorov scaling of Eq. (1.24) have so far been performed for a superfluid only in the case of finite temperature [19, 20], in the limit of zero temperature indirect measurements of Eq. (1.24) have been performed by evaluating the decay rate of the energy of a tangle [17]. In fact, by measuring  $\mathcal{L}$  it has been possible to verify the decay law [21]

$$\mathcal{L} \sim t^{-3/2} \quad (1.25)$$

which has been argued [22] to be consistent with the Kolmogorov spectrum. Experiments of this quasi-classical regime in the zero temperature limit have been performed by first producing a polarised array of vortex lines through the rotation of a vessel containing superfluid liquid helium-4 at velocity  $\Omega$  and then creating an un-oriented vortex tangle by an impulsive spin-down of the apparatus from  $\Omega$  to rest [23].

Beside this experimental confirmation, further tests have been provided by numerical simulations confirming the Kolmogorov scaling given by Eq. (1.24) using both the vortex filament model [24] and the Gross-Pitaevskii (GP) model [25]. A direct illustration of the presence of polarised vortex bundles immersed within a vortex tangle can be found in [26] where a particular approach was developed to separate coherent regions of the flow from the incoherent regions.

### 1.2.3 Ultra-Quantum or Vinen Turbulent Regime

In the opposite limit, corresponding to  $l_f \leq l$  the flow exhibits a different behaviour from the quasi-classical turbulence, which we will denote as the ultra-quantum or Vinen turbulence regime. For these scales, the quantised nature of superfluid vortices can not be neglected. In particular, in this regime no large scale flow is present in the system and vortices form an incoherent vortex tangle. At scales of the intervortex distance each vortex interacts only with its neighbors and eventually undergoes reconnection events which cause the rearrangement of the topology of the tangle. Reconnections also produce excitations, namely Kelvin waves (KWs), which propagate along the core of the vortices. Moreover, the interaction between KWs is believed to be one of the main mechanisms responsible for the energy transfer to the smallest length scales in this regime. It is believed that this cascade terminates when KWs attain length scales of the order of the size of the vortex core where the energy associated with these excitations can be radiated effectively into sound waves (phonons) [27, 28]. However, the predicted energy spectrum associated with the KW cascade has not been experimentally measured so far and the exponent associated to its power law scaling is still the subject of debate [29, 30, 31, 32].

Despite some of the uncertainties surrounding the role of the KW energy spectrum, the differences between the quantum and the quasi-classical regimes can be studied during the decay of a vortex tangle. Unlike the quasi-classical regime that is characterised by Eq. (1.25), the theoretical prediction for the decay law of the vortex line density in the quantum regime is given by Vinen's law [33]

$$\mathcal{L} \sim t^{-1}. \tag{1.26}$$

This law has been confirmed recently using, as an experimental technique, the impulsive injection of quantised vortex rings in liquid helium-4 [34]. Numerical simulations using the vortex filament model [35] also measured this expected power law. However, further confirmation with different models, such as the GP model, that can represent the dissipation of the energy contained in KWs by the emission of sound waves is still needed. This will form one of the objectives that will be investigated in this thesis.

## 1.3 Open Problems

Starting from the pioneering experiment of Vinen [36] for counterflow turbulence, the study of quantum turbulence in superfluid liquid helium-4 was for a long time restricted to finite temperatures. However, over the last decade, a lot of research has been devoted to the investigation of quantum turbulence in the zero temperature limit [17, 23, 34, 37]. Thanks to new experimental techniques that allow such ultracold temperatures, and the usage of electrically charged particles to detect the presence of quantum vortices, it has become possible to establish the vortex line density characterising a turbulent vortex tangle and to confirm Vinen's predictions concerning the decay rates of the density of the vortex lines as given by Eqs. (1.25) and (1.26).

Despite this recent experimental progress, several questions still remain in our understanding of quantum turbulence at  $T = 0$  K. In particular, it is not yet clear what is the main mechanism responsible for the transfer of energy in the the so-called crossover range of scales that lies in between the quasi-classical and the ultra-quantum regimes. This problem stems from the different energy spectra describing how energy cascades in the limit of large and small length scales, respectively. In particular, as has been shown in [38], the quasi-classical (Kolmogorov) cascade can not match the predicted ultraquantum (Kelvin wave) cascade. In order to match the two regimes, several different scenarios have been proposed. According to the phenomenological theory proposed by Lvov *et al.* [38], there is a bottleneck that is associated with the accumulation of energy within the crossover range of scales. In contrast to the bottleneck scenario, Svistunov and Kozik [39] introduced a model based on different types of reconnections, such as reconnection between bundles, between single vortex lines and self reconnections. They argued that this scenario will sustain the transfer of energy down to scales where KW excitations propagating on a single line becomes applicable.

The problem associated with the mismatch of the energy cascades in the crossover regime has raised questions on whether or not the KW cascade should be considered as the main process responsible for the energy transfer down to the dissipative scales. For example, both Salman [40] and Nemirovkii [41] suggested a scenario where vortex rings provide an equally important contribution to the transfer of energy down to the smallest scales in a manner that is reminiscent of the cascade of vortex rings introduced by Feynman [15]. Moreover, the KW cascade has currently been the subject of debate concerning the slope of the its energy spectrum. Competing theories based on different symmetry assumptions [29, 30, 31], predict different universal exponents and even question the universality of such exponents [32].

The problems we listed are related to the difficulty in experimentally exploring length scales that are much smaller than the intervortex length or scales that are of the order of the size of the vortex core. On the other hand, new promising technologies based on the use of nanometer particles or excimer molecules [42, 43], represent a new frontier for visualizing the vorticity field that can allow us to explore the vortex dynamics down to the dissipative length scales. For these reasons, new theoretical and numerical modelling of some of these physical processes is necessary in order to better understand both the small scale process in quantum turbulence as well as the interaction between nano sized particles with superfluid vortices.

## 1.4 Aim of the Thesis

This thesis finds its natural application in the study of quantum turbulence in liquid helium-4 in the limit of zero temperature. One of the aims of this work is to extend our current knowledge of superfluid vortex dynamics in order to elucidate the main mechanisms responsible for the transfer of energy in a superfluid turbulent flow in the zero temperature limit. To accomplish this we have decided to focus on the study of

superfluid vortex dynamics using a new approach based on the combination of the GP model to describe the evolution of a superfluid with an innovative numerical method [44] to accurately detect the presence of superfluid vortices in the flow. This tool will allow us to address the following questions:

- Can the GP model be used to study turbulent flows in liquid helium in the limit of zero temperature? Can we obtain the correct scaling that has been predicted to occur for liquid helium for the decay of the total vortex length of a tangle?
- Can the sound wave excitations present in the system alter the rate of decay of the tangle?
- Can we analyse in detail a vortex reconnection event in the GP model? Does the emission of vortex sound waves play an important role in the time scale governing the approach and the separation rate between two vortex filaments?
- Can we measure a KW cascade during the decay of the vortex tangle and what is the universal exponent associated to the cascade in the GP model? Does it match with the theoretical predictions made using weak wave turbulence in the Biot-Savart model?
- Most of the theories developed to describe turbulence in liquid helium are based on the Local Induction Approximation (LIA), a problem that is of interest is to compare the GP and LIA models for a simple but fundamental interaction such as the scattering of a vortex ring with a vortex line?

Answering these questions will allow us to understand the range of applicability of the GP model in the study of turbulent flows in liquid helium and to focus on the energy dissipation in a superfluid through the emission of sound waves.

The second aim of this thesis is to study the motion of electron bubbles and their interactions with superfluid vortices. Given the fact that impurities play a central role in the existing experimental techniques in order to investigate vortices and quantum turbulence in superfluid liquid helium-4 in the zero temperature limit [45], such a study can greatly facilitate the interpretation of future experimental measurements. In particular in this work we will address the following questions:

- A commonly used model to study this problem is the so called Gross-Clark model [46, 47] that employs a mean field model for the superfluid coupled to a Schrödinger equation for the electron. Given the fact that the Gross-Clark model can neither describe the presence of roton excitations nor the correct equation of state for liquid helium, can this minimalistic model well capture the correct physics in the study of the dynamics of an electron bubble and its interaction with quantised vortices?
- Is there a regime of pressures and temperatures where this model leads to a quantitative agreement with experimental measurements performed in liquid helium?

- Can this model help to clarify certain dynamics where the motion of the electron bubble is mainly dominated by the presence of vortex excitations in the superfluid?

Much of the work presented in this thesis finds its natural application in the study of quantum turbulence in liquid helium-4. However, given the relevance that the GP model has in the study of atomic Bose–Einstein condensates, we note that many of our results also provide important insight on relevant dynamical processes that can possibly be modelled in these other system [48, 14].

## 1.5 Outline of the Thesis

This thesis is organised in the following way. In the second chapter we will present the GP model [49], which is the main mathematical model we have used throughout the thesis. After discussing why the GP model provides a good phenomenological description for the dynamics of a superfluid in the zero temperature limit, we will relate it to the two most widely adopted mathematical models that have been used to investigate vortex dynamics in superfluid turbulence: the Vortex Filament model [50] (VF) and the Local Induction Equations [51] (LIE) which are also referred to as the Local Induction Approximation (LIA).

One of the main differences between the GP model and the VF (or LIA) model is the different specification of the superfluid flow. In the GP model, an Eulerian representation of the flow is used and the superfluid is defined by a complex scalar field  $\psi$ . In contrast, in the VF model, a Lagrangian representation is used where the dynamic variables of the system are given by the instantaneous position of the superfluid vortices. One of the advantages of investigating quantum turbulence with the VF model is that it naturally provides access to all the information related to each vortex line present in the flow. Such knowledge is particularly useful for example when the decay of a turbulent flow is investigated. In this case, in order to investigate Eq. (1.26) becomes necessary to estimate the total vortex line density. On the other hand, the VF model is valid only when the incompressible approximation for the fluid holds. Therefore, this model is applicable for scales much larger than the vortex core size and can not be readily extended to model compressible effects. For example, the VF model is not suitable to understand the microscopic processes associated with reconnections between vortices or the emission of sound waves, which are two key mechanisms that are needed to correctly interpret quantum turbulence for length scales of the order of the intervortex distance. The GP model is also more relevant when modelling impurities that have dimensions of the order of the size of the vortex core and for particles that are found in a bubble state. This bubble scenario turns out to be relevant for the study of electrons in liquid helium-4.

The third chapter will be devoted to the introduction of a novel numerical technique that permits accurate identification of the positions of each superfluid vortex contained in a GP simulation of a superfluid. This method provides us with a versatile tool that allows us to tackle a whole range of problems from performing detailed diagnostics of quantum turbulence simulations, such as the evolution of the total length

of a vortex tangle, to the determination of the KW spectrum along vortex lines with different configurations. The material presented in the chapter is based on the work [44].

After explaining the model and the method used to investigate quantum vortices, in the fourth chapter we apply our method to study the scenario of the scattering between a perfectly circular vortex ring and a straight vortex line. This vortex configuration, which represents one of the most elementary types of vortex interactions arising in superfluid turbulence, plays a crucial role in the understanding of vortex dynamics within the crossover range of scales. As stated above, it is unclear what are the main mechanisms regulating the energy transfer within the crossover range. However, by considering one of the eddies present in the quasi-classical turbulent regime, and zooming down to length scales of the order of the inter-vortex distance, one can envisage a configuration characterised by the presence of a bundle of vortex lines with vortex rings travelling through them and contributing to the transfer of energy from one vortex line to another one. With this picture in mind, the scattering between a vortex ring and a line can then be considered as a prototype of the interaction that arises between vortices within the crossover range. Moreover, in view of the original idea of superfluid turbulence proposed by Feynman, this study is also relevant to investigate the role played by vortex rings in the transfer of energy across different scales by quantum turbulence. This chapter will follow the already published work [52].

In Chapter 5, we will present a study of the evolution and the decay of a turbulent vortex tangle. To analyse such a system we will make extensive use of the vortex tracking algorithm developed in Chapter 3. In contrast to the idealised vortex interaction modelled in Chapter 4, a vortex tangle consists of an extremely complicated vortex configuration with a large number of vortex lines and rings involved which can eventually form hydrodynamic structures with a non-trivial topology [53]. The work in this chapter aims to measure the decay rate of the vortex tangle and whether Vinen's decay law given by Eq. (1.26) applies also for a compressible system characterised by the presence of sound waves. Thereafter, motivated by the open debate concerning the KW cascade, we will provide the first analysis of the KW energy spectrum measured during the evolution of a turbulent tangle. The results obtained in this study have been presented in [54].

Motivated by the important role played by vortex reconnections in helium-4 superfluid liquid helium-4 [11] and in atomic BECs [14] and by the increasing interest that this problem attracted in recent years in the contest of superfluid turbulence, in Chapter 6 we apply the tracking algorithm discussed in Chapter 3 to several types of vortex reconnections. Following some previous numerical works on superfluid vortex reconnections in both the GP [55, 56, 57]. and the VF model [58], we will focus on the analysis of the reconnections arising from the instability between two anti-parallel vortex lines and the reconnection during the scattering of two perpendicular vortex lines moving in the opposite direction. Our method will allow us to revisit some of the previously obtained numerical results and to shed some lights on the universal and non universal aspects which characterise a reconnection. This study will also be extended to other

relevant examples of superfluid vortex reconnections, such as the ones characterising the rearrangement in the topology of a trefoil knot and the ones extracted from the decay of the vortex tangle presented in Chapter 5. The chapter will follow the recently published work [59].

In Chapter 4 we presented the scattering of a vortex ring with a vortex line. Aside from its relevance in the context of quantum turbulence, such dynamics also represents one of the first experimental studies of the interaction of vortices in superfluids. By injecting ions in liquid helium-4, Schwarz [60] estimated the cross section of the line-ring scattering and the probability for the ion to escape from the core of a vortex. These dynamics illustrate two of the main ways that ions can be used to study superfluid vortices which continue to be employed to investigate different properties of quantum turbulence. On the one hand, by an externally applied electric field the ion can be driven through a superfluid vortex tangle where it can eventually be trapped on the core of a superfluid vortex. Through the measurement of intensity of electrical current it is possible to indirectly detect, for example, the vortex line density of such tangle. On the other hand, once the ion trapped on a vortex line it can subsequently slides along such a filament and this motion can be used to study the structure and the key excitations which propagate along the core of a vortex.

In the last part of this thesis, we will model these two different types of motion for a negatively charged ion, an electron, that is widely used in the context of zero temperature turbulence. In the first part of the chapter, we will present the mathematical model used to include the presence of an electron in a superfluid described by the GP equation and we will consider the motion of the ion under the influence of an applied electric field. We then investigate the conditions under which the bubble nucleates a vortex ring and is subsequently captured by the ring forming a charged vortex ring (CVR). Thereafter, we will discuss how the formation of a CVR can be suppressed. In the second part of the chapter, we model the motion of an ion trapped along a vortex line and moving along the core of the vortex under the effect of an applied electric field.

Even though the motivation for modelling the motion of an electron in the self-trapped bubble state with or without superfluid vortices is mainly related to the interpretation of quantum turbulence measurements, this study also allow us to approach several long standing problems concerning the interaction of ions and vortices. For instance, we will explore a range of electric fields under which an ion can emit a stream of vortex rings that can lead to the formation of a small vortex tangle in the wake of the ion. We will show how the drag experienced by the ion, as a result of this tangle can explain the previously measured drift velocities in [61, 62]. In the case of an ion trapped on a vortex line and sliding along its length, we will use simulation to reveal the dynamical structures that can form which can help explain the anomalous mobility and limiting velocity measured in [63] for temperatures approaching the absolute zero. Parts of this chapter will follow the work [64].

As a final remark, A.V. would like to state that although most of the work presented

here has been carried out in collaboration with Dr. Hayder Salman, Dr. Davide Pro-  
ment and Dr. Giorgio Krstulovic, all the numerical simulations and the data analysis  
presented in this thesis were obtained using codes developed independently by A.V.

# Chapter 2

## Mathematical Models

In this chapter we introduce the main equations used, throughout this thesis, to describe the dynamics of a superfluid, with particular attention focused on the GP equation. This equation represents a mean field theory formally derived to model weakly interacting Bose gases. However, in this chapter we discuss how this equation also contains some the key ingredients to describe the dynamics of superfluid liquid helium in the limit of zero temperature. In particular, we show how this model satisfies Landau's criterion for superfluidity and supports quantised vorticity distributions (superfluid vortices). Moreover, we will discuss how the vortex filament description of superfluid vortices naturally arises from the GP model when the limit of incompressible flow is taken as has recently shown in [65].

### 2.1 The Gross Pitaevskii Equation

In quantum mechanics, in the absence of an external potential, a system with  $N$  particles interacting through binary collisions can be described in terms of an  $N$ -body Schrödinger equation given by

$$i\hbar\frac{\partial}{\partial t}\Psi(\mathbf{x}_1; \dots; \mathbf{x}_N, t) = \hat{H}_N\Psi(\mathbf{x}_1; \dots; \mathbf{x}_N, t), \quad (2.1)$$

with

$$\hat{H}_N = -\sum_i \frac{\hbar^2}{2m}\nabla_i^2 + \sum_{i \neq j} V(\mathbf{x}_i - \mathbf{x}_j) \quad (2.2)$$

being the  $N$ -body Hamiltonian operator for the system. The first sum in Eq. (2.2) represents the kinetic energy operator while the second sum represents the potential energy operator associated to the 2-body interaction potential  $V$ . We recall that neglecting the three (or higher) body collision is, in general, a valid approximation when ultracold dilute gases are considered. Since solving Eq. (2.1) is rather complicated, unless a very small number of particles is considered together with a limited number of available energy states, a possible way to find an approximate solution to Eq. (2.1) is given by the variational method called Hartree method [66, 67]. We begin by recalling

that for a system with action given by

$$A = \int \Psi^* \left( i\hbar \frac{\partial}{\partial t} \right) \Psi d^3 \mathbf{x}_1 \dots d^3 \mathbf{x}_N dt - \int \Psi^* H_N \Psi d^3 \mathbf{x}_1 \dots d^3 \mathbf{x}_N dt \quad (2.3)$$

the principle of least action can be used to recover Eq. (2.1) by minimizing Eq. (2.3)

$$\frac{\delta A}{\delta \Psi^*} = 0 \quad (2.4)$$

with respect to either  $\Psi^*$  (or  $\Psi$ ). The Hartree method is then based on the assumption that the correlations between different particles are negligible and, hence, the wave function  $\Psi(\mathbf{x}_1; \dots; \mathbf{x}_N, t)$  can be written as a product of  $N$  single-particle wave functions,  $\Psi_i(\mathbf{x}_i, t)$ ,

$$\Psi(\mathbf{x}_1; \dots; \mathbf{x}_N, t) = \Psi_1(\mathbf{x}_1, t) \Psi_2(\mathbf{x}_2, t) \dots \quad (2.5)$$

The assumption of neglecting quantum correlations can be justified when a dilute system is considered. By substituting Eq. (2.5) into Eq. (2.3) one can obtain  $N$  equations

$$i\hbar \partial_t \Psi_i(\mathbf{x}_i, t) = \left( -\frac{\hbar^2}{2m} \nabla_i^2 + \sum_{i \neq j} \int \Psi_j^*(\mathbf{x}_j, t) V(\mathbf{x}_i - \mathbf{x}_j) \Psi_j(\mathbf{x}_j, t) d\mathbf{x}_j \right) \Psi_i(\mathbf{x}_i, t), \quad (2.6)$$

one for each single particle wave function  $\Psi_i$ , which minimize the action given by Eq. (2.3). The Hartree equations (2.6) are also called mean field equations since each particle interacts with an effective potential

$$V_H = \sum_{i \neq j} \int \Psi_j^*(\mathbf{x}_j, t) V(\mathbf{x}_i - \mathbf{x}_j) \Psi_j(\mathbf{x}_j, t) d^3 \mathbf{x}_j \quad (2.7)$$

given by mean effect of the other  $N - 1$  particles. We note that the ansatz given by Eq. (2.5) needs to be modified in order to respect the correct quantum statistics [68]. In fact, a collection of  $N$  indistinguishable bosons requires the system wave function to be symmetric with respect to any permutation of the index labelling each particle

$$\Psi(\mathbf{x}_1, \mathbf{x}_2 \dots \mathbf{x}_N, t) = \Psi(\mathbf{x}_2, \mathbf{x}_1 \dots \mathbf{x}_N, t). \quad (2.8)$$

Furthermore, for sufficiently low temperatures, the system undergoes a Bose–Einstein phase transition which implies the macroscopic occupation of the ground state of the system. Hence, one can make the stronger assumption that each particle can be described by the same single particle wave function. Equation (2.5) can then be rewritten as

$$\Psi(\mathbf{x}_1, \dots \mathbf{x}_N, t) = \prod_i \Psi(\mathbf{x}_i, t), \quad (2.9)$$

which respects the correct quantum statistics for bosons. Under the assumption (2.9), the Hartree equations become the non-linear Schrödinger equation (NLSE)

$$i\hbar \frac{\partial}{\partial t} \Psi(\mathbf{x}, t) = \left( -\frac{\hbar^2}{2m} \nabla^2 + (N - 1) \int \Psi^*(\mathbf{x}', t) V(\mathbf{x} - \mathbf{x}') \Psi(\mathbf{x}', t) d^3 \mathbf{x}' \right) \Psi(\mathbf{x}, t). \quad (2.10)$$

If we are interested in describing the lower energy dynamics of the dilute Bose gas, where most of the particles are in the ground state, we can neglect the presence of particles with high momenta and replace the actual two-body potential  $V$  with an effective contact interaction between particles in order to write

$$V(\mathbf{x} - \mathbf{x}') \approx g\delta(\mathbf{x} - \mathbf{x}'), \quad (2.11)$$

where  $g = 4\pi\hbar^2 a/m > 0$  is the effective repulsive interaction strength and  $a$  is the s-wave scattering length [69]. Substituting Eq. (2.11) into Eq. (2.10) we obtain the (local) NLSE

$$i\hbar\frac{\partial}{\partial t}\Psi(\mathbf{x}, t) = \left(-\frac{\hbar^2}{2m}\nabla^2 + (N-1)g|\Psi(\mathbf{x}, t)|^2\right)\Psi(\mathbf{x}, t). \quad (2.12)$$

We note that in quantum mechanics  $|\Psi(\mathbf{x}, t)|^2$  represents a probability density. However, by writing

$$\Psi(\mathbf{x}, t) = \frac{\psi(\mathbf{x}, t)}{\sqrt{N}} \quad (2.13)$$

we can now interpret  $|\psi(\mathbf{x}, t)|^2$  as the particle number density of the condensate, since

$$\int |\psi(\mathbf{x}, t)|^2 d^3\mathbf{x} = N. \quad (2.14)$$

Moreover, considering a large number of particles such that  $N-1 \approx N$  and substituting Eq. (2.13) into Eq. (2.12) we finally obtain an equation, more commonly known in this context, as the GP equation [70], given by

$$i\hbar\frac{\partial}{\partial t}\psi(\mathbf{x}, t) = \left(-\frac{\hbar^2}{2m}\nabla^2 + g|\psi(\mathbf{x}, t)|^2\right)\psi(\mathbf{x}, t). \quad (2.15)$$

### 2.1.1 Conserved Quantities

This equation defines an Hamiltonian system characterized by the following conserved quantities: the total mass

$$M = m \int |\psi(\mathbf{x}, t)|^2 d^3\mathbf{x} = Nm, \quad (2.16)$$

and the total energy

$$E = \frac{\hbar^2}{2m} \int |\nabla\psi(\mathbf{x}, t)|^2 d^3\mathbf{x} + \frac{g}{2} \int |\psi(\mathbf{x}, t)|^4 d^3\mathbf{x}. \quad (2.17)$$

If the system is translationally invariant (e.g. for periodic boundary conditions) then the total linear momentum

$$\mathbf{P} = \frac{\hbar}{2i} \int (\psi^*(\mathbf{x}, t)\nabla\psi(\mathbf{x}, t) - \psi(\mathbf{x}, t)\nabla\psi^*(\mathbf{x}, t)) d^3\mathbf{x} \quad (2.18)$$

is also conserved. See Appendix for a proof of time independence of the above quantities.

## 2.2 Elementary Excitations and Superfluidity

The concept of superfluidity, according to Landau's interpretation already discussed in sections 1.1.1, is related to the possibility of moving an object within a fluid without generating quasi-particle excitations. Since this property is directly related to the shape of the energy spectrum of the elementary excitations of the fluid, we will recover the energy spectrum predicted by the GP model. To do so we must first determine the ground state of the system.

### 2.2.1 Ground State

To find the ground state of the system, we will seek a steady state solution. We will, therefore, look for a wave function  $\psi(\mathbf{x}, t)$  such that at each point  $\mathbf{x}$  the amplitude  $|\psi|^2$  is time independent. This requirement implies a solution of the form

$$\psi_0(\mathbf{x}, t) = \psi_0(\mathbf{x})e^{-i\frac{\mu}{\hbar}t}. \quad (2.19)$$

By substituting Eq. (2.19) into Eq. (2.15) we obtain the stationary GP equation

$$\mu\psi_0(\mathbf{x}) = \left( -\frac{\hbar^2}{2m}\nabla^2 + g|\psi_0(\mathbf{x})|^2 \right) \psi_0(\mathbf{x}). \quad (2.20)$$

The time dependence of a stationary solution is given by the value of the constant  $\mu$ . We note that, for a spatially uniform ground state,  $\mu$  and  $E$  are related through the expression

$$\mu = \frac{1}{N} \left[ E + \frac{g}{2} \int |\psi_0|^4 d^3\mathbf{x} \right]. \quad (2.21)$$

The above equation can be obtained by multiplying Eq. (2.20) by  $\psi^*$  and then integrating the result with respect to  $\mathbf{x}$ . For a system defined in an unbounded domain, the solution with minimum energy is given by the constant function[70]

$$\psi_0(\mathbf{x}) \equiv \psi_\infty. \quad (2.22)$$

Taking into consideration the normalisation condition (2.14) and the thermodynamic limit, it follows that

$$\psi_\infty = \sqrt{\frac{N}{V}} \quad (2.23)$$

where  $V$  is the volume of the system. By substituting Eq. (2.23) into Eq. (2.20) we obtain

$$\mu = g|\psi_\infty|^2 = g\frac{N}{V}, \quad (2.24)$$

and hence

$$E = N\mu - \frac{g}{2} \int |\psi_\infty|^4 d^3\mathbf{x} = g\frac{N^2}{V} - \frac{g}{2}\frac{N^2}{V} = \frac{g}{2}\frac{N^2}{V}. \quad (2.25)$$

From Eqs. (2.24) and (2.25) it is possible to see that

$$\mu = \frac{\partial E}{\partial N}. \quad (2.26)$$

Recalling the definition of the thermodynamic potential, this allows us to conclude that the time dependence of a stationary solution of the GP equation is governed by the chemical potential of the system.

### 2.2.2 Fluctuations on the Ground State

Given knowledge of the ground state, we can find the energy spectrum of the excitations by applying perturbation theory for the infinitesimal fluctuations  $\delta\psi$  propagating on the top of  $\psi_\infty$ . The perturbed ground state can then be written as

$$\psi(\mathbf{x}, t) = \psi_\infty e^{-i\mu t/\hbar} + \delta\psi. \quad (2.27)$$

Since we are working with a uniform Bose gas, the translational invariance of the system allows us to express the general solution for the density variation  $\delta\psi$  as

$$\delta\psi = u_k e^{i(\mathbf{k}\cdot\mathbf{x} - (\omega + \mu/\hbar)t)} + v_k e^{-i(\mathbf{k}\cdot\mathbf{x} - (\omega - \mu/\hbar)t)}, \quad (2.28)$$

with  $u_k$  and  $v_k$  are complex constants. Substituting Eqs. (2.27) and (2.28) into the time dependent GP equation

$$i\hbar \frac{\partial\psi}{\partial t} + \frac{\hbar^2}{2m} \nabla^2 \psi = g|\psi|^2 \psi, \quad (2.29)$$

and considering only terms of first order in  $\delta\psi$  we obtain for the left-hand side

$$\left[ (\hbar\omega + \mu) - \frac{\hbar^2 k^2}{2m} \right] u_k e^{i(\mathbf{k}\cdot\mathbf{x} - (\omega + \mu/\hbar)t)} + \left[ (-\hbar\omega + \mu) - \frac{\hbar^2 k^2}{2m} \right] v_k e^{-i(\mathbf{k}\cdot\mathbf{x} - (\omega - \mu/\hbar)t)}, \quad (2.30)$$

and for the right-hand side

$$\mu(2u_k + v_k^*) e^{i(\mathbf{k}\cdot\mathbf{x} - (\omega + \mu/\hbar)t)} + \mu(2v_k + u_k^*) e^{-i(\mathbf{k}\cdot\mathbf{x} - (\omega - \mu/\hbar)t)}. \quad (2.31)$$

Comparing Eq. (2.30) with Eq. (2.31), we obtain

$$\begin{bmatrix} \hbar\omega - \mu - \frac{\hbar^2 k^2}{2m} & -\mu \\ -\mu & -\hbar\omega - \mu - \frac{\hbar^2 k^2}{2m} \end{bmatrix} \begin{bmatrix} u_k \\ v_k^* \end{bmatrix} = 0. \quad (2.32)$$

We can find a non trivial solution of the above matrix if the determinant is equal to zero which leads to

$$\omega = \sqrt{\frac{k^2}{2m} \left( \frac{\hbar^2 k^2}{2m} + 2\mu \right)}. \quad (2.33)$$

Recalling the de Broglie relations  $\epsilon = \hbar\omega$  and  $p = \hbar k$ , it follows that the dispersion relation given by Eq. (2.33) corresponds to the elementary excitation energy spectrum first evaluated by Bogoliubov [70] using a second quantised formalism for a weakly interacting Bose gas.

### 2.2.3 Bogoliubov Dispersion Relation

The dispersion relation given by Eq. (2.33) exhibits two different asymptotic behaviours for the fluctuations on the top of a uniform ground state:

$$\omega \sim k \sqrt{\frac{\mu}{m}} \quad k^2 \ll \frac{4\mu m}{\hbar^2}, \quad (2.34)$$

and

$$\omega \sim \frac{\hbar k^2}{2m} \quad k^2 \gg \frac{4\mu m}{\hbar^2}. \quad (2.35)$$

The first regime, characterised by a linear dispersion relation, is called phononic regime, in analogy with the case of phonons propagating in a crystal. Since

$$\frac{\omega}{k} = \frac{\partial \omega}{\partial k}, \quad (2.36)$$

this regime is non-dispersive, which means that each low energy excitation moves with the same velocity given by

$$c = \sqrt{\frac{\mu}{m}}. \quad (2.37)$$

which defines the speed of sound of the system. The second regime is called a free particle regime, since it exhibits a quadratic dispersion relation which is typical for free particles described by the linear Schrödinger equation. Considering the condition when

$$ck \sim \frac{\hbar k^2}{2m}, \quad (2.38)$$

it is possible to identify the characteristic length scale given by

$$\xi = \frac{\hbar}{\sqrt{2m\mu}}, \quad (2.39)$$

at which the transition between the two regimes takes place. This length is usually called the *healing length*.

Recalling the Landau superfluid criteria already discussed in section Section 1.1.1, if the excitation energy spectrum admits a critical velocity given by Eq. (1.8) that is different from zero, then the system can exhibit a superfluid behaviour. By substituting Eq. (2.33) into Eq. (1.8) we can conclude that a weakly interacting Bose gas satisfies Landau's criterion for superfluidity with a critical velocity set by the speed of sound of the system.

## 2.3 Hydrodynamics Interpretation

Having shown that the GP equation satisfies Landau's superfluidity criterion, given by Eq. (1.8), we now want to emphasise the connection between the GP equation and

a superfluid by interpreting Eq. (2.15) as a hydrodynamic system [49]. Following the work by Madelung [71], we can rewrite  $\psi$  using the transformation

$$\psi(\mathbf{x}, t) = f(\mathbf{x}, t)e^{i\phi(\mathbf{x}, t)} \quad (2.40)$$

where both  $f$  and  $\phi$  are real functions. Then, we can relate  $f$  to the density field of a fluid by

$$f(\mathbf{x}, t) = \sqrt{\frac{\rho(\mathbf{x}, t)}{m}} \quad (2.41)$$

and  $\phi$  to the velocity field of an irrotational flow by

$$\mathbf{v}(\mathbf{x}, t) = \frac{\hbar}{m} \nabla \phi(\mathbf{x}, t) \quad (2.42)$$

which is consistent with follows Landau's assumption that the superfluid is irrotational. Substituting Eq. (2.40) into Eq. (2.15) we obtain the two equations,

$$\frac{\partial \rho}{\partial t} + \nabla \cdot (\rho \mathbf{v}) = 0, \quad (2.43)$$

$$-\frac{\hbar}{m} \frac{\partial \phi}{\partial t} + \frac{1}{2} \mathbf{v}^2 + \frac{g}{m^2} \rho - \frac{\hbar^2}{2m^2} \frac{\nabla \cdot \nabla \sqrt{\rho}}{\sqrt{\rho}} = 0. \quad (2.44)$$

The first equation represents the continuity equation for a fluid of density  $\rho$ , while the second equation is a Bernoulli-type of equation describing the evolution of an inviscid and compressible potential flow. By applying the gradient operator to Eq. (2.44) we obtain

$$\frac{\partial \mathbf{v}}{\partial t} + (\mathbf{v} \cdot \nabla) \mathbf{v} = -\frac{g}{m^2} \nabla \rho + \frac{\hbar^2}{2m^2} \nabla \left[ \frac{\nabla^2 \sqrt{\rho}}{\sqrt{\rho}} \right], \quad (2.45)$$

which is similar to the Euler equation of a classical fluid

$$\frac{\partial \mathbf{v}}{\partial t} + (\mathbf{v} \cdot \nabla) \mathbf{v} = -\frac{1}{\rho} \nabla p \quad (2.46)$$

with a fluid pressure given by

$$p = \frac{g}{2m^2} \rho^2. \quad (2.47)$$

Since the pressure depends exclusively on the gradient, in the context of classical fluid dynamics this type of flow is usually called barotropic.

We point out that for both Eq. (2.45) and Eq. (2.44), the analogy with classical hydrodynamics is broken by the term  $\frac{\hbar^2}{2m^2} \frac{\nabla \cdot \nabla \sqrt{\rho}}{\sqrt{\rho}}$ . This term does not have a classical counterpart and for that reason is commonly referred to as a *quantum pressure*. By rewriting the quantum pressure in terms of the healing length, given by Eq. (2.39), and the speed of sound, given by Eq. (2.37), we obtain

$$\frac{\hbar^2}{2m^2} \frac{\nabla \cdot \nabla \sqrt{\rho}}{\sqrt{\rho}} = \xi^2 c^2 \frac{\nabla \cdot \nabla \sqrt{\rho}}{\sqrt{\rho}}. \quad (2.48)$$

From the above equation it is possible to see that the quantum pressure scales as  $\frac{\xi^2}{\tilde{l}^2}$ , where  $\tilde{l}$  is the characteristic length scale for the density variation, which means that the quantum pressure becomes negligible when  $\tilde{l}$  is much larger than the healing length. In this regime (or by setting  $\hbar = 0$ ), it is possible to recover the classical hydrodynamic equations.

As a final remark, we note that the ground state solution given by Eq. (2.19) for an unbounded system, with  $\mu = g|\psi_\infty|^2$ , can be interpreted as a fluid characterised by uniform density and uniform velocity potential in space. For such a fluid, the solution of Eq. (2.44) is indeed given by  $\phi = \frac{g}{m\hbar}\rho t = \frac{\mu}{\hbar}t$ .

## 2.4 Vortex Solutions

We have shown how the GP equation can be correctly interpreted as a superfluid according to the definition of superfluidity given by Landau and how the GP model can be reformulated in terms of a modified version of the classical equations governing the motion of an inviscid, barotropic, irrotational and compressible flow. However, in order to draw a more complete analogy between the GP equation and a superfluid, it is essential to consider solutions corresponding to quantised vortices in the superfluid.

### 2.4.1 Terminology

In order to consider a solution corresponding to a quantum vortex for the GP equation it is useful to recall some terminology typical of classical vortex dynamics [72]. Firstly, it is natural to associate the notion of a vortex to rotations present within a fluid. The concept of rotations in a fluid can be expressed mathematically through the definition of the vorticity field given by Eq. (1.13). We can then call a *vortex line* a curve in the space such that, for each point  $\mathbf{x}$  belonging to that curve, the vorticity field evaluated at  $\mathbf{x}$  has the same direction as the tangent vector of the curve at that point. Similarly, the surface formed by all the vortex-lines passing through a given closed curve is said to be a *vortex tube*. Recalling the definition of circulation given by Eq. (1.14), and Stokes' theorem (1.19), if a curve  $\mathcal{C}$  can be deformed continuously to a point without going outside the fluid domain then the fluid circulation is equal to the flux of the vorticity through the area delimited by  $\mathcal{C}$

$$\Gamma = \int_{\delta\mathcal{C}} \boldsymbol{\omega} \cdot \hat{\mathbf{n}} dA. \quad (2.49)$$

If we now consider the integral

$$\int_V \nabla \cdot \boldsymbol{\omega} dV, \quad (2.50)$$

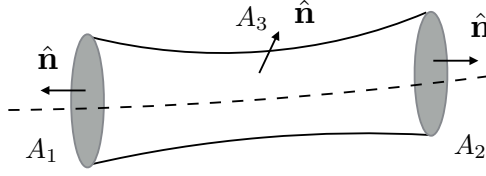


Figure 2.1: Illustration of a vortex tube. The dash line represents the axis of the tube.

where  $V$  (see Fig. 2.1) is the volume contained within the vortex tube delimited by the surfaces  $A_1$  and  $A_2$ , then using the divergence theorem, we can rewrite Eq. (2.50) as

$$\int_V \nabla \cdot \boldsymbol{\omega} dV = \int_{A_1} \boldsymbol{\omega} \cdot \hat{\mathbf{n}} dA + \int_{A_2} \boldsymbol{\omega} \cdot \hat{\mathbf{n}} dA + \int_{A_3} \boldsymbol{\omega} \cdot \hat{\mathbf{n}} dA, \quad (2.51)$$

where  $\hat{\mathbf{n}}$  are the outgoing unit normal vectors to  $A_1$ ,  $A_2$  and  $A_3$ . By definition of the vortex tube,  $\boldsymbol{\omega} \cdot \hat{\mathbf{n}} = 0$  along the surface  $A_3$ , and Eq. (2.51) reduces to

$$\int_V \nabla \cdot \boldsymbol{\omega} dV = \int_{A_1} \boldsymbol{\omega} \cdot \hat{\mathbf{n}} dA + \int_{A_2} \boldsymbol{\omega} \cdot \hat{\mathbf{n}} dA. \quad (2.52)$$

Recalling the vector identity

$$\nabla \cdot \nabla \times \mathbf{v} = 0, \quad (2.53)$$

and redefining the sign of  $\hat{\mathbf{n}}$  according to the direction of the vorticity flux, we obtain

$$\int_{A_1} \boldsymbol{\omega} \cdot \hat{\mathbf{n}} dA = \int_{A_2} \boldsymbol{\omega} \cdot \hat{\mathbf{n}} dA. \quad (2.54)$$

This implies that the flux of vorticity through any cross-section along a vortex tube is constant. This flux is also called the *strength* (or circulation) of a vortex tube that can be related to the intensity of a vortex. Since the strength of the tube does not vary with position along the tube, we can conclude that vortex tubes can either form closed loops, can end at the boundaries when hard walls are considered or extend to infinity. We can now give a definition of a *vortex filament*, which is the main hydrodynamical structure investigated throughout this thesis. When a vortex tube with infinitesimal cross-section is immediately surrounded by irrotational fluid, such an object is called a vortex filament. By taking the limit where the cross-section of such vortex filament tends to zero, the conservation of the circulation of the vortex implies that the vorticity tends to the limiting form of a Dirac delta distribution along the vortex filament. These considerations underlie the assumption made by Feynman on the structure of superfluid vortices.

## 2.4.2 Stationary Vortex Solution

The condition required to have a potential flow with non-zero circulation, given by Eq. (2.55), suggests that a suitable superfluid vortex filament solution for the GP equation could be given by a flow with a velocity field

$$\mathbf{v}(r, \theta, z) = \frac{\Gamma}{2\pi r} \hat{\mathbf{u}}_\theta. \quad (2.55)$$

Recalling the relation given by Eq. (2.42) between the phase field  $\phi$  of the GP wave function and the velocity field  $\mathbf{v}$  of a fluid, we can define

$$\phi = \Gamma \frac{m}{h} \theta, \quad (2.56)$$

which allows us to write a stationary vortex solution as

$$\psi(r, \theta, z, t) = f(r) e^{i\Gamma m \theta / h} e^{-i\frac{\mu}{\hbar} t}, \quad (2.57)$$

where cylindrical coordinates  $(r, \theta, z)$  are used. Since  $\Gamma$  explicitly appears in the condensate wave function, in contrast to a classical vortex filament,  $\Gamma$  can only assume values

$$\Gamma = n \frac{h}{m} \quad (2.58)$$

where  $n \in \mathbf{Z}$ , in order to ensure that  $\psi$  remains single-valued. This condition results in the quantisation of the circulation for superfluid vortices. Unless particular types of anharmonic trapping potentials are considered [73], quantum vortices, in general, appear to be energetically stable only when  $n = \pm 1$  [74]. The condition on the quantisation of the circulation can then be simplified to the particular case

$$\Gamma = \pm \frac{h}{m} \quad (2.59)$$

which provides confirmation of what was already stated in Section 1.1.3. We note that from knowledge of the value of the circulation, it is possible, using Eq. (2.49), to define the vorticity of a straight vortex filament in terms of Dirac's delta distribution as

$$\boldsymbol{\omega}(r, \theta, z) = \pm \frac{h}{m} \delta(r) \hat{e}_z \quad (2.60)$$

where  $\hat{e}_z$  is the unit vector pointing in the  $z$ -direction.

Therefore we have shown that the GP equation can admit vortex solutions consisting of a phase defect of the condensate wave function  $\psi$  or singularities in the velocity field (equivalently of the distribution corresponding to a Dirac delta function for the vorticity field). We now want to investigate how the modulus of  $\psi$  behaves for a vortex solution. To do this, we substitute Eq. (2.57) into the stationary GP equation (2.20) that is written using cylindrical coordinates. This leads to an ordinary differential equation (ODE) for the function  $f(r)$  given by

$$-\frac{\hbar^2}{2m} \frac{1}{r} \frac{d}{dr} \left( r \frac{df(r)}{dr} \right) + \frac{\hbar^2}{2mr^2} f(r) + g f(r)^3 - \mu f(r) = 0. \quad (2.61)$$

By rescaling  $r$  as  $r \rightarrow r\xi$  and using the healing length given by Eq. (2.39), and normalising  $f$  according to the ground state solution of Eq. (2.22) ( $f \rightarrow \psi_\infty f$ ) it is possible to rewrite equation (2.61) as

$$\frac{1}{r} \frac{d}{dr} \left( r \frac{df(r)}{dr} \right) + \frac{1}{r^2} f(r) + f(r)^3 - f(r) = 0. \quad (2.62)$$

As shown in [75], Eq. (2.62) shows that  $f \sim r$  for small distances, while  $f \sim 1 - 1/(2r^2)$  at large distances from the vortex filament. The fact that the density field  $\rho(r) = m\psi_\infty^2 f(r)^2$  is zero along the vortex line is crucial in order to ensure that the condensate wave function is regular along the vortex line. In fact, the singularity arising from the presence of the phase defect is cancelled by the fact that  $|\psi|$  vanishes along the vortex. This is a confirmation that superfluid vortices exist in the form of holes in the density field which ensures the existence of a solution with non-zero circulation.

## 2.5 Vortex Motion

By considering a straight vortex filament aligned along the  $z$ -axis, we found the main results characterising superfluid vortices in the GP model. We will now consider a vortex filament described by a generic geometrical configuration where

- I The vorticity field is confined along a curve and equal to the quantum of circulation:

$$\boldsymbol{\omega}(\mathbf{x}) = \pm \frac{h}{m} \int_s \delta(\mathbf{x} - \mathbf{s}(\sigma)) d^3\sigma, \quad (2.63)$$

where  $\mathbf{s}(\sigma)$  is a curve with parametrisation  $\sigma$ ,

- II Vortex filaments correspond to nodal lines in the density field of the fluid.

### 2.5.1 Vortex Dynamics

In order to understand the dynamics of vortices it would be ideal to rewrite the main equations of motion for a fluid described by Eq. (2.45) in terms of the vorticity field. However, to avoid complication given by the presence of the quantum pressure term, we will now assume an incompressible fluid. The incompressibility assumption requires that the density is materially conserved so that

$$\frac{D\rho}{Dt} = 0, \quad (2.64)$$

where the material derivative is defined as

$$\frac{D}{Dt} = \frac{\partial}{\partial t} + \mathbf{v} \cdot \nabla, \quad (2.65)$$

which reduces the continuity equation (2.43) to

$$\nabla \cdot \mathbf{v} = 0. \quad (2.66)$$

Such an approximation corresponds to neglecting all the variation in the density field. On the one hand, this assumption requires that no compressible waves can be considered, which is a reasonable assumption when we are interested in the vortex dynamics in the limit of zero temperature where phonons are rarely present in the system. On the other hand, the range of variation  $\tilde{l}$  of the density field in proximity of the vortex

core or close to a hard wall must be neglected too. Since in both cases  $\tilde{l}$  is of the order of the healing length [75], the incompressibility approximation is restricted to the study of vortex dynamics at scales much larger than the healing length. This also implies that the quantum pressure terms can also be neglected according to Eq. (2.48).

By using the vector identity

$$\mathbf{v} \times (\nabla \times \mathbf{v}) = \frac{1}{2} \nabla |\mathbf{v}|^2 - (\mathbf{v} \cdot \nabla) \mathbf{v}, \quad (2.67)$$

and taking the curl of Eq. (2.46) one can obtain an equation for the vorticity given by

$$\frac{\partial \boldsymbol{\omega}}{\partial t} - \nabla \times (\mathbf{v} \times \boldsymbol{\omega}) = 0. \quad (2.68)$$

Recalling the relation

$$\nabla \times (\mathbf{v} \times \boldsymbol{\omega}) = \mathbf{v}(\nabla \cdot \boldsymbol{\omega}) - \boldsymbol{\omega}(\nabla \cdot \mathbf{v}) + (\boldsymbol{\omega} \cdot \nabla) \mathbf{v} - (\mathbf{v} \cdot \nabla) \boldsymbol{\omega} \quad (2.69)$$

and using the definition of the material derivative given by Eq. (2.65), we can rewrite Eq. (2.68) as

$$\frac{D\boldsymbol{\omega}}{Dt} = \boldsymbol{\omega} \cdot \nabla \mathbf{v}, \quad (2.70)$$

also called the *vorticity equation* which is true for every barotropic fluid [76]. From the knowledge of Eq. (2.70) it is possible to derive one of main theorems concerning vortex dynamics, the so-called *Helmholtz theorem*, which states that for an inviscid and barotropic flow, vortex filaments are materially transported by the fluid. To prove this theorem we have to focus on Eq. (2.70). We first define the concept of material line as a set of passive particles, for example tracers, lying on a curve  $l$  which is transported by the flow. When the vorticity field is evaluated along a material line  $l$  Eq. (2.70) becomes

$$\frac{d}{dt} (\boldsymbol{\omega})_l = (\boldsymbol{\omega} \cdot \nabla)_l \mathbf{v}. \quad (2.71)$$

Since Eq. (2.71) is the same as the equation governing the motion of an infinitesimal material line

$$\frac{d}{dt} \delta \mathbf{x} = \delta \mathbf{x} \cdot \nabla \mathbf{v}, \quad (2.72)$$

where here  $\delta \mathbf{x}$  is the distance between two passive particles placed respectively at  $\mathbf{x}$  and at  $\mathbf{x} + \delta \mathbf{x}$ , it follows that vortex lines, and hence vortex tubes, are transported with the fluid like material lines.

## 2.5.2 Kelvin Circulation Theorem

We now introduce another fundamental theorem for studying vortex dynamics, the *Kelvin circulation theorem*. This theorem states that the circulation around a closed material line  $\mathcal{C}(t)$  enclosing a vortex line, a vortex tube, or a vortex filament is an invariant of motion. This theorem can be proved by writing

$$\frac{d\Gamma(t)}{dt} = \frac{d}{dt} \oint_{\mathcal{C}(t)} \mathbf{v} \cdot d\mathbf{r} = \oint_{\mathcal{C}(t)} \frac{d}{dt} (\mathbf{v} \cdot d\mathbf{r}) = \oint_{\mathcal{C}(t)} \frac{d\mathbf{v}}{dt} \cdot d\mathbf{r} + \oint_{\mathcal{C}(t)} \mathbf{v} \cdot d\mathbf{v}; \quad (2.73)$$

and then, using Eq. (2.45) we obtain

$$\frac{d\Gamma(t)}{dt} = \int_{\mathcal{C}(t)} \nabla \left( -\frac{g}{m^2} \rho + \frac{\hbar^2}{2m^2} \frac{\nabla^2 \sqrt{\rho}}{\sqrt{\rho}} \right) \cdot d\mathbf{r} + \oint_{\mathcal{C}(t)} \mathbf{v} \cdot d\mathbf{v}. \quad (2.74)$$

If we focus on length scales such that the contribution arising from the quantum pressure term can be neglected, the circulation then results materially transported by the fluid since both the density and the velocity of the fluid must be single-valued. This theorem is valid for the GP model but also for every inviscid and barotropic fluid. It follows that the circulation around a superfluid vortex is not only conserved along the filament, according to Eq. (1.22), but also conserved in time.

## 2.6 Incompressibility Approximation and the Vortex Filament Model

In the previous section we stated the main theorems governing the motions of superfluid vortices. In the zero temperature limit, where superfluid vortices do not experience drag as a result of the interaction with the elementary excitations present in the normal fluid component, we have shown how vortices can be materially transported by the fluid as material lines. In principle, Eq. (2.70) also described how these vortices evolve in time. However, this requires knowledge of the velocity field  $\mathbf{v}(\mathbf{x}, t)$  which in turn depends on the vorticity distribution. In order to determine the required flow field we must invert Eq. (1.13).

### 2.6.1 Biot-Savart Law

As shown by Saffman [72], one of the sufficient condition to invert Eq. (1.13) is to assume the flow to be incompressible. Under this assumption we can invert Eq. (1.13) making use of the well know Helmholtz decomposition

$$\mathbf{v}(\mathbf{x}, t) = \nabla\Phi(\mathbf{x}, t) + \nabla \times \mathbf{A}(\mathbf{x}, t), \quad (2.75)$$

where the velocity field can be expressed in terms of a scalar and a vector potential given by  $\phi$  and  $\mathbf{A}$ , respectively. We note that the incompressibility assumption implies that, in contrast to Eq. (2.42), the scalar potential is well defined and so all the vortex excitations are contained in the vector potential. Hence, for an incompressible flow satisfying Eq. (2.66), the scalar potential  $\Phi$  has to satisfy Laplace's equation

$$\nabla^2\Phi = 0 \quad (2.76)$$

whose solutions have been extensively studied. If we insist that  $\Phi$  is a continuous function then  $\Phi$  will only depend on the boundary conditions chosen. For simplicity, we will neglect the effect induced by the boundary condition in what follows.

By applying the curl operator to Eq.(2.75), and imposing the gauge  $\nabla \cdot \mathbf{A} = 0$ , it is possible to show that the vector potential  $\mathbf{A}$  satisfies Poisson's equation

$$\boldsymbol{\omega}(\mathbf{x}, t) = -\nabla^2 \mathbf{A}(\mathbf{x}, t). \quad (2.77)$$

A solution to the above equation can be expressed in terms of

$$\mathbf{A}(\mathbf{x}, t) = \int G(\mathbf{x} - \mathbf{x}') \boldsymbol{\omega}(\mathbf{x}', t) d^3 \mathbf{x}', \quad (2.78)$$

where the Green function  $G(\mathbf{x} - \mathbf{x}')$  satisfies

$$\nabla_{\mathbf{x}}^2 G(\mathbf{x} - \mathbf{x}') = -\delta(\mathbf{x} - \mathbf{x}'). \quad (2.79)$$

Recalling the known result

$$\nabla^2 \left( \frac{1}{|\mathbf{x} - \mathbf{x}'|} \right) = -4\pi \delta(\mathbf{x} - \mathbf{x}') \quad (2.80)$$

we obtain

$$G(\mathbf{x} - \mathbf{x}') = \frac{1}{4\pi} \frac{1}{|\mathbf{x} - \mathbf{x}'|}. \quad (2.81)$$

This gives

$$\mathbf{A}(\mathbf{x}, t) = \frac{1}{4\pi} \int \frac{1}{|\mathbf{x} - \mathbf{x}'|} \boldsymbol{\omega}(\mathbf{x}', t) d^3 \mathbf{x}'. \quad (2.82)$$

whereas the velocity field induced by corresponding vorticity distribution is given by

$$\begin{aligned} \mathbf{v}(\mathbf{x}, t) &= \frac{1}{4\pi} \int \nabla_{\mathbf{x}} \times \frac{1}{|\mathbf{x} - \mathbf{x}'|} \boldsymbol{\omega}(\mathbf{x}', t) d^3 \mathbf{x}' \\ &= -\frac{1}{4\pi} \int \frac{(\mathbf{x} - \mathbf{x}') \times \boldsymbol{\omega}(\mathbf{x}', t)}{|\mathbf{x} - \mathbf{x}'|^3} d^3 \mathbf{x}' \end{aligned} \quad (2.83)$$

For a superfluid vortex, we know from Eq. (2.63) that the vorticity is a Dirac delta distribution; hence the velocity induced by the vortex is given by the Biot-Savart equation

$$\mathbf{v}(\mathbf{x}, t) = -\frac{\Gamma}{4\pi} \int_s \frac{(\mathbf{x} - \mathbf{s}(\sigma, t)) \times d\mathbf{s}(\sigma, t)}{|\mathbf{x} - \mathbf{s}(\sigma, t)|^3}, \quad (2.84)$$

where the integration is performed along the filament where the vortex lies. Recalling the first Helmholtz theorem, we also know that the vorticity field is materially transported by the flow, so a vortex filament induces its own velocity according to

$$\dot{\mathbf{s}}(\sigma_0, t) = -\frac{\Gamma}{4\pi} \int_s \frac{(\mathbf{s}(\sigma_0, t) - \mathbf{s}(\sigma, t)) \times d\mathbf{s}(\sigma, t)}{|\mathbf{s}(\sigma_0, t) - \mathbf{s}(\sigma, t)|^3}. \quad (2.85)$$

This equation underlies the so-called vortex filament model, which is one of the most used methods to describe the motion of superfluid vortex filaments in an incompressible

superfluid. Give the linearity of Eq. (2.77), for many filaments present in the system, the above equation of motion for filament  $i$  generalises to

$$\dot{\mathbf{s}}_i(\sigma_0, t) = - \sum_j \frac{\Gamma_j}{4\pi} \int_{s_j} \frac{(\mathbf{s}_i(\sigma_0, t) - \mathbf{s}_j(\sigma, t)) \times d\mathbf{s}_j(\sigma, t)}{|\mathbf{s}_i(\sigma_0, t) - \mathbf{s}_j(\sigma, t)|^3}, \quad (2.86)$$

where the sum is performed over all the vortex filaments. We note that Eq. (2.85) can also be obtained by minimizing the action [77]

$$A = \int \dot{\mathbf{q}} \cdot \mathbf{p} d\sigma dt - \int H dt, \quad (2.87)$$

where the filament's position  $\mathbf{s}(\sigma, t)$  represents the Lagrangian variable  $\mathbf{q}(\sigma, t)$  with conjugate momentum

$$\mathbf{p}(\sigma, t) = \rho \frac{\Gamma}{6} \mathbf{s}(\sigma, t) \times \mathbf{s}'(\sigma, t), \quad (2.88)$$

while  $H$  is the system Hamiltonian defined as

$$H = \rho \frac{\Gamma^2}{16\pi} \int_{s_1} \int_{s_2} \frac{d\mathbf{s}(\sigma_1, t) \cdot d\mathbf{s}(\sigma_2, t)}{|\mathbf{s}(\sigma_1, t) - \mathbf{s}(\sigma_2, t)|}. \quad (2.89)$$

We note that the Hamiltonian is equal to the Eulerian kinetic energy

$$E = \frac{1}{2} \rho \int |\mathbf{v}(\mathbf{x}, t)|^2 d^3\mathbf{x} \quad (2.90)$$

for a fluid characterised by a vortex filament vorticity distribution in an unbounded domain.

## 2.7 Local Induction Approximation

We have shown that in the limit of zero temperature, and when the characteristic length scales involved in the dynamics of a vortex (its local radius of curvature or the distance between vortices) are much larger than the healing length, the GP equation can be reduced to the Euler equation for an incompressible and irrotational fluid. Under this assumption, the motion for a vortex filament in the GP model can be governed by Eq. (2.85). A difficulty with the equations we have obtained for a vortex filament is that the integral in Eq.(2.85) is singular when  $\sigma \rightarrow \sigma_0$ . We will now focus on how to regularise this feature of the equation.

### 2.7.1 Singularity Regularisation

Let us focus on the integral of Eq. (2.85) in the proximity of the singularity. To proceed we will parametrize the curve  $\mathbf{s}(\sigma, t)$  by its *arc-length*  $\eta$ , such that  $\mathbf{s}(\sigma, t) =$

$\mathbf{s}(\eta(\sigma, t), t)$ . Omitting the time dependence and defining  $\eta(\sigma_0) = 0$ , we can Taylor-expand  $\mathbf{s}(\eta)$  around  $\eta = 0$ ,

$$\mathbf{s}(\eta) = \mathbf{s}_0 + \mathbf{s}'\eta + \frac{1}{2}\mathbf{s}''\eta^2 + \dots \quad (2.91)$$

where

$$\mathbf{s}_0 = \mathbf{s}(0), \quad \mathbf{s}' = \left. \frac{\partial \mathbf{s}}{\partial \eta} \right|_{\eta=0}, \quad \mathbf{s}'' = \left. \frac{\partial^2 \mathbf{s}}{\partial \eta^2} \right|_{\eta=0}.$$

Making use of the following relations,

$$d\mathbf{s} = \mathbf{s}'d\eta, \quad (2.92)$$

$$\mathbf{s}_0 - \mathbf{s} = -\mathbf{s}'\eta - \frac{1}{2}\mathbf{s}''\eta^2 - \dots, \quad (2.93)$$

$$|\mathbf{s}_0 - \mathbf{s}| = |\eta| \left( 1 + \frac{1}{2}\mathbf{s}' \cdot \mathbf{s}''\eta + O(\eta^3) \right), \quad (2.94)$$

$$|\mathbf{s}_0 - \mathbf{s}|^{-3} \sim |\eta|^{-3} \left( 1 - \frac{3}{2}\mathbf{s}' \cdot \mathbf{s}''\eta \right), \quad (2.95)$$

$$(\mathbf{s}_0 - \mathbf{s}) \times d\mathbf{s} = \left( \frac{1}{2}\mathbf{s}' \times \mathbf{s}''\eta^2 + O(\eta^3) \right) d\eta \quad (2.96)$$

and substituting them into Eq. (2.85), we can isolate the singularity of the vortex filament velocity found in Eq. (2.85) into the local contribution

$$\dot{\mathbf{s}}_0(\text{local}) = -\frac{\Gamma}{8\pi} \int_{-\eta^*}^{\eta^*} \left[ \frac{\mathbf{s}' \times \mathbf{s}''}{|\eta|} + O(1) \right] d\eta, \quad (2.97)$$

where  $\eta^*$  is an upper cut-off parameter of the order of the radius of curvature and  $\dot{\mathbf{s}}$  stands for  $\frac{\partial \mathbf{s}}{\partial t}$ . It is now possible to eliminate the divergence by introducing a lower cut-off  $\xi_0$  of the order of the vortex core, such that

$$\int_{-\eta^*}^{\eta^*} \frac{d\eta}{|\eta|} \longrightarrow \int_{-\eta^*}^{\xi_0} \frac{d\eta}{|\eta|} + \int_{\xi_0}^{\eta^*} \frac{d\eta}{|\eta|} = 2 \log \left( \frac{\eta^*}{\xi_0} \right). \quad (2.98)$$

The introduction of the cut-off parameter  $\xi_0$  is consistent with the assumption made on the density in the vortex filament model. Indeed such a model is based on the assumption that we are neglecting scales smaller than the vortex-core.

We have, therefore, arrived at the regularized local contribution to the self-induced motion for a vortex filament that is given by:

$$\dot{\mathbf{s}}_0(\text{local}) = -\frac{\Gamma}{4\pi} (\mathbf{s}' \times \mathbf{s}'') \left[ \log \left( \frac{\eta^*}{\xi_0} \right) + O(1) \right]. \quad (2.99)$$

### 2.7.2 Local Induction Equations

Upon neglecting the non-local term of Eq. (2.85), the motion of a vortex filament is essentially assumed to be governed entirely by the local term given by Eq. (2.99). However, in order to ensure that the local contribution can correctly describe the dynamics of a vortex, the choice of the parameter  $\eta^* \equiv L$ , normally called the induction length, turns out to be crucial. According to Eq. (2.99), this parameter should in theory depend on the vortex configuration considered and thus be a function of the arclength. For example, concerning the study of helical excitations along a vortex line, by choosing  $L$  to be the inverse of the wave number characterising the vortex excitation, we are able to recover the correct dispersion relation for Kelvin waves propagating along a vortex line in the limit of long waves (see Eq. (7.69)). In contrast, in several problems related to the dynamics of a complicated vortex tangle the correct choice of the induction length turns out to be less important and for numerical convenience such a parameter is normally taken to be constant.

Using the Frenet-Serret frame, the filament can be expressed in terms of its tangent vector

$$\mathbf{t} = \mathbf{s}', \quad (2.100)$$

the normal vector

$$\mathbf{n} = \frac{1}{\kappa} \mathbf{s}'' \quad (2.101)$$

and the binormal vector

$$\mathbf{b} = \mathbf{t} \times \mathbf{n}. \quad (2.102)$$

In this frame, Eq. (2.99) can be expressed as

$$\dot{\mathbf{s}} = \beta \mathbf{b} \quad (2.103)$$

where

$$\beta = \frac{\Gamma}{4\pi} \left[ \log \left( \frac{L}{\xi_{\text{eff}}} \right) \right]. \quad (2.104)$$

We note that  $\xi_{\text{eff}}$  is an effective core radius which accounts for the next to leading order in Eq. (2.99). For instance the velocity for a perfectly circular vortex filament with radius  $R$ , strength  $\Gamma$  and a solid rotating core of size  $\xi_0$  is given by

$$v = \frac{\Gamma}{4\pi R} \left[ \log \left( \frac{8R}{\xi_0} \right) - \frac{1}{4} \right], \quad (2.105)$$

according to classical hydrodynamics [78, 79]. Equation (2.105) suggests that in order to study the motion of a vortex ring using Eq. (2.103), the induction length should be equal to  $L = 8R$  and the effective radius should be  $\xi_{\text{eff}} = e^{1/4} \xi_0$ . A different example is given by the motion of a vortex ring in the GP model [80]. In this case, for an induction length  $L = 8R$ , the effective radius should be  $\xi_{\text{eff}} = e^{0.615} \xi$  with  $\xi$  being the healing length of the system.

Using the Frenet-Serret frame of reference it becomes clear that each vortex filament point moves according to the local geometry of the filament. More specifically, the velocity vector  $\dot{\mathbf{s}}$  points in the direction of the binormal vector and has magnitude proportional to the curvature  $\kappa = |\mathbf{s}''|$ . This purely geometrical model is usually called *local-induction approximation* or simply LIA [51]. Describing the motion of a vortex filament by considering just the local contribution given by Eq. (2.103) is a reasonable approximation when a large scale separation is considered between  $\xi_{\text{eff}}$  and  $L$ .

It is possible to show that this model does not allow self-stretching of a vortex filament. To prove the above statement it is useful to work with curve parametrizations which are time independent. Hence equation (2.103) becomes

$$\frac{\partial \mathbf{s}}{\partial t} = \frac{(\partial \mathbf{s} / \partial \sigma) \times (\partial^2 \mathbf{s} / \partial \sigma^2)}{|(\partial \mathbf{s} / \partial \sigma)|^3}, \quad (2.106)$$

where the constant term  $\beta$  can be factorised out through an appropriate rescaling of time. Writing the length of vortex filament

$$\mathcal{L}(t) = \int_{\sigma_1}^{\sigma_2} \left| \frac{\partial \mathbf{s}}{\partial \sigma} \right| d\sigma \quad (2.107)$$

we can show that this quantity is conserved in time; that is

$$\frac{d\mathcal{L}(t)}{dt} = \int_{\sigma_1}^{\sigma_2} \frac{\partial}{\partial t} \left| \frac{\partial \mathbf{s}}{\partial \sigma} \right| d\sigma = 0, \quad (2.108)$$

since

$$\begin{aligned} \partial_t |\partial_\sigma \mathbf{s}| &= \frac{\partial_\sigma \mathbf{s}}{|\partial_\sigma \mathbf{s}|} \cdot \partial_t \partial_\sigma \mathbf{s} \\ &= \frac{\partial_\sigma \mathbf{s}}{|\partial_\sigma \mathbf{s}|} \cdot \partial_\sigma \left( \frac{\partial_\sigma \mathbf{s} \times \partial_{\sigma\sigma} \mathbf{s}}{|\partial_\sigma \mathbf{s}|^3} \right) \\ &= \frac{\partial_\sigma \mathbf{s}}{|\partial_\sigma \mathbf{s}|} \cdot (\partial_\sigma |\partial_\sigma \mathbf{s}|^{-3} \partial_\sigma \mathbf{s} \times \partial_{\sigma\sigma} \mathbf{s} + |\partial_\sigma \mathbf{s}|^{-3} \partial_{\sigma\sigma} \mathbf{s} \times \partial_{\sigma\sigma} \mathbf{s} + |\partial_\sigma \mathbf{s}|^{-3} \partial_\sigma \mathbf{s} \times \partial_{\sigma\sigma\sigma} \mathbf{s}) \\ &= \frac{\partial_\sigma |\partial_\sigma \mathbf{s}|^{-3}}{|\partial_\sigma \mathbf{s}|} [\partial_\sigma \mathbf{s} \cdot (\partial_\sigma \mathbf{s} \times \partial_{\sigma\sigma} \mathbf{s})] + \frac{|\partial_\sigma \mathbf{s}|^{-3}}{|\partial_\sigma \mathbf{s}|} [\partial_\sigma \mathbf{s} \cdot (\partial_\sigma \mathbf{s} \times \partial_{\sigma\sigma\sigma} \mathbf{s})] \\ &= 0 \end{aligned} \quad (2.109)$$

where  $\partial_\sigma = \frac{\partial}{\partial \sigma}$ .

The total vortex length in LIA plays the same role as the energy (Eq. (2.89)) in the vortex filament model. Indeed, by Taylor expanding Eq. (2.89) about the singularity it is seen that, to logarithmic corrections, the energy in the vortex filament is proportional to the vortex length  $\mathcal{L}$ . It is also possible to show the analogy between the energy of

a vortex and its length by considering Lamb's expression [81] for the Eulerian kinetic energy (Eq. (2.90))

$$E = \rho\Gamma \int_s \dot{\mathbf{s}} \cdot (\mathbf{s} \times \mathbf{s}') d\eta. \quad (2.110)$$

Substituting (2.99) into (2.110) one obtains

$$E = \rho \frac{\Gamma^2}{4\pi} \log\left(\frac{L}{\xi_{\text{eff}}}\right) \int_s d\eta \quad (2.111)$$

which provides how the relation between the vortex length and the vortex energy in the local induction approximation.

Despite the fact that a non-local contribution to the motion of a vortex is neglected in LIA, this model represents a useful simplified model for the study of superfluid turbulence. The equation of motion given by Eq. (2.99) is numerically less expensive to integrate than the full vortex filament equation (2.85). Moreover, most of the theoretical predictions, concerning the scaling of the energy spectra in superfluid turbulence, are formulated within the local induction approximation limit [7, 33].

## 2.8 Vortex Energy

The energy associated with vortex excitations is undoubtedly an important quantity for the understanding of superfluidity. Due to the quantised nature of superfluid vortices a finite energy always needs to be transferred to the superfluid in order to produce a single vortex line. Moreover, when the presence of many vortices interacting together is considered, knowledge of the energy spectra of the kinetic energy associated with vortex excitations becomes crucial in order to interpret how energy is redistributed and ultimately transferred to different length scales in a superfluid turbulent flow.

For an incompressible superfluid, the total vortex energy is simply given by summing the energy of each vortex filament present in the system using either Eq. (2.89) or its local version given by Eq. (2.111). Even though these formulas represent the leading order of the kinetic energy for a vortex in the GP model, their applicability requires knowledge of the positions of each vortex filament present in the system. This problem turns out to be non trivial for the GP model, particularly when complicated vortex tangles are considered.

A more useful working definition for the kinetic energy associated to vortex excitation in the GP model was suggested by Nore *et al.* [82]. Starting from the formula for the total energy of a superfluid (Eq. (2.17)) and making use of the Madelung transformation (Eq. (2.40)) we can separate the total energy into three different contributions given by

$$E_{kin} = \frac{1}{2} \int \rho |\mathbf{v}|^2 d^3\mathbf{x}, \quad (2.112)$$

$$E_{int} = \frac{g}{2} \int \rho^2 d^3 \mathbf{x}, \quad (2.113)$$

$$E_{qu} = \frac{\hbar^2}{2m} \int |\nabla \sqrt{\rho}|^2 d^3 \mathbf{x}. \quad (2.114)$$

The first term given by Eq. (2.112) is the GP counterpart of the hydrodynamic kinetic energy for a classical compressible flow, the second term (Eq. (2.113)) is the internal energy of the flow and the last term given by Eq. (2.114) arises from the presence of the quantum pressure term in Eq. (2.45). By using the Helmholtz decomposition as given by Eq. (2.75) the velocity field appearing in the kinetic energy (see Eq. (2.112)) can be further separated into an incompressible and a compressible component. However, in the presence of a vortex filament the velocity field is not a well defined quantity in the GP model. Hence, we introduce a velocity weighted by the square root of the superfluid density such that

$$\sqrt{\rho} \mathbf{v} = (\sqrt{\rho} \mathbf{v})^i + (\sqrt{\rho} \mathbf{v})^c, \quad (2.115)$$

$$\nabla \cdot (\sqrt{\rho} \mathbf{v})^i = 0, \quad \nabla \times \nabla (\sqrt{\rho} \mathbf{v})^c = 0. \quad (2.116)$$

It has become standard in the literature to interpret

$$E_{kin}^i = \frac{1}{2} \int |(\sqrt{\rho} \mathbf{v})^i|^2 d^3 \mathbf{x}, \quad (2.117)$$

as the incompressible linear energy associated with vortex lines, instead

$$E_{kin}^c = \frac{1}{2} \int |(\sqrt{\rho} \mathbf{v})^c|^2 d^3 \mathbf{x}, \quad (2.118)$$

as the compressible energy associated with the sound excitation.

# Chapter 3

## Vortex Tracking Method

### 3.1 Introduction

The GP model provides a natural framework in which to address many open questions regarding the dynamics of vortices in both weakly interacting Bose gases and superfluid liquid helium-4. This includes physical processes that are involved during vortex reconnections [83, 84, 85], the non-linear interaction and the decay of helical excitations of vortex lines in the form of KWs [28, 86, 87], the interaction of sound with vortices [33], and helicity considerations associated with the dynamics of superfluid vortices [88, 89, 90]. All of these aspects of the vortex dynamics are encountered during a vortex scattering process [52] and within a turbulent vortex tangle [82, 91, 92]. It follows that in order to understand aspects of turbulence and the constituent elementary processes involved during the relaxation of a superfluid vortex tangle, it is essential to be able to extract the location of the vortex filaments from high fidelity numerical simulations. An accurate and reliable numerical method is, therefore, needed for this purpose.

Tracking vortex lines of a complex wave function in three spatial dimensions is in general a challenging problem. Among the range of different methods present in the superfluid literature we recall: zero-crossing [93], standard interpolation techniques [85, 94], low-density averages [95, 86], two-dimensional Newton-Raphson (NR) method on planes corresponding to the Cartesian mesh [28], plaquette method [96, 97, 98] and contour plots of the pseudo-vorticity field [56]. Many of these methods turn out to be either geometry dependent or not accurate enough to evaluate non-trivial geometrical quantities such as curvature, torsion and small-scale KWs on any vortex configuration.

In this chapter we present a novel method for extracting vortex lines of the complex wave function based on the NR method for finding the zeros of a given function [99] for a three-dimensional periodic domain. In order to demonstrate the method's accuracy and robustness, we will present a detailed validation using different test cases. Our aim is to demonstrate the potential broad applicability of the algorithm through consideration of different physical scenarios that are important in superfluids. Application of the method to address specific physical questions is deferred to Chapters 4, 5 and 6.

The chapter is organised as follows. In the first section, we describe how to implement the NR method to track vortices in two-dimensional complex wave functions and the role played by the pseudo-vorticity field. In the second section, we generalize the ideas presented for the 2D case to allow us to develop a novel algorithm to track vortex lines of a three-dimensional wave function by making use of the NR method in combination with the pseudo-vorticity field. In the last section, we demonstrate our algorithm on a number of case studies consisting of different vortex configurations to test the accuracy and the robustness of the method. This includes a detailed evaluation of the curvature and torsion of a perfectly circular vortex ring and a torus knot, two quantities that are very useful to characterise the intrinsic properties of a vortex filaments. As a further test, we also evaluate the KW spectra of a perturbed vortex line and vortex ring to illustrate how the algorithm can accurately extract information of a filament across a broad range of scales. Finally we demonstrate that the method is capable of tracking several vortex rings and even a dense vortex tangle.

## 3.2 Tracking Vortices in Two-Dimensional Complex Fields

In section 2.4.2 we show that quantum vortices represent nodal lines in 3D, or zero points in 2D, in the solutions of the GP equation (2.15). To numerically track quantized vortices in a two-dimensional complex field we can make use of the root-finding routine based on the NR method. This approach has already been used to accurately track quantized vortices in GP simulations [28, 100]. In order to present our method, we will begin by recalling the key elements of the NR method for the vector function  $\Psi : \mathbb{R}^2 \rightarrow \mathbb{R}^2$  defined as

$$\Psi(\mathbf{x}) \equiv \begin{pmatrix} \psi_r(\mathbf{x}) \\ \psi_i(\mathbf{x}) \end{pmatrix} = \mathbf{0}, \quad (3.1)$$

with  $\psi_r \equiv \text{Rw}\psi$  and  $\psi_i \equiv \text{Im}\psi$  and  $\psi$  being a solution of the GP equation. We will assume that we are able to find a good initial guess  $\mathbf{x}^g$  for the true position of the vortex, denoted by  $\mathbf{x}^v$ , such that  $\|\Psi(\mathbf{x}^g)\|^2 < \epsilon |\psi_\infty|^2$ , where  $\psi_\infty$  represents the uniform ground state solution given by Eq. (2.23) and  $\epsilon$  is a parameter assumed to be sufficiently small. We can then express  $\Psi(\mathbf{x}^v) \equiv 0$  in terms of a Taylor-expansion of the function  $\Psi$  about the initial guess to obtain

$$\Psi(\mathbf{x}^v) = \Psi(\mathbf{x}^g) + J(\mathbf{x}^g)(\mathbf{x}^v - \mathbf{x}^g) + \mathcal{O}[(\mathbf{x}^v - \mathbf{x}^g)^2] = \mathbf{0}, \quad (3.2)$$

where

$$J(\mathbf{x}) = \begin{pmatrix} \partial_x \psi_r(\mathbf{x}) & \partial_y \psi_r(\mathbf{x}) \\ \partial_x \psi_i(\mathbf{x}) & \partial_y \psi_i(\mathbf{x}) \end{pmatrix}, \quad (3.3)$$

is a Jacobian  $2 \times 2$  matrix. Assuming that the Jacobian is invertible when evaluated at  $\mathbf{x}^g$ , Eq. (3.3) can be used to obtain a better approximation for the vortex position,  $\mathbf{x}^v$  given by

$$\mathbf{x}^v = \mathbf{x}^g - J^{-1}(\mathbf{x}^g)\Psi(\mathbf{x}^g) + \mathcal{O}[(\mathbf{x}^v - \mathbf{x}^g)^2]. \quad (3.4)$$

This procedure can in principle be iterated as many times as necessary (using the most recent evaluation of  $\mathbf{x}^v$  as the new initial guess for each iteration) in order to converge to the exact location of the vortex. In practice, we will assume a reasonably converged solution when the condition  $\|\Psi(\mathbf{x}^g)\| < \Delta |\psi_\infty|$  is satisfied, where  $\Delta$  is an arbitrarily small parameter which we typically set to be of the order of machine precision. The advantage of this method is the fast quadratic convergence provided by the NR method but does have the drawback that convergence is not ensured if the initial guess,  $\mathbf{x}^g$ , is far from the true solution,  $\mathbf{x}^v$ . A further important requirement to ensure a reliable and accurate numerical method is the accurate evaluation of  $\mathbf{x}^g$  and the Jacobian  $J(\mathbf{x}^g)$  at points that do not necessarily coincide with the grid where the field data is stored. We address these issues by setting a sufficiently small value of  $\epsilon$  and by using a Fourier series expansion of our wavefunction to maintain full consistency with the spectrally accurate representation of our complex scalar field that is recovered from our pseudo-spectral numerical simulations.

We note that simply finding a root of  $\Psi$  is not enough to detect a quantized vortex since certain solitons or solitary wave excitations can also result in a zero density field. We, therefore, also check that the circulation is non-zero. For a classical fluid, the circulation can be evaluated from knowledge of the vorticity field given by Eq. (1.13). However, we recall that in the GP model the vorticity is identically zero everywhere except at the vortex points where it corresponds to a Dirac  $\delta$ -function (see Eq. (1.22)). A related quantity in quantum fluids can be recovered from the density current

$$\mathbf{j} = \rho \mathbf{v} = \frac{\hbar}{2i} (\psi^* \nabla \psi - \psi \nabla \psi^*) \quad (3.5)$$

arising from the definition of the total linear momentum given by Eq. (2.17). This allows us to define a pseudo-vorticity field as

$$\boldsymbol{\omega}_{ps} = \frac{1}{2} \nabla \times \mathbf{j}, \quad (3.6)$$

and has the advantage that it remains regular even at the axis of the vortices. Now writing  $\psi_r = (\psi + \psi^*)/2$  and  $\psi_i = (\psi - \psi^*)/(2i)$ , it is possible to define Eq. (3.6) in terms of the gradients of the real and the imaginary parts of  $\psi$ :

$$\begin{aligned} \boldsymbol{\omega}_{ps} &= \frac{\hbar}{4i} [\nabla \psi^* \times \nabla \psi - \nabla \psi \times \nabla \psi^*] \\ &= \hbar \nabla \left[ \frac{\psi + \psi^*}{2} \right] \times \nabla \left[ \frac{\psi - \psi^*}{2i} \right] \\ &= \hbar \nabla \psi_r(\mathbf{x}) \times \nabla \psi_i(\mathbf{x}). \end{aligned} \quad (3.7)$$

The pseudo-vorticity encodes important information about a vortex. For example, recalling Eqs. (2.41) and (2.57), the wavefunction of a 2D vortex of winding number  $n = \pm 1$  located at the origin can be simply expressed in polar coordinates  $(r, \theta)$  as  $\psi(r, \theta) = \sqrt{\rho(r)/m} e^{in\theta}$ . Substituting this into the expression for  $\psi$  in Eq. (3.7), we obtain

$$\boldsymbol{\omega}_{ps} = n \frac{\hbar}{m} \frac{1}{2r} \frac{\partial \rho}{\partial r} \hat{\mathbf{k}}, \quad (3.8)$$

where  $\hat{\mathbf{k}}$  is a unit vector perpendicular to the plane containing the point vortex. As already discussed in section 2.4.2, for a GP vortex having winding number  $n = \pm 1$  the

density vanishes quadratically at the vortex core but relaxes to a constant far from the vortex. It follows that the pseudo-vorticity is finite at the vortex core and vanishes outside. Furthermore, its sign determines the charge of the vortex.

To provide an example of the ability of the NR algorithm in tracking vortices in a complex field in two spatial dimensions, we simulated a turbulent superfluid state characterised by several vortices and density fluctuations (sound waves) obtained using a two-dimensional GP model. The computational domain considered was periodic and was discretised using a uniform grid with  $256^2$  points and a resolution of  $\Delta x = \Delta y = 0.5\xi$  with  $\xi$  representing the healing length (see Eq. (2.39)) of the superfluid. The initial condition was generated by imprinting 120 vortices onto the condensate. 30 of these vortices were distributed randomly within a quarter of the domain within the interval  $((x, y) \in [0, 128]\xi \times [0, 128]\xi)$ . Half of the 30 vortices had a winding number  $n = 1$  whilst the remainder had a winding number  $n = -1$ . The vortices in the remaining three quarters were then obtained by reflecting the vortex positions along the lines  $x = 128\xi$  and  $y = 128\xi$ . This initial condition contained a fourfold mirror symmetry which ensures the periodicity in both the phase and the modulus of the complex wave function  $\psi$ .

The imprinting of the vortices was accomplished by taking a product of the single-vortex wave function defined using a Padé approximation as described in [101]. Starting with this initial condition, we allowed the system to evolve and interact for a sufficiently long time in order to lose the initial symmetry and to reach a more chaotic state containing 50 vortices coexisting with sound waves. The GP equation was integrated in time using a Strang splitting pseudo-spectral method. In figures 3.1(a) and 3.1(b)

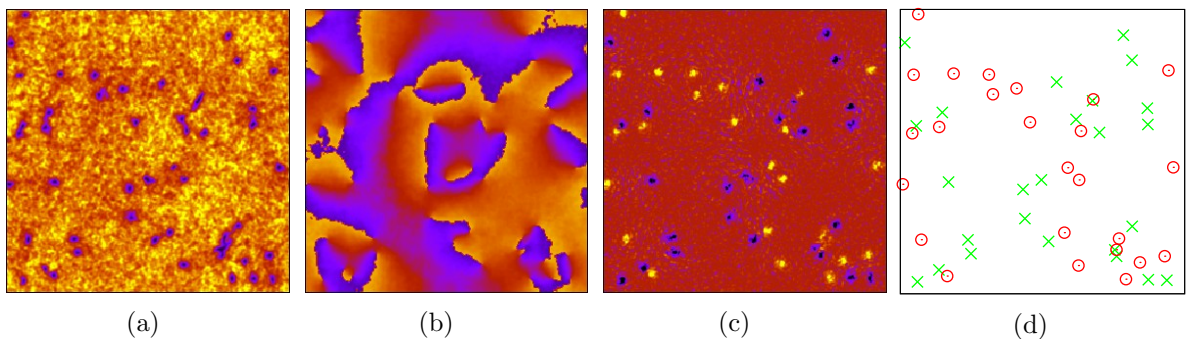


Figure 3.1: Latest stage of the dynamics of 50 vortices in a two-dimensional GP model: (a) plot of the squared modulus of  $\psi$  where dark colors represent depletions in  $|\psi|^2$  and light colors high values of  $|\psi|^2$ ; (b) plot of phase field varying continuously from  $-\pi h/m$ , blue color, to  $\pi h/m$ , yellow color; (c) plot of the pseudo vorticity field, where yellow and blue points are respectively maxima and minima, while the field vanishes in the red area; (d) tracked vortex positions, where red circles are vortices with negative circulations, while green crosses are vortices with positive circulations.

we plot the squared modulus and the argument of  $\psi$ , respectively, at an intermediate time when a turbulent state has emerged. The vortices are clearly discernible in these plots and correspond to localised density depletions within a field that is otherwise dominated by density fluctuations extending over space. However, in regions where

the vortices are tightly clustered together (see for instance the bottom right region), it is not immediately obvious what are the corresponding number of vortices in these regions. In figure 3.1(c) we present the computed pseudo-vorticity field. As can be seen, this field clarifies not only the number of vortices present in tight clusters but also their charge. In figure 3.1(d) we plot the extracted vortex positions as computed using the NR technique, distinguishing between vortices characterized by positive (red circle) and negative (green cross) values of circulation. We remark that the tracking parameters chosen here were  $\Delta = 10^{-13}$  and  $\epsilon = 0.3$ . The average number of NR iterations were around 4-5 per vortex while the computational time involved was of the order of a few seconds on a standard desktop machine.

### 3.3 Tracking Vortex Filaments in Three-Dimensional Complex Fields

In contrast to the two-dimensional case where vortices appear in the form of point-like defects, in three spatial dimensions, quantized vortices correspond to filaments which can either form closed loops or end at domain boundaries. The configuration of the filaments can be arbitrarily complicated usually exhibiting non-trivial functional dependence on the local curvature and torsion [40, 102]. Aside from the complex vortex geometries that can arise, quantized vortices can also have a non-trivial topology by organizing themselves into knotted and/or linked structures [88, 103, 53, 104, 105].

Given the much more diverse range of scenarios that can arise in 3D, tracking vortex filaments has remained a significant challenge in simulations of the GP equation. In order to generalize our method to vortex filaments, we will firstly note that the NR method cannot be directly applied to the function  $\Psi : \mathbb{R}^3 \rightarrow \mathbb{R}^2$  since the Jacobian (see Eq. (3.3)) would no longer be a square matrix. Alternatively, one might try to apply the method to  $\psi$  defined on planes orthogonal to the Cartesian coordinates. This approach would present difficulties in the case when the vortex filament is (almost) tangent to the plane since the determinant of Eq. (3.3) becomes almost singular thereby severely degrading the convergence and stability of the method. Another separate problem that arises in 3D is associated with how to recognise that different points in space correspond to zeros of the wavefunction belonging to the same vortex. This information concerning the connectivity of vortex filaments within a tracking algorithm presents a major issue when either a high density of vortex filaments are present in the computational domain or when two vortex filaments are extremely close to one another.

To circumvent these potential difficulties, we will make use of the pseudo-vorticity field defined by Eq. (3.7). Considering that a vortex filament is a curve where both  $\psi_r$  and  $\psi_i$  have to vanish, it follows that projections of both  $\nabla\psi_r$  and  $\nabla\psi_i$  onto the curve must also vanish. These considerations reveal that the pseudo-vorticity field given by Eq. (3.7) is always tangent to the vortex filament. Such a vector field evaluated in the vicinity of a filament not only allows us to identify a plane that is essentially orthogonal to the filament, but it also provides the connectivity information that allows us to determine which points belong to the same vortex.

The tracking algorithm we propose can now be summarised into the following steps

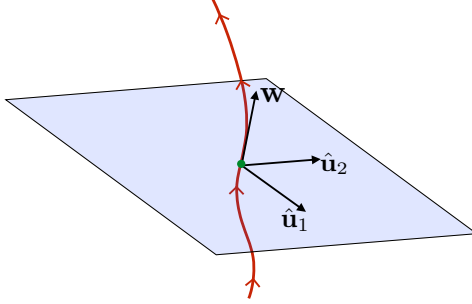


Figure 3.2: Sketch of the plane  $\Pi$  where we develop the tracking.

(see also Fig. 3.2 for an illustration):

1. we begin with an arbitrary initial guess for a zero of  $\Psi$  which we denote by  $\mathbf{x}^g$  such that  $\|\Psi(\mathbf{x}^g)\|^2 < \epsilon |\psi_\infty|^2$ ;
2. for  $\epsilon$  sufficiently small,  $\mathbf{x}^g$  will be sufficiently close to the vortex filament. We can then evaluate the pseudo-vorticity field  $\boldsymbol{\omega}_{ps}(\mathbf{x}^g)$  and assume that it points in a direction that is almost parallel to the vortex.
3. we define  $\Pi$  as the plane that passes through the point  $\mathbf{x}^g$  and orthogonal to the direction of  $\boldsymbol{\omega}_{ps}(\mathbf{x}^g)$ . This allows us to identify an orthogonal basis  $(\hat{\mathbf{u}}_1, \hat{\mathbf{u}}_2)$  for such a plane up to some arbitrary rotation.
4. we apply the NR method on the plane  $\Pi$  obtaining

$$\mathbf{x}^v = \mathbf{x}^g - J_\Pi^{-1}(\mathbf{x}^g)\Psi(\mathbf{x}^g) + \mathcal{O}[(\mathbf{x}^v - \mathbf{x}^g)^2], \quad (3.9)$$

where the  $2 \times 2$  Jacobian matrix projected on the plane  $\Pi$  is given by

$$J_\Pi(\mathbf{x}) = \begin{pmatrix} \nabla\psi_r(\mathbf{x}) \cdot \hat{\mathbf{u}}_1 & \nabla\psi_r(\mathbf{x}) \cdot \hat{\mathbf{u}}_2 \\ \nabla\psi_i(\mathbf{x}) \cdot \hat{\mathbf{u}}_1 & \nabla\psi_i(\mathbf{x}) \cdot \hat{\mathbf{u}}_2 \end{pmatrix}. \quad (3.10)$$

We note that by construction  $\mathbf{x}^v$  will always lie on the plane  $\Pi$ . As for the application of the NR method in the two-dimensional case, we now keep iterating Eq. (3.9) until the condition  $\|\Psi(\mathbf{x}^v)\| < \Delta |\psi_\infty|$  is satisfied;

5. we now interpret the point  $\mathbf{x}^v$  to belong to the  $j$ 'th vortex filament and store it as  $\mathbf{x}_i^{(j)} = \mathbf{x}^v$ . The integer,  $i$ , is set to one at the beginning of the tracking for each vortex filament and is incremented for each consecutive point extracted along a given filament. In order to identify the next point,  $\mathbf{x}_{i+1}^{(j)}$ , along the filament, we make use of the fact that the pseudo-vorticity field is tangent to the curve. We, therefore, set our next guess to correspond to

$$\mathbf{x}^g = \mathbf{x}_i^{(j)} + \zeta \hat{\boldsymbol{\omega}}_{ps}(\mathbf{x}_i), \quad (3.11)$$

where  $\zeta$  is an arbitrary small parameter and  $\hat{\boldsymbol{\omega}}_{ps}(\mathbf{x}_i)$  is the pseudo-vorticity vector normalised to unity;

6. we return to step (2.) in our algorithm unless  $i > 1$  and one of the following closing conditions for the  $j$ 'th vortex filament is satisfied:
  - a) the Euclidean distance  $d_{1k}^{(j)} = \|\mathbf{x}_1^{(j)} - \mathbf{x}_k^{(j)}\|$  is much less than the parameter  $\zeta$  (we typically set  $d_{1k}^{(j)} < \zeta/3$ ). Indeed, for values of  $\zeta$  that are small relative to the local radius of curvature of the filament, we can assume that the arclength between two consecutive points is approximately equal to  $\zeta$ . Hence, when the distance  $d_{1n}^{(j)}$  becomes much smaller than  $\zeta$ , we assume that the  $j$ 'th vortex filament to be closed and identify it with a vortex loop;
  - b) the point  $\mathbf{x}_i^{(j)} = (x_i^{(j)}, y_i^{(j)}, z_i^{(j)})$  on the  $j$ 'th vortex filament is identified with a vortex line if it satisfies the conditions  $\mathbf{x}_i^{(j)} \simeq (x_1^{(j)} \pm L_x, y_1^{(j)}, z_1^{(j)})$  or  $\mathbf{x}_i^{(j)} \simeq (x_1^{(j)}, y_1^{(j)} \pm L_y, z_1^{(j)})$  or  $\mathbf{x}_i^{(j)} \simeq (x_1^{(j)}, y_1^{(j)}, z_1^{(j)} \pm L_z)$  where  $L_x$ ,  $L_y$  and  $L_z$  denote the dimensions of the periodic domain along the three coordinate directions, respectively. We note that due to the assumed periodicity of the field, points such as  $(x_1^{(j)} \pm L_x, y_1^{(j)}, z_1^{(j)})$  do not need to lie within the computational domain;
7. the  $j$ 'th vortex loop or line is then stored and we return to step (1.) to search for the next vortex filament. In order to avoid re-tracking the same filament multiple times, we make use of a Boolean matrix, initially having all values set to zero, with same size of the grid on which  $\psi$  is discretized. After tracking the  $j$ 'th vortex filament, we set the Boolean matrix equal to unity on all the grid points close to it. The initial guess for the  $(j + 1)$ 'th vortex filament is then explored within the remaining volume grid points that correspond to zero entries of the Boolean matrix.

## 3.4 Case Studies

In order to demonstrate the accuracy and robustness of the tracking method described above, we will present several test cases corresponding to different vortex configurations.

### 3.4.1 Vortex Ring and Torus Vortex Knot

We will initially focus on systems containing a single vortex filament in the form of a vortex loop. We will begin with the simplest possible geometry, a perfectly circular vortex ring before proceeding to track a topologically non-trivial vortex such as a torus vortex knot. To test the accuracy of the method, we compute geometrical quantities such as the coordinates, curvature and torsion of the filaments and compare these against their respective theoretical values. Both cases are evaluated in a computational domain consisting of a grid of  $128^3$  points and a resolution  $\Delta x = \Delta y = \Delta z = 0.5\xi$ .

We begin by considering a ring with a radius  $R = 4\xi$  moving along the  $z$ -coordinate direction. To set the initial condition, we use the analytical expressions obtained using a Padé approximant by Berloff [101] for a two-dimensional vortex on the  $x$ - $y$  plane

centred at  $(0, R)$  and then rotating such a plane around the  $z$ -axis. This produces a vortex ring that is located along the curve given by

$$\mathbf{s}(\sigma) = (R \cos \sigma, R \sin \sigma, 0), \quad (3.12)$$

where the parameter  $\sigma \in [0, 2\pi)$ . After tracking the filament, we computed the geometrical distance between the tracked vortex points and the exact vortex filament to evaluate the error. This gave a maximum value of the order of  $\sim 10^{-7}$  thus verifying the precision to which we are able to track the vortices. To further check the accuracy of the method, we calculated the curvature  $\kappa$  and torsion  $\tau$ , that require the evaluation of high order derivatives of the positions of the filament with respect to the parametrisation of the curve. These can be obtained using the expressions

$$\kappa = \frac{|\mathbf{s}' \times \mathbf{s}''|}{|\mathbf{s}'|^3}, \quad \tau = \frac{(\mathbf{s}' \times \mathbf{s}'') \cdot \mathbf{s}'''}{|\mathbf{s}' \times \mathbf{s}''|^2}, \quad (3.13)$$

where  $\mathbf{s}'$ ,  $\mathbf{s}''$  and  $\mathbf{s}'''$  represent the derivatives with respect to the parameter  $\sigma$ . From the tracked points, we estimated the constant curvature of the ring to be  $\kappa = (0.25 \pm 0.2 \times 10^{-5})\xi$  and the torsion to be  $\tau = (0 \pm 10^{-4})\xi$ . These values are in excellent agreement with the theoretical values for the curvature and torsion given by  $\kappa_{th} = 1/4\xi$  (inverse of the ring radius) and  $\tau_{th} = 0$ , respectively. We remark that accurate evaluation of these quantities is necessary in several problems involving the dynamics of vortices. For example, establishing a connection between the GP model and the vortex filament model of a superfluid allows us to attribute energy and momentum to each vortex excitation [106, 107]. This makes it possible to identify the energy spectrum on each vortex filament [108]. Moreover, curvature and torsion provide an intrinsic description of the geometry of a vortex filament that could be used to identify soliton-like excitations [109]. On the other hand, accurate evaluation of the torsion is relevant to the study of helicity for vortex filaments [110, 111]. Therefore, the ability to extract these quantities will be invaluable in understanding fundamental aspects of the dynamics of superfluid vortices.

Having demonstrated the algorithm on a simple vortex ring, we will now consider a vortex with a non-trivial topology: a torus vortex knot. The study of vortex knots in superfluids has attracted much interest in recent years as it provides an ideal paradigm to address questions related to helicity conservation in superfluids [53, 88, 90]. A torus knot  $\mathbb{T}^{p,q}$  is a closed curve built on the surface of a torus having toroidal and poloidal radii  $R_0$  and  $R_1$  respectively that has been twisted  $p$ -times around the toroidal axis and  $q$ -times around the poloidal axis, where  $p$  and  $q$  are co-prime integers. Its parametrisation  $\mathbf{s}(\sigma) = (s_1(\sigma), s_2(\sigma), s_3(\sigma))$  is given by

$$s_1(\sigma) = [R_0 + R_1 \cos(p\sigma)] \cos(q\sigma), \quad (3.14)$$

$$s_2(\sigma) = [R_0 + R_1 \cos(p\sigma)] \sin(q\sigma), \quad (3.15)$$

$$s_3(\sigma) = R_1 \sin(p\sigma), \quad (3.16)$$

where  $\sigma \in [0, 2\pi)$ . The wave function containing a vortex knot  $\mathbb{T}^{p,q}$  is based on the

formula introduced in Proment *et al.* [53] and given by

$$\begin{aligned}
 \psi_{p,q}(x, y, z) = & \prod_{i=1}^p \psi_{2D} \left\{ s(x, y) - R_0 - R_1 \cos \left[ \alpha(x, y) + i \frac{2\pi q}{p} \right], \right. \\
 & \left. z - R_1 \sin \left[ \alpha(x, y) + i \frac{2\pi q}{p} \right] \right\} \\
 & \times \prod_{i=1}^p \psi_{2D}^* \left\{ s(x, y) + R_0 + R_1 \cos \left[ \alpha(x, y) + i \frac{2\pi q}{p} \right], \right. \\
 & \left. z - R_1 \sin \left[ \alpha(x, y) + i \frac{2\pi q}{p} \right] \right\}, \tag{3.17}
 \end{aligned}$$

where

$$s(x, y) = \text{sgn}(x) \sqrt{x^2 + y^2}, \quad \text{and} \quad \alpha(x, y) = \frac{q \text{atan2}(x, y)}{p}. \tag{3.18}$$

Here,  $\psi_{2D}(s - s_0, z - z_0)$  describes the two-dimensional wave function of a single vortex centred at  $(s_0, z_0)$  [101],  $\text{sgn}(\cdot)$  is the sign function, and  $\text{atan2}(\cdot, \cdot)$  is the four-quadrant arctangent. In order to account for the periodic boundary conditions assumed in this work, we modify Eq. (3.17) by setting

$$\psi_{p,q}^{(per)}(x, y, z) = \psi_{p,q}(x_p, y_p, z_p), \tag{3.19}$$

where  $x_p, y_p$  and  $z_p$  is a periodic approximation of the identity at  $(L_x/2, L_y/2, L_z/4)$ . Namely

$$x_p = -\frac{L_x}{\pi} \cos \frac{\pi}{L_x} x, \quad y_p = -\frac{L_y}{\pi} \cos \frac{\pi}{L_y} y, \quad z_p = -\frac{L_z}{2\pi} \cos \frac{2\pi}{L_z} z. \tag{3.20}$$

Torsion and curvature displayed in figures 3.3(c) and 3.3(d) are then computed by accounting for corrections due to the assumed periodicity of the field according to Eq. (3.20). The knot is thus defined by the line

$$(x_p^{-1}(s_x(\sigma)), y_p^{-1}(s_y(\sigma)), z_p^{-1}(s_z(\sigma))),$$

obtained from Eq. (3.16). As an example, we consider the torus knot  $\mathbb{T}^{2,5}$  built on a torus with a toroidal radius  $R_0 = 8\xi$  and a poloidal radius  $R_1 = \xi/2$ . In figure 3.3(a) we plot the iso-surfaces of the density field of the wave function corresponding to  $|\psi|^2 = 0.1 |\psi_\infty|^2$ . For a knot with such a small poloidal radius (smaller than  $\xi$ ), an iso-surfaces of the density does not allow us to clearly distinguish its geometry from a vortex ring. However, after tracking the filament, its topology becomes apparent, as shown in Fig. 3.3(b). In figures 3.3(c) and 3.3(d) we present a comparison between the numerically computed and analytical expressions for the curvature and torsion, respectively. The numerical results (shown as a blue circled line) coincide with the theoretical predictions with only a small amount of noise observed in the torsion that is caused by the way the initial condition for the wavefunction is generated.

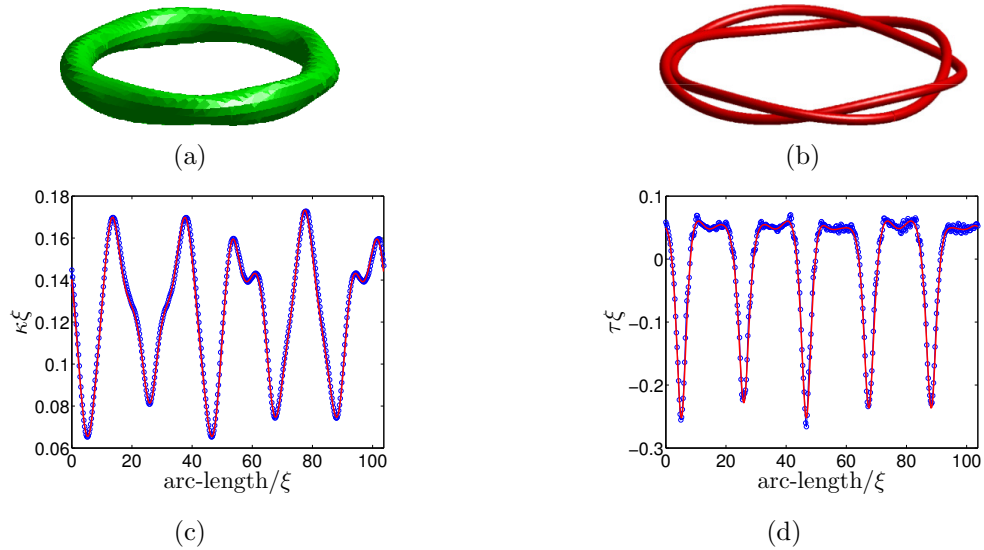


Figure 3.3: (a) Iso-surface plot corresponding to  $|\psi|^2 = 0.1 |\psi_\infty|^2$  for a torus vortex knot; (b) Plot of the tracked vortex filament where the vortex line has been rendered as a vortex tube to clearly demonstrate the non-trivial topology; (c) Plot of the curvature and (d) Plot of torsion versus arc-length. The numerical data (blue circled line) has been superimposed on the theoretical predictions (red line).

### 3.4.2 Kelvin Wave Spectra

In order to illustrate the applicability of the algorithm to a problem containing multiple length scales, we now demonstrate how it can be reliably used to detect small amplitude KWs on a vortex filament [112]. Kelvin waves and their energy spectra have been the object of investigation for some time since their nonlinear interactions is believed to provide a key mechanism in quantum turbulence to transfer energy down to length scales of the order of the vortex core where it can be dissipated through phonon emission. An accurate measurement of the KWs and their spectra on an almost straight vortex line using the two-dimensional NR method has already been performed by Krstulovic [28]. However, the tracking technique described in that work relied on a-priori knowledge of the vortex line configuration, namely that the vortex line was almost orthogonal to planes where the NR method is applied. Since our method is completely independent of the filament's configuration as well as orientation relative to the computational grid, we are able to measure not only the KW spectrum of a vortex line but also the KW spectrum of a vortex ring.

To create a wave function characterised by KWs on a straight vortex line that is aligned along the  $z$ -axis, we first consider the wave function of the straight vortex line and then shift the  $x-y$  planes accordingly (for more details refer to [28]). KWs on a ring lying on the  $x-y$  plane are imposed in a similar way by using the Padé approximation with a perturbed radius together with a small  $z$ -component. To test the ability of the algorithm to capture small amplitude KWs, we impose steep KW spectra corresponding to  $n(k) \sim k^{-6}$  and  $n(k) \sim k^{-3}$  on the vortex line and the ring, respectively. We now

provide further details on the procedure used to define the KW spectra on a vortex line and on a vortex ring. We begin with the a straight line with small amplitude KWs which can be parametrised as

$$\mathbf{S}_{\text{KW}}(\sigma) = (X(\sigma), Y(\sigma), \sigma). \quad (3.21)$$

Assuming that the line is periodic in the  $z$  direction, the KW spectrum is defined as

$$n_k = |\widehat{\mathbf{S}}_{\text{KW}}(k)|^2 + |\widehat{\mathbf{S}}_{\text{KW}}(-k)|^2, \quad (3.22)$$

where  $\widehat{\mathbf{S}}_{\text{KW}}(k)$  is the Fourier transform of  $\mathbf{S}_{\text{KW}}(\sigma) = (X(\sigma), Y(\sigma))$ . Note that lines obtained from the tracking are not directly parametrised in terms of  $\sigma$ . In order to numerically compute the Fourier transform, the line is remeshed on a regular partition of the interval  $[0, L_z]$  (where  $L_z$  is the size of the periodic domain along the  $z$ -coordinate direction) obtained by a high-order interpolation. In Krstulovic [28], KWs on a straight line were accurately tracked by a NR method using planes perpendicular to the line. The algorithm used in [28] provided a parametrization on a regular mesh that directly allows for the evaluation of the Fourier transform. We have checked that the interpolation does not affect the values of the spectrum at the scales of interest.

In order to obtain the KW spectrum of waves on a ring we proceed as follows. Starting from a ring with KWs  $\mathbf{S}_{\text{KW}}(s)$  expressed in its natural parametrisation, we obtain a long-scale averaged ring  $\mathbf{S}_{\text{smooth}}(s)$  by convolving the line with a Gaussian kernel of width  $\alpha L$ , where  $\alpha \in (0, 1)$  and  $L$  is the total length of the line. Once this smooth ring is computed, we define the KWs as

$$\mathbf{S}_{\text{KW}}(s) = \mathbf{S}(s) - \mathbf{S}_{\text{smooth}}(s). \quad (3.23)$$

Figure 3.4 (a) displays a test case with KWs (shown in blue) and the corresponding smooth ring (shown in red). By construction,  $\mathbf{S}_{\text{KW}}(s)$  is a periodic set of 3 signals (one for each spatial dimension). The KW spectrum is then simply defined as in Eq. (3.22) using the Fourier transform of  $\mathbf{S}_{\text{KW}}(s)$ .

Note that the tracking algorithm provides a parametrisation  $\sigma$  that is close to the natural one but not necessarily equal as after each step  $\zeta$ , the location of the vortex is re-evaluated in the new plane so the distance between the previous point and the new one can be slightly different from  $\zeta$ . As in the case of KWs on a straight vortex, the line obtained from the algorithm is re-parametrised in a regular partition of  $[0, L]$  by using a high order interpolation. In this work we used a value of  $\alpha = 0.1$ . Varying this coefficient only slightly modifies the large-scale values of the spectrum as demonstrated in Fig. 3.4 (b), but values at scales where scaling is observed remain unchanged.

Finally, to smooth out any possible strong gradients in the field arising from the shifts used to construct the initial condition, we integrate our initial conditions over a short duration within the GP equation. The insets of Figs. 3.5(a) and 3.5(b) illustrate the vortex line and the ring, respectively, with their corresponding KW excitations. In figures 3.5(a) and 3.5(b) we present the numerically computed KW spectra (blue circled line) together with the imposed scalings on the KWs that are shown as a red dashed line. The results clearly show that the spectra are reproduced by the algorithm

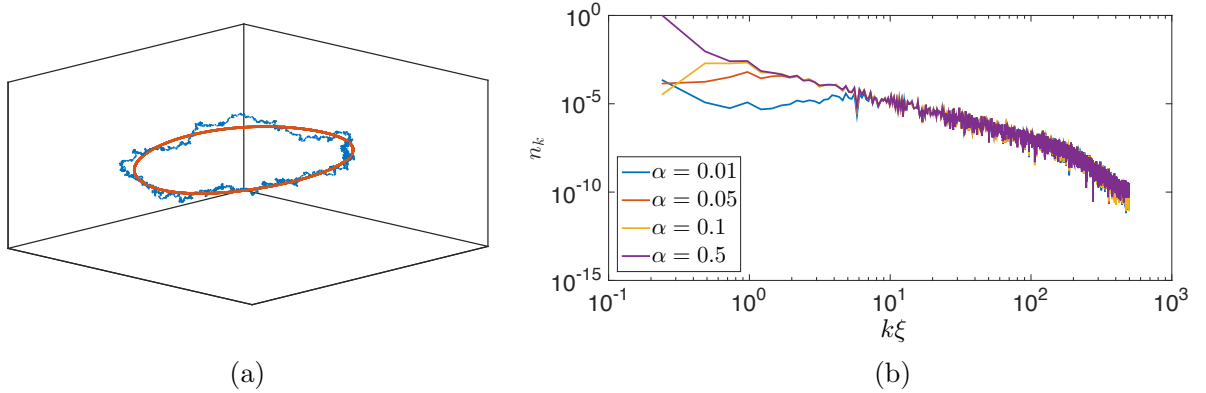


Figure 3.4: (a) Smooth (red line) and perturbed vortex ring with imposed KW spectrum (blue line); (b) KW spectra of the vortex ring presented in (a) computed for different values of the smoothing kernel coefficient  $\alpha$ .

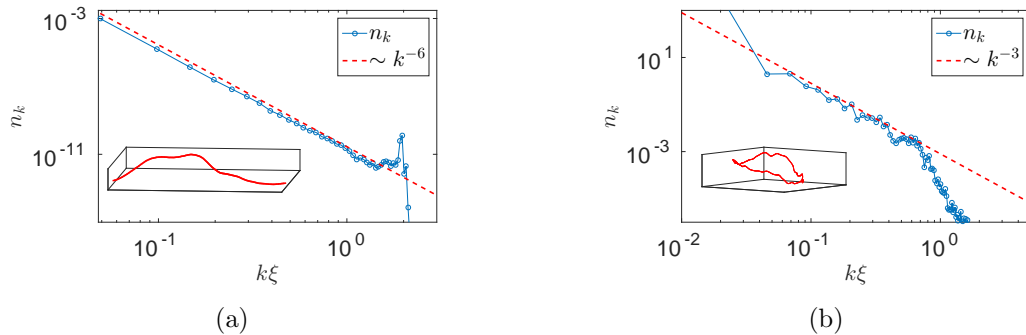


Figure 3.5: (a) Log-log plot of the KW spectrum induced on a vortex line and (b) on a vortex ring, where a power law (red line) has been introduced for comparison with the numerical data (blue circled line). The insets show both the perturbed vortex line and the vortex ring.

down to the vortex core size. Note that whereas for the KWs on a straight line the spectrum is uniquely defined, on a ring KWs are defined as the perturbation of a smooth ring. To obtain the smooth ring, a convolution with some kernel is needed. The large scales of its spectra are thus kernel dependent, but small scales are independent.

### 3.4.3 Several Rings

Having demonstrated the accuracy of the method, we now aim to test the robustness of the algorithm on more complex scenarios. More specifically, we will show that the method is able to track complex vortex configurations characterized by several vortex loops. As an example, we consider 20 vortex rings all having the same radii of  $R = 8\xi$  but randomly placed and oriented in the computational domain. To prepare the initial condition, we multiply 20 wave functions (randomly translated and rotated) of a single vortex ring discretized on a grid with  $256^3$  points and with a resolution

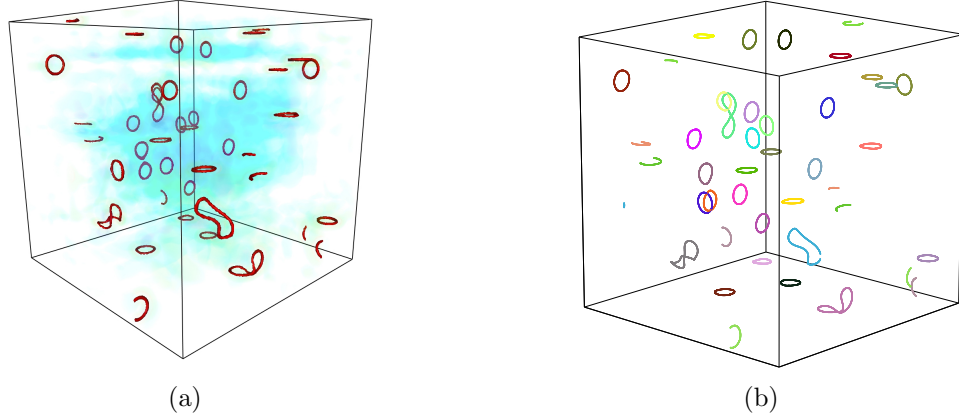


Figure 3.6: a) iso-surface plot corresponding to  $|\psi|^2 = 0.1 |\psi_\infty|^2$  for a wave function containing several rings, blue colours renders the sound waves; b) Plot of the vortex rings obtained by tracking zeros of the wave function  $\psi$ .

$\Delta_x = \Delta_y = \Delta_z = \xi$ . We then evolve this initial condition for a short time before extracting the vortex positions to obtain a more realistic vortex configuration where also sound waves are present. In figures 3.6(a) and 3.6(b) we plot the iso-surfaces corresponding to  $|\psi|^2 = 0.1 |\psi_\infty|^2$  and the tracked vortex loops, respectively. Visually inspecting the two sub-plots provides qualitative confirmation that the method correctly detects all the vortex rings present in the system. We remark that the computational time needed to track this configuration is less than one hour on a standard desktop machine.

### 3.4.4 Vortex Tangle

For our final case study, we test the tracking method on a GP simulation containing a dense tangle of quantized vortices. Such a configuration corresponds to a particularly important scenario in the study of quantum fluids since it represents an example of isotropic and homogeneous quantum turbulence. Due to the high density of vortices and the broad range of length scales involved in the dynamics, a vortex tangle also represents one of the most challenging vortex configurations to track. Following the work of Nore *et al.*[82], we created a tangle of vortices by evolving an initial configuration characterised by a so-called Taylor-Green (TG) flow. For further details see Appendix. The iso-surfaces of the low-density field and the tracked vortex filaments corresponding to the initial condition are shown respectively in figures 3.7(a) and 3.7(b). We remark that the tracking has been carried out by setting  $\zeta = \xi$  in Eq. (3.11) and required a computational time of less than 1 hour on 64 cores running in parallel using MPI. Upon integrating this initial condition forward in time with the GP equation, the interaction between the large scale vortex rings drives the system toward a vortex configuration characterised by a dense tangle where the superfluid motion occurs on a range of time and length scales within the system. This produces a quantum turbulent state as

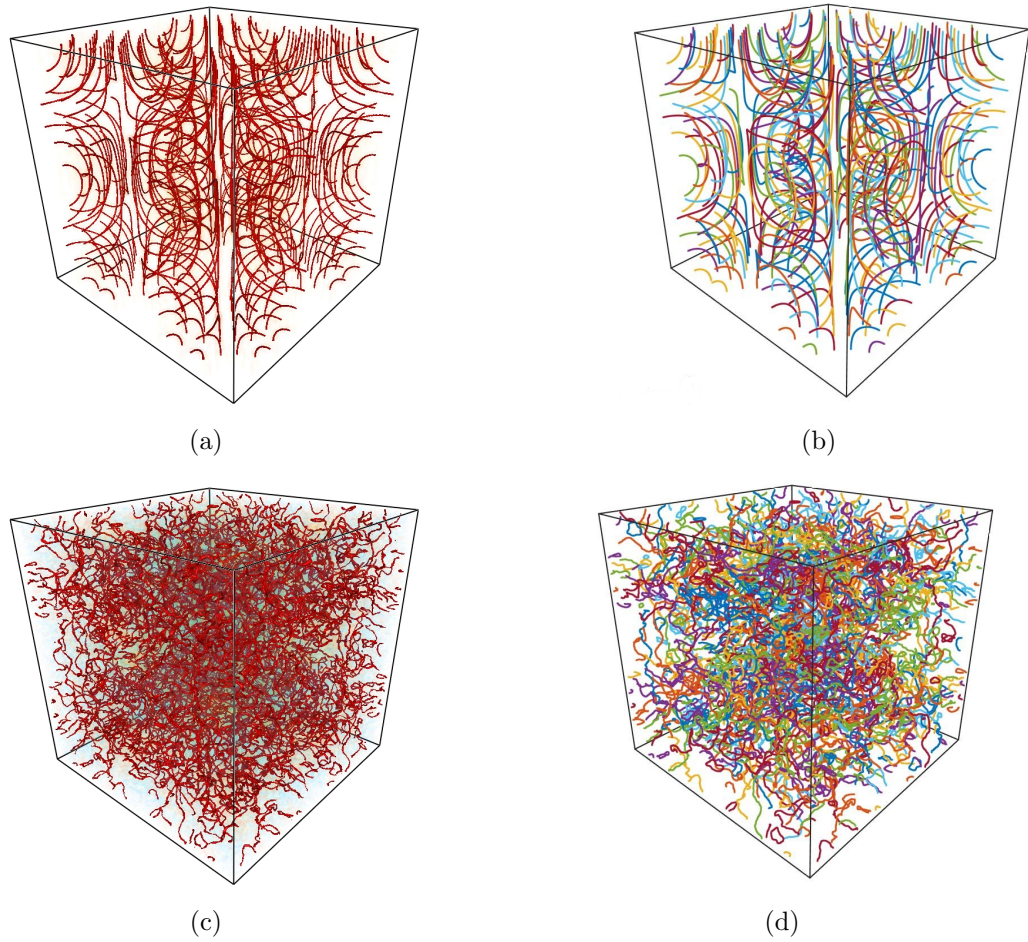


Figure 3.7: Iso-surface plot corresponding to  $|\psi|^2 = 0.1 |\psi_\infty|^2$  for the TG flow (a) at the initial condition and (c) after evolving the system for a time  $t = 10 t_{ed}$ , where  $t_{ed}$  corresponds to the largest eddy turnover time of the TG flow; tracked vortex filaments corresponding to (b)  $t = 0 t_{ed}$  and (d)  $t = 10 t_{ed}$ .

illustrated in the low density iso-surface plots shown in Fig. 3.7(c) that were obtained after a time  $t \simeq 10 t_{\text{ed}}$ , where  $t_{\text{ed}}$  corresponds to the largest eddy turnover time of the TG flow. In contrast to the initial condition, the tracking of such a complicated tangle requires us to set  $\zeta = 0.25\xi$  in order to explore all the small scales associated with the vortex dynamics. Figure 3.7(d) shows the tracked vortex filaments; the tracking process took a computational time of approximately 6 hours on a cluster with 64 cores working in parallel using MPI. Since we have no a-priori knowledge of the number of vortex rings composing the tangle displayed at  $t = 10 t_{\text{ed}}$ , no direct validation of the tracking is possible.

The tracking process reveals that the tangle is composed of 576 rings with arc-lengths that vary from  $L_{\text{ring}} = 8.4\xi$  to  $L_{\text{ring}} = 1108\xi$ . We point out that these smallest vortex rings found have radii of the order of the numerical resolution. Such small rings tend to shrink due to their interaction with sound waves that act as a thermal bath [113]. Given that our smallest rings are of the order of the healing length, smaller rings would not be expected to arise in our simulations as they would become rarefaction pulses [114] with no topological charge. A more complete analysis of the rings making up the vortex tangle is given by the probability distribution function (PDF) of the ring sizes displayed in figure 3.8(a). We see that most of the rings have relatively small size. Such insight into the statistical properties of small vortices can help in estimating the amount of energy transferred into sound waves that compose the bath of thermal excitations through the process of vortex shrinking and annihilation. It is also true that the same PDF exhibits quite large fluctuations which indicates the presence of relatively large vortex rings. Such large vortices are good candidates for testing predictions of KW spectra [31, 115, 116, 117] because they span a broad range of scales.

Our tracking algorithm also allows us to explore the spatial distribution of the vortex tangle. For instance, we can evaluate the minimal inter-vortex distance between the  $i$ 'th and  $j$ 'th vortex rings

$$\ell_{\min}^{(i,j)} = \min (\| \mathbf{x}^{(i)} - \mathbf{x}^{(j)} \|) , \quad (3.24)$$

defined by choosing the minimum value of the distance between their vortex points. The PDF of the minimal inter-vortex distances obtained by considering all the combinations of vortex ring pairs is displayed in Fig. 3.8(b). The mean value of this distribution is given by  $\langle \ell_{\min} \rangle = 102.7\xi$ . Another important quantity to quantify in superfluid turbulence is the mean inter-vortex distance which is estimated to be  $\ell_{\text{est}} \sim 1/\sqrt{\mathcal{L}}$  where  $\mathcal{L}$  is the total vortex length per unit volume [7]. Using our tracking algorithm, we are able to precisely determine the total vortex line length which we find to be  $80765.6\xi$ , providing an estimated mean inter-vortex distance of  $\ell_{\text{est}} = 14.4\xi$ . We can define the average inter-vortex distance between the  $i$ 'th and  $j$ 'th vortex rings as

$$\ell_{\text{mean}}^{(i,j)} = \frac{1}{\mathcal{N}_i \mathcal{N}_j} \sum_{k,l} \| \mathbf{x}_k^{(i)} - \mathbf{x}_l^{(j)} \| , \quad (3.25)$$

where  $\mathcal{N}_i$  and  $\mathcal{N}_j$  are the number of points contained in the  $i$ 'th and  $j$ 'th vortex rings, respectively. The tracked mean inter-vortex distance can then be evaluated as

$$\langle \ell \rangle_{\text{track}} = \frac{1}{n_v} \sum_{i=1}^{n_v} \min_{j \neq i} (\ell_{\text{mean}}^{(i,j)}) , \quad (3.26)$$

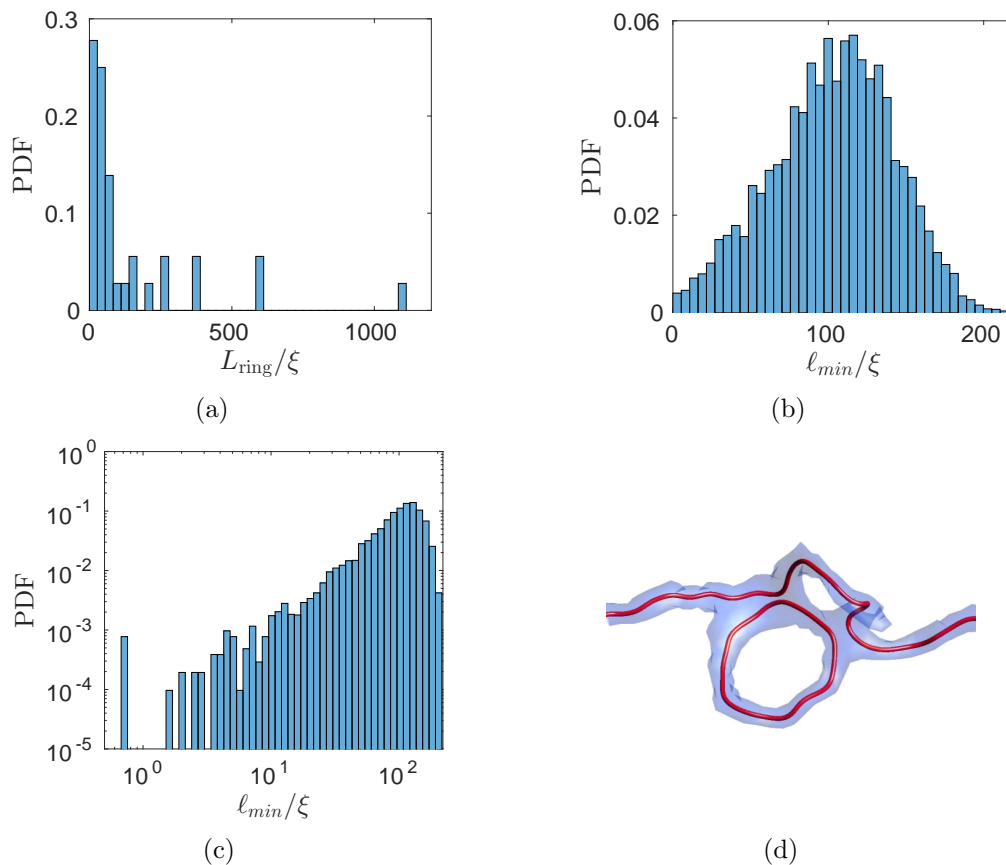


Figure 3.8: (a) PDF plot of the sizes of the vortex rings; PDF plot of the minimal inter-vortex distance between each pair of vortex rings: (b) in linear scale and (c) in log-log scale; (d) Iso-surface plot (light blue) at  $|\psi|^2 = 0.1 |\psi_\infty|^2$  for two vortices extracted from the tangle undergoing a reconnection. The tracked vortex positions are rendered with a red tube.

where  $n_v$  is the total number of vortices in the system. In this particular case we obtain  $\langle \ell \rangle_{track} = 25.7\xi$  which is of the same order of  $\ell_{est}$ .

Finally, in Fig. 3.8(c) we plot the minimal inter-vortex distance in logarithmic scales in order to uncover the trend of the distribution at distances close to zero. Remarkably, we notice that the algorithm is able to track vortex filaments whose minimal inter-vortex distance is smaller than the computational grid ( $\Delta x = \Delta y = \Delta z = \xi$ ). In figure 3.8(d), we zoom in on a part of the tangle to reveal two vortices with a minimal inter-vortex separation of  $0.6\xi$ . This figure further illustrates the accuracy of the algorithm and demonstrates the possibilities it provides in studying processes occurring on very small scales including vortex reconnection events that have generated significant interest in recent years [56, 85].

## 3.5 Conclusions

In this Chapter we described a method to detect and analyse quantum vortices within a flow governed by the GP equation. For a given GP complex wave function  $\psi$ , this method uses a Newton-Raphson root-finding algorithm to detect the zeroes of a complex scalar field and employs the pseudo-vorticity field to reconstruct the entire distribution of vortex filaments. Our assumption on the periodicity of the complex field allowed us to make extensive use of spectral techniques to compute the configuration of the field and its derivatives at any point in the computational domain. The method is formulated in a general way making no assumptions about the geometry or topology of the vortex filaments. It is, therefore, applicable to any vortex configuration that might arise in the dynamics of superfluid vortices. We presented several case studies to assess the accuracy and robustness of our vortex tracking algorithm which are relevant to our understanding of the role of quantized vortices in superfluids. We demonstrated the accuracy of the method by showing that it can be used to accurately calculate the curvature and torsion, two quantities that are important in quantifying properties of superfluid vortices. We remark that, because of the spectral representation that we adopted for the complex wave function, our method allows us to compute any high order directional derivative along the vortex line by using the tangent vector along the filament (that can be computed from the pseudo-vorticity field) rather than using a spline interpolation scheme. Moreover, we showed that the method can be used to extract information over a broad range of scales including small scale KWs oscillations. It is also capable of distinguishing between different filaments with an inter-vortex separation that can be smaller than the computational grid size.

# Chapter 4

## Scattering of Line-Ring Vortices

### 4.1 Introduction

Quantized vortex rings in superfluids constitute one of the most fundamental localised topological excitations in quantum turbulence. In recent years, such vortex rings have attracted much attention as they continue to provide a key mechanism in understanding the transition to quantum turbulence [118]. At the same time, they can serve as a vital mechanism in understanding how different regimes of turbulence can coexist on disparate length and time scales. When forced at large scales, quantum turbulence can give rise to a Kolmogorov-like  $5/3$  scaling in the inertial range in the energy spectrum. It has been proposed that this gives way to the KW cascade at higher wave numbers for liquid helium-4 within the ultra-low temperature regime [34, 106]. Within the cross-over range of scales, the emission of vortex rings from individual quantized vortex filaments acts to assist in the transfer of energy from large quasi-classical motion to the small Kelvin-wave cascade. Indeed, without such a mechanism, a bottleneck can form within the energy cascade [38]. However, once these rings are emitted, their subsequent role in the direct energy cascade of superfluid turbulence remains unclear. This is particularly so since no measurements of the characteristics of turbulence within the cross-over range has thus far been made. The possible scenarios are that the emitted vortex rings can either pass through the tangle with little interaction or they could be reabsorbed. This question of the transparency of the tangle to the emission of vortex rings remains an open and not well understood problem in superfluid turbulence.

The important role that vortex rings occupy in the study of quantum turbulence has prompted detailed experimental studies of these excitations in both helium-4 and helium-3 [37, 119]. This has revealed that the number density of vortex rings strongly determines the likelihood of neighbouring vortex rings to reconnect. This subsequently influences their time of flight. Such studies can help uncover the nature of turbulence within the cross-over range of scales. However, a better understanding of how vortices interact and scatter with vortex lines is also important in order to establish a clear understanding of the role of vortex rings within this range of scales. In this chapter, we will present a detailed numerical study of the scattering of a single vortex ring with a straight superfluid vortex. This scenario is in contrast to the scattering between vortex rings [120] and can be viewed as a paradigm of how vortex rings interact with vortex

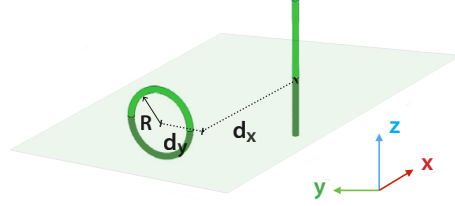


Figure 4.1: The initial configuration used to study the scattering between a line vortex and a vortex ring. The ring, having initial radius  $R$ , lies in the  $y$ - $z$  plane and moves along the  $x$  direction, while the line is aligned with the  $z$ -coordinate direction and passes through the origin  $(0, 0)$ .

lines or bundles [121] within fully developed quantum turbulence. Our approach relies primarily on the mean field theory of the GP equation. However, to relate this to the hydrodynamic interpretation of quantum turbulence, we also interpret our results using the Biot-Savart law and its simpler approximate form given by the local induction approximation. To accomplish this, we develop diagnostics to extract the location of topological excitations from our mean-field model simulations that allows us to track the evolution of key quantities including vortex line length that provide a direct measure of key attributes associated with these topological defects.

## 4.2 Numerical Method

In this chapter, we numerically solve a dimensionless form of the GP equation (2.15). Using the transformations  $x \rightarrow \xi x$ , where  $\xi$  is the healing length (2.39),  $t \rightarrow \gamma t$ , where  $\gamma = \xi/\sqrt{2}c$  is the unit of time arising from the definition of the speed of sound  $c$  (2.37) and  $\psi \rightarrow \psi_\infty \psi$ , with  $\psi_\infty$  defined by Eq. (2.22), Eq. (2.15) becomes

$$i \frac{\partial}{\partial t} \psi = -\frac{1}{2} \nabla^2 \psi + \frac{1}{2} |\psi|^2 \psi. \quad (4.1)$$

The initial conditions we use for Eq. (4.1) always correspond to a single straight line vortex and a vortex ring that is perfectly circular. We make the hypothesis that the ring is small compared to the line by assuming that the radius,  $R$ , of the ring is much smaller than the distance,  $d_x$ , between the ring and the line vortex. Due to the size of the computational domain that extends over a length  $L = 128$  in each direction, we are restricted to set  $R/d_x = 1/6$ . The boundary conditions are taken to be periodic along the  $z$ -coordinate direction which coincides with the axis of the straight line vortex, and reflecting in the other two directions corresponding to the  $x$ - $y$  plane. We note that the choice of reflective boundary conditions is essential in order to study a system characterised by non-zero overall circulation. We also remark that the reflective boundary conditions are equivalent to the fourfold mirror symmetry used in Section 3.2. Figure 4.1 provides an illustration of a typical initial condition.

The complex wave-function  $\psi$  is discretised in a cubic box having a uniform grid of  $256^3$  points. In order to accurately resolve the vortex core, we set the grid resolution

to  $\Delta x = \Delta y = \Delta z = 0.5$  so that  $L = 128$  as required. The radius of the ring is set to  $R = 8$  and its initial distance from the line is set to  $d_x = 48$  to minimize the influence of the reflective boundaries and the line vortex on the ring. The line vortex is centred at the origin located at the centre of the computational domain while the vortex ring is located at  $(-d_x, d_y, 0)$  and lies in the  $y$ - $z$  plane. The initial condition is then obtained by setting  $\psi(\mathbf{x}, t = 0) = \psi_{\text{Line}}(x, y, z) \times \psi_{\text{Ring}}(x, y, z)$  where

$$\psi_{\text{Line}}(x, y, z) = f(r)e^{in\theta}, \quad (4.2)$$

with  $r = \sqrt{x^2 + y^2}$  and  $\theta = \arctan(y/x)$ . This irrotational vortex has quantized circulation characterized by the discrete winding number  $n$ . The radial density profile  $f(r)$  can be obtained from a Padé approximation as described by Berloff [101]. The solution for a vortex ring with radius  $R$  moving along the  $x$ -direction is given by [53]

$$\psi_{\text{Ring}}(x, y, z) = f(\eta_1)f(\eta_2)e^{i(\arctan((\sqrt{z^2+y^2}-R)/x)-\arctan((\sqrt{z^2+y^2+R}/x))}, \quad (4.3)$$

where  $\eta_1 = \sqrt{(\sqrt{z^2 + y^2} - R)^2 + x^2}$  and  $\eta_2 = \sqrt{(\sqrt{z^2 + y^2} + R)^2 + x^2}$ .

The non-dimensional GP equation (4.1) is integrated forward in time using a standard Strang splitting pseudo-spectral method. Defining the linear and non-linear operators appearing in Eq. (4.1) as  $\hat{\mathcal{L}} = 1/2\nabla^2$  and  $\hat{\mathcal{N}} = -1/2|\psi|^2$  respectively, we can write for a sufficiently small time step  $\Delta t$

$$\psi(\mathbf{x}, t + \Delta t) = e^{i\Delta t(\hat{\mathcal{N}}+\hat{\mathcal{L}})}\psi(\mathbf{x}, t) \approx e^{i\frac{\Delta t}{2}\hat{\mathcal{N}}} e^{i\Delta t\hat{\mathcal{L}}} e^{i\frac{\Delta t}{2}\hat{\mathcal{N}}} \psi(\mathbf{x}, t). \quad (4.4)$$

This approximation has an error of order  $\mathcal{O}(\Delta t^2)$ . The integration of the non-linear operator can be easily computed in physical space using

$$\psi(\mathbf{x}, t) = \psi(\mathbf{x}, t^*) e^{-i|\psi|^2(t-t^*)/2}. \quad (4.5)$$

On the other hand the integration of the linear operator part is performed in Fourier space as

$$\tilde{\psi}(\mathbf{k}, t) = \tilde{\psi}(\mathbf{k}, t^*) e^{-i\omega(\mathbf{k})(t-t^*)}, \quad (4.6)$$

where  $\tilde{(\cdot)}$  denotes the Fourier-cosine transformed quantity and  $\omega(\mathbf{k}) = |\mathbf{k}|^2/2$  is the angular frequency of the Fourier mode  $\mathbf{k}$ . This is accomplished by decomposing the field  $\psi$  using discrete cosine transforms in the  $x, y$  directions and the discrete Fourier transform in the  $z$  direction in order to satisfy the reflective and periodic boundary conditions in the respective coordinate directions. In all our simulations, we set  $\Delta t = 0.02$ , such that it is much smaller than the fastest linear period  $T_{\text{fast}} = 2\pi/\omega$  of the system.

### 4.3 Results

In Fig. 4.2(a), we present an example of the scattering of a vortex ring by a line vortex for an initial condition corresponding to  $d_y/R = 0$ . In contrast to the scattering of a 2D dipole with a single vortex [122], in general, for the 3D case, we observe the

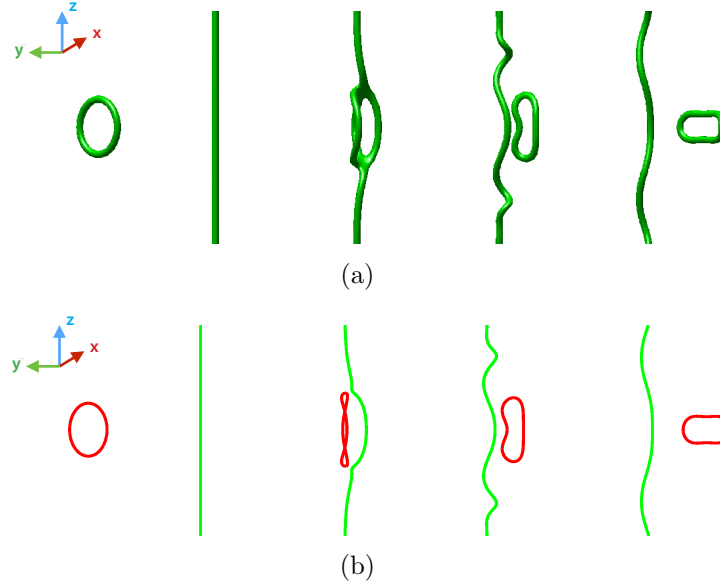


Figure 4.2: Time sequence of scattering of a vortex ring by a line vortex computed by integrating the GP equation (4.1) shown at  $t = 0, 225, 250, 300$ : (a) iso-surfaces of the density field at the value  $|\psi|^2 = 0.3$ ; (b) Vortex filament representation of topological excitations obtained by tracking zeros of the wavefunction.

sequence of events: (i) the ring approaches the line vortex with a trajectory that is slightly deviated by the induced velocity field; (ii) if the two objects are sufficiently close to one another, a reconnection takes place and a new ring escapes from the line; (iii) excitations in the form of KWs are generated both on the line and on the ring. These features are clearly discernible in Fig. 4.2(a).

In order to quantify the properties of the interaction between the two objects, it is useful to evaluate the momentum of each topological excitation. The GP model can be used to evaluate the total energy and momentum of the system arising from the total contribution associated with all excitations present in the flow. However, in the limit when the healing length is very small compared to other characteristic length scales within the flow, it is often possible to approximate the flow by an incompressible system as described in §2.5.1. In principle, this allows us to attribute momentum and energy to different contributions arising from the Biot-Savart integral for each vortex. In order to do this, we need to find the collection of points describing the vortex defects, by tracking the vortices in the computed GP wave-function. To accomplish this, we make use of the 2D vortex tracking method explained in Section 3.2 to find a zero of the wave-function in a plane. By applying this to the  $x$ - $y$ ,  $x$ - $z$ , and  $y$ - $z$  planes of our numerical domain, and appropriately connecting all the points, we are able to separately extract the ring and the line vortex from the wavefunction field as presented in Fig. 4.2(b). The results are in agreement with the vortices identified by the low-density isosurfaces of Fig. 4.2(a) which confirms the reliability of our tracking algorithm.

For the same run, we evaluated how the different contributions to the GP energy

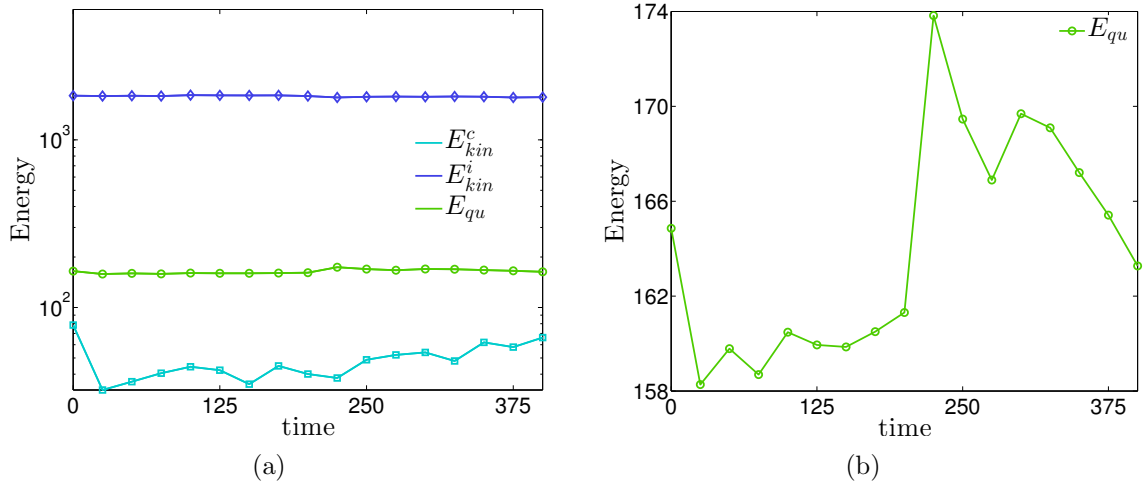


Figure 4.3: Variation of energy as function of time: (a) different components of the energy on a semi-logarithmic plot, (b) evolution of quantum energy during a reconnection event (color figure online).

vary during the scattering. The evolution of the quantum energy  $E_{qu}$ , the incompressible kinetic energy  $E_{kin}^i$ , and the compressible kinetic energy  $E_{kin}^c$  as given in Eqs. (2.114), (2.117) and (2.118) are plotted in Fig. 4.3(a). The results confirm that the contribution from the compressible kinetic energy is negligible with respect to the incompressible one; it remains two orders of magnitude smaller in comparison to the other components even during reconnections. Nevertheless, we expect that the compressible energy per unit volume can become large locally during reconnections. Upon closer inspection of the quantum energy as shown in Fig. 4.3(b), we observe a sharp increase within the time interval between  $t = [200, 250]$ . This time period coincides with a reconnection event as indicated in Fig. 4.2. Despite the substantial increase in the quantum energy during such events, it remains significantly below the incompressible kinetic energy. This verifies that our simulations are performed within a regime where a hydrodynamic approximation is expected to be valid. For this reason, we will analyse our results in terms of the Biot-Savart or LIA models after applying the vortex tracking algorithm.

In particular, we will focus on how the scattering process depends on the initial ring offset by varying this parameter within the interval  $d_y/R \in [-1.5, 3.5]$ . To extract the information on the final quantities after the scattering, we computed the centre of mass of the ring  $\mathbf{x}_{CM}^{Ring}$  as the average of the positions of the points tracked with the algorithm. Once the ring had reached a threshold distance of  $d/R = 6$  from the line vortex (where  $d$  is the total distance between the ring and the line vortex), the ringline interaction was assumed to be small at which point the relevant quantities were computed. The corresponding time at which such quantities are evaluated is denoted by  $t_f$ .

We begin by presenting in Fig. 4.4(a) results for the variation of the vortex ring and line lengths as a function of time for two cases corresponding to  $d_y/R = 0$  and  $d_y/R = 2$ . In each case, the length of each vortex has been normalised with respect to its initial value given at time  $t_i$ . For the offset value  $d_y/R = 0$ , we observe that both

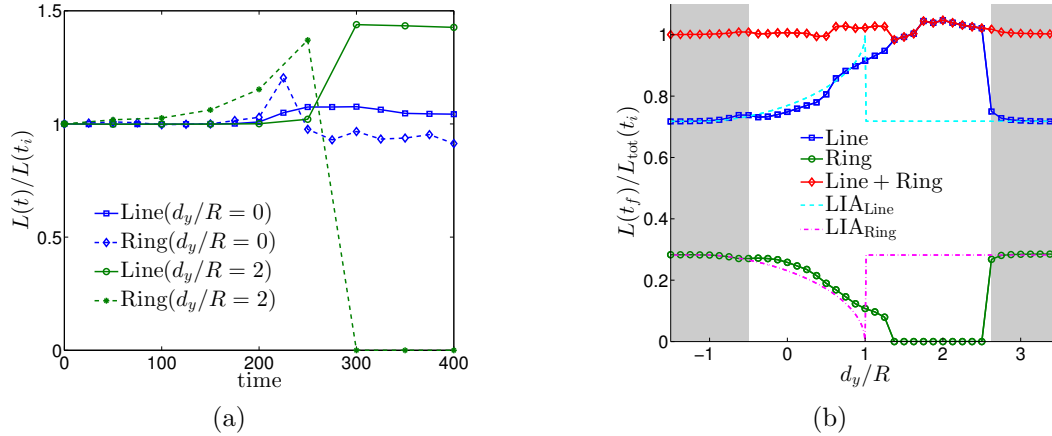


Figure 4.4: (a) Variation of length of line and ring vortex as a function of time during a reconnection; (b) Final length for the line vortex and the ring normalised by the total initial initial length for different values of the initial offset parameter  $d_y/R$ . Also shown is the theoretical prediction made with the LIA.

lengths remain essentially constant up to the point of a reconnection, during which the line vortex absorbs part of the ring length. At later times, both lengths show some fluctuations due to the presence of propagating KWs on both vortices which is in agreement with the results reported in [123]. In contrast, the case with the offset value  $d_y/R = 2$  reveals a markedly different trend in the time dependence of the line length. In particular, following a reconnection, the ring is completely absorbed by the line vortex.

In Fig. 4.4(b), we evaluated the ratio of the initial and final lengths separately for the vortex ring  $L_{\text{Ring}}$  and the line vortex  $L_{\text{Line}}$  as a function of initial ring offset  $d_y/R$ . Also presented is the total length. For comparison, we have included predictions obtained from LIA in which the reconnected segments of the line and ring vortices can be obtained from purely geometric considerations. The most striking feature of this plot is the asymmetric dependence of the computed line length on initial vortex offset. This is attributed to the severe constraints imposed by the winding around the line vortex and the vortex ring which enforces a very specific change of topology onto the system. Consequently, for our configurations, positive offset values lead to smaller rings being produced whereas negative offset values result in larger rings. Despite the strong nonlocal nature of the line vortex interaction that arises from the Biot-Savart integral upon close approach of the ring to the line vortex, it is interesting that LIA captures the integrated quantities such as line length quite well away from the reconnections. Close inspection of Fig. 4.4(b) shows that the agreement between the LIA predictions and numerical results is particularly good within the interval  $d_y/R \in [-1.5, -0.5] \cup (2.5, 3.5]$ .

To explain this, we note that within the LIA, a reconnection can only occur if the projection of the initial vortex ring position in the direction along the centreline of the ring crosses the line vortex, that is for  $d_y/R \in [-1, 1]$ . Hence, reconnections



Figure 4.5: Asymmetric behaviour for two collisions having two opposite starting offset positions ( $d_y/R$ ). Different colours are used for the vortex line and ring for ease of visualisation; (a)  $d_y/R = -0.75$ , (b)  $d_y/R = 0.75$ . The initial vortex ring positions relative to the initial location of the line vortex are shown in the insets.

are not permitted outside this interval which leads to the stepwise jump at  $d_y/R = 1$  seen in Fig. 4.4(b). For  $d_y/R \in [-1, -0.5)$ , reconnections occur within the LIA but lead to small depletions in the length of the ring. On the other hand, GP simulations show no reconnections within this interval. This is caused by the nonlocal nature of the line vortex interaction in which the ring significantly distorts the line such that it can pass by without reconnecting. For this reason, the agreement between the GP and LIA turns out to be exceptionally good within the interval  $d_y/R \in [-1.5, -0.5)$ . For  $d_y/R \in [-0.5, 2.5]$ , reconnections occur within the GP simulations which results in a departure of the calculated final line lengths in comparison to LIA. For values of  $d_y/R \in [1, 2.5]$ , the discrepancies are greatest since reconnections still occur in our GP simulations but cease for LIA due to the geometric considerations discussed above. Moreover, we observe a complete absorption of the ring by the vortex line in the interval  $d_y/R \in [1.4, 2.5]$ . A modified LIA model that accounts for some non-local effects was proposed by Schwarz [60]. The non-local term reduces the interval over which reconnections can occur from  $d_y/R \in [-1, 1]$  to  $d_y/R \in [-0.5, 1]$ . This extended model of Schwarz is also in good agreement with our numerical results. We point out that the ratio between the ring radius and initial distance from the line vortex in Schwarz's work is  $1/10$  so that the vortex ring is initially located further away than in our simulations which have a ratio  $d_x/R = 1/6$ . A quantitative comparison, therefore, cannot be made.

As a clear illustration of the asymmetry seen in our simulations, we present in Fig. 4.5 plots of the vortex line and ring positions following a reconnection event for two opposite values of the ring offset parameter. These plots were obtained by extracting the vortex positions using our tracking algorithm to elucidate the differences seen for the two different values of the initial offset corresponding to ( $d_y/R = -0.75$ ) and to ( $d_y/R = 0.75$ ). Due to the conservation of the circulation, reconnections always lead to the new ring being located to the *left* in our figures. Thus the emitted rings have very different size following their encounter with the line vortex.

Under the LIA, smaller circular rings are known to travel faster than larger ones. We

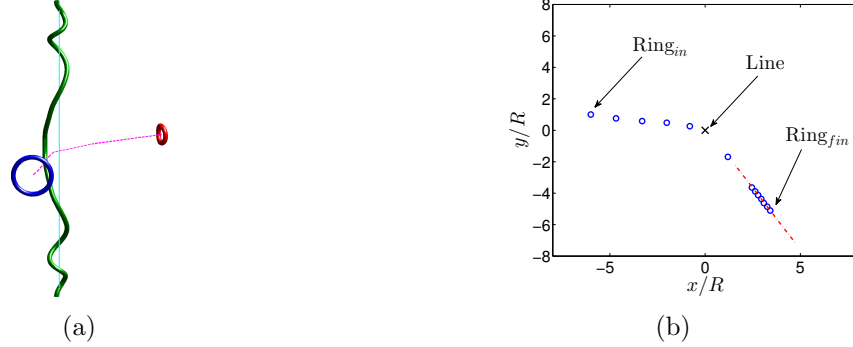


Figure 4.6: (a) Illustration of the scattering of a ring by a line resulting in line length loss and deflection of the ring. (b) Trajectory of a ring on the  $x-y$  plane during an encounter with a line vortex. The vortex ring positions are plotted at the times,  $t = 0, 50, 100, 150, 200, 250, 300, 306, 312, 318, 324, 330, 336$  (color figure online).

can, therefore, infer the velocities of the rings from knowledge of their size. However, we are in the position to evaluate their velocities directly from the variation of the ring centre of mass  $\mathbf{x}_{\text{CM}}^r$  with time. Figure 4.6(a) provides an illustration of how an initially circular vortex ring scatters with a straight line vortex. The computed trajectory of the ring is also included to illustrate the deflection that a ring experiences as it encounters the line vortex. Since the linear momentum of the initial condition has no  $z$ -component (the single line carries null linear momentum and the axis of the ring is by construction aligned along the  $x$ -coordinate direction), we expect the motion of the ring to be purely on the  $x-y$  plane. Therefore, in Fig. 4.6(b) we have plotted the position of the ring at different times on the  $x-y$  plane. In this plot, lengths are measured in units of the initial ring radius  $R$ . The results indicate that in the latter stages of the simulation, the ring moves with almost linear velocity. As the ring velocity may drastically change direction, it is natural to infer that the linear momentum of the line associated to KWs and sound emission will counter balance this change. This important conservation mechanism will be the object of forthcoming works.

To simplify the analysis, we can assume that, at the initial and final stages, the motion of the ring is essentially uniform as the interaction with the line vortex is weak. By fitting the trajectory of the ring given by its centre of mass with a straight line, we are able to evaluate the characteristic deflection angle  $\theta = \theta_{\text{fin}} - \theta_{\text{in}}$  as well as the variation in the velocity magnitude  $|\mathbf{v}_{\text{fin}}|/|\mathbf{v}_{\text{in}}|$ . Figures 4.7(a) and 4.7(b) show the behaviour of these two parameters versus the initial offset value  $d_y/R$ , respectively. The deflection angle depends strongly on whether or not a reconnection occurs. As discussed previously, reconnections take place for offset values greater than  $d_y/R \in [-0.5, 2.5]$ , resulting in a drastic change in the behaviour of the deflection angle when the ring is not absorbed by the line. On the other hand, the variation in the velocity magnitude grows as a smooth and essentially monotonically increasing function of the initial offset up to the critical absorption offset given by  $d_y/R = 2.5$ . As expected, smaller rings that are produced at positive values of the offset, have very large velocities. It is important to note that when smaller rings are produced, a larger fraction of the energy is transferred

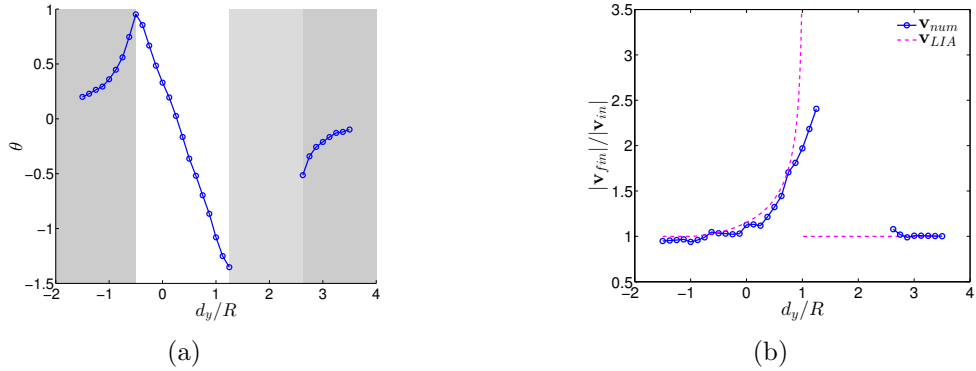


Figure 4.7: (a) Variation of the deflection angle  $\theta = \theta_{fin} - \theta_{in}$  as a function of the initial offset  $d_y/R$ ; (b) variation of the final ring velocity magnitude as a function the initial offset  $d_y/R$  (color figure online).

into large amplitude excitations along the line vortex. These subsequently could interact as soliton like excitations [109]. On the other hand, the scattering of large rings imparts small amplitude Kelvin-wave excitations onto the line vortex.

## 4.4 Conclusions

We have studied the scattering of vortex rings by a line vortex using the GP equation. In particular, we have identified the effect of varying the initial offset parameter of the vortex ring on its subsequent scattering properties. Our results have revealed that a strong asymmetry is seen in the scattering of vortex rings by a line vortex due to the severe topological constraints imposed on the system. By using a vortex tracking algorithm, we have evaluated how the length of the ring and line vary after scattering as a function of the initial offset parameter. We showed that predictions made by LIA based upon simple geometric considerations lead to reasonably good agreement with results based on full GP simulations. Moreover, we find that reconnections resulting in the emission of smaller vortex rings that move at higher velocities result in strong deflections in the trajectory of the ring whilst the emission of larger rings results in weak deflections.

The production of smaller rings during scattering corresponds to the deposition of a larger fraction of the energy from the ring onto the line. This leads to large amplitude KWs that can behave more like Hasimoto solitons [109] propagating along a vortex. On the other hand, larger loops correspond to small amplitude KWs being produced on the line vortex. These observations have direct relevance to our understanding of the cross-over range of scales in superfluid turbulence where the emission of vortex rings due to the direct energy cascade as discussed by Svistunov [30] or due to breather excitations as reported by Salman [40] turns out to be very important. Indeed, the production of large amplitude KWs can result in the emission of further rings following self-reconnections on a vortex line. These findings raise the question of how transparent

is a turbulent tangle to vortex rings that can be emitted within the cross-over range as this can have direct relevance to the question of how energy is dissipated within the ultra-low temperature regime of turbulence.

# Chapter 5

## Turbulent Vortex Tangle

### 5.1 Introduction

The full understanding of turbulence in a fluid is one of the oldest yet still unsolved problems in physics. A fluid is said to be turbulent when it manifests excitations occurring at several length scales. Due to the large number of degrees of freedom and the nonlinearity of the governing equations of motion, the problem is usually tackled statistically by introducing assumptions and closures in terms of correlators. This is the case in the seminal work of Kolmogorov in 1941 based on the idea of Richardson's energy cascade, where energy in classical fluids is transferred from large to small scales [16].

As already discussed in Section 1.2.1, in the case of a superfluid in the limit of zero temperature, vortices interact together given rise to a complicated vortex tangle where different types of turbulences can occur and coexist on a disparate range of length and time scales. In fact, if one looks at individual vortex filaments, energy is believed to be carried by a weak wave-turbulence cascade of Kelvin waves (KW) [31, 115, 116, 117] that excite sound waves. However, the collective effect of filaments composing such tangle can give rise to a quasi-classical Richardson cascade, characterized by a Kolmogorov inertial range in the energy spectrum [82]. One of the most fundamental questions in QT concerns the way that energy is transferred down to the smallest scales where it can be effectively dissipated through the emission of sound waves. In this chapter we focus on the evolution and decay of the tangle using the GP model. Such model, in fact, naturally contains all the key ingredients for the study of superfluid turbulence, such as quantised vorticity, vortex reconnections, phonon emission and it also presents Kolmogorov turbulence at large scales.

Firstly, using the numerical method discussed in Chapter 3 we show that after the onset of turbulence, the vortex line density satisfies Vinen's decay law [124] with a coefficient that is in agreement with He II. Thereafter, we investigate the complexity of the tangle by measuring both its topological and geometrical properties. Finally, we perform a direct measurement of KWs during the dynamics and compute a KW spectrum that appears to be consistent with the L'vov and Nazarenko theoretical prediction [31].

## 5.2 Method

In order to study the evolution of a vortex tangle we integrate numerically a non-dimensional form of Eq. (2.15). Similarly to Section 4.2 we choose the healing length  $\xi$  (see Eq. (2.39)) as the unit of length and we scale the wave function with respect to  $\psi_\infty$  (2.22). However, here we make a different choice concerning the unit of time, in fact  $t$  scales according to  $\xi/c$ . Therefore, the dimensionless GP equation becomes

$$i\frac{\partial}{\partial t}\psi = -\frac{1}{2}\nabla^2\psi + |\psi|^2\psi. \quad (5.1)$$

Numerical integration of Eq.(5.1) is performed using a standard pseudo-spectral code. As initial condition we choose the so-called Taylor-Green flow [82], a well-studied flow in superfluid turbulence. Further information concerning the Taylor-Green initial condition is given in Appendix A. Symmetries are not enforced during the evolution and we use resolutions of  $256^3$  and  $512^3$  with  $\xi = 2\pi/256$  and  $\xi = 2\pi/512$  respectively. Mirror symmetries are broken during the evolution although traces of such symmetries will be present even at very large times. With units used in this work, the large eddy turnover time is of the order of the unity. The Taylor-Green flow initially contains a configuration of unstable large-scale rings that develop to create a turbulent tangle. Vortices can be spotted by plotting the low-value isosurfaces of the density field as displayed in Fig. 5.1 Low-density regions corresponding to vortex lines are plotted in red, while density fluctuations (sound waves) are rendered in light blue. The initial condition is visualized in Fig. 5.1(a), the complex turbulent tangle at  $t = 12$  in Fig. 5.1(c), and the final state at  $t = 105$ , where few vortices are present with a lot of sound in the background, in Fig. 5.1(e). We track the vortex lines with numerical method explained in chapter 3 that allows for identifying separately each single line forming the tangle. The algorithm is robust and accurate as it takes full advantage of the spectral resolution. The intermesh values of the field  $\psi$  and its derivatives needed for the Newton-Raphson method are directly evaluated by Fourier transforms; the locations of vortices are thus found with precision given by the *machine- $\epsilon$*  (double in the present simulations). Figures 5.1(b), 5.1(d), and 5.1(f) show the corresponding tracked vortices displayed in different colors.

## 5.3 Vinen's Law for the Decay of a Vortex Tangle

We focus first on the later evolution times. As suggested by Vinen [124], in the limit zero temperature the decay of a superfluid vortex tangle should be analogous to the decay of an ordinary turbulent flow at high Reynolds number. In classical turbulence large eddies breaks into smaller vortex configurations without substantial lost in the kinetic energy until the viscous scale is reached and energy is converted into heat. Similarly, in superfluid turbulence, vortices interact and reconnect generating small scales structures until length scales of the order of the healing length are attained and energy is transferred into sound waves. The large amount of phonon excitations present in the system acts as a thermal bath that exchanges energy and momentum with the vortices.

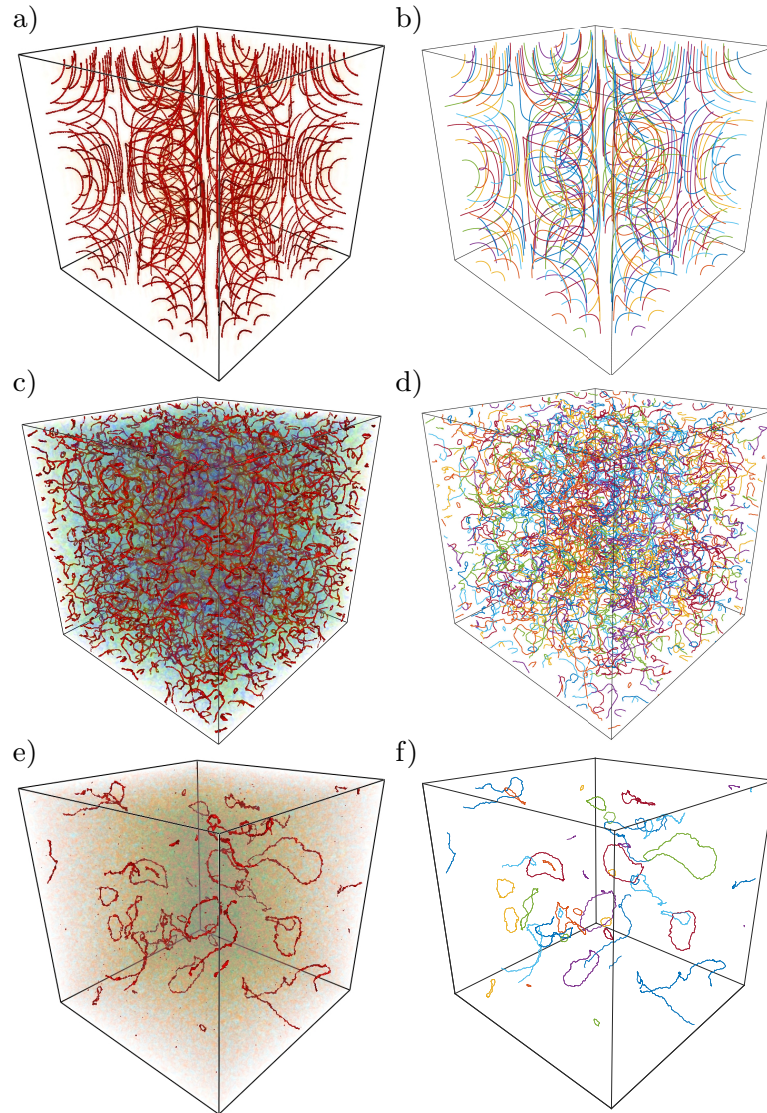


Figure 5.1: Left: Isosurfaces of density field at different times. Low-density regions that correspond to vortex lines are plotted in red, while density fluctuations (sound) are rendered in light blue. Right: Corresponding tracked vortices. Different colors correspond to different vortices. Snapshots taken at  $t = 0$  [(a) and (b)],  $t = 12$  [(c) and (d)], and  $t = 105$  [(e) and (f)]. Resolution  $256^3$ .

This process mimics mutual friction and leads eventually to the total annihilation of vortex rings [113].

To better explain this dynamics, we recall that the kinetic energy for an ordinary fluid characterised by a high value of Reynolds number is given by

$$\frac{du^2}{dt} = -\chi_2 \frac{u^3}{l}, \quad (5.2)$$

where  $u$  is the characteristic velocity associated to the energy containing eddies,  $l$  is a characteristic length (for example the reciprocal of the wave number associated to the maximum in the energy spectrum  $E(k, t)$ ) and  $\chi_2$  is a constant of the order of unity. In the case of a superfluid vortex tangle,  $l$  represents the inter-vortex distance defined according to Eq. (1.23) while the characteristic velocity is given by  $u_l = \Gamma/2\pi l$ . Therefore, rewriting Eq. (5.2) in terms of the total vortex line density  $\mathcal{L}$ , we can derive the equation describing the decay of superfluid turbulence as

$$\frac{d\mathcal{L}}{dt} = -\chi_2 \frac{\Gamma}{2\pi} \mathcal{L}^2. \quad (5.3)$$

Its solutions manifest a  $\mathcal{L} \sim t^{-1}$  behaviour at long times: this rate of decay has been named ultra-quantum or Vinen's turbulent decay law and measured in He II experiments [34] and VF numerical simulations [35]. In Fig. 5.2a we show the temporal evolution of  $\mathcal{L}$ . It is worth noticing that it grows at the initial stages: this is caused by the instability of the initial Taylor-Green configuration and the subsequent vortex stretching due to numerous vortex reconnections. The data is compared with an estimation of  $\mathcal{L}$  obtained by computing the ratio between the volume of points such that  $|\psi|^2 < 0.2$  and the corresponding surface of a perfect two-dimensional vortex profile. This latter method has become a standard technique within GP numerical simulations to compute the vortex line density [125]. Even if this technique is able to capture the qualitative behaviour of  $\mathcal{L}$ , it fails to describe the power-law predicted by Vinen's equation at long times. This is shown in Fig. 5.2b where the measured  $\Delta\mathcal{L}(t) = (\mathcal{L}(t)^{-1} - \mathcal{L}(t_0)^{-1})^{-1}$ , setting  $t_0 = 17$ , is compared to Vinen's prediction. We can explain this discrepancy by reasoning that the vortex core size (proportional to the uniform condensate state) varies in time because more and more sound excitations are created by the superfluid decay, altering the estimation of  $\mathcal{L}$  by fixing the (non time-dependant) density threshold. The tracked data also allow for determining the numerical constant  $\chi_2 = 0.65$ . This value is in remarkable agreement with experimental values  $\chi_2 \sim 10^{-1}$  measured in He II in the low temperature limit [34]. Between the time of maximal vortex length ( $t \approx 8.5$ ) and  $t_0$  there is a faster decay that could be explained by the quasi-classical turbulent decay law [126], although the data (not shown here) do not allow for a precise corroboration and further studies are needed.

## 5.4 Complexity Measures for a Vortex Tangle

From Fig. 5.1, it is clear that the complexity of tangle first increases and then decreases. Such complexity can be measured by computing the changes in some of

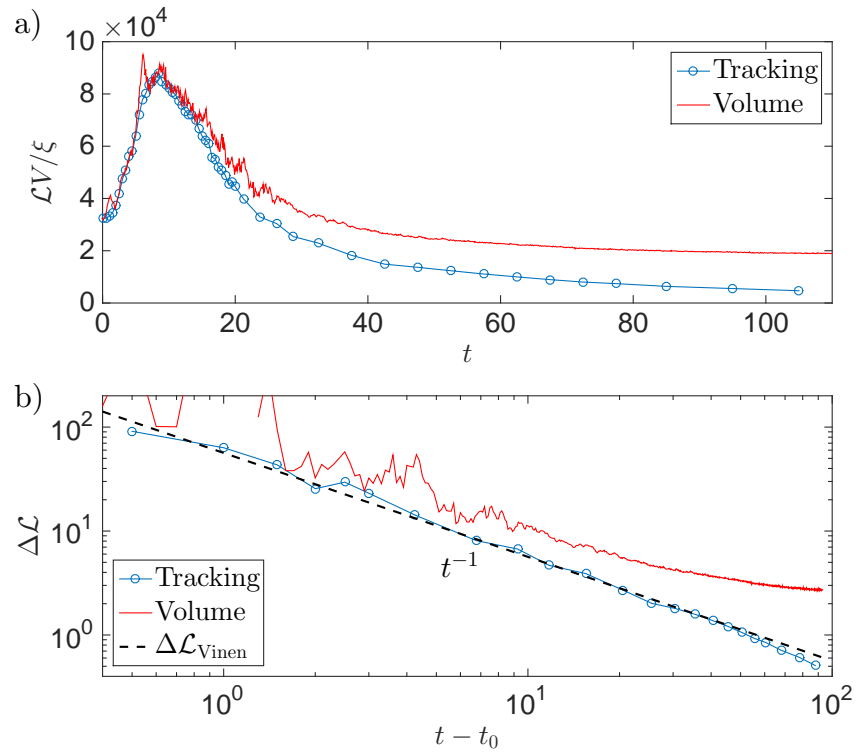


Figure 5.2: a) Temporal evolution of the vortex line density: tracked data are plotted using blue circles, volume estimation in solid red line. b) Long time decay of  $\Delta\mathcal{L}$  (see text), together with Vinen's prediction  $\Delta\mathcal{L}_{\text{Vinen}} = [\chi_2 \frac{\Gamma}{2\pi} (t - t_0)]^{-1}$ , setting  $\chi_2 = 0.65$  (solid black line). Resolution  $256^3$ .

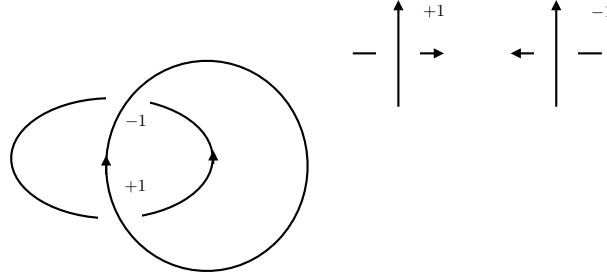


Figure 5.3: Example of how to arbitrary associate a sign to each point where two loops cross each other. The example shows a two unlinked rings having linking number equal to zero.

the algebraic and topological quantities of the tangle[81, 127]. In particular we are going to focus mainly on the crossing, the linking and the writhing number. For two given loops, we can interpret the crossing number as the number of times the two loops cross each other once projected onto a two dimensional plane. The linking number is related to the crossing number since it refers to the average number of times the two loops cross each other but associating also a positive or a negative sign to each crossing point according to an arbitrary choice. An example of how to associate a sign to each crossing point is shown in Fig. 5.3. The writhe number instead refers to a single loop and it provides an information on the coiling of the loop. We compute the total average crossing  $\bar{C} = \sum_{i \neq j} C_{i,j}$ , the total linking  $Lk = \sum_{i \neq j} Lk_{ij}$ , and the writhe  $Wr = \sum_i Wr_i$ , by directly performing the line integrals over the vortex ring(s) [81] as

$$\begin{aligned}
 \bar{C}_{i,j} &= \frac{1}{4\pi} \oint_{\mathcal{C}_i} \oint_{\mathcal{C}_j} \left| \frac{(\mathbf{R}_i - \mathbf{R}_j) \cdot d\mathbf{R}_i \times d\mathbf{R}_j}{|\mathbf{R}_i - \mathbf{R}_j|^3} \right| \\
 Lk_{ij} &= \frac{1}{4\pi} \oint_{\mathcal{C}_i} \oint_{\mathcal{C}_j} \frac{(\mathbf{R}_i - \mathbf{R}_j) \cdot d\mathbf{R}_i \times d\mathbf{R}_j}{|\mathbf{R}_i - \mathbf{R}_j|^3} \\
 Wr_i &= \frac{1}{4\pi} \oint_{\mathcal{C}_i} \oint_{\mathcal{C}_i} \frac{(\mathbf{R}_i - \mathbf{R}'_i) \cdot d\mathbf{R}_i \times d\mathbf{R}'_i}{|\mathbf{R}_i - \mathbf{R}_j|^3}.
 \end{aligned} \tag{5.4}$$

Here  $\mathbf{R}_i$  corresponds the points identifying the  $i$ th ring  $\mathcal{C}_i$ ; for the writhe number,  $\mathbf{R}_i$  and  $\mathbf{R}'_i$  correspond to two different points of the same ring. In Fig. 5.4(a) we plot the total number of rings  $N_{\text{rings}}$  and  $\bar{C}$  normalised by their initial values versus time. It is worth noticing that the average crossing number reaches qualitatively a maximum at the same stage of the vortex line  $\mathcal{L}$  maximum, while the ring number maximum is slightly shifted forward in time. The former observation follows the idea that vortex lines simultaneously stretch, bend and coil during reconnection events. The latter is due to the fact that longer vortex rings continue to break into pieces during the evolution until the tangle density becomes low enough and the main vortex length dissipation mechanism is given by sound interaction. We then focus on the center-line helicity  $H_c/\Gamma^2 = Lk + Wr$  [128] related to the helicity in classical fluid dynamics, an important inviscid invariant. The linking number  $Lk$  takes integer values and gives information about the number of linked rings present in the system, whereas the writhe takes real values and its contribution comes from self-linked (knots), an integer contribution, and

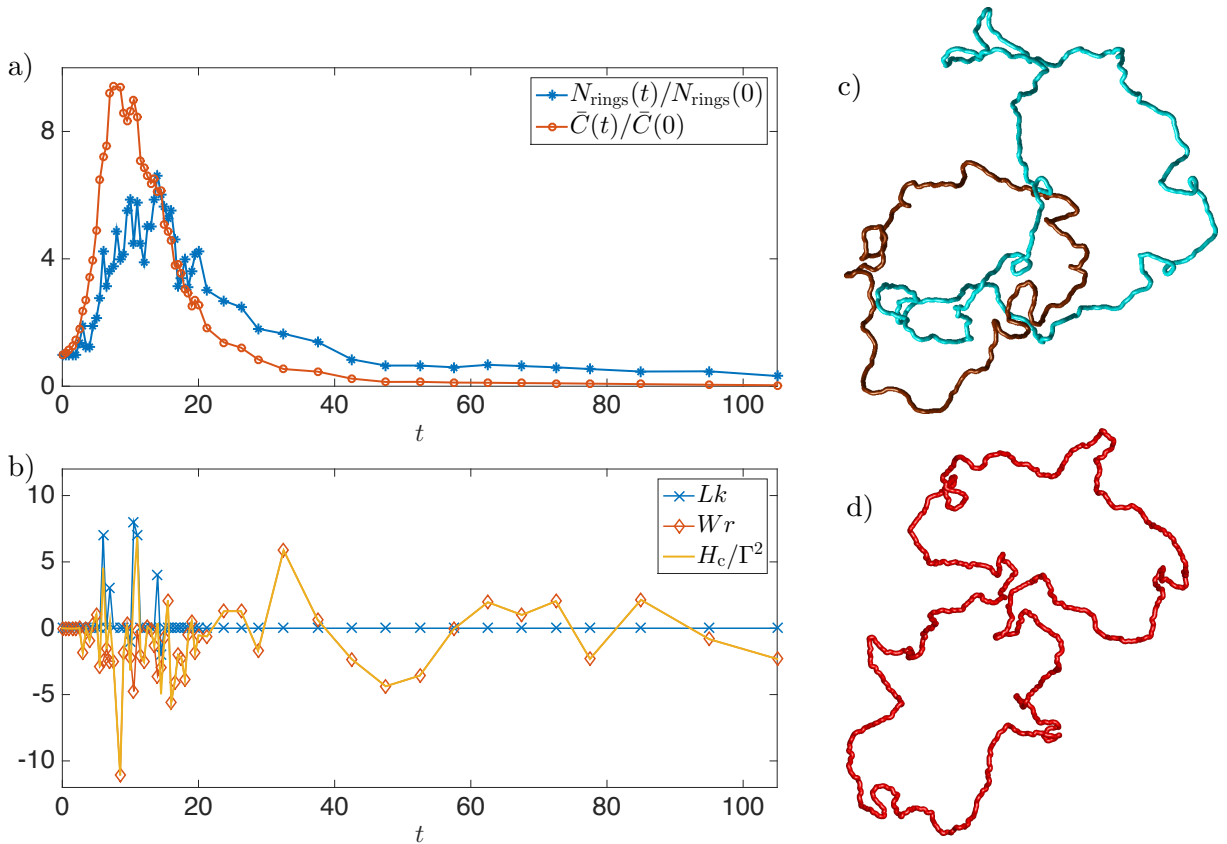


Figure 5.4: a) Temporal evolution of the (normalised) total number of rings and crossing number. At  $t = 0$ ,  $N_{\text{rings}}(0) = 128$  and  $\bar{C}(0) = 758$ . b) Temporal evolution the total linking  $Lk$ , writhe  $Wr$  and center-line helicity  $H_c/\Gamma^2$ . c) Visualisation of two linked rings at  $t = 21$ . d) Visualisation of a ring with high  $Wr$  at  $t = 24.5$ . Resolution  $256^3$ .

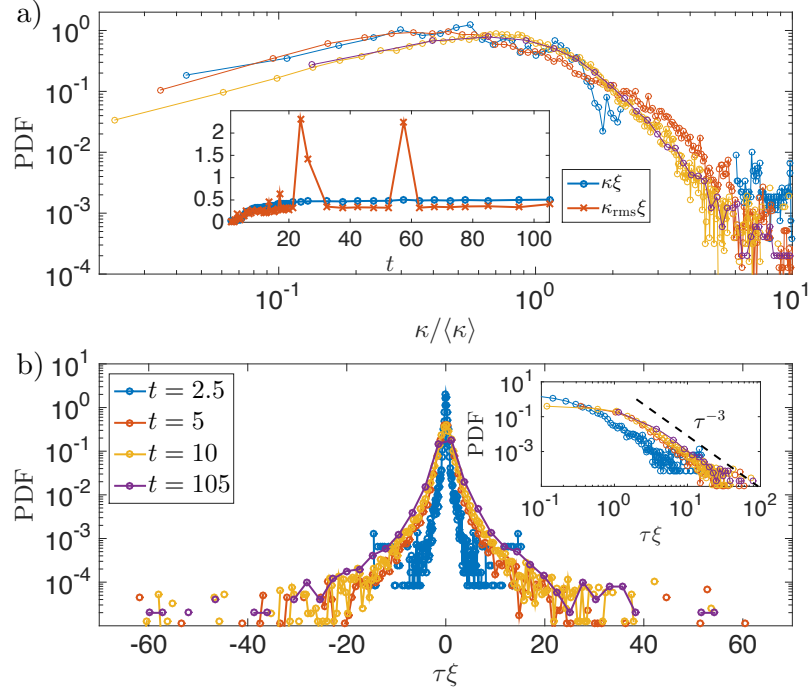


Figure 5.5: a) PDFs of curvature  $\kappa$  normalised by their respective mean values  $\langle \kappa \rangle$  at different times (same legend as (b)). The inset displays the temporal evolution of the mean and rms values of  $\kappa$ . b) PDFs of torsion  $\tau$  at different times. The inset emphasises their  $\tau^{-3}$  power-law tail. Resolution  $256^3$ .

KWs [129]. Figure 5.4(b) shows the temporal evolution of these three quantities. Initially,  $Lk = Wr = 0$ , as expected for the Taylor-Green flow. Surprisingly, during the evolution  $Lk$  becomes non-zero, indicating the presence of linked rings, such as the ones displayed in Fig. 5.4(c)<sup>1</sup>. This is remarkable as in the GP model sufficiently simple vortex configurations usually decay by reducing their complexity [105]. Once the decay is established, no linked rings are present and only writhe contributes to  $H_c$ . Note that the writhe number is not enough to determine whether a ring is self-linked (knotted) or not. The center-line helicity however fluctuates about a zero mean, an indication of the presence of KWs. KWs are indeed apparent in Fig. 5.4(d) where an unknotted ring with high  $Wr$  is displayed. KWs have already been indirectly observed in the Taylor-Green flow during the turbulent stage [87], in agreement with the large values of writhe observed around  $t \sim 10$ .

We now study statistical properties of some geometrical quantities of the vortex filaments by exploring the time behaviour of the probability density functions (PDFs) of the curvature  $\kappa$  and torsion  $\tau$  of the entire set of vortices in the system. In Fig. 5.5(a) we present the PDF of curvature, normalised by its mean value, at different stages. The temporal evolution of the mean curvature  $\langle \kappa \rangle$  and its *rms* value  $\kappa_{\text{rms}}$  are also displayed

<sup>1</sup>Although linked rings are present in the flow, the probability of finding them is very small. It can be estimated counting all the linked rings and it is at most of order  $10^{-4}$  for the Taylor-Green flow.

in the inset. We can observe that  $\langle \kappa \rangle$  increases rapidly at early stages and then almost saturates, an indication that the average vortex size (inversely proportional to the curvature) slowly decreases at later times. The rms value of the curvature presents the same tendency with the exception of peaks. These are evidences of reconnection events where high values of curvature are found in localised regions. It is worth noticing that the PDFs, rescaled by their mean curvature, exhibit a relatively good collapse to a self-similar form. This latter observation indicates a power-law behaviour  $\sim \kappa^1$  at small curvature values, while an exponentially-decaying tail is present at large curvature values. A similar behaviour has also been observed within the VF model [102]. In Fig. 5.5(b) we plot the torsion PDFs at the same stages. The mean torsion is always about zero and there is no evidence of any skewness in the PDFs. The distributions' tails show an universal power-law behaviour of  $\tau^{-3}$  at all times, meaning that the second and higher moments of the torsion diverge during the decay. The same scaling appears in vortex tangles of random wave fields that are solutions of the Helmholtz equation [130]. This may be an indication that for one-time small-scale quantities, quantum turbulent tangles can be interpreted simply as random vortices.

## 5.5 Kelvin Waves Cascade

The large curvature fluctuations and the torsion fluctuation about a zero mean are evidence of KWs at all scales propagating on quasi-planar vortex rings. By exploiting the accuracy of the tracking algorithm we are able to directly detect KWs on those rings. Competing theories have been put forward to statistically predict a power-law KW spectrum in the form of  $n_k \sim k^{-\alpha}$  (here  $k$  is the KW-number) and explain the energy transfer through KW scales. Assuming weak non-linearity (small amplitude KWs compared to their respective wavelengths), Kozik and Svistunov [115] and L'vov and Nazarenko [31] obtained two universal exponents  $\alpha_{KS} = 17/5$  and  $\alpha_{LN} = 11/3$ . Even though the difference between the two cascades is not large, the source of the disagreement relies on symmetry arguments. Differently from Kozik and Svistunov, the theory by L'vov and Nazarenko breaks the tilt symmetry allowing for a four-wave interaction and leading to non-locality in the energy transfer. Another theory by Vinen *et al.* considered strong non-linear interactions and derived by a scaling argument the exponent  $\alpha_V = 3$  [116]. Finally, it was suggested by E. Sonin [32] that no universality can be expected for the KW spectrum.

In order to test these competing theories numerically, we compute the KW spectrum of a ring by applying a Gaussian kernel following the procedure explained in Section 3.4.2. In Fig. 5.6 (a) we show the KW spectra, for different times, obtained by averaging over the spectra of the 50 largest rings in order to include both small fluctuations and also to span over two Kelvin wavelength decades. For the Gaussian filter, we use the value  $\alpha = 0.1$  (see notation used in Section 3.4.2); varying this parameter weakly modifies the large-scale values of the spectrum, but the data in the inertial range remain unchanged.

It is evident that all accessible KW modes get populated at early times due to reconnection events that trigger the cascade [131]. We observe KW spectra exhibiting

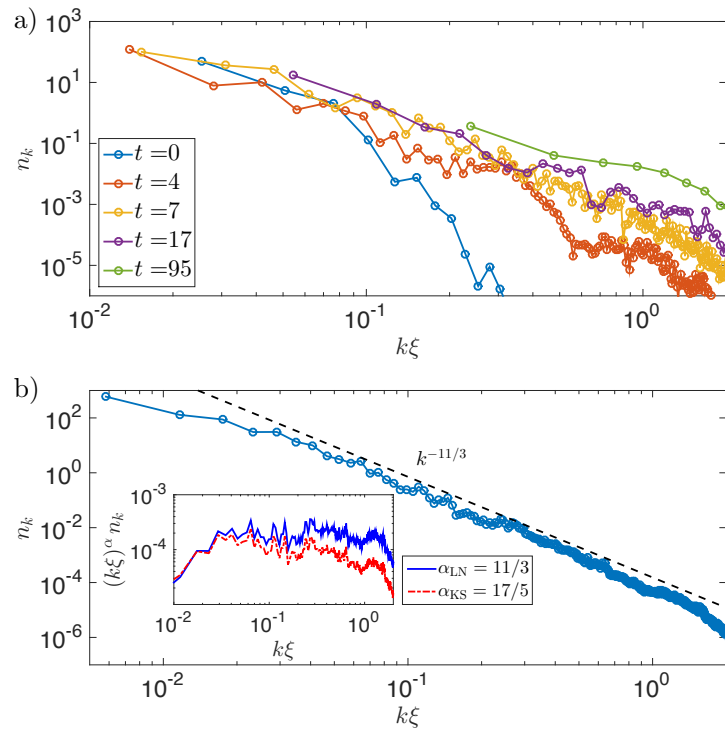


Figure 5.6: a) Temporal evolution of KW spectra (averaged over the 50 longest rings). Resolution  $256^3$ . b) KW spectrum at  $t \sim 5$  (averaged over the 50 longest rings) for run at resolution  $512^3$ . The dashed line displays the  $k^{-11/3}$  scaling. The inset displays the respective  $k^{11/3}$  (solid blue) and  $k^{17/5}$  (dashed red) compensated spectra.

power-laws with an exponent independent of time where the best scaling is appreciated at the time where the rings are the longest ( $4 \leq t \leq 7$ ). To get the best estimation of the power-law exponent, we repeated the Taylor-Green decay in a simulation box twice larger; in this new configuration the scaling range spans almost two wavenumber decades. In Fig. 5.6(b) we show the spectrum at  $t \sim 5$ : the observed power-law exponent is close to the weak-wave turbulence predictions and seems to agree with the L’vov and Nazarenko  $\alpha_{LN} = 11/3$  one. This can be better appreciated by looking at the compensated spectra with respect to  $\alpha_{LN}$  and  $\alpha_{KS}$  showed in the inset. This finding supports the result in favour of L’vov and Nazarenko’s prediction previously obtained while studying the KW oscillations about a perfect straight line in the GP model [132]. We highlight that although the weak-wave turbulence prediction for the KW spectrum is formally derived for KWs on an isolated straight vortex line using the VF model, it remarkably turns out to be valid in a dense turbulent tangle also driven by the GP model. This is certainly due to the fact that the predicted KW spectrum was found for the longest rings. Small rings quickly lose their energy by phonon radiation and exchange momentum with sound waves. Both contributions are important to understand dissipation of superfluids at very low temperature and further studies are still needed to fully comprehend the relevance of such mechanisms.

## 5.6 Conclusions

In this Chapter we studied the evolution and the decay of a Taylor-Green flow. Even though this vortex configuration is characterised by large scale vortex rings, our numerical simulations showed a clear emergence of a Vinen type of turbulence. We remark that a trace of quasi-classical turbulence characterised by a  $t^{-3/2}$  time dependence in the decay of the total vortex line seems to appear in the earliest stage of the tangle decay. However, the following observation appears to be very sensitive to the time interval chosen for the evaluation of the  $t^{-3/2}$  behaviour. For this reason, we believe that the question of whether or not a Taylor-Green tangle can give rise to a quasi-classical regime requires further investigation made on a larger computational domain. Such a simulation may allow large scale vortex structures to survive for longer and thus to contribute to the development of a Kolmogorov like turbulent flow. We note that the non-dimensional coefficient in the Vinen decay law is in agreement with the values obtained in numerical simulations performed using the vortex filament (VF) method. Since the VF model does not include compressibility, we conclude that the main mechanisms responsible for the energy transfer in Vinen turbulence are due to vortex reconnections and to non-linear interaction between KWs, whereas the effect of phonons on vortex lines seems to have a negligible effect. Finally, our simulations revealed some evidence of a cascade associated with weak KWs on vortex lines. The universal exponent in the wave action spectrum seems to be in agreement with the prediction of Lvov and Nazarenko [31]. We note that this is consistent with the result obtained for a single vortex line within the vortex filament model by Laurie and Bagaley [133] although we have not quantified how sound emission in our GP model can influence the spectrum.

# Chapter 6

## Vortex Reconnections

### 6.1 Introduction

Reconnections in fluids have been an object of study for long time in the context of plasma physics [134] and both classical [135] and superfluid dynamics [136]. Depending on the physical system considered, such reconnections are events characterized by a rearrangement in the topology of either magnetic field, (magnetic reconnections) or vorticity field (vortex reconnections). Such topological modifications are believed to play a fundamental role in several physical phenomena like eruptive solar events [137], energy transfer and fine-scale mixing [138] and turbulent states in superfluids [139]. Despite their physical relevance, reconnections represent also a stand-alone mathematical problem, related for instance, to the presence of singularities in the Euler equation [135, 140, 141].

In classical fluids described by the Navier–Stokes-type equations, reconnecting vortex tubes stretch and deform, leading to complicated dynamics and formation of structures like vortex bridges [138]. In order to understand fundamental aspects of vortex reconnections it is often desirable to work with vortex filament configurations which naturally arises in superfluids.

Due to Kelvin’s circulation theorem explained in Section 2.5.2 (or the Alfvén’s theorem in magneto-hydrodynamics), in a barotropic ideal flow reconnections should be forbidden since the circulation of vortex lines transported by the flow is conserved and so their topology is frozen. However, as already suggested by pioneering works of Feynman [15] and Schwarz [142], vortex reconnections in superfluids do exist and play a fundamental role in superfluid turbulence. This was indeed confirmed in the early 90’s by Koplik and Levine [136] who performed numerical simulations of reconnecting vortex lines within the GP model. With the progress of experimental techniques in the last decade, reconnecting superfluid vortices have been visualized in He II [139, 143] and in BECs [144, 145]. From the theoretical side, many works have been devoted to studying the reconnecting vortex filaments in superfluids, either by using the vortex filament model or the GP model already introduced in Chapter 2.

One of the simplest questions to ask, although contradictory answers appear in the literature, is related to the rates of approach and separation of two reconnecting vortices. Assuming that a reconnection event is a local process in space and the circulation  $\Gamma$

is the only relevant dimensional quantity involved, by simple dimensional analysis it follows that the distance  $\delta(t)$  between two reconnecting filaments should scale as

$$\delta(t) \sim (\Gamma t)^{1/2}, \quad (6.1)$$

independently if it is measured before or after the reconnection. Such prediction has been confirmed by numerical simulations of the VF model [58] and in He II experiments [143]. In the framework of the GP model, the same scaling was asymptotically derived in [146] but a number of numerical studies report disparate scaling exponents that may differ between the before and after reconnection stages [55, 57].

Another fundamental question regards the universality of the geometrical shape of the vortex filaments at the reconnection. It is expected that vortices become locally antiparallel during the reconnection process [146]. However, using the VF model it has been reported that the reconnection angle may follow a broad distribution that depends on turbulent regime that is considered [58]. It has been also observed that during a reconnection event cusps are generated on the filaments and argument has been given either in favor of those cusps being universal [147] or not [148]. Finally, a lot interest has arisen recently on the generation of KWs (helical waves propagating along vortex filaments) [131, 139, 149, 150] and evolution of hydrodynamical helicity [129, 151, 152, 153, 154] during reconnection events.

The VF model is based on Biot-Savart equations (2.84) that describe a regularized Dirac's  $\delta$  vorticity distribution field in the incompressible Euler equation. However, due to Kelvin's circulation theorem in the Euler equation, reconnections need here to be added by some ad-hoc cut-and-connect mechanism. In addition the VF model introduces a small scale cut-off to regularize the Biot-Savart integral divergence and thus cannot explore the vortex dynamics at the smallest scales where the reconnection events take place. The GP model represents an alternative in the study vortex dynamics and reconnections, the main advantages being that it naturally contains vortex reconnections in its dynamics and that the entire reconnection process is regular due to the identically zero superfluid density field at the vortex core.

In order to understand what is universal in vortex filament reconnection mechanisms, we study the dynamics of four different initial configurations: (a) perpendicular and (b) almost anti-parallel lines, (c) a trefoil knot, and (d) reconnections occurring in a full turbulent tangle dynamics. We will show that reconnecting vortex lines always obey the dimensional analysis scaling given by Eq. (6.1) (both before and after reconnection), and they generally separate faster than they approach. In addition we report that regardless of the initial configuration, vortices become anti-parallel at the reconnection. We also report a self-similar behavior of the curvature close to the reconnection point when torsion does not play an important role and shock-like structures appearing in the torsion evolution for some configurations. Those findings are explained by some asymptotic calculations.

## 6.2 The reconnection Case Studies

In this chapter the GP equation (2.15) is expressed in a dimensionless form using the transformation already introduced in Section 5.2. The GP equation (5.1) is numerically integrated with a standard pseudo-spectral code. The resolution is chosen carefully to sufficiently resolve the vortex core in space and the reconnections in time. We consider four different initial configurations in a box of size  $L$  with a resolution of  $N$  points in each dimension:

**a) Perpendicular Lines.** The order parameter field characterized by straight vortex filaments perpendicular to each other and having initial distance of  $6\xi$ . This initial configuration is shown in Fig. 6.1a.1.  $L/\xi = 128, N = 256$ .

**b) Antiparallel Lines.** Vortex filaments with opposite circulation are set at an average distance of  $6\xi$  and weakly perturbed by introducing a KW of amplitude  $\xi$  and wavelength equal to the system size. The initial configuration is shown in Fig. 6.1b.1.  $L/\xi = 128, N = 256$ .

**c) Trefoil Knot.** A vortex filament reproducing a trefoil knot is produced following the procedure explained in Section 3.4.1; the torus on which the knot is built has toroidal and poloidal radii of  $R_0 = 16\xi$  and  $R_1 = 4\xi$  respectively. The initial configuration is shown in Fig. 6.1c.1.  $L/\xi = 128, N = 256$ .

**d) Turbulent Tangle.** We prepare an initial condition consisting of several large-scale vortex rings that replicates a Taylor–Green flow as explained in App. A. The initial condition is then evolved in time: the rings reconnect breaking the initial symmetry and creating a dense turbulent tangle displayed in Fig. 6.1d.1 (see [54] for complete description of the field evolution). We study four successive vortex reconnection events occurring in a small volume (Fig. 6.1d.2) at stages when the tangle density is higher.  $L/\xi = 256, N = 256$ .

## 6.3 Approach and Separation Rates

Apart from the characteristic length scale  $\xi$  inherently present in the GP model, when quantized vortices are considered, the quantum of circulation  $\Gamma$  can be used to formulate an extra length scale. Hence, by dimensional analysis the distance between two reconnecting lines it is expected to be

$$\delta^\pm(t) = A^\pm \xi^{1-2\alpha^\pm} |\Gamma(t - t_r)|^{\alpha^\pm}, \quad (6.2)$$

where  $\alpha^\pm$  and  $A^\pm$  are dimensionless parameters and the superscript  $\pm$  stands for before (-) and after (+) the reconnection event. The temporal evolution of the minimal distances between reconnecting filaments for the different case studies are displayed in Fig. 6.2a-d. Remarkably, in all cases the approach and separation rates follow the same dimensional  $t^{1/2}$  scaling. For each event we estimate the reconnection time  $t_r$  by doing

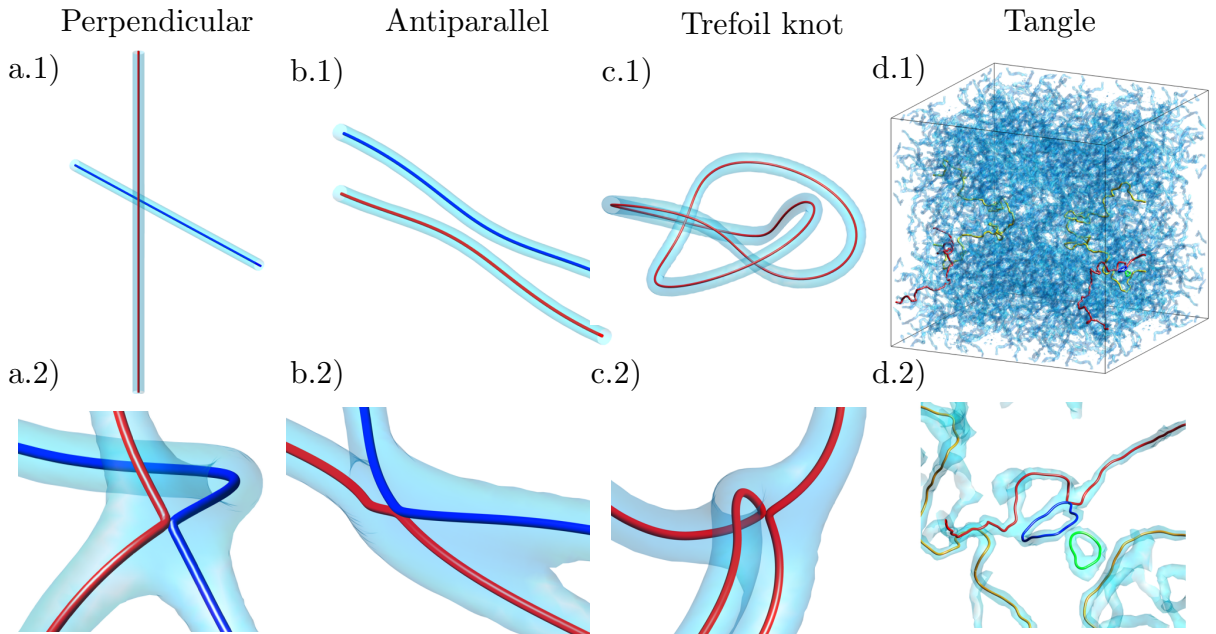


Figure 6.1: 3D plot showing the reconnection events explored numerically. The initial configuration is displayed for the perpendicular vortex lines (a.1), the anti-parallel lines (b.1) and the trefoil know (c.1). Figures (a.2), (b.2), (c.2) show a corresponding zoom at the moment of reconnection. Figure (d.1) displays the turbulent tangle and (d.2) a zoom in a place where a reconnection takes place. Red and blue correspond to the reconnecting vortex filaments, the light blue iso-surfaces render the density field at low values.

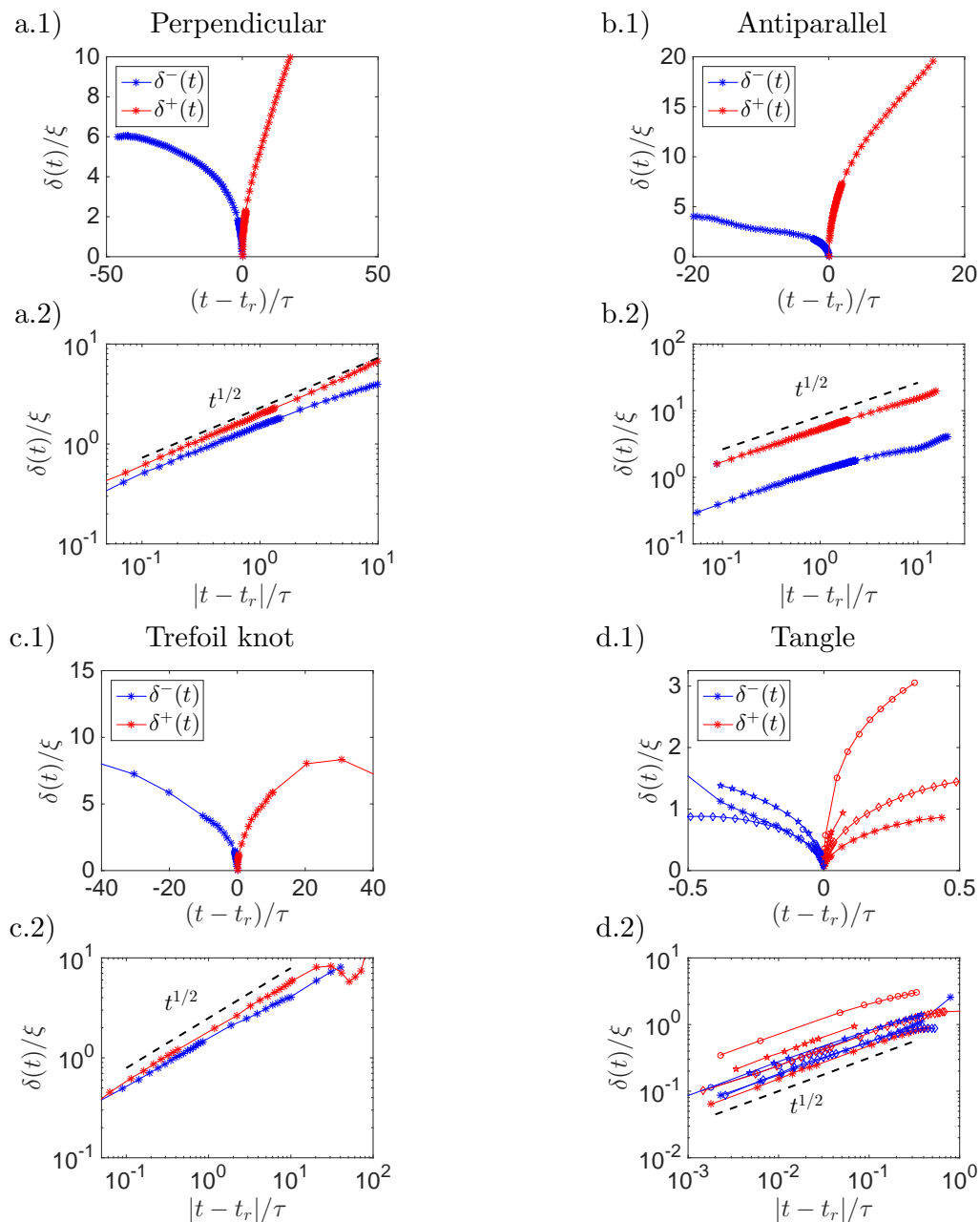


Figure 6.2: Temporal evolution of the distance between the reconnecting vortex filaments before (blue) and after (red) the estimated reconnection time  $t_r$  for the perpendicular (a), antiparallel (b), trefoil knot (c) and turbulent tangle (d) configurations. For the turbulent tangle four different reconnection events have been tracked. a.2-d.2) same plots as in a.1-d.1 but in log-log scales.

a linear fit on  $\delta^\pm(t)^2$  and compute  $t_r$  as the arithmetic mean between  $t_r^\pm$  that satisfy  $\delta^\pm(t_r^\pm)^2 = 0$ . The  $t^{1/2}$  scaling extends beyond  $\xi$  and only slight deviations are observed in some cases. Perhaps this fact could explain the different results for the scaling obtained in [55, 57, 56] where it was concluded that the exponents before and after the reconnection are different. For instance in [55] it was found that  $\alpha^- \in (0.3, 0.44)$  and  $\alpha^+ \in (0.6, 0.73)$  and in [56] that either  $\alpha^\pm = 1/2$  or  $\alpha^- = 1/3$  and  $\alpha^+ = 2/3$  depending on the initial vortex filament configuration. Let us underline for the moment that the tracking algorithm we used is able to measure the inter-vortex distances even in presence of sound waves (the Taylor-Green tangle analyzed contains moderate sound at all scales) and no asymmetry concerning the exponent is observed.

Although the measured exponent is always  $\alpha^\pm = 1/2$ , the full dynamics is not symmetrical with respect to the reconnection time as it can be immediately deduced by observing Fig. 6.2. By estimating the pre-factors  $A^\pm$  with a fit, shown in Fig. 6.3a, we conclude that these are always order of the unity but are not universal. Moreover, we observe that the vortex filaments usually separate faster than they approach ( $A^- \lesssim A^+$ ).

The tracking algorithm we use follows the pseudo-vorticity and it naturally provides the orientation of the filament with respect to the circulation. It thus allows us to compute the tangent vectors to the lines and infer the orientation of the filaments by evaluating the cosine of the angle  $\theta$  between the vectors at the two closest points as illustrated in Fig. 6.3b. By approaching to the reconnection point each vortex filament develops a cusp-like structure characterized by high and localized values of the curvature (displayed in green/blue colors). The temporal evolution of  $\cos \theta$  for all the case studies is presented in Fig. 6.3c. It is apparent that, independently of the initial configurations, vortices are always antiparallel at the reconnection point. This behavior appears to be time-symmetric about the reconnection time and is smooth, as highlighted in the inset of Fig. 6.3c where we show  $\cos \theta$  in LogLin coordinates for a better view on the short times before and after reconnection.

## 6.4 Analytical Predictions Using a Linear Approximation

A first analytical study of a reconnection event in the GP model have been provided by Nazarenko and West [146], where it is shown that two vortices are anti-parallel during a reconnection and their distance scales as  $\delta(t) \sim t^{1/2}$ . In the same spirit of the work [146], we assume that inside the vortex core the non-linear term of the GP equation can be neglected and so a reconnection event should be governed by the (linear) Schrödinger equation. For the sake of simplicity, in dimensionless units this equations reads

$$i\partial_t\psi + \frac{1}{2}\nabla^2\psi = 0. \quad (6.3)$$

We remark that in [146] reconnections are studied just on a plane, whereas here we consider vortex filaments with non-zero torsion. At the reconnection time  $t_r$  we use as

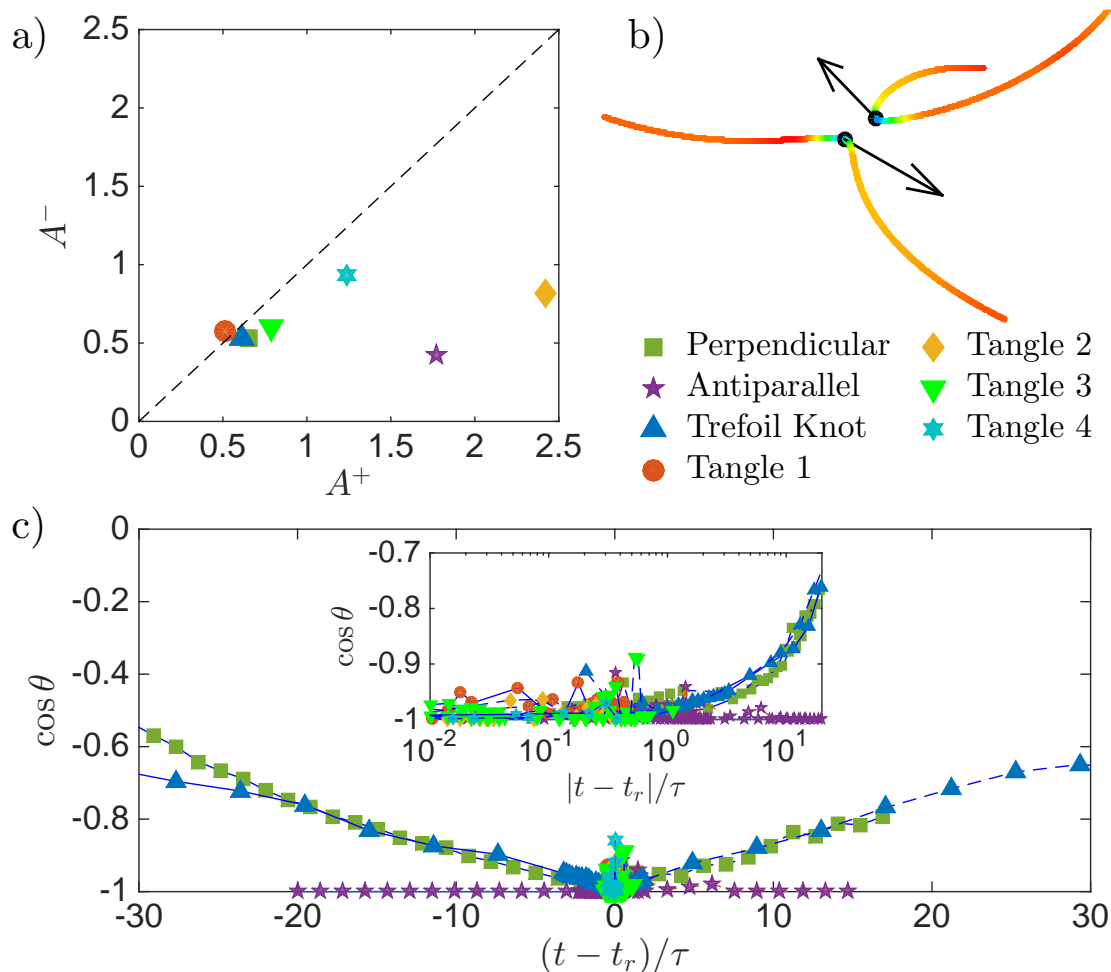


Figure 6.3: a) Fitted values of the pre-factors  $A^\pm$  corresponding to Eq. (6.2). b) An example of reconnecting filaments (trefoil knot case): the black dots represent the points of minimal distances and are used to compute  $\delta(t)$ , the arrows are the tangents of the filaments at those points, the reconnection angle  $\theta$  is defined by using the scalar product of the tangents. The coloring is proportional to the filament curvature (low in red and high in green/blue). c) Temporal evolution of the cosine of the reconnecting angle. The inset displays the same plot in log-lin scales.

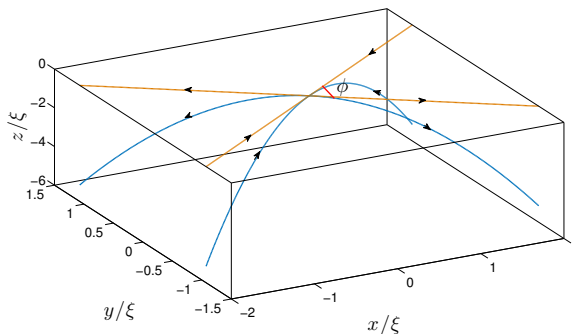


Figure 6.4: Plot of the initial condition using  $\gamma = 0.01$ ,  $\beta = 1/2$  and  $a = 1$ . The vortex filaments are shown in blue while their projection on the  $x$ - $y$  is shown in orange. The arrows identify the circulation around each vortex.

initial condition the ansatz

$$\psi_r(x, y, z) = z + \frac{\gamma}{a}(x^2 + y^2) + i(az + \beta x^2 - y^2). \quad (6.4)$$

Looking for  $\psi_r = 0$  one can recover the vortex profile, given by the curves

$$\mathbf{R}(s) = \left( s, \pm s \sqrt{\frac{\beta - \gamma}{\gamma + 1}}, -s^2 \frac{\gamma(\beta + 1)}{a(\gamma + 1)} \right), \quad (6.5)$$

where  $s$  is the parametrization of the curve. We note that Eq. (6.5) requires that

$$\frac{\beta - \gamma}{\gamma + 1} > 0. \quad (6.6)$$

In figure 6.4 we plot the the vortex filaments  $\mathbf{R}(s)$  (blue lines) for our initial condition. The vortices projected on the  $x$ - $y$  planes form two hyperbola (orange lines) crossing at the reconnection point. We note that the values  $\beta$  and  $\gamma$  fix the angle

$$\phi = 2 \tan^{-1} \left( \sqrt{\frac{1 + \gamma}{\beta - \gamma}} \right) \quad (6.7)$$

between the two hyperbola. The arrows identify the circulation around each vortex.

The formal solution of equation (6.3) is given by

$$\psi(t) = e^{i\frac{1}{2}(t-t_r)\nabla^2} \psi_r \quad (6.8)$$

where  $t_r$  is the time when the reconnection occurs. The choice of a second order polynomial for  $\psi_r$  allows us to find the exact solution of Eq. (6.3):

$$\psi(t) = z + \frac{\gamma}{a}(x^2 + y^2) - 2t(\beta - 1) + i \left( az + \beta x^2 - y^2 + 4(t - t_r) \frac{\gamma}{a} \right). \quad (6.9)$$

Assuming  $a > 0$  and  $\gamma < \beta < \frac{a^2 - 2\gamma}{a^2}$  and looking for  $\psi(t) = 0$ , in similar a way to what was already carried out in deriving Eq. (6.5), the vortex lines before the reconnection

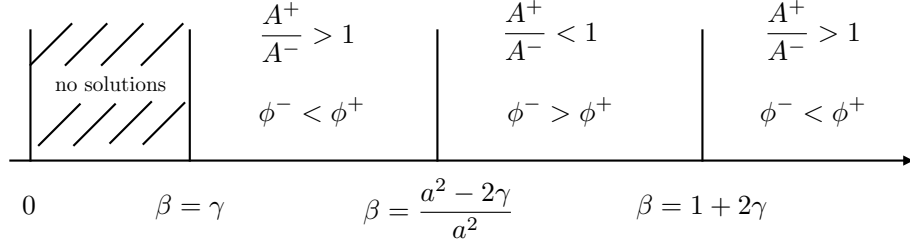


Figure 6.5: Dependence of the ratio  $\frac{A^+}{A^-}$  and the angles  $\phi^-$  and  $\phi^+$  on different values of  $\beta$ .

( $t < t_r$ ) are given by

$$\mathbf{R}_{1,2}^-(s, t) = (s, \pm \sqrt{\frac{(t_r - t)(a^2(1 - \beta) - 2\gamma) + as^2(\beta - \gamma)}{a(\gamma + 1)}}, \frac{(t - t_r)(a^2(\beta - 1) - 2\gamma^2) - a\gamma(\beta + 1)s^2}{(\gamma + 1)a^2}) \quad (6.10)$$

while after the reconnection ( $t > t_r$ )

$$\mathbf{R}_{1,2}^+(s, t) = (\pm \sqrt{\frac{(t - t_r)(a^2(1 - \beta) - 2\gamma) + as^2(1 + \gamma)}{a(\beta - \gamma)}}, s, \frac{(t - t_r)(a^2(\beta - 1) + 2\gamma^2) - a\gamma(\beta + 1)s^2}{(\beta - \gamma)a^2}). \quad (6.11)$$

From the above curves we observe that the two vortices approach along the  $y$ -direction and separate along the  $x$ -direction. It follows that

$$\delta^\pm(t) = |\mathbf{R}_1^\pm(0, t) - \mathbf{R}_2^\pm(0, t)| = \sqrt{2\pi}A^\pm|t - t_r|^{1/2}, \quad (6.12)$$

where the ratio of pre-factors satisfies

$$\frac{A^+}{A^-} = \sqrt{\frac{1 + \gamma}{\beta - \gamma}} > 1. \quad (6.13)$$

From equation (6.7) we can see how the quantity  $\frac{A^+}{A^-}$  is related to the angle  $\phi$ . Calling  $\phi^-$  the angle of the approaching vortices and  $\phi^+$  the angle of the separating vortices, we can conclude that for  $\beta < \frac{a^2 - 2\gamma}{a^2}$  then  $\phi^- > \phi^+$ . On the other hand, when  $\beta > \frac{a^2 - 2\gamma}{a^2}$  the two vortices approach along the  $x$ -direction and separate along the  $y$ -direction with  $\frac{A^+}{A^-} = \sqrt{\frac{\beta - \gamma}{1 + \gamma}}$ . For sake of completeness in Fig. 6.5 we show the values of the ratio  $\frac{A^+}{A^-}$  and the angles  $\phi^-$  and  $\phi^+$  for different values of  $\beta$ . We note that  $\frac{A^+}{A^-} < 1$  for  $\frac{a^2 - 2\gamma}{a^2} < \beta < 1 + 2\gamma$  while  $\frac{A^+}{A^-} > 1$  for  $\beta > 1 + 2\gamma$ . As a final remark, we note that changing the sign of  $a$  corresponds to looking at the reconnection backward in time, hence each value of  $\frac{A^+}{A^-}$  in Fig. 6.5 will then be reversed.

The linear approximation also allows for computing the curvature

$$\kappa(s, t) = \frac{|\mathbf{R}'(s, t) \times \mathbf{R}''(s, t)|}{|\mathbf{R}'(s, t)|^3} \quad (6.14)$$

and torsion

$$\mathcal{T}(s, t) = \frac{(\mathbf{R}'(s, t) \times \mathbf{R}''(s, t)) \cdot \mathbf{R}'''(s, t)}{|\mathbf{R}'(s, t) \times \mathbf{R}''(s, t)|^2} \quad (6.15)$$

of the vortex lines.

The curvature can be directly evaluated. Its maxima as a function of time before and after reconnection are given by

$$\kappa_{\max}^-(t) \sqrt{\frac{4\gamma^2(1+\beta)^2[a^2(\beta-1)+2\gamma](t-t_r)+a^3(\beta-\gamma)^2(1+\gamma)}{a^2(1+\gamma)^2[a^2(\beta-1)+2\gamma](t-t_r)}} \quad (6.16)$$

and

$$\kappa_{\max}^+(t) = \sqrt{\frac{4\gamma^2(1+\beta)^2[a^2(\beta-1)+2\gamma](t-t_r)-a^3(\beta-\gamma)(1+\gamma)^2}{a^2(\beta-\gamma)^2[a^2(\beta-1)+2\gamma](t-t_r)}} \quad (6.17)$$

respectively. The present calculation predicts in the limit of  $t \rightarrow t_r$ .

$$\kappa_{\max}^{\pm}(t) \propto |t - t_r|^{-1/2} \quad \text{and} \quad \frac{\kappa_{\max}^+(t)}{\kappa_{\max}^-(t)} = \left(\frac{A^+}{A^-}\right)^3. \quad (6.18)$$

Note that the  $t^{-1/2}$  scaling could be directly inferred by dimensional analysis arguments but not the scaling of the dimensionless pre-factors.

As pointed out by Schwarz in [142], one can show that  $\kappa^{\pm}$  presents a self-similar behavior close to the reconnection point of the form  $\kappa^{\pm}(s, t) = \kappa_{\max}^{\pm}(t)\Phi^{\pm}(\zeta_{\pm})$ , where  $\zeta^{\pm} = (s - s_r)\kappa_{\max}^{\pm}(t)$  and  $s_r$  is the coordinate of the reconnecting point. For small values of  $\gamma$  and  $(t - t_r)$ , these self-similar functions can be found to be

$$\begin{aligned} \Phi^{\pm}(\zeta) &= \frac{1 \pm \frac{3}{2} \frac{(\beta^{\pm 1} + 1)\zeta^2}{1 + (\beta^{\pm 1} + 1)\zeta^2} \gamma}{(1 + (\beta^{\pm 1} + 1)\zeta^2)^{3/2}} + O(\gamma^2) \\ &= \frac{1}{\left[1 + \left(\left(\frac{A^{\mp}}{A^{\pm}}\right)^2 + 1\right) \xi^2\right]^{3/2}} + O\left(\eta^{\pm} \gamma^2 \frac{(t - t_r)}{\tau}\right), \end{aligned} \quad (6.19)$$

where  $\eta^{\pm} = (A^{\mp}/A^{\pm})^2 - 1$ . This function corresponds to a cusp in the vortex filament at  $t = t_r$  and  $s = s_r$ . The dependence on the coefficient  $(A^{\mp}/A^{\pm})^2 + 1$  multiplying the self-similar variable  $\zeta^{\pm}$  is unexpected and could also not be guessed by dimensional arguments. We also remark that within this approximation, self-similarity is only exact when  $\gamma = 0$  or  $\eta^{\pm} = 0$  and it is destroyed when  $\eta^{\pm} \gamma^2 (t - t_r) / \tau$  is of order 1.

We note that in case one chooses  $\beta > \frac{a^2 - 2\gamma}{a^2}$  then  $\frac{A^+}{A^-} = \sqrt{\frac{\beta - \gamma}{1 + \gamma}}$  and

$$[\Phi^{\pm}(\zeta)]_{\beta > \frac{a^2 - 2\gamma}{a^2}} = [\Phi^{\mp}(\zeta)]_{\beta < \frac{a^2 - 2\gamma}{a^2}}. \quad (6.20)$$

The former calculations were evaluated using a symbolic computation software.

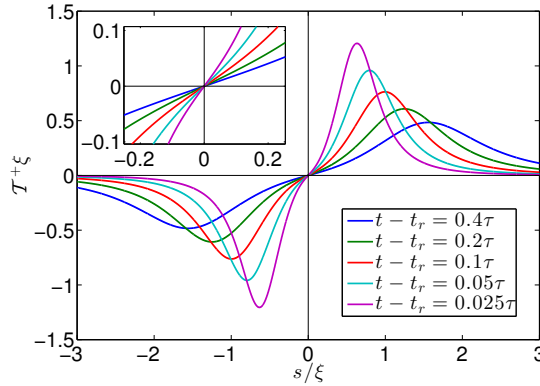


Figure 6.6: Plot of the torsion versus the  $y$ -coordinate, for different time steps using  $\gamma = 0.01$ ,  $\beta = 1/2$  and  $a = 1$ .

Finally, the torsion  $\mathcal{T}^\pm(s, t)$  of vortex line can be also computed within this approximation. When  $\gamma \neq 0$  torsion is not identically null but it vanishes at  $s_r$ , confirming that reconnections occur locally on a plane. Also, it can be proved that it changes sign linearly at  $s_r$  with a slope

$$\frac{d\mathcal{T}^+}{ds} = -\gamma \frac{3\sqrt{2}(1 + \beta)}{\sqrt{a(\beta - \gamma)}\sqrt{(t - t_r)[a^2(1 - \beta) - 2\gamma]}}, \quad (6.21)$$

that diverges as  $\gamma|t - t_r|^{-1/2}$ , creating shock-like structures as displayed in Fig. 6.6. The inset in Fig. 6.6 shows the linear behavior close to the reconnection point. It is possible to prove analytically that the slope ratio before and after the reconnection satisfies the relation  $\left. \frac{d\mathcal{T}^+}{ds} / \frac{d\mathcal{T}^-}{ds} \right|_{s=s_r} = A^+/A^-$ . The full formulas for the torsion are too long to be presented here. We observe that in the context of Euler and Navier–Stokes flows, dynamical equations for torsion and curvature have been derived in [155]. To our knowledge, these non-linear equations do not allow for predicting the generation of curvature cusps and shock-like torsion structures. It would be interesting to investigate if the scaling laws reported above also remain valid in classical fluids and MHD flows.

## 6.5 Numerical Measurements of the Curvature and Torsion

Motivated by the previous asymptotic results we analyze the data coming from simulations. We start looking at the curvature at a fixed time very close to the reconnection. In Fig. 6.7a the curvature just before  $t_r$  normalized using  $\kappa_{\max}$  is shown for all configurations. We indeed observe the formation of a cusp at the reconnection point  $s_r$  in all cases. Note that strictly speaking, no universal function of the curvature is observed. This is actually expected from the calculations of the curvature given by Eq. (6.19) which shows a dependence on the values  $A^+/A^-$  that differ from case to case. However, Eq. (6.19) suggests that if the variable  $\sqrt{1 + (A^+/A^-)^2}(s - s_r)\kappa_{\max}$  is

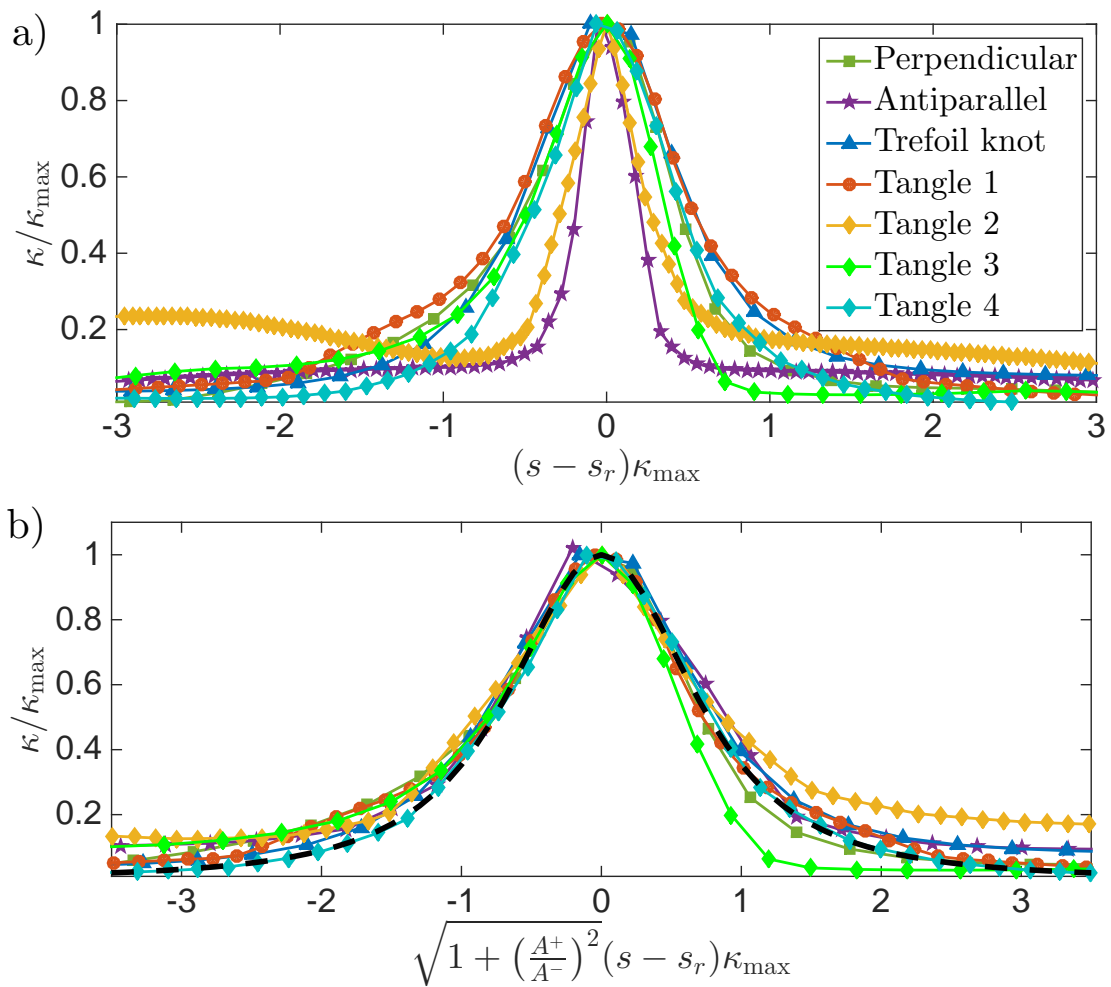


Figure 6.7: a) Curvature normalized by  $\kappa_{\max}$  close to the reconnection time (just before) for all reconnection events explored as a function of  $(s - s_r)\kappa_{\max}$ . b) Same data represented using the scaling suggested by the self-similar form (see Eq. 6.19). The black dashed line displays the theoretical prediction.

used instead, a universal form should be recovered. As shown in Fig. 6.7b the data indeed collapse into one universal function when using this new variable. The theoretical prediction given by Eq. (6.19) is also plotted with dashed black line to appreciate the remarkable agreement.

We now study the temporal evolution of the curvature to determine if a self-similar evolution is observed. Figure 6.8a shows how the trefoil knot curvature, rescaled by their maximum values, almost perfectly collapse into one single plot, demonstrating the self-similar behavior for this configuration. In the inset we plot the maximum value of the curvature as a function of time in log-log scale. The predicted  $t^{-1/2}$  scaling of Eq. (6.18) is clearly observed. In Fig. 6.8b, we present the same analysis done for the antiparallel case where a clear break-down of the self-similar behavior is observed. This can be explained by assuming a non-negligible value of  $\gamma$ , hence a strong torsion, that breaks the validity of the expansion done to obtain Eq. (6.19), only recovered when times are very closed to  $t_r$  as evident when comparing with the theoretical prediction displayed in dashed black line. The temporal evolution of the maximum of curvature, shown in the inset of Fig. 6.7b, still confirms the relations presented in Eq. (6.18), namely the  $t^{-1/2}$  scaling normalized by the ratio of the pre-factors are confirmed. Note that the agreement is very good given the large value  $(A^+/A^-)^3 = 4.15^3$ . For all other cases except tangle 2, self-similarity is observed (data not shown).

The breakdown of self-similarity is predicted by Eq. (6.19) when  $A^+/A^- \neq 1$  and  $\gamma \neq 0$ . A non-zero value of  $\gamma$  is related, as we have seen, to torsion close to the reconnection point and a shock-like structure formation. In Fig. 6.9a we show the temporal evolution of the torsion  $\mathcal{T}$  for the antiparallel case. The shock-like structure formation, and the linear behavior close to the reconnection point is clearly visible, thus explaining the breakdown of the self-similarity in Fig. 6.8b. The inset shows that the temporal evolution of the slope of the torsion at  $s_r$  obeys the scaling  $|t - t_r|^{-1/2}$  with the correct normalization  $A^+/A^-$  suggested by the analytical calculations. For completeness, in Fig. 6.9b we show the torsion normalized by the maximum value of the curvature for all the configurations close to the reconnection time. In all the other cases, except for tangle 2, the slope of torsion is almost zero at the reconnection point. Remarkably, the tangle 2 and antiparallel configurations correspond to the cases where vortices separate much faster than they approach (see Fig. 6.3a).

We remark finally that measuring quantities such as curvature and torsion is numerically very challenging as they involve high-order derivatives.

## 6.6 Conclusions

The reconnection of quantized vortex filaments within the GP model displays both universal and non-universal phenomena. We found that close to the reconnection, the approach and separation rates follow the same scaling  $\delta \sim (\Gamma t)^{1/2}$  and the vortex filaments always become locally anti-parallel. Previous numerical studies reported scaling rates in the form of power-law with exponents depending on the configuration. By dimensional analysis, any scaling different from  $\alpha = 1/2$  would introduce necessarily a new time or length-scale to the problem that needs to be made explicit. The discrep-

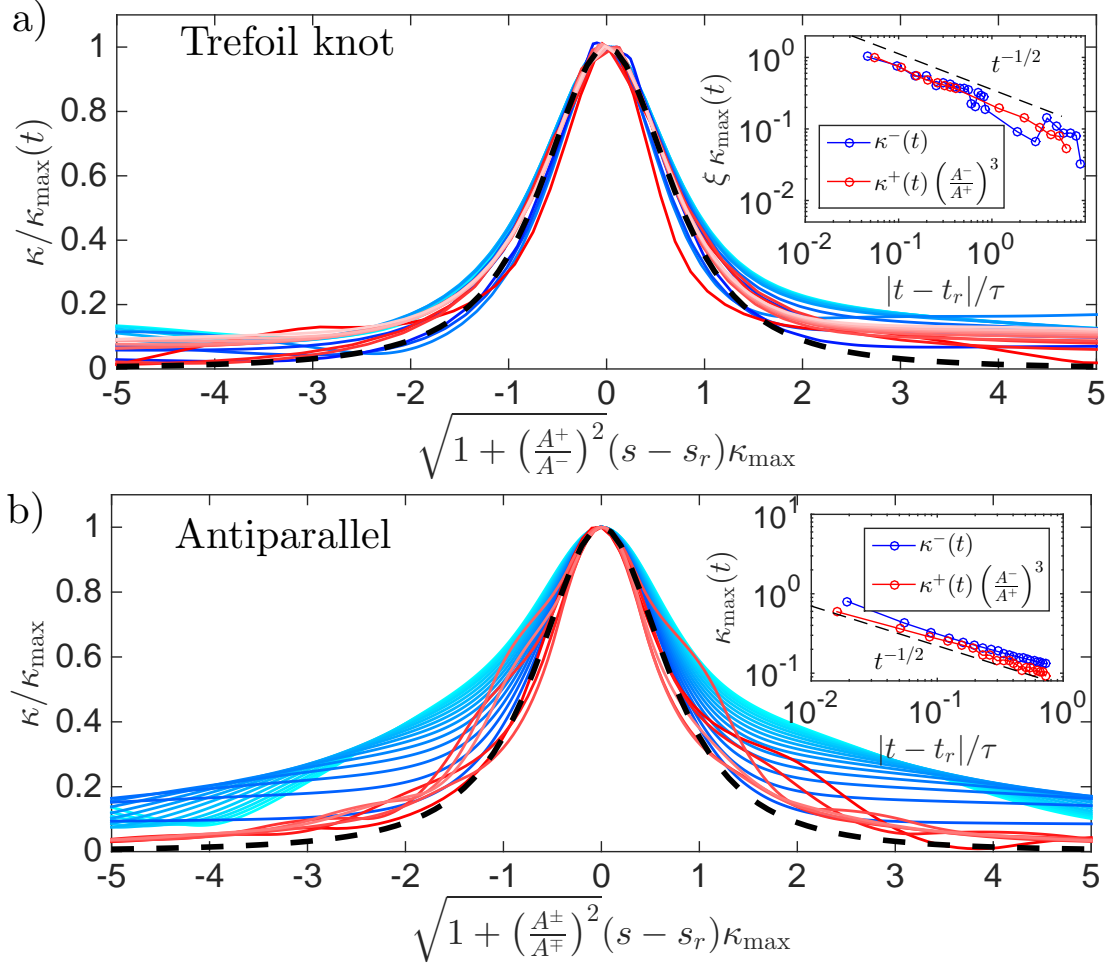


Figure 6.8: a) Self-similar evolution of the curvature close to the reconnection point for the trefoil vortex. Blue lines (from light to dark) correspond to times before reconnection and red lines (from dark to light) to times after reconnection. The inset displays the temporal evolution of the maximum value of the curvature in log-log scales before and after, normalized as suggested in Eq. (6.18). b) Same plot as in a) but for the reconnection occurring in the antiparallel case. In both the figures we consider times such that  $|t - t_r| < 0.5\tau$  and the dashed line shows the  $t^{-1/2}$  scaling. In both figures the black dashed line displays the theoretical prediction (see Eq. 6.19).

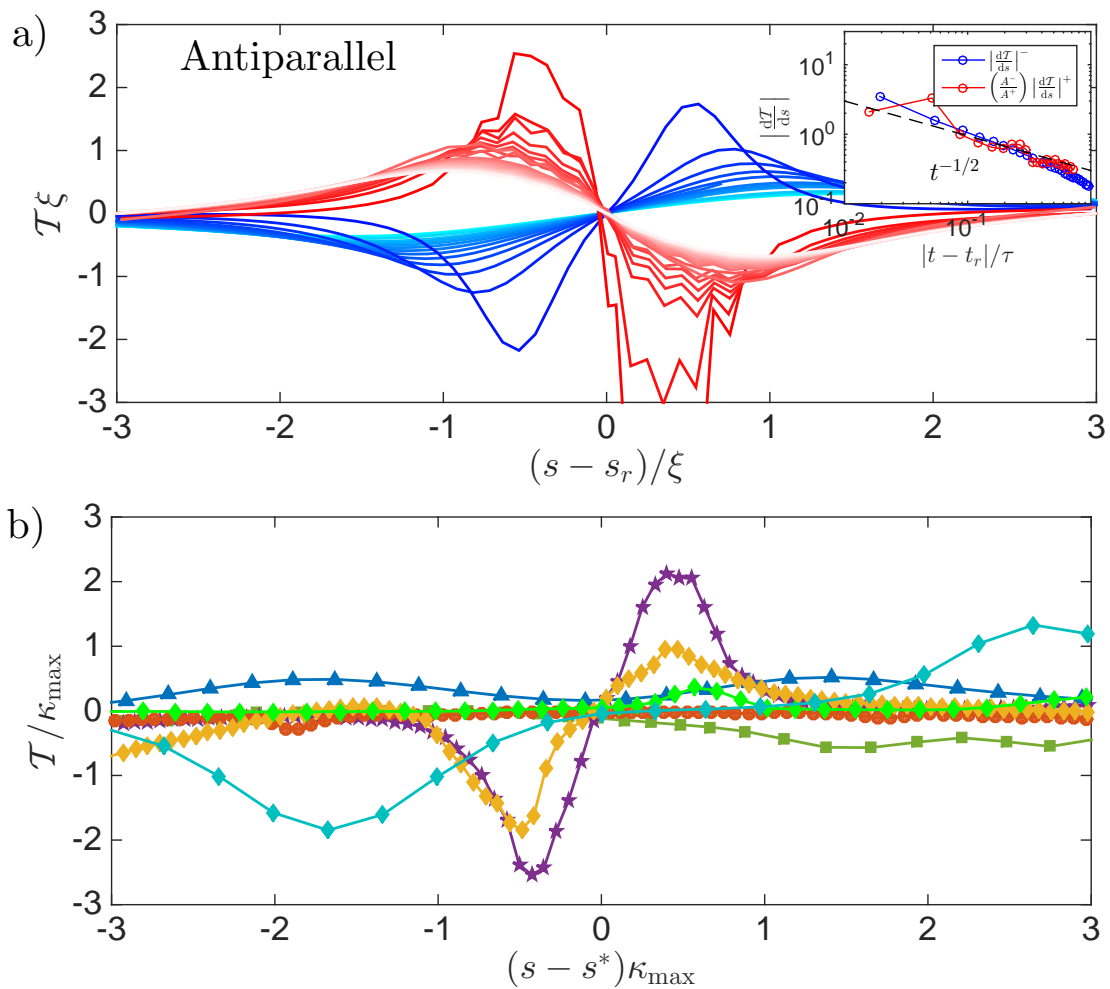


Figure 6.9: a) Temporal evolution of the torsion  $\mathcal{T}$  as a function of the arc-length in the antiparallel case. Blue lines (from light to dark) correspond to times before reconnection and red lines (from dark to light) to times after reconnection. The inset displays the temporal evolution of the slope of torsion computed at the reconnection point  $s_r$  in log-log scales before and after, normalized as  $(A^+/A^-)$ . b) Torsion  $\mathcal{T}$  as a function of the arc-length close to the reconnection (just before) reconnection for all configurations (same legend as in Fig. 6.7).

ancies in previous studies might be due to the fact that: (i) the computational domain is not big enough hence introducing a non-negligible system size length-scale, or (ii) the initial condition contains a considerable amount of sound waves such that the root mean square value of the compressible kinetic energy can be used to construct an extra time-scale, or (iii) the observed scaling correspond to dynamical regimes occurring much later than the reconnection event and thus driven by the specific vortex configuration and therefore non-universal. In that spirit, reconnections within Navier–Stokes flows, modified versions of the GP model with non-local potential and/or high-order non-linearities to better replicate superfluid liquid helium, or coupled GP equations modeling multi-component or spinorial BECs could indeed lead to different scalings.

Our findings demonstrate that the pre-factors  $A^\pm$  are not universal in the GP model. However, once measured on a case by case basis, their ratio determines many properties of the reconnection dynamics. Note that the easiest way to determine this ratio is to look at the medium/large scale reconnection angle  $\phi$  between the hyperbola asymptotes which should be an accessible quantity in superfluid experiments [143, 145, 156]. Let us also remark that the  $t^{1/2}$  scaling we observed extends beyond the distance  $\xi$ . This suggests that the linear approximation might be used as a matching theory in order to relate measurements performed well before and long after the reconnection events. BEC experimentalists are able today to study vortex dynamics and reconnections [145, 156]. Our predictions should directly apply to those systems.

Finally, let us underline that understanding the dynamics of the reconnection events is crucial in order to provide a full understanding of the dissipative processes occurring in superfluids in the low-temperature limit. It is largely believed that KWs play a fundamental role in carrying the energy to the smallest scales where it is finally dissipated by sound radiation. The cusps arising in the vortex filaments due to reconnection events are responsible for a rapid and efficient excitation of KWs at all scales. Here we provided an analytical formula for the dynamical formation of the cusps and we aim to use this result in further theoretical studies to estimate the rate of radiation during reconnections. Also, we have shown that non-negligible torsion of the reconnecting filaments implies the break-down of self-similarity, results in the formation of shock-like structures of the torsion. This phenomenon seems to be linked to the large difference observed in the  $A^\pm$  pre-factors and hence to extreme events where vortices separate much faster than they approach, and to the irreversibility of the reconnection events. We do not yet have a theoretical understanding of this behaviour and more data would be desirable in order to perform a detailed statistical analysis.

# Chapter 7

## Dynamics of Electron Bubbles

### 7.1 Introduction

Electrically charged particles have been one of the most effective probes to test the superfluidity of liquid helium. Starting with the pioneering works of Williams [157], Careri et al. [158] and Reif and Mayer [159], it has been observed that electrons moving through liquid helium due to an applied external electric field can experience different types of interactions. On one hand, when exceeding a critical velocity, they can nucleate vortices and, subsequently, be captured by these hydrodynamical structures. On the other hand, they can scatter with elementary excitations such as phonons and rotons. These characteristics make electrons a perfect candidate for investigating not only the microscopic aspects of superfluidity, such as the breakdown of Landau's criterion, or the structure of the core of quantum vortices, but also macroscopic properties, such as the development of a quantum turbulent flow.

In this work we will mainly focus on the study of the so called *electron bubbles*. The formation of these type of structures was initially suggested by [158, 160, 161] to explain the anomalous low temperature data observed for electrons in liquid helium-4. The rationale behind this model is that it is energetically favourable for a single electron to carve out a spherical cavity within the superfluid due to the short-range repulsive interactions that would otherwise exist between the bare electron and the cloud of electrons of the helium atoms. Although the electron bubble hypothesis has received further experimental confirmation [162], there are many aspects characterising the dynamics of these electrons that remain obscure. For example, the nature of drag forces acting on electron bubbles at low pressure and high electric fields [61] or the mechanisms affecting the mobility of electrons sliding along a vortex at low temperatures [163]. Motivated by these questions and the increasing interest in the use of electron bubbles for the study of quantum turbulence in the zero temperature limit [23, 34], we will present a numerical study of the 3D motion of an electron bubble inside a superfluid using the so called Gross-Clark model [164, 165].

Since there is no universally accepted microscopic model for liquid helium, we will describe the superfluid using the GP equation that is coupled to a Schrödinger equa-

tion to model the state of the electron. We note that such a model does not provide an accurate description for helium-4 since it neither reproduces the correct equation of state nor does it describe the correct dispersion relation since a roton minimum is not present. However it has been shown by the work of Berloff and Roberts [47] that this model can account for the deformations affecting the bubble in its motion and it also captures all the main qualitative physics characterising the interaction between electron bubbles and superfluid vortices, such as the nucleation of vortex rings and the electron capture inside the vortex core. The purpose of our research is then to provide a qualitative description of the effects that vortices have on the motion of electron bubbles for different values of electric field.

The chapter is structured as follows: in the first section we introduce the mathematical model and the main physical assumptions made to describe the motion of electron bubbles, in the second section we explain the numerical set up used in the simulations and in the third section we present the main results obtained. In particular, we have focused on the motion of a free electron and the transport of an electron sliding along a straight vortex line, both of which provide important scenarios that are often investigated in experiments.

## 7.2 Mathematical Model

### 7.2.1 The Gross-Clark Model

We begin by adopting the Gross-Clark model in which the superfluid is modelled by a GP equation. The energy of the system is then given by the Hamiltonian

$$H = H_{GP} + H_e + H_{GP-e}. \quad (7.1)$$

Here liquid helium is governed by the GP Hamiltonian

$$H_{GP} = \int \left( \frac{\hbar^2}{2m_4} |\nabla\psi|^2 + \frac{V_0}{2} |\psi|^4 \right) d^3\mathbf{x}, \quad (7.2)$$

the electron by the free particle Schrödinger Hamiltonian

$$H_e = \int \frac{\hbar^2}{2m_e} |\nabla\phi|^2 d^3\mathbf{x}, \quad (7.3)$$

while the interaction between the superfluid and the electron is modelled by term

$$H_{GP-e} = \int U_0 |\psi|^2 |\phi|^2 d^3\mathbf{x}. \quad (7.4)$$

In this model the parameters  $U_0 = 2\pi\hbar^2/m_e$  and  $V_0 = 4\pi d\hbar^2/m_4$  represent the two-body short-range fermion-boson and the boson-boson interactions, respectively. Since we are not interested in describing high momenta collisions between the electron and the superfluid we can adopt the pseudo potential description to describe this interaction.

We also note that, as argued by Gross [46] and shown by Grant and Roberts [80], the effects of polarization on a structure as large as the electron bubble are not great and thus can be safely neglected for the purpose of this work. The resulting equations of motion are

$$i\hbar\frac{\partial\psi}{\partial t} = -\frac{\hbar^2}{2M}\nabla^2\psi + (U_0|\phi|^2 + V_0|\psi|^2)\psi, \quad (7.5)$$

$$i\hbar\frac{\partial\phi}{\partial t} = -\frac{\hbar^2}{2m_e}\nabla^2\phi + U_0|\psi|^2\phi, \quad (7.6)$$

where the wave functions are subject to the normalization conditions

$$\int |\psi|^2 d^3\mathbf{x} = N, \quad (7.7)$$

and

$$\int |\phi|^2 d^3\mathbf{x} = 1. \quad (7.8)$$

It is known that the GP model does not provide an accurate description of liquid helium. In fact, the dispersion relation does not present a roton minimum. Moreover the pressure of the liquid, given by

$$p = \frac{V_0|\psi|^4}{2}, \quad (7.9)$$

provides an inaccurate relation between pressure and density. Although other models have been proposed, providing a more accurate description of liquid helium [166], in this work we are interested in regimes where the motion of the electron is strongly dominated by the presence of superfluid vortices. We have therefore opted to focus on the simplest model containing all the phenomena characterising the interaction between an electron and quantum vortices. In order to study the transport of the electron through the liquid, an additional term is included in Eq. (7.6) to model the effect of a constant applied electric field  $Q$ . This leads to

$$i\hbar\frac{\partial\phi}{\partial t} = -\frac{\hbar^2}{2m_e}\nabla^2\phi + (U_0|\psi|^2 + eQy)\phi. \quad (7.10)$$

where  $e = 1.6 \times 10^{-19}C$  is the electric charge of the electron. For simplicity we have assumed the electric field to be directed along the  $y$ -coordinate direction of the domain.

## 7.2.2 A Simplified Mathematical Model of Electron Bubble

In order to gain further insight into the electron bubble state, we will use the equations presented in Section 7.2.1 to derive a simple model of a perfectly spherical bubble at equilibrium. This will help reveal the key length scales that arise and which need to be correctly modelled and well resolved in our numerical simulations.

We begin by assuming that, the electron is in its s-state and is trapped within a perfectly spherical cavity of radius  $b$  that represents the bubble state. For simplicity, the cavity is assumed to have an infinite depth. The lowest eigenvalue of Eq. (7.3) will then be given by

$$E_q = \frac{\hbar^2 \pi^2}{2m_e b^2}. \quad (7.11)$$

This expression corresponds to the quantum mechanical energy associated with the zero-point motion of the electron. Another key contribution to the total energy of the electron bubble and superfluid system is one that arises from the (nonlinear) interaction part of the GP Hamiltonian (7.2). From this term, we can determine the work required to carve out a cavity within the superfluid due to the pressure field  $p$  given by Eq. (7.9). This contribution to the energy is given by

$$E_V = pV = \frac{4\pi b^3}{3} p = \frac{2\pi b^3 V_0 \rho^2}{3m_4^2} \quad (7.12)$$

for a spherical cavity. The third principal contribution to the electron bubble energy is given by kinetic energy term in Eq. (7.2)

$$\frac{\hbar^2}{2m_4} \int |\nabla\psi|^2 d\mathbf{x} \sim \frac{2\pi\hbar^2 \rho}{3m_4^2 \xi^2} [(\xi + b)^3 - b^3], \quad (7.13)$$

Here,  $\xi$  is the healing length that sets the length scale over which the density of the fluid rapidly falls off from its farfield value (see [46]). For experimentally relevant parameters, we can assume that  $\xi \ll b$ . The dominant contribution to Eq. (7.13) is then proportional to the area of the bubble and we can interpret this term as the energy associated with the surface tension,  $T$ , of the cavity wall that can be expressed as

$$E_T = 2\pi \frac{\hbar^2 \rho b^2}{m_4^2 \xi} = 4\pi T b^2. \quad (7.14)$$

In the cavity model of the electron bubble, the wavefunctions for the electron and the superfluid do not overlap and hence the interaction term given by Eq. (7.4) does not contribute. The total energy for the electron bubble-superfluid system is then given by

$$E = E_q + E_V + E_T = \frac{\hbar^2 \pi^2}{2m_e b^2} + \frac{4\pi b^3}{3} p + 4\pi T b^2. \quad (7.15)$$

For a more accurate description for this model see Gross in [46], where the fermion-boson interaction in Eq. (7.1) is modelled using a hard-core type of interaction.

Using this model, we can estimate the radius  $b$  of the electron bubble and subsequently its hydrodynamic mass  $m_h$  [76]. Since the electron mass  $m_e$  is much smaller than the helium mass  $m_4$ ,

$$\delta = \frac{m_e}{m_4} \sim 1.4 \times 10^{-4}, \quad (7.16)$$

the effective mass of the bubble can be approximated by

$$m_h = \frac{2}{3} \pi \rho b^3. \quad (7.17)$$

We note that in the case of zero pressure, it is possible to obtain the radius of the bubble which minimizes the electron energy  $E$ :

$$b = \left( \frac{\pi \hbar^2}{8m_e T} \right)^{1/4}. \quad (7.18)$$

Considering typical values of liquid helium at zero temperature, such as the surface tension based on measurements of bulk helium [167],  $T = 375 \mu J m^2$  and the liquid density  $\rho = 0.145 g/cm^3$ , one can finally estimate both the effective radius  $b = 18.91 \text{ \AA}$  and the mass  $M = 309 m_4$  for an electron bubble at zero pressure.

For non-zero pressure, it is possible to estimate a radius of the bubble by using the method of dominant balance under the assumption that  $\delta \rightarrow 0$ . We begin by noting that a stationary value for the energy given by Eq. (7.15) is given by the solution of

$$\frac{\partial E}{\partial b} = -\frac{\hbar^2 \pi^2}{m_e b^3} + 4\pi b^2 p + 8\pi T b = 0. \quad (7.19)$$

Now we can assume that Eq. (7.19) is balanced by two dominant terms. Assuming the first term to be negligible we find

$$b = -\frac{2T}{p}. \quad (7.20)$$

Since  $b$  is negative, it follows that we can not neglect the first term in the equation. Now, assuming the second term to be negligible, we find

$$b = \left( \frac{\hbar^2 \pi}{8m_e T} \right)^{1/4}. \quad (7.21)$$

Substituting Eq. (7.21) into Eq. (7.15) we obtain

$$E = \frac{\hbar^2 \pi^2}{2} \left( \frac{\hbar^2 \pi}{8T} \right)^{-1/2} m_e^{-1/2} + \frac{4\pi p}{3} \left( \frac{\hbar^2 \pi}{8T} \right)^{3/4} m_e^{-3/4} + 4\pi T \left( \frac{\hbar^2 \pi}{8T} \right)^{1/2} m_e^{-1/2}. \quad (7.22)$$

Motivated by the physics of the problem we consider the limit  $\delta \rightarrow 0$ . In this regime the second term is dominant, which is inconsistent with our initial assumption.

Assuming the third term to be negligible, then

$$b = \left( \frac{\pi \hbar^2}{4m_e p} \right)^{1/5}. \quad (7.23)$$

Substituting Eq. (7.23) into Eq. (7.15) we obtain

$$E = \frac{\hbar^2 \pi^2}{2} \left( \frac{\pi \hbar^2}{4p} \right)^{-2/5} m_e^{-3/5} + \frac{4\pi p}{3} \left( \frac{\pi \hbar^2}{4p} \right)^{3/5} m_e^{-3/5} + 4\pi T \left( \frac{\pi \hbar^2}{4p} \right)^{2/5} m_e^{-2/5}. \quad (7.24)$$

In the limit  $\delta \rightarrow 0$  the third term is negligible, which leads to a self-consistent estimate. It follows that, by using the method of the dominant balance, we can conclude that the value of the radius of the bubble will be given by Eq. (7.23). This provides an important length scale in the problem that dictates the size of the computational domain that will be needed in our simulation to resolve the relevant physical scales of interest

## 7.3 Numerical scheme

### 7.3.1 Non-dimensional Form of the Equations of Motion

In order to integrate the above superfluid-electron system numerically, we will now rewrite the equations of motion in non-dimensional form. We begin introducing the transformations

$$\mathbf{x} \rightarrow \xi \mathbf{x}, \quad t \rightarrow \gamma t, \quad \psi \rightarrow \psi_\infty \psi, \quad \phi \rightarrow \Phi \phi, \quad Q \rightarrow qQ \quad (7.25)$$

where we use the the superfluid healing length

$$\xi = \frac{\hbar}{\sqrt{2m_4\mu}} = (8\pi d\psi_\infty^2)^{-1/2}, \quad (7.26)$$

as unit of length, the ratio between  $\xi$  and the speed of sound  $c$  as unit of time

$$\gamma = \frac{\xi}{\sqrt{2}c} = \frac{\hbar}{2\mu} \quad (7.27)$$

and the chemical potential  $\mu$  for a uniform ground state characterised by  $N$  and described by the wave function

$$\psi_\infty = \sqrt{\frac{\rho_\infty}{m_4}} = \sqrt{\frac{\mu}{V_0}}. \quad (7.28)$$

Using the re-scalings given by Eq. (7.25), Eq. (7.5) transforms to

$$i\frac{\partial\psi}{\partial t} = -\frac{1}{2}\nabla^2\psi + \frac{1}{2}\left(4\pi\xi^2\left[\frac{m_4 l}{m_e\xi}\Phi|\phi|^2 + |\psi|^2\right]\right). \quad (7.29)$$

We, therefore, introduce the small parameter

$$\epsilon = \left(\frac{\xi m_e}{lm_4}\right)^{1/5} \quad (7.30)$$

Noting that  $1/\epsilon$  is of the same order as the dimensionless radius of the bubble  $b/\xi$ , we chose to rescale the electron wave function such that such that

$$\Phi = \left(\frac{\epsilon^3}{4\pi\xi^3}\right)^{1/2} \quad (7.31)$$

with

$$\int |\phi|^2 d^3\mathbf{x} = \frac{4\pi}{\epsilon^3}. \quad (7.32)$$

Finally, we express the electric field in units of

$$q = \left(\frac{\mu}{\delta e\xi}\right). \quad (7.33)$$

We can now rewrite Eq. (7.5) and Eq. (7.6) as

$$i\frac{\partial\psi}{\partial t} = -\frac{1}{2}\nabla^2\psi + \frac{\chi}{2}|\phi|^2\psi + \frac{1}{2}|\psi|^2\psi, \quad (7.34)$$

and

$$i\frac{\partial\phi}{\partial t} = -\frac{1}{2\delta}\nabla^2\phi + \frac{1}{2\delta}(\Upsilon^2|\psi|^2 + yQ)\phi \quad (7.35)$$

where

$$\chi = \frac{1}{\epsilon^2} \quad \Upsilon^2 = \frac{l}{2d} \quad \delta = \frac{m_e}{m_4}. \quad (7.36)$$

Motivated by modelling electrons in superfluid Helium-4, we follow the work by Berloff and Roberts [47] and assume  $\xi = 1 \text{ \AA}$ ,  $\Upsilon = 0.41$ ,  $\epsilon = 0.187$ ,  $\mu = 5.22 \times 10^{-4} \text{ eV}$ ,  $\delta = 1.4 \times 10^{-4}$  and  $\rho_\infty = 0.145 \text{ Kg/cm}^2$ . Hence, we can derive the unit of electric field  $q = 3.72 \text{ V/\AA}$ , the unit of time  $\chi = 0.63 \times 10^{-12} \text{ s}$ , and the unit of velocity  $\xi/\gamma = 1.58 \times 10^2 \text{ m/s}$ .

### 7.3.2 Adiabatic Approximation

The non-dimensional form of the equations presented above reveals a major difficulty arising from any attempt to directly integrate these equations using the values of parameters of relevance to helium-4. In particular, the small value of  $\delta$  appearing in the kinetic energy term of the Schrödinger equation (7.35) leads to a clear disparity in the time scales of the superfluid and the electron. Therefore direct solution of Eqs. (7.34) and (7.35) for scenarios of physical relevance becomes impractical. Although the disparity in time scales leads to numerical challenges, it can also be used to simplify the problem to eliminate the source of difficulty. In particular, we observe that, for an electron trapped within the potential  $|\psi(\mathbf{x}, t)|^2$  created by the surrounding fluid, if the time scale over which the potential changes is much larger than the typical quantum time scale  $m_e b^2 / \pi \hbar$  of the electron, then we are in a regime where the so called *adiabatic approximation* holds. In quantum mechanics the *adiabatic theorem* states that a particle starting from  $n$ th-eigenstate  $\phi_n$  will remain in that  $n$ th-eigenstate  $\tilde{\phi}_n$  but will acquire some extra phase factors, such that

$$\tilde{\phi}(t) = \phi_n(t) e^{i\theta_n(t)} e^{i\gamma_n(t)} \quad (7.37)$$

where  $\theta$  and  $\gamma$  are respectively called the dynamical and the geometrical phase factors [168]. The adiabatic theorem can therefore be linked to study the dynamics of the superfluid-bubble complex. In fact, by starting with an electron bubble in its ground state, we expect the bubble to remain in its lowest energy level. This allows us to reformulate our original problem as

$$i\frac{\partial\psi}{\partial t} = -\frac{1}{2}\nabla^2\psi + \frac{\chi}{2}|\phi_g|^2\psi + \frac{1}{2}|\psi|^2\psi, \quad (7.38)$$

where  $\phi_g$  corresponds to the ground state that is determined by finding the minimum energy,  $E$ , for which

$$E_g\phi_g = \left[ -\frac{1}{2\delta}\nabla^2 + \frac{1}{2\delta}(\Upsilon^2|\psi|^2 + yQ) \right] \phi_g. \quad (7.39)$$

and Eq. (7.8) are satisfied. Since the contribution of the electron wave-function in Eq. (7.38) is given by the squared modulus  $|\phi_g|^2$ , the evaluation of the dynamical and the geometrical phases turns out to be unimportant in studying the dynamics of an electron bubble in a superfluid within the adiabatic approximation.

### 7.3.3 Initial Condition

In order to initialise an electron in its ground state, we need to find the correct initial condition describing the lowest energy state for the system of equations (7.34) and (7.35) with  $Q = 0$ . We accomplish this by using the so-called gradient flow method [169] which consists of integrating both Eq. (7.34) and Eq. (7.35) in imaginary time. To ensure convergence of the method to the correct ground state solution, we need to find a good initial guess for such a ground state. We therefore consider the wave-function of an electron confined in an infinite spherical well potential. Solving the Helmholtz equation

$$\nabla^2\phi + k^2\phi = 0 \quad (7.40)$$

in a sphere of radius  $\pi/k$  we obtain

$$\phi_0(r, \theta, \varphi) = \left(\frac{2k^3}{\pi\epsilon^3}\right)^{1/2} \frac{\sin(kr)}{kr} \quad r < \pi/k. \quad (7.41)$$

where  $k$  represents the different eigenvalues that can be supported by the system. For the ground state with energy  $E_q$  given by Eq. (7.11), we find

$$k^2 = \frac{m_e E_q}{m_4 \mu} = \frac{\hbar^2 \pi^2}{2m_4 \mu b^2} = \frac{\pi^2 \xi^2}{b^2} = 0.0342 \quad (7.42)$$

to obtain

$$4\pi \int_0^{\pi/k} |\phi|^2 r^2 dr = \frac{4\pi}{\epsilon^3}. \quad (7.43)$$

For the superfluid wave-function we choose a density profile given by

$$\psi_0(r, \theta, \varphi) = \tanh\left(\frac{r-b}{\sqrt{2}}\right) \quad r \geq b \quad (7.44)$$

$$\psi_0(r, \theta, \varphi) = 0 \quad r \leq b. \quad (7.45)$$

With the above initial conditions for the two fields  $\psi = \psi_0$  and  $\phi = \phi_0$ , we can then integrate the system of equations

$$\frac{\partial}{\partial \varrho} \begin{pmatrix} \psi \\ \phi \end{pmatrix} = \frac{1}{2} \begin{bmatrix} \nabla^2 & 0 \\ 0 & \delta^{-1} \nabla^2 \end{bmatrix} \begin{pmatrix} \psi \\ \phi \end{pmatrix} - \frac{1}{2} \begin{bmatrix} \chi|\phi|^2 + |\psi|^2 & 0 \\ 0 & \delta^{-1} \Upsilon^2 \end{bmatrix} \begin{pmatrix} \psi \\ \phi \end{pmatrix}, \quad (7.46)$$

with respect to the parameter  $\varrho$ . Restricting attention to periodic boundary condition we use a symmetric Strang splitting pseudo-spectral method given by

$$\begin{pmatrix} \psi(\mathbf{x}, \varrho + \Delta\varrho) \\ \phi(\mathbf{x}, \varrho + \Delta\varrho) \end{pmatrix} = e^{(\Delta\varrho/2)\hat{N}(\mathbf{x})} e^{\Delta\varrho\hat{L}} e^{(\Delta\varrho/2)\hat{N}(\mathbf{x})} \begin{pmatrix} \psi_0(\mathbf{x}, \varrho) \\ \phi_0(\mathbf{x}, \varrho) \end{pmatrix} \quad (7.47)$$

and we iterate to obtain an improved approximation of our initial conditions. In equation (7.47),  $\hat{\mathcal{N}}(\mathbf{x})$  is defined in the physical space as

$$\hat{\mathcal{N}}(\mathbf{x}) = \begin{bmatrix} \hat{\mathcal{N}}_{GP} & 0 \\ 0 & \hat{\mathcal{N}}_e \end{bmatrix} = -\frac{1}{2} \begin{bmatrix} \chi|\phi|^2 + |\psi|^2 & 0 \\ 0 & \delta^{-1}\Upsilon^2 \end{bmatrix} \quad (7.48)$$

and  $\hat{\mathcal{L}}(\mathbf{x})$  is defined in the Fourier space as

$$\hat{\mathcal{L}}(\mathbf{k}) = \begin{bmatrix} \hat{\mathcal{L}}_{GP} & 0 \\ 0 & \hat{\mathcal{L}}_e \end{bmatrix} = -\frac{1}{2} \begin{bmatrix} |\mathbf{k}|^2 & 0 \\ 0 & \delta^{-1}|\mathbf{k}|^2 \end{bmatrix}. \quad (7.49)$$

Such method is iterated until the  $L^2$  norm defined as

$$\text{Err} = \int \left| \begin{pmatrix} \psi(\mathbf{x}, \varrho + d\varrho) \\ \phi(\mathbf{x}, \varrho + d\varrho) \end{pmatrix} - \begin{pmatrix} \psi(\mathbf{x}, \varrho) \\ \phi(\mathbf{x}, \varrho) \end{pmatrix} \right|^2 d^3\mathbf{x}, \quad (7.50)$$

drops below a specified threshold.

### 7.3.4 Dynamical Evolution

Once we determine the equilibrium state of the system, we set  $Q \neq 0$  and integrate Eq. (7.38) to study the dynamics of the superfluid and electron bubble in the adiabatic approximation. The numerical integration is performed using periodic boundary conditions and adopting the same pseudo-spectral method that is described in the previous section. The evolution of the superfluid at time  $t = t_0 + \Delta t$  is given by

$$\psi(\mathbf{x}, t + \Delta t) = e^{(\Delta t/2)\hat{\mathcal{L}}_{GP}} e^{\Delta t \hat{\mathcal{N}}_{GP}(\mathbf{x}, t_1)} e^{(\Delta t/2)\hat{\mathcal{L}}_{GP}} \psi(\mathbf{x}, t) \quad (7.51)$$

where  $t_1 = \Delta t/2 + t$ . We note that  $\hat{\mathcal{N}}_{GP}$  is defined in terms of

$$\psi(\mathbf{x}, t_1) = e^{(\Delta t/2)\hat{\mathcal{L}}_{GP}} \psi(\mathbf{x}, t) \quad (7.52)$$

while  $\phi(\mathbf{x}, t_1)$  corresponds to the ground state for an electron governed by Eq. (7.39) for an electron in the presence of an external potential given by  $\frac{\Upsilon^2}{2\delta} |\psi(\mathbf{x}, t_1)|^2$ . In order to find the ground state of Eq. (7.39), we use the gradient flow method described in the previous section but applied only to the Schrödinger equation given by the form

$$\frac{\partial \phi}{\partial \varrho} = \frac{1}{2\delta} \nabla^2 \phi - \frac{1}{2\delta} (\Upsilon^2 |\psi|^2 \phi + yQ) \phi. \quad (7.53)$$

We note that the presence of the  $y$ -dependent term  $(yQ/2\delta)\phi$  in the equation of motion of the bubble could in principle cause a discontinuous jump, and hence Gibbs oscillations, in the  $y$ -direction since periodic boundary conditions are chosen. However, since the bubble is a localized object, confined in the cavity-potential created by the superfluid, the wave-function will decay exponentially outside this cavity. Therefore, considering a sufficiently large domain, we are still able to decompose the wave-function in Fourier space. On the other hand, the motion of the electron bubble towards the

boundaries will lead to numerical instabilities due to the discontinuous form of the potential across the boundaries arising from the last term in Eq. (7.53). To avoid this, we apply a coordinate transformation that re-centers the bubble within the computational domain after a time interval  $\Delta t_s$ . The spatial translations are defined by setting  $\mathbf{X}' = \mathbf{x} - \mathbf{x}_{CM}(\Delta t_s)$ , where

$$\mathbf{x}_{CM}(\Delta t_s) = \frac{\int \mathbf{x} |\phi(\mathbf{x}, \Delta t_s)|^2 d^3 \mathbf{x}}{\int |\phi(\mathbf{x}, \Delta t_s)|^2 d^3 \mathbf{x}} \quad (7.54)$$

is the centre of mass of the bubble at time  $\Delta t_s$ . To keep track of the real position of the ion, we evaluate the cumulative displacement of the bubble by defining

$$\mathbf{X}_{CM}(\Delta t_i) = \mathbf{x}_{CM}(t_i - \Delta t_s) + \sum_{j < i} \mathbf{x}_{CM}(\Delta t_s)_j \quad (7.55)$$

with  $i \geq 1$  and  $j > 0$ . The wave function  $\psi(x', t)$  in the new frame of reference can then be recovered from

$$\psi(\mathbf{x}', t) = \hat{\mathcal{F}}^{-1} \left[ e^{i\mathbf{k} \cdot \mathbf{x}_{CM}} \hat{\mathcal{F}} [\psi] \right] \quad (7.56)$$

where  $\hat{\mathcal{F}}$  stands for the fast Fourier transform. Concerning  $\phi$ , the problem can be simply reduced to finding a new ground state subject to the shifted potential  $\frac{\Upsilon^2}{2\delta} |\psi(\mathbf{x}', t)|^2$ .

### 7.3.5 Projected Gross-Pitaevskii Equation

An issue affecting pseudo-spectral numerical methods applied to non-linear partial differential equations is the well known aliasing error [170]. To present the key observations, we will consider a periodic 1D system discretised on  $n_{max}$  collocation points in a domain of length  $L_x$ . Expressing the GP equation in terms of Fourier harmonics, such that

$$\psi(x, t) = \sum_k A_k(t) e^{ik \cdot x}, \quad (7.57)$$

we obtain

$$2i \frac{dA_k}{dt} = A_k + \sum_{k_1, k_2} A_{k_1} A_{k_1+k_2}^* A_{k+k_2} \quad (7.58)$$

Here  $k = n\Delta k$  and  $\{n \in \mathbb{Z} : -n_{max} < n \leq n_{max}\}$  with  $\Delta k = 2\pi/L_x$ . Hence the number of modes is then defined up to a cut-off scale given by  $k_{max} = n_{max}\Delta k/2$ . For such a discrete system, the harmonic  $e^{inx\Delta k}$  is equivalent to  $e^{i(n+jn_{max})x\Delta k}|_{j \in \mathbb{Z}}$ . Now the non-linear term will typically excite modes with a higher harmonic (e.g.  $k_1 + k_2$ ) from the interaction of the modes corresponding to  $k_1$  and  $k_2$  lying within the range  $-k_{max} < k_1, k_2 \leq k_{max}$ . It follows that if not handle correctly, this  $k_1 + k_2$  higher mode will project back into the modes within the range  $-k_{max} < k_1, k_2 \leq k_{max}$  leading to inaccurate solution of the equations. This is the essence of the aliasing phenomena. To avoid such errors, associated with the biasing of the amplitude of the lower modes, we introduce a low-pass filter acting in Fourier space. Such a filter consists of truncating

all the modes higher than  $2/3k_{max}$ . Defining a projector  $\hat{\mathcal{P}}$  acting on the Fourier space as

$$\hat{\mathcal{P}}[A_k] = \theta(2/3k_{max} - |k|)A_k, \quad (7.59)$$

where  $\theta(\dots)$  is the Heaviside step function, the correct discrete representation of the GP equation using a Fourier basis is then the truncated GP equation, TGP:

$$2i\frac{\partial\psi}{\partial t} = \hat{\mathcal{P}} \left[ -\nabla^2\psi + \hat{\mathcal{P}}[|\psi|^2]\psi \right]. \quad (7.60)$$

This equation can be derived from the truncated Hamiltonian

$$H = \int \left( \frac{1}{2}\hat{\mathcal{P}}[|\nabla\psi|^2] + \frac{1}{2}\left(\hat{\mathcal{P}}[|\psi|^2]\right)^2 \right) d^3\mathbf{x}. \quad (7.61)$$

As shown by Krstulovic and Brachet [171], such system also conserves the number of particles and the linear momentum. Including the interaction with the electron wave function, we can finally write the projected Gross-Clark equation, as

$$i\frac{\partial\psi}{\partial t} = \hat{\mathcal{P}} \left[ -\frac{1}{2}\nabla^2\psi + \frac{\chi}{2}\hat{\mathcal{P}}[|\phi_g|^2]\psi + \frac{1}{2}\hat{\mathcal{P}}[|\psi|^2]\psi \right]. \quad (7.62)$$

## 7.4 Result for the Motion of a Free Electron

The first problem addressed in this section is the study of the motion of a free electron in helium-4 i.e. one that is not trapped on a vortex line. The transport of negative electrons in liquid helium has been experimentally investigated for long a time in order to understand different types of drag forces acting on an object moving through a superfluid [172, 173]. While at finite temperature the velocity of an electron is limited by the scattering of thermal excitations, in the limit of  $T = 0K$  it is less clear what are the main mechanisms limiting the motion of a electron moving under the influence of an applied electric field. In fact, at sufficiently low temperatures, the kinetic energy of the electron cannot be dissipated due to interaction with rotons, phonons or helium-3 atoms. The electron will therefore accelerate until it attains a critical velocity for the nucleation of vortex rings. Subsequently, the electron can become trapped on the core of a shed ring.

Nancolas and McClintock [174] showed that such a transition in which the electron is captured by the nucleated ring can be suppressed by operating at high pressures and by applying a sufficiently high electric field. In this regime, the electron can exceed Landau critical velocity, which corresponds to the velocity at which rotons should be excited. They also demonstrated that as the operating pressure is lowered below 16 bar, the experimental data of Nancolas et al. showed a clear drop in the drift velocity of the electron (see Fig. 7.1). They attributed this behaviour to the continuous generation of vortex rings in which the electron can undergo intermittent vortex capture events. Hence a natural question that arises is what limits the velocity of the electron in this parameter range. Nancolas *et al.* [61] speculated about the emission of a stream of

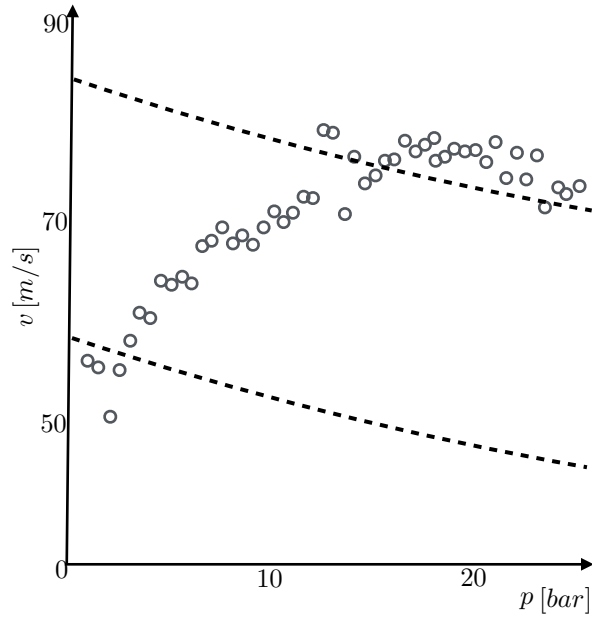


Figure 7.1: Plot of the drift velocity of negative electrons as a function of pressure in He II at 0.3 K moving under the influence of an applied electric field of  $2.6[MV/m]$ . The lower dashed line represents the dependence of the Landau critical velocity on the pressure while the upper line represents the expected drift velocity of the electron due to the emission of rotons. (Nancoles et al. [61])

vortex rings, while Guo and Jin [166] proposed the emission of sound waves as new mechanism to dissipate kinetic energy. In order to resolve the question concerning the nature of the dissipation mechanism at low temperatures, we will numerically model the motion of an electron under different electric fields. The model we choose neglect both the presence of thermal excitations and the emission of rotons allowing us to focus on the role of the emitted vortex rings affecting the motion of a bare electron bubble.

### 7.4.1 Numerical Results

All the numerical simulations were carried out in a periodic domain using the algorithm explained earlier, implemented on a Tesla K40 NVIDIA graphics card. We model a flow in a channel of length  $L_x = 1024$ ,  $L_y = 128$  and  $L_z = 128$  with resolution set to  $\Delta x, \Delta y, \Delta z = 1$ . Given the localised nature of the electron wave-function, this was resolved on a smaller domain of size  $L_x = 128$ ,  $L_y = 128$  and  $L_z = 128$ , and constrained within the central region of the channel as illustrated in Fig. 7.9. The time step used for integrating the GP equation (7.62) was  $\Delta t = 0.01$  while the step used for the gradient flow method to find the ground state of the Schrödinger equation (7.53) was set  $\Delta \rho = 0.0001$ . The gradient flow method was applied at each step until the  $L^2$  norm, given by Eq. (7.50), satisfied the threshold  $\text{Err} < 10^{-7}$  in Eq. (7.46) and  $\text{Err} < 10^{-6}$  in Eq. (7.53). Throughout the numerical solution procedure, we allowed the bubble to evolve over 100 time steps before shifting the entire fields, such that the bubble was recentred within the channel using the procedure described in Section 7.3.4.

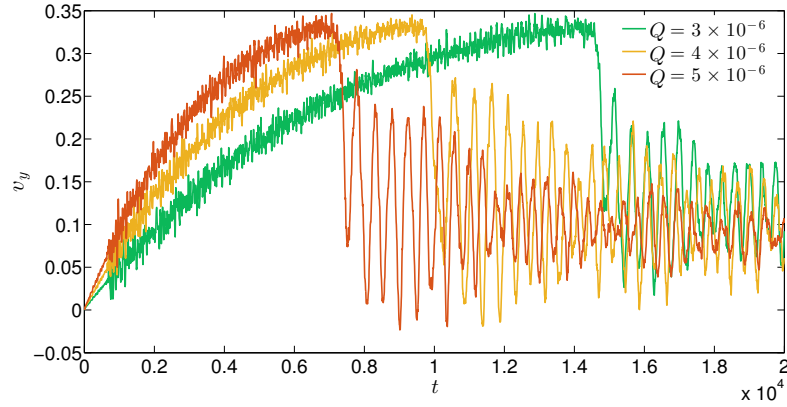


Figure 7.2: Plot showing the variation in time of the velocity of electron bubbles moving under the influence of electric fields of different strength. Each run shows an essentially discontinuous change in the velocity due to the capture of the electron by a nucleated vortex ring. After the sudden drop in velocity, the electron experiences large fluctuations due to KWs excited during the capture process.

In the absence of thermal excitations, the velocity of the electron under the influence of an externally applied electric field will increase until a critical velocity  $v_c$  is reached for the onset of the nucleation of vortex rings. In Fig. 7.2, we plot the time variation of the  $y$ -component of the velocity of the bubble estimated as

$$v_y \simeq \frac{Y_{CM}(t + \Delta t_s) - Y_{CM}(t)}{\Delta t_s}, \quad (7.63)$$

where  $Y_{CM}$  represents the  $y$ -coordinate of the centre of mass of the bubble defined as in Eqs. (7.54) and (7.55). Since the electron does not experience any drag during the early stages of the dynamics, the change on velocity is initially governed by the equation

$$\dot{v}_y = \frac{eq\gamma^2}{m_h \xi} = \frac{1}{2\gamma} \frac{m_4}{m_h} Q \quad (7.64)$$

with  $m_h$  is the effective mass of the electron given by Eq. (7.17). By doing a linear fit when  $0 < t < 500$  we obtain the bubble acceleration  $\dot{v}_y = 1.9 \times 10^{-5}$  which correspond to an effective mass of  $184m_4$  and to an effective radius of  $16\text{\AA}$ . After the initial linear growth, the velocity starts decreasing in time due the deformations of the bubble which causes the effective mass to grow. When the velocity reaches a critical value  $v_c \sim 0.32$  the bubble nucleates a vortex ring and is subsequently captured by it. This process gives rise to the formation of a charged vortex ring. Details of this transition are shown in Fig 7.3.

The transition to a charged vortex ring is associated with a sudden drop in the velocity of the bubble. During the capture process, the sudden sideways movement of the electron generates large perturbations of the vortex ring. These fluctuations are clearly visible in Fig. 7.2 after the discontinuity in the electron velocity. We expect that the decay of these oscillations is mediated by non-linear interactions that act to transfer

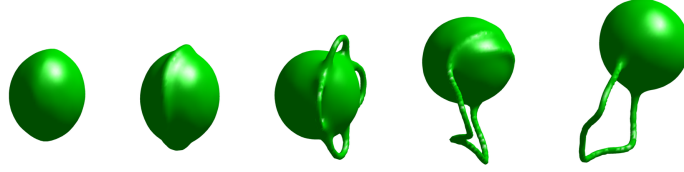


Figure 7.3: Isosurface plot corresponding to  $|\psi|^2 = 0.3$  of an electron bubble moving in the presence of a constant applied electric field of  $Q = 3 \times 10^{-6}$ . The sequence of images correspond to times  $t = 12500$ ,  $t = 14750$ ,  $t = 15000$ ,  $t = 15500$  and  $t = 15750$  respectively, and show the transition from a free electron to a charged vortex ring

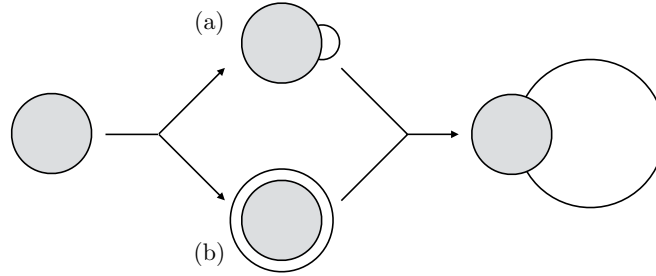


Figure 7.4: Scheme of the two alternative models describing the nucleation process: a) the peeling model; b) the girdling model. The arrows indicate the direction of time.

energy to smaller scales until they get dissipated through sound emission.

As suggested in [175], the size of the charged vortex ring continues to increase with its velocity approaching the self-induced velocity of a circular vortex ring.

Many theories have been proposed in the past to explain the mechanism of vortex nucleation. In particular we recall the works by Bowley *et al.* [176] and Murihead *et al.* [177]. In these works, two different competing mechanisms were presented. In the first one, named the girdling model, a vortex ring detaches simultaneously from the equator of the bubble, while in the second one, named the peeling model, a vortex ring grows out from a small vortex loop attached to the bubble. A schematic plot of these two models is presented in Fig. 7.4. In contrast to previous numerical studies [175, 178] we conclude that an electron bubble, accelerated by a constant electric field, nucleates a vortex ring according to the peeling model. In Fig. 7.3 it is possible to see how small loops, initially attached to the bubble, merge together forming a charged vortex ring with large amplitude KWs on it.

As a final remark, we note that independent of the strength of the applied electric field, the nucleation always takes place at the critical velocity  $v_c \sim 0.32$ , which is in good agreement with what was observed numerically for a deformable electron bubble in [47]. Such a value is closely related to the critical velocity associated with the motion of a hard sphere in an incompressible fluid as discussed by Berloff *et al.* [47] and Frisch *et al.* [179]. From classical fluid mechanics it is known that the laminar flow around



Figure 7.5: Isosurface plot corresponding to  $|\psi|^2 = 0.3$  of an electron bubble moving in the presence of a constant applied electric field of  $Q = 10^{-5}$ . The sequence of images correspond to times  $t = 5250$ ,  $t = 5500$  and  $t = 5750$  respectively, and show the nucleation of a vortex ring according to the girdling model.



Figure 7.6: Isosurface plot corresponding to  $|\psi|^2 = 0.3$  of an electron bubble moving in the presence of a constant applied electric field  $Q = 2 \times 10^{-5}$ . The sequence of images correspond to times  $t = 16250$ ,  $t = 16500$  and  $t = 16750$  respectively, and show the transition to a charged vortex ring.

such an object has a maximum velocity at the equator equal to  $(3/2)v_\infty$ , where  $v_\infty$  is the velocity in the far-field. According to [47, 179] when  $(3/2)v_\infty$  matches the speed of sound  $c$  set by the dispersion relation of the superfluid, the vortex nucleation takes place. Small corrections due to the deformations of the bubble during its motion can modify the value of the critical velocity to  $v_c \sim 0.34$  [47] which turns out to be in good agreement with our observed numerical value.

For higher electric fields the electron enters a regime where a vortex ring is nucleated and manages to escape from the electron (see Fig. 7.5). At the centre of the vortex ring, Bernoulli effects result in a pressure drop which causes the electron to become more susceptible to perturbations that causes the electron to begin to move in the transverse direction. This deflection of the trajectory of the electron leads to the development of chaotic dynamics. For example, in Fig. 7.6 we observe that this can lead to the formation of two vortex loops with different sizes, the smaller of which detaches from the electron while the larger one captures the bubble. In Fig. 7.7, the nucleation of several vortex rings is evident by the abrupt fall off in the velocity of the electron that takes place at different instants in time. In particular, for  $Q = 10^{-5}$  at  $t = 3000$  the electron reaches the critical velocity  $v_c$ , nucleates a vortex ring with a consequent drop-off in the velocity. Thereafter, the electron accelerates until it again reaches the critical velocity,  $v_c$ , and the system cycles again through the same sequence of events. Eventually, after the nucleation of several vortices, the electron finally becomes trapped, resulting in a charged vortex ring with the velocity fluctuating around the value  $v_y \sim 0.1$ . As can be

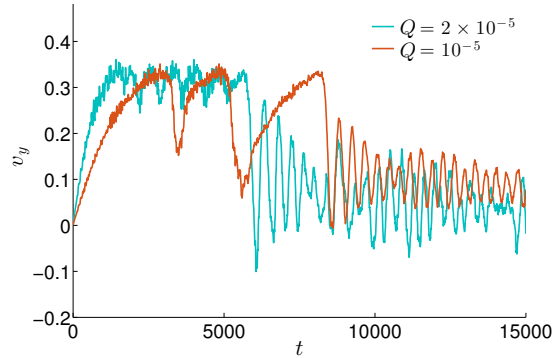


Figure 7.7: Plot of the time evolution of the velocity of an electron bubble for two different values of the applied electric field. The transition to a charged vortex ring take place after the emission of several vortex rings. The time between two subsequent nucleation processes decreases with the increasing strength of the electric field.

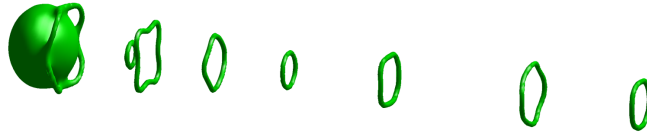


Figure 7.8: Isosurface plot corresponding to  $|\psi^2| = 0.3$  for an applied electric field  $Q = 10^{-4}$ . The figure shows the emission of a stream of vortex rings.

seen in Fig. 7.7, the time between two subsequent vortex nucleation processes decreases with the increasing strength of the electric field.

Nancolas *et al.*, [174], suggested that the transition to a charged vortex ring can be suppressed by applying high electric fields. In Fig. 7.8 we show a stream of vortex rings having more or less the same size as the bubble for  $Q = 10^{-4}$ . The nucleated rings interact together giving rise to a leapfrogging type behaviour. In particular, vortex rings nucleated at earlier time can be slowed down and eventually propelled toward the electron until they scatter off the ion. Because of the collective motion of the nucleated rings, the velocity of the electron initially exceeds the critical value  $v_c$  but subsequently enters a regime characterized by highly chaotic dynamics with irregular vortex shedding (see Fig. 7.9). Upon increasing the strength of the electric field, the frequency for the emission of vortex rings increases. As shown in Fig. 7.9, for  $Q = 5 \times 10^{-4}$ , the nucleation becomes so rapid that a small vortex tangle starts developing. In Fig. 7.10, we also present the evolution of the velocity of the bubble for different values of the electric field. The figure shows that the electron experiences two different regimes during its dynamics. More specifically, by looking at the case of  $Q = 5 \times 10^{-4}$  (purple line), it is possible to see that the velocity of the bubble initially plateaus at  $v_y \sim 0.5$  (see solid line). The same behaviour is confirmed also by the other runs performed under different values of the electric field. The value at which the velocity plateaus is associated with the axis-symmetric nucleation of vortex rings. Once the symmetry breaks down at later times, the motion of the electron becomes chaotic and the value of the velocity

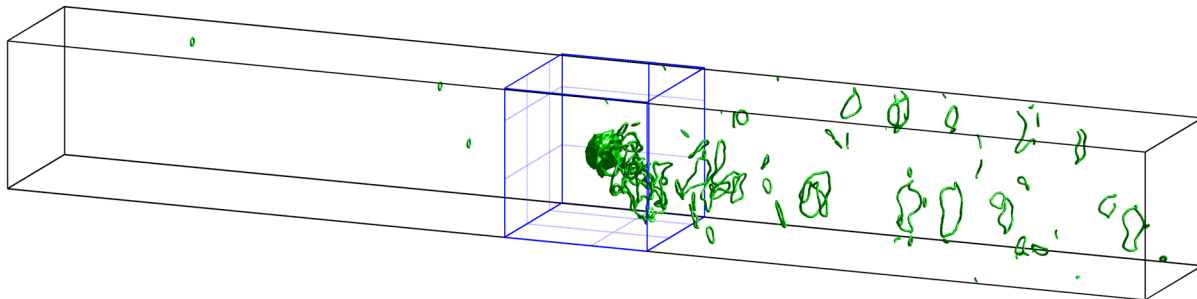


Figure 7.9: Isosurface plot corresponding to  $|\psi^2| = 0.3$  for an electric field  $Q = 5 \times 10^{-4}$ . The figure shows the highly irregular generation of vortex rings that interact together to form a small vortex tangle behind the ion. The size of the computational domain used to numerically integrate the superfluid wave-function  $\psi$  is shown in black while the extent of the domain used for the electron wave function  $\phi$  is shown in blue.

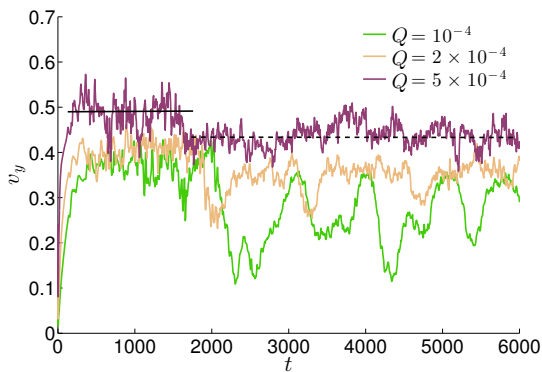


Figure 7.10: Plot of the time evolution of velocity of an electron bubble under different values of electric fields. The velocity is plateauing at different values depending on whether the axis-symmetry is broken (solid line) or not (dash line).

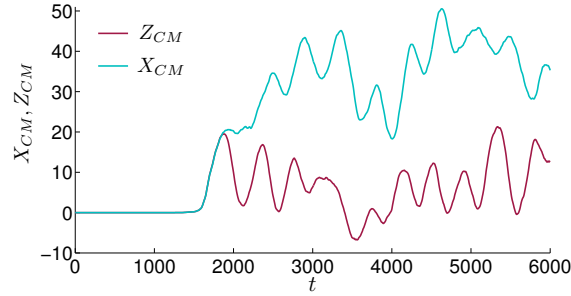


Figure 7.11: Plot of the time dependence of the  $x$  and  $z$  coordinates of the centre of mass of the bubble during its motion under the value of electric field  $Q = 10^{-4}$ . The fluctuating behaviour is the signature of the transition into a chaotic regime.

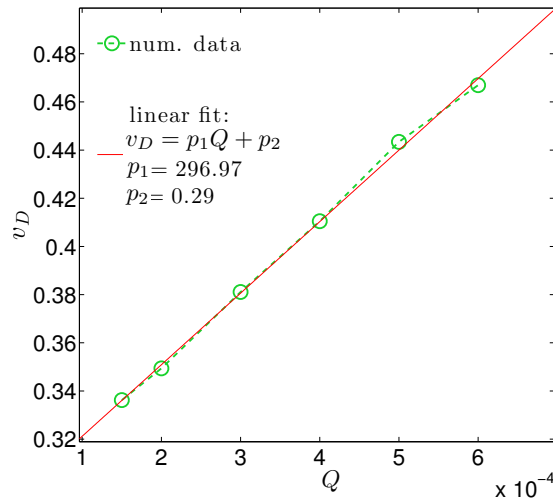


Figure 7.12: Plot of the drift velocity of an electron bubble under different applied electric fields. A linear relation between  $v_D$  and  $Q$  is found by fitting the numerical data with a first order polynomial  $v_D = p_1 Q + p_2$

significantly changes (see dash line). To detect the moment when the transition into a chaotic regime takes place, in Fig. 7.11 we plot respectively the  $x$  and the  $z$ -coordinates of the centre of mass of the bubble  $X_{CM}$  and  $Z_{CM}$ , evaluated according to Eq. (7.54). From the figure, it is possible to see how the trajectory of the bubble, at time  $t_c \sim 1600$  starts exhibiting large fluctuations that characterises the chaotic motion of the bubble. A drift velocity for the bubble can be evaluated by averaging over time the velocity,  $v_y$ , of the bubble after the transition  $t_c \sim 1600$  has occurred. In Fig. 7.12 we plot the drift velocities for different values of the applied electric field. An interesting observation that we make is the linear relationship that exists between  $v_D$  and  $Q$  within the range of values shown.

It is well known that the mobility of the electron is defined as  $\mu_{phonon} = v_D/Q$  in the limit as  $Q \rightarrow 0$ . In experiments, this mobility is typically determined by the phonon limited drift velocity (see dashed blue line in Fig. 7.13) since a finite fraction of phonons is typically present in experiments at low temperatures that scatter off the

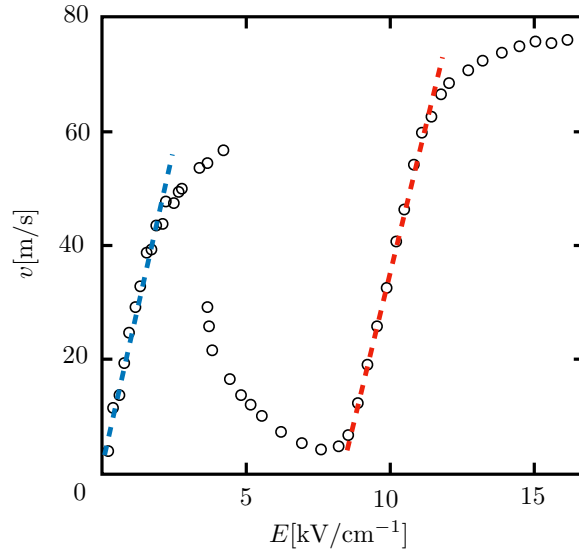


Figure 7.13: Plot of the drift velocity of an electron bubble under different applied electric fields at  $T = 1.00$  K under a pressure of 25 bar. Data from Allum and McClintock [173].

electron and lead to a drag force. However, experiments also reveal that for higher electric fields, exceeding the critical velocity coinciding with the formation of charged vortex rings where the drift velocity of the electron is seen to rapidly fall off, another regime is encountered. In this regime the ion's velocity is seen to again increase with increasing field strength (see dashed red line in Fig. 7.13). This regime which is the one that is relevant to our numerical studies can be used to define a vortex nucleation limited mobility [180] given by  $\mu_{\text{ring}} = v_D / (Q - Q_{\text{cr}})$ . Here,  $Q_{\text{cr}}$  coincides with the critical threshold of the electric field for which the drift velocity of the electron is seen to rise again. Using our results presented in Fig. 7.12, we find  $\mu_{\text{ring}} = 1.26 \text{ m}^2 \text{ s}^{-1} \text{ M}^{-1} \text{ V}^{-1}$ .

Our value for the vortex nucleation limited mobility of ions, within the range of electric fields explored, can be compared against previously performed measurements of the same quantity. We note that previous work has studied the mobility of electrons at high electric fields as a function of both pressure and temperature [180, 181]. We could not find data obtained for pressures that correspond directly to the conditions associated with the parameters used in our model. We will, therefore, consider two sets of data. The first is taken from [180] which contains measurements for a pressure of  $p = 1$  MPa and taken over a range of temperatures that is of most relevance to our work. When comparing with experimental data collected at high pressures, consideration must be given to the fact that the mechanism that determines the maximum drift velocity of the electron is dependent on the pressure. In particular, as demonstrated in [62, 181], roton pair creation is believed to be the dominant mechanism above 10 bar, whereas vortex ring nucleation is the main mechanism below 10 bar. This is consistent with the observation that the Landau critical velocity for roton creation and the critical velocity for vortex ring nucleation both vary with pressure but the two velocities coincide at

$p = 10$  bar (see Fig. 1 in [181]). The measurements presented in [180] for  $p = 10$  bar are, therefore, most relevant for our simulations. Taking the measured vortex limited mobility presented in Fig. 19 of [180], we find  $\mu_E = 1.1 \text{ m}^2 \text{ s}^{-1} \text{ M}^{-1} \text{ V}^{-1}$  which is in remarkably good agreement with our value quoted above.

To establish the sensitivity of these results with changes in the operating pressure and, more specifically, to quantify to what extent the emission of roton pairs affects the measured mobility, we have also analysed a second set of data presented in [62] for  $p = 2.5$  MPa and  $T = 0.34$  K. In fact, in that work, the measured drift velocity  $v_D(Q)$  of an electron had a discrepancy from the expected behaviour that is predicted if pair-roton emission is taken to be the main source of drag. As suggested in [61], such a discrepancy could be accounted for if one takes into account corrections arising from the emission of vortex rings. We have, re-analysed the experimental data to determine the measured mobility of the electron at this higher pressure. As can be seen from the

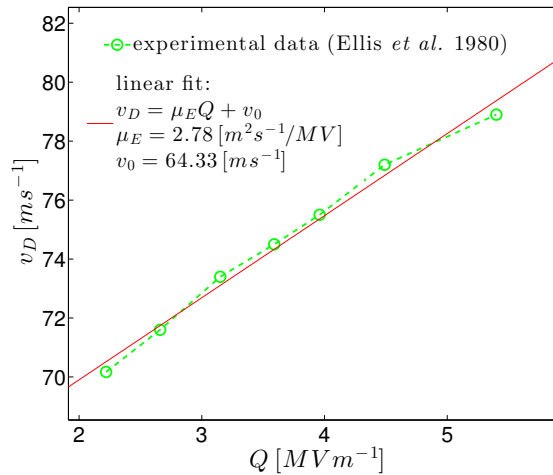


Figure 7.14: Plot of the measured drift velocity of a negative electron taken from [62] under different applied electric fields. A linear relation between  $v_D$  and  $Q$  is found by fitting the experimental data with a first order polynomial  $v_D = \mu_E Q + v_0$ .

data shown in Fig. 7.14, a linear relation can be identified between the measured drift velocity of the electron and the applied electric field. This allows us to obtain an experimental value of the measured mobility of  $\mu_E = 2.76 \text{ m}^2 \text{ s}^{-1} \text{ M}^{-1} \text{ V}^{-1}$ . This reveals that increasing the pressure increases the measured mobility. We note that at higher pressures, the radius of the electron bubble is reduced. Therefore, if vortices are nucleated together with pair-roton emission, the rings are expected to be significantly smaller in comparison to those formed at lower pressures. Despite these different physical effects, the measured mobility only increases by around a factor of 2. Therefore, given the simplicity of the model we have used, we are able to replicate within good quantitative agreement, the measured mobilities of the negative electrons at high electric fields.

We end by noting that Guo and Jin [166] have shown, using a density functional theory that emission of sound waves by disturbances of the bubble can provide a significant channel for dissipating energy. While we also observe the emission of sound waves

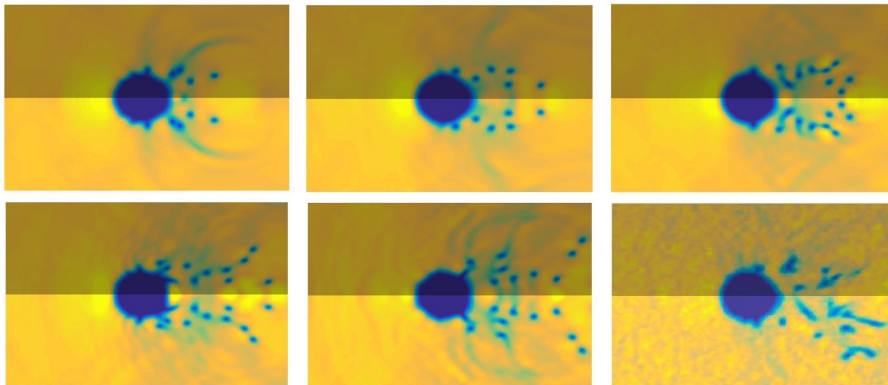


Figure 7.15: Plot of two slices corresponding to the plane  $z = 0$  and  $x = 0$  extracted from the 3D numerical domain. Dark areas represent depletions in the field  $|\psi|^2$  while bright areas stands for high values of  $|\psi|^2$ .

as illustrated in Fig. 7.15, the model used in [166] allows the correct equation of state for  ${}^4\text{He}$  to be used thereby providing a more accurate description of this dissipation mechanism. However, as shown in this work, their assumption of axisymmetry inhibits the transverse chaotic motion of the bubble that appears to be the dominant factor in determining the subsequent velocity of the electron at late times. Future work will aim to extend the 3D simulations we have performed to more realistic models such as the ones considered in [166]. This would permit a more quantitative determination of the different contributions to the drag force exerted on the ion.

## 7.5 Motion of an Electron Trapped on a Vortex Line

Having presented in the previous section the dynamics of a free ion, in this section we will focus on the scenario of an electron that is trapped on a vortex and sliding along its core due to an electric field applied along the principal axis of the vortex.

The study of the electrons trapped on vortices is a problem of significant interest to experimentalists since it can provide important insights into properties of vortex lines produced by rotating a superfluid [182] and the structure of the vortex core [183]. Moreover, it has provided a useful tool to test theories concerning how KWs [184] affect the motion of the electron [163]. Nevertheless, many questions remain concerning the motion of an electron bubble along a vortex in the limit of zero temperature. In particular, we note that in the work by Ostermeier and Glaberson [163] very low temperatures revealed anomalously high mobilities for a trapped electron, approaching that of the free electron, that thus far has not been explained. Moreover, in the same work it was shown that for high values of the electric field the bubble reaches a limiting velocity that appears to be independent of temperature, whose nature still needs to be clarified. The failure of many previous attempts to explain these observations can be attributed to the emphasis on KWs as the key vortex excitations that can be supported

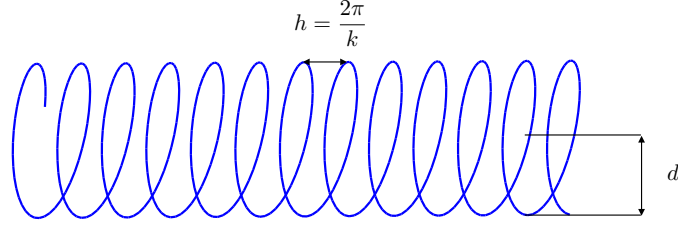


Figure 7.16: Schematic illustration of a helix with radius  $d$  and pitch  $h$  .

on the cores of vortices. However, in this section we will demonstrate through numerical simulations that non-linear excitations can emerge in the limit of low temperatures which can explain the measured experimental trends.

### 7.5.1 Excitations on a Vortex Line

In order to understand the motion of an electron bubble sliding along a superfluid vortex line, it is essential to identify the different excitations which can propagate along the vortex core. We will, therefore, begin by reviewing key properties of KWs which constitute the most studied and well established excitations that are recognised to arise in superfluid vortices. These KWs are of the form of helical perturbations.

To a first approximation, the motion of a helical vortex of radius  $d$  and having pitch  $h = 2\pi/k$ , see Fig. 7.16, can be described using the local induction equations (2.103). In the limit where  $k^{-1} \gg d$  the binormal vector on each point of the helix is perpendicular to both the axis of the helix and the distance between that point and the axis. Hence, each point of the helix rotates around the unperturbed vortex with angular velocity  $\omega = v/d$ . Since the velocity of a vortex in the local induction approximation depends on the local curvature  $\kappa$  of the filament, for the considered helix the velocity is constant and equal to

$$v = \frac{\Gamma\kappa}{4\pi} \log\left(\frac{L}{\xi}\right) = \frac{d}{d^2 + (1/k)^2} \frac{\Gamma}{4\pi} \log\left(\frac{L}{\xi}\right) \simeq \frac{\Gamma k^2 d}{4\pi} \log\left(\frac{L}{\xi}\right), \quad (7.65)$$

where  $L$  is the induction length. In the long wave approximation, we can then obtain the dispersion relation

$$\omega(k) = \frac{v(k)}{d} = \frac{\Gamma k^2}{4\pi} \log\left(\frac{L}{\xi}\right). \quad (7.66)$$

A more general expression for the dispersion relation

$$\omega(k) = \frac{\Gamma}{4\pi} \log\left(\frac{L}{\xi}\right) \frac{k^2}{\sqrt{1 + k^2 d^2}}, \quad (7.67)$$

which includes also large amplitude KWs, is given by Sonin in [32]. We note that the above expression is equivalent to Eq. (7.66) in the limit  $k^2 d^2 \ll 1$ . As a further remark, we point out that the ratio  $\log(L/\xi)$  has been kept constant and so variations of the vortex core are neglected.

The first attempt to include the core structure for the propagation of helical waves was presented by Thomson (1890) and Pocklington (1895). In particular, they obtained the dispersion relation

$$\omega^\pm = \frac{\Gamma}{2\pi\xi^2} \left( 1 + \left[ 1 \pm k\xi \frac{K_0(k\xi)}{K_1(k\xi)} \right]^{1/2} \right) \quad (7.68)$$

for helical waves propagating on an essentially straight vortex with a hollow core. Here  $K_0$  and  $K_1$  are the modified Bessel functions and the vortex core radius  $\xi$  is assumed to be smaller than the radius of the helix. The positive upper branch of Eq. (7.68) corresponds to waves whose motion does not follow the local induction equations (2.103). This fast positive rotation is an effect due to the fact that the hollow core vortex has a non-zero effective mass. In fact,  $\omega^+$  arises from balancing the centrifugal force per unit length  $\rho\pi\omega^2\xi^2d$  with the Magnus effect per unit length  $\rho\Gamma\omega d$  (see [7]). We therefore focus on the more relevant and energetically more accessible negative branch  $\omega^- \equiv \omega(k)$ , which corresponds to slow waves. By taking the limit  $k\xi \ll 1$  in Eq. (7.68), we can obtain an asymptotic expression for the dispersion relation of polarized long waves

$$\omega(k) = -\frac{\Gamma k^2}{4\pi} \left[ \log \left( \frac{2}{k\xi} \right) - \gamma \right], \quad (7.69)$$

where  $\gamma$  is the Euler-Mascheroni constant. The intuitive expression given by Eq. (7.66) can be recovered from Eq. (7.69) if the induction length  $L$  is taken to be of the order of  $k^{-1}$ .

In 1979, Ashton and Glaberson performed the first experimental measurement of the dispersion relation of KWs given by Eq. (7.69) in superfluid liquid helium. They accomplished this by studying the motion of an electron trapped on a vortex line under a constant (dc) electric field, applied in the direction parallel to the vortex line, and an alternating radio-frequency (rf) field applied in the transversal direction. Hence, the presence of both an dc and an rf field causes the electron undergo a spiraling motion. Their experiment was motivated by the theoretical prediction of Halley and Cheung stating that, in the presence of an rf field with frequency  $\omega_{\text{rf}}$ , a resonant condition for the generation of KWs can be obtained when

$$\omega_{\text{rf}} = \omega(k) - kv_{\text{ion}}, \quad (7.70)$$

with

$$v_{\text{ion}} = \frac{\partial\omega(k)}{\partial k}. \quad (7.71)$$

The first condition requires that the Doppler shifted frequency of the generated KWs is the same as the imposed frequency of the imposed rf field. The second equation implies that the energy remains localised around the ion. In Fig. 7.17 the drift velocity of a negative electron is plotted as a function of different values of the applied electric field. When the electron is rotating counter-clockwise (CCW in Fig. 7.17), a kink is clearly discernible at about 3 m/s which corresponds to the resonant velocity obtained by solving Eq. (7.70) and Eq. (7.71) with parameters corresponding to helium-4. Further confirmation of this interpretation of the experimental observation was obtained by

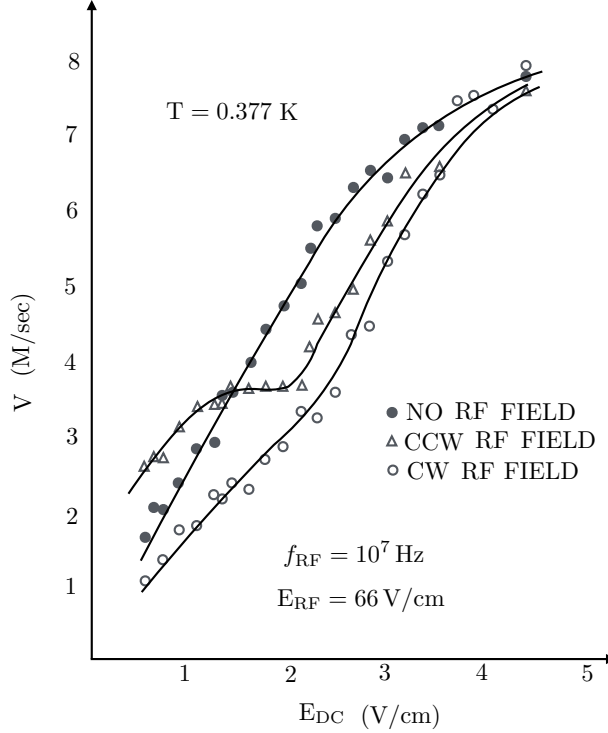


Figure 7.17: Plot of electron drift velocity for different dc electric fields at  $T = 0.377$  K. Different marker styles correspond to: (dot) no rf electric applied, (triangle) counter-clockwise rf electric and (circle) clockwise rf electric. Data taken from Ashton and Glaberson [184].

inverting the sign of the rf field, causing the electron to spin clockwise (CW in Fig. 7.17). Since the KWs group velocity is always larger than the phase speed (assuming that the log term is constant), the condition given by Eq. (7.70) can only be satisfied if  $\omega_{rf}$  has the same sign as the circulation  $\Gamma$  of the vortex. This can be seen in Fig. 7.17 which illustrates that the resonance condition is indeed satisfied only for values of  $\omega_{rf}$  corresponding to counter-clockwise rotation of the ion.

Having described the KW excitations, we now discuss the existence of solitary waves propagating along the vortex line. The study of these types of excitations began when Betchov and Da Rios [185, 186] independently derived two equations

$$\beta^{-1}\dot{\kappa} = -(\kappa\tau)' - \kappa'\tau \quad (7.72)$$

and

$$\beta^{-1}\dot{\tau} = [(\kappa'' - \kappa\tau^2)/\kappa]' + \kappa'\kappa \quad (7.73)$$

that describe the evolution of both curvature  $\kappa$  and torsion  $\tau$  of a vortex filament governed by the local induction equations (2.103). For simplicity the parameter  $\beta$  in Eq. (2.103) is considered to be a constant. Thereafter, by using the transformation

$$\Phi(\zeta, t) = \kappa(\zeta, t) \exp \left[ i \int_0^\zeta \tau(\tilde{\zeta}, t) d\tilde{\zeta} \right], \quad (7.74)$$

Hasimoto [109] showed that equations (7.72) and (7.73) can be reduced to a 1D self-focusing non-linear Schrödinger (NLS) equation of the form

$$\frac{1}{i\beta} \frac{\partial \Phi}{\partial t} = \frac{\partial^2 \Phi}{\partial \zeta^2} + \frac{1}{2} (|\Phi|^2 \Phi + A), \quad (7.75)$$

where  $A = A(t)$  is real function depending on time. Since the 1D NLS equation is integrable, it admits soliton solutions. In particular, by setting  $A = 2\beta \left( \nu^2 - \frac{c^2}{4\beta^2} \right)$  one can find the so-called *bright solitons*

$$\Phi(\zeta, t) = 2\nu \operatorname{sech}[\nu(\zeta - ct)] \exp \left[ -i \frac{c}{2\beta} \zeta \right], \quad (7.76)$$

moving at speed  $c$ . Comparing Eq. (7.76) with (7.74) it is possible to relate the bright soliton solution with the curvature and torsion of a filament such that

$$\kappa(\zeta - ct) = 2\nu \operatorname{sech}[\nu(\zeta - ct)], \quad (7.77)$$

and

$$\tau = \frac{c}{2\beta}. \quad (7.78)$$

By using the Frenet-Serret frame of reference give by Eq. (2.100) and introducing a set of differential equations (called the Frenet-Serret formulas)

$$\begin{bmatrix} \mathbf{t}' \\ \mathbf{n}' \\ \mathbf{b}' \end{bmatrix} = \begin{bmatrix} 0 & \kappa & 0 \\ -\kappa & 0 & \tau \\ 0 & -\tau & 0 \end{bmatrix} \begin{bmatrix} \mathbf{t} \\ \mathbf{n} \\ \mathbf{b} \end{bmatrix}, \quad (7.79)$$

one can recover the vortex filament corresponding to the bright soliton solution given by Eq. (7.76) by substituting Eqs. (7.77) and (7.78) into Eq. (7.79).

Following Hasimoto's work we can write the shape of the filament  $\mathbf{s}(\zeta, t) \equiv (s_x, s_y, s_z)$  as

$$s_x = \zeta - r_{max} \tanh \varrho, \quad s_y = r_{max} \operatorname{sech} \varrho \cos \theta, \quad s_z = r_{max} \operatorname{sech} \varrho \sin \theta, \quad (7.80)$$

with

$$\varrho = \nu(\zeta - ct), \quad r_{max} = \frac{2}{\nu(1 + T^2)}, \quad T = \frac{\tau}{\nu}, \quad (7.81)$$

and

$$\theta = T\varrho + \beta\nu^2(1 + T^2)t = T\varrho + \omega t. \quad (7.82)$$

This solution describes a localised wave moving along a vortex with principal axis aligned with the  $x$ -coordinate direction with velocity  $c$ . The wave envelope is given by  $r_{max} \operatorname{sech} \varrho$ . At  $x = 0$ , the envelope attains its maximum amplitude and it tends to zero as  $\varrho \rightarrow \pm\infty$ . The envelope is not only moving with group velocity  $c$  but is also rotating along the  $x$ -direction with angular frequency  $\omega$ .

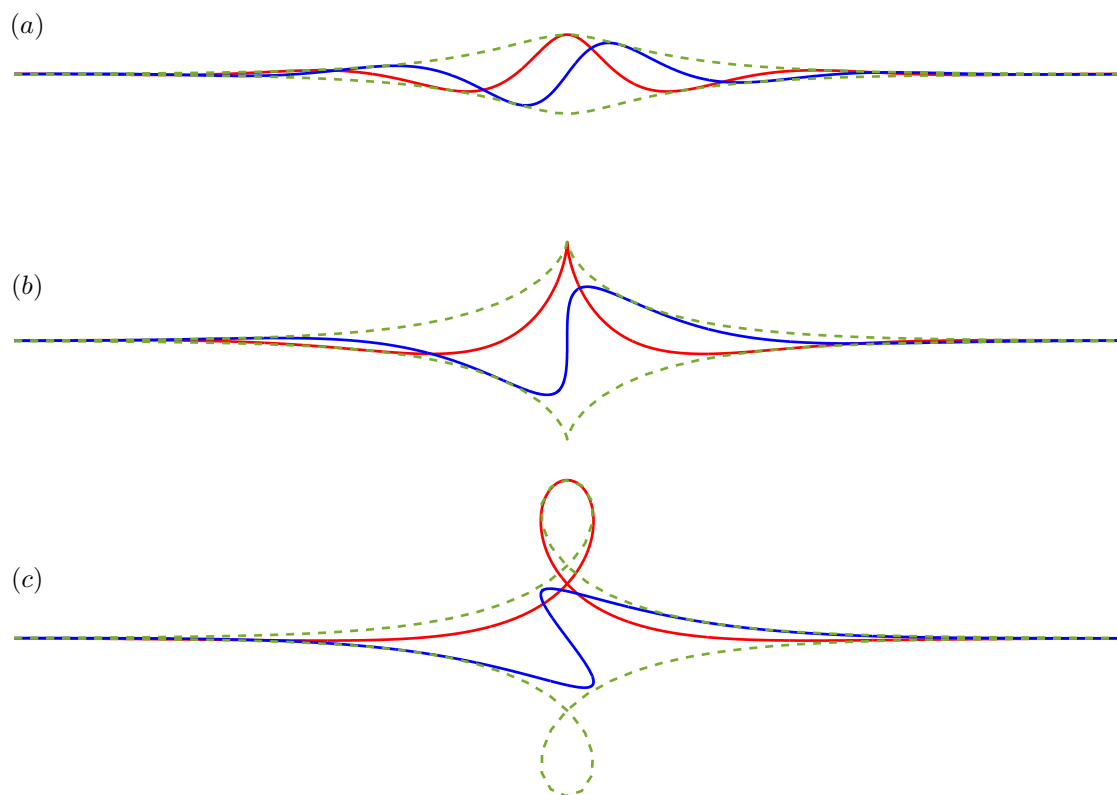


Figure 7.18: Projection of the filament on the  $x-y$  plane, red line, and on the  $x-z$  plane, blue line. The contour of the envelope is shown with dash line. (a)  $T=2$ , (b)  $T=1$ , (c)  $T=0.5$ .

The parameter  $T$  is a similarity parameter that sets the shape of the soliton. Figure 7.18 presents the projection of the filament at  $t = 0$  on the  $x$ - $y$  plane and on the  $x$ - $z$  plane, for different values of  $T$ . From the figure we can observe three different behaviours: when  $T > 1$ , thereafter denoted as the *hump soliton*, the filament is single-valued function of  $x$ , when  $T = 1$ , denoted as *cusp soliton*, a singularity arises at  $x = 0$  and when  $T < 1$ , referred to as a *loop soliton*, the filament is no more a single-valued function of  $x$ .

If we consider  $\theta = \pm\pi$  in Eq. (7.82) at  $t = 0$ , it is possible to define a wave-length given by

$$\lambda = |s_x(\pi/T) - s_x(-\pi/T)| = \frac{2\pi}{\tau} - 2r_{max} \tanh \frac{\pi}{T}. \quad (7.83)$$

If we consider the long wave limit,  $\lambda/r_{max} \gg 1$ , then the wave-length can be approximated by  $\lambda \sim 2\pi/\tau$ . By recalling expression (7.82) for the angular frequency of the soliton

$$\omega = \beta\nu^2(1 + T^2) = \frac{2\beta\nu}{r_{max}}, \quad (7.84)$$

we can define a phase speed given by

$$c_p = \frac{\omega}{k} = \frac{\beta\nu\lambda}{\pi r_{max}}. \quad (7.85)$$

Since in the long wave limit,  $\lambda/r_{max} \sim \pi T$ , the phase speed can be written as

$$c_p = \beta\tau \quad (7.86)$$

which is half of the group velocity

$$c = 2\beta\tau \quad (7.87)$$

at which the soliton is moving. This relation is the same one obtained above for helical KWs (see Eq. (7.69)).

## 7.5.2 Numerical Results

Our simulations for a trapped electron bubble have been carried out using a numerical set-up similar to the one used in the study of a free electron moving in bulk superfluid. The main difference with the previous study concerns the size of the domain which now corresponds to  $L_x = 512$ ,  $L_y = 256$  and  $L_z = 256$ . The size of domain is chosen in order to accommodate 2 vortex lines and two anti-vortex lines in order to ensure neutrality and symmetry of the vortex configuration. The four-fold mirror symmetry allows periodic boundary conditions to be used and prevents the migration that would otherwise arise if only a single vortex and anti-vortex were considered. The bubble is initialised to lie on just one of them. Concerning the threshold used for Eq. (7.50) of the gradient flow method, we considered different values of it varying from  $10^{-6}$  to  $10^{-8}$  depending on the strength of the applied electric used.

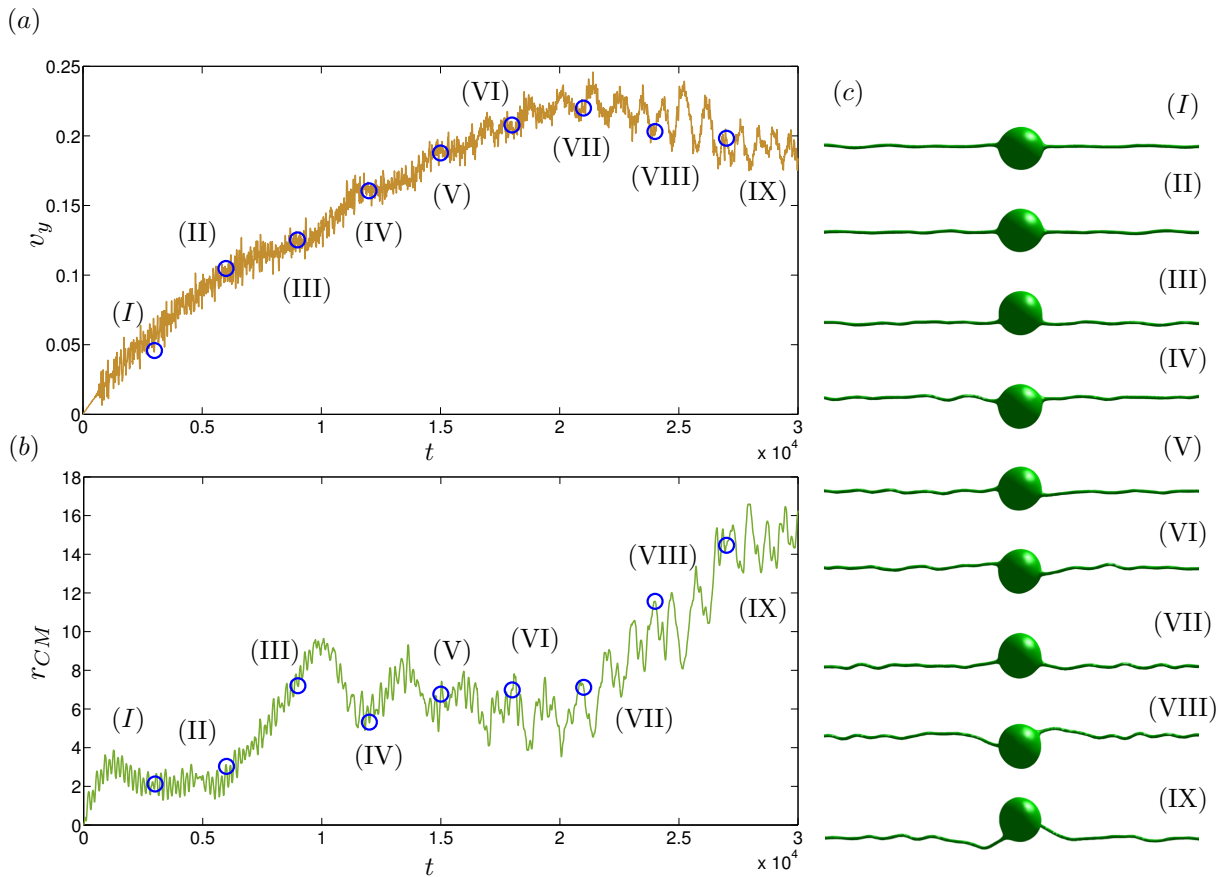


Figure 7.19: Dynamics of an electron bubble sliding along a vortex line under the influence of an applied electric field  $Q = 10^{-6}$ . a) time evolution of the component of the velocity of the bubble that is in the direction of the axis of the vortex; b) time evolution of the transverse displacement of the bubble; c) isosurface plots corresponding to  $|\psi|^2 = 0.3$  at time  $t = 3000$ ,  $t = 6000$ ,  $t = 9000$ ,  $t = 12000$ ,  $t = 15000$ ,  $t = 18000$ ,  $t = 21000$ ,  $t = 24000$  and  $t = 27000$ . The values of  $v_y$  and  $r_{CM}$  corresponding to the time of the isosurface plots are shown in a) and b) using blue circles.

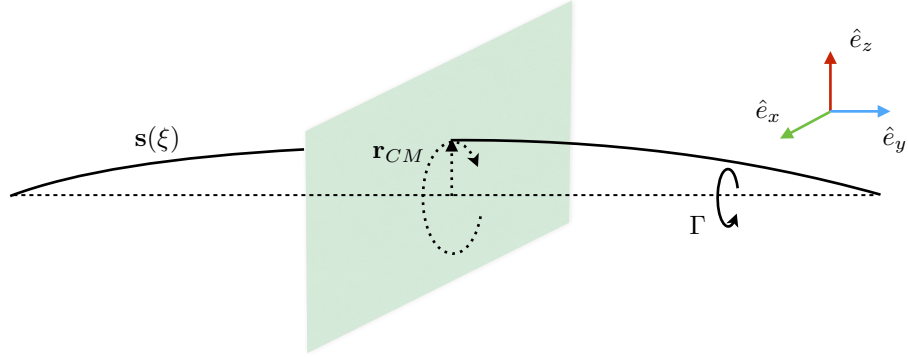


Figure 7.20: Schematic illustration for the transversal displacement  $\mathbf{r}_{CM}$  of the centre of mass of the bubble.

We now present results of a numerical simulation for an electric field  $Q = 10^{-6}$  applied along the axis of the vortex line. The analysis of the numerical results arising from the dynamics are shown in figure 7.19. By focusing on the first three snapshots presented in Fig. 7.19 (c) we observe low amplitude perturbations on the vortex line. Hence, for  $t < 10^4$ , we would anticipate the motion of the bubble to be affected by low amplitude KWs. In this regime, a theoretical model that has been proposed by Ostermeier and Glaberson [163], based on the initial work by Ohmi and Usui [187], is expected to apply. We will therefore recall the main arguments invoked in arriving at their model.

In the previous section, we have seen that the motion of an electron in the limit of zero temperature does not experience any form of drag until the critical velocity corresponding to the nucleation of a vortex ring is reached. However, for an electron sliding along a vortex line the dynamics changes significantly. As soon as the electron accelerates along the line, the vortex becomes susceptible to the excitations of KWs. This behaviour can be explained in terms of an analogue of Landau criterion for superfluidity, which requires that the group velocity is equal to the phase speed. For a KWs having energy  $\hbar\omega$ , with  $\omega$  given by the dispersion relation (7.69), the criterion implies that KWs are excited at a critical velocity

$$v_c = \min \left( \frac{\hbar\omega}{\hbar k} \right) = 0. \quad (7.88)$$

Since the critical velocity is equal to zero, this implies that any finite velocity of the bubble would excite KWs.

If the oscillations generated by the electron have wave-lengths  $\lambda$  larger than the amplitude  $r_{CM}$ , such that  $\lambda/r_{CM} \gg 1$ , and the amplitude  $r_{CM}$  is assumed to be smaller than the effective radius of the bubble, the vortex line can be considered to be approximately straight. By choosing a frame of reference moving at the same velocity  $v_y$  as the bubble, the transversal displacement  $\mathbf{r}_{CM}$  (see Fig. 7.20 ) can be described by the

equation [163, 187]

$$m_h \ddot{\mathbf{r}}_{CM} = -\frac{3}{2} |\Gamma| \rho b \hat{e}_y \times \dot{\mathbf{r}}_{CM} - m_h \omega_0^2 \mathbf{r}_{CM}, \quad (7.89)$$

where  $\hat{e}_y$  is the unit vector along the vortex and  $m_h$  the effective mass of the bubble. We note that the first term on the right hand side of the above equation represents the Magnus force acting on the bubble. The Magnus effect always acts along a direction normal to the motion of the bubble. The second term on the right hand side is a restoring force arising from the electron-vortex potential. By using a model of a vortex derived from a weakly interacting Bose-gas, Donnelly and Park [188] derived an expression for  $\omega_0$  that is given by

$$\omega_0^2 = \frac{\rho \Gamma^2}{4\pi b m_h} \left[ \frac{(2 + S^2)}{(1 + S^2)^{3/3}} \sinh^{-1} \left( \frac{1}{S} \right) - \frac{1}{1 + S^2} \right] \quad (7.90)$$

where  $S = \xi/b$ . If we assume that  $\mathbf{r}_{CM}$  varies as  $(\hat{e}_x + i\hat{e}_z)e^{i\omega t}$  we obtain a quadratic equation for  $\omega$  given by

$$\omega^2 - \frac{3\rho b \Gamma}{2m_h} \omega - \omega_0^2 = 0. \quad (7.91)$$

Using the values found in Section 7.4.1 for the effective radius and mass of the bubble, the solution of the above equation gives two frequencies:  $\omega_+ = 2.73 \times 10^9 \text{Hz}$  and  $\omega_- = 3.11 \times 10^{10} \text{Hz}$ . We recall that KWs are polarised in a sense that is opposite to the circulation and we therefore focus on  $\omega_-$ . Since in the model given by Eq. (7.89) we assumed positive circulation, the right frequency will then be  $|\omega| = 3.11 \times 10^{10} \text{Hz}$ . Recalling the unit of time for our numerical simulation  $\gamma = 0.63 \times 10^{-12} \text{s}$ , we can define the unit of frequency as  $\tilde{\omega} = 1.58 \times 10^{12} \text{Hz}$  and obtain the resonant dimensionless frequency  $\omega = 0.0196$  that is associated with the generation of KWs as predicted by Eq. (7.89).

To check if the frequency associated with the rotation of the bubble matches with the theoretical prediction, in Fig. 7.21 we plot the angular velocity extracted from the numerical simulation. For  $t < 10^4$ , we observe that, despite the large fluctuations, the frequency seems to agree with the theoretical angular velocity  $\omega = 0.0196$  evaluated using Eq. (7.91). Since the model given by Eq. (7.89) assumes that the vortex line is locally parallel to the rotation axis of the bubble, its validity is restricted to long wave oscillations with  $r_{CM}/\lambda \ll 1$ . Moreover, modelling the electron-vortex potential according to Eq. (7.90) also requires the amplitude of the oscillations be much less than the radius of the bubble. From Fig. 7.19 (b) we can see that, at  $t \sim 10^4$ , the deformations along the line become of the order of the radius of the bubble and the electron seems to enter a new regime, which can no longer be described by Eq. (7.89). Between  $t \sim 10^4$  and  $t \sim 2 \times 10^4$ , we observe that the velocity of the bubble continues to grow in time while  $r_{CM}$  remains constant overall. The presence of high amplitude oscillations is also confirmed by referring to the snapshots of the isosurfaces of the density as seen in (IV), (V) and (VI) of Fig. 7.19 (c).

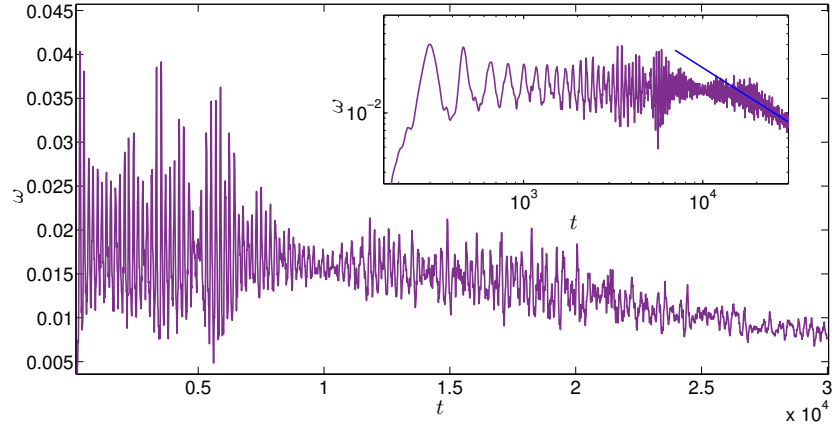


Figure 7.21: Plot of the angular velocity of an electronic bubble rotating during the motion along a vortex line under the influence of an applied electric field  $Q = 10^{-6}$ . A log-log plot is shown in the inset. The blue line superimposed on the data inside the inset represents a power law  $\propto t^{-1}$ .

From Fig. 7.19 (a), we observe how the velocity of the bubble continues to increase until it saturates at a maximum value of  $v_y \sim 0.22$  around  $t = 2 \times 10^4$ . At this time the dynamics seems to change significantly. The magnitude of the displacement of the electron,  $r_{CM}$ , increases rapidly while the velocity begins gradually to fall off. We attribute this behaviour to the formation of a solitary wave-electron complex that is reminiscent of the hump soliton described by Eq. (7.74) as first predicted by Hasimoto [109]. In order to confirm this assertion, in Fig. 7.22 we plot the analytical solution, given by Eq. (7.80), overlying on the isosurface plot (IX) of Fig. 7.19 (c). This fit was performed to produce convincing visual agreement without any attempt to optimise the fitting parameters. We found that the central kink on the line matched well with the analytical solution when the parameters  $T = 2.5$  and  $\nu = 0.028$  were chosen for Eq. (7.80). For the given  $T$  and  $\nu$ , we can estimate both the maximum amplitude  $r_{max} = 9.98$  and the wavelength  $\lambda = 75$  of the central kink using Eqs. (7.81) and (7.83) respectively. By measuring the ratio between the wavelength and the amplitude  $r_{max}/\lambda = 0.13$ , we can see that we are no longer deep in the long wavelength regime that is required for Eq. (7.89). Moreover, from the measurement of  $r_{max} = 9.98$  we can also notice that  $r_{max}$  differs from the transversal amplitude of the electron  $r_{CM} \sim 14$ , based on the instantaneous configuration presented in (IX) of Fig. 7.19. Such a difference indicates that the bubble is positioned significantly off from the centre of the vortex core. Under these conditions, Eq. (7.90), which was derived assuming an electron displaced slightly off the centre of the vortex, can no longer be taken as the approximation of the electron-vortex potential.

In our discussion above, we have fitted the vortex line profile to a Hasimoto soliton solution at one instant of time using only two fitting parameters  $\tau$  and  $\nu$ . Knowledge of how those parameters vary in time can provide useful information in predicting the long time behaviour of the bubble-vortex complex. We will, therefore, aim to estimate these parameters from knowledge of key properties of the soliton, such as its group

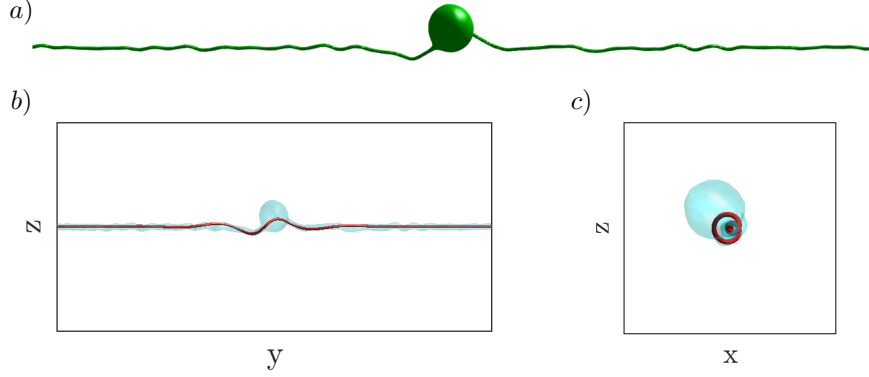


Figure 7.22: Plot of an electron bubble sliding along a vortex line for an electric field  $Q = 10^{-6}$ , at time  $t = 27000$ . The analytical solution corresponding to a Hasimoto hump-soliton having  $T = 2.5$  and  $\nu = 0.028$  is also shown. a) Isosurface plot, corresponding to  $|\psi|^2 = 0.3$ , of the bubble-vortex complex ; b) analytical solution for the Hasimoto soliton, rendered with a red tube, projected on the  $z$ - $y$  plane; c)  $x$ - $z$  plane. Comparison between analytical and numerical solution projected into the isosurfaces, corresponding to  $|\psi|^2 = 0.9$ , shown in b) and c) .

velocity  $c = v_y$  or its angular velocity  $\omega$ . However, both

$$\tau = \frac{v_y}{2\beta}, \quad (7.92)$$

and

$$\nu = \frac{\omega r_{max}}{2\beta} \quad (7.93)$$

also depend on the parameter

$$\beta = \frac{\Gamma}{4\pi} \log \frac{L}{\xi}. \quad (7.94)$$

Therefore, in order to establish how these parameters evolve in time it becomes essential to estimate the value of the induction length,  $L$ , and consequently of the parameter  $\beta$ . The most common choice for estimating the induction length are either given by the local radius of curvature  $1/\kappa$  of the vortex filament or by the wavelength given by Eq. (7.83). However, since  $\kappa \sim 1/2\omega r_{max}/2\beta$  and  $\lambda \sim 2\beta/v_y$  neither is ideal since they both depend on the parameter  $\beta$  itself. We have therefore set the induction length using the expression

$$L = \frac{v_y}{2\omega}. \quad (7.95)$$

We remark that in the long wavelength limit  $\frac{1}{2}v_y$  correspond to the soliton phase speed, as shown in Eq. (7.86) and so  $L \sim \lambda$ . Hence, by defining  $\beta$  as

$$\beta = \frac{\Gamma}{4\pi} \log \frac{v_y}{2\omega} \quad (7.96)$$

we are able to determine the evolution of the parameters  $\tau$  and  $\nu$ , as shown in Fig. 7.23. Since in the long wavelength limit the hump soliton ( $T \gg 1$ ) has the same dispersion

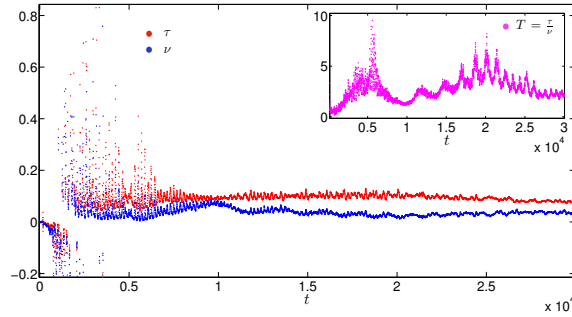


Figure 7.23: Time evolution of the coefficient  $\tau$ , red dots, and  $\nu$ , blue dots, evaluated from the dynamics of an electron bubble sliding along a vortex under the electric field  $Q = 10^{-6}$ . The inset shows the evolution of the parameter  $T = \tau/\nu$ .

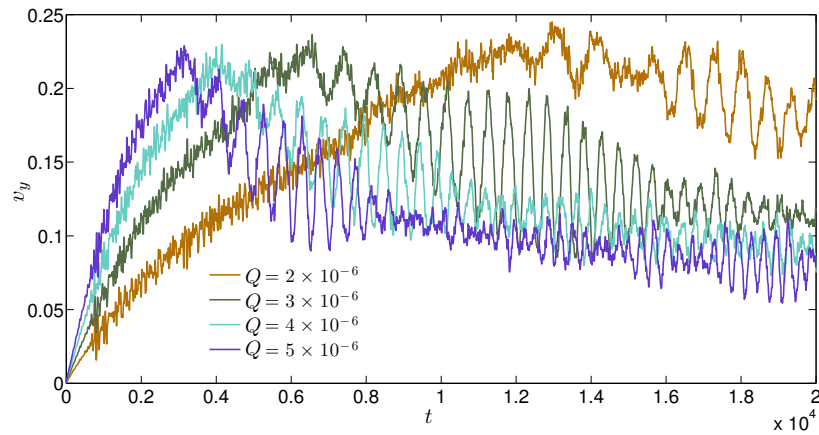


Figure 7.24: Plot of the electron bubble velocity throughout its motion along a vortex line under different values of the applied electric field.

relation as the KWs given by Eq. (7.69), we expect to see a transition in the time dependence of  $T$  from high values to small values, when a large amplitude solitary wave forms. By looking at the inset of Fig. 7.23, we can see how this trend is confirmed after  $t > 2 \times 10^4$  when  $T$  starts decreasing. The fact that in the early stage we do not observe the expected behaviour of  $T$  it can possibly be explained by the the large fluctuations in the measurement of  $\omega$ . These fluctuations can create large errors in the evaluation of the parameter  $\beta$  and consequently in the value of  $\tau$  and  $\nu$  in the early stages of the dynamics.

Having demonstrated that the motion of an electron along a vortex line can lead to the formation of hump solitons, we now want to investigate whether from the dynamics we can observe other types of soliton solutions which can be described in the framework of Hasimoto's theory. To achieve this, we now investigate the motion of an electron along a line for higher values of the applied electric field.

In Fig. 7.24 we plot the time evolution of the bubble velocity  $v_y$  for different values of the electric field ranging from  $Q = 2 \times 10^{-6}$  to  $Q = 5 \times 10^{-6}$ . All the runs appear to produce similar qualitative dynamics. The figure shows that for each run the bubble

always reaches the same maximum velocity of  $v \sim 0.22$ . After that, the bubble begins to slow down accompanied by the occurrence of large velocity fluctuations. Detailed inspection of the dynamics extracted from our simulations reveals that this fluctuations appear to be associated with the bubble undergoing strong oscillations on the vortex core that appears to excite KWs propagating on the vortex. However, for the bubble with larger values of the electric field, the transition from the generation of linear KWs to the excitation of high amplitude Hasimoto solitons occurs over a shorter time interval.

We will now focus on the dynamics of an electron for an electric field  $Q = 10^{-5}$ . In analogy with Fig. 7.19, in Fig. 7.25 we present the dynamics of the bubble-vortex interaction in terms of the bubble velocity  $v_y$ , the transversal displacement  $r_{CM}$  of the bubble, and six snapshots of the instantaneous electron-vortex configuration at times  $t = 1000$ ,  $t = 1500$ ,  $t = 3000$ ,  $t = 4250$ ,  $t = 12500$  and  $t = 18250$ . At time  $t = 1000$  we can see that, as in the case of the low electric field, the dynamics is initially characterized by the presence of low amplitude KWs. However, in contrast to the low electric field scenario studied earlier, this phase lasts for a very short time. At around  $t = 1500$ , the bubble already attains its maximum velocity of  $v \sim 0.22$  which coincides with the presence of a hump soliton with amplitude of the order of the radius of the bubble. As the hump soliton grows, it transits into a higher amplitude cusp soliton, as shown in snapshots (III) and (IV). This is confirmed further by the sudden increase of  $r_{CM}$  seen in Fig. 7.25 (b). At late times the soliton appears to be settle into a loop which persists from  $t \sim 0.5 \times 10^4$  to the end of the run at  $t = 2 \times 10^4$ . During this time, the dynamics is characterised by a slow decrease in the velocity of the bubble associated with the growing size of the soliton.

In Fig. (7.26) we compare the isosurface plot of snapshot (IV) with the analytical solution for a loop soliton. A good match is obtained for values of  $T = 0.65$  and  $\nu = 0.017$  appearing in Eq. (7.80). By looking at the projection along the  $x$ - $z$  plane we see how the centre of mass of the bubble does not correspond to the position of maximum height of the soliton. In fact, by measuring  $r_{max} = 82.70$  of the central kink of the soliton using Eq. (7.81) at time  $t = 18250$ , we found a significant difference with respect to the computed value of  $r_{CM} \sim 70$ . We point out that the bubble settle into this position as it provides the most stable location that inhibits the electron from sliding along the vortex.

The above observations do not establish what would be the final state of the soliton at later times. By measuring the angular frequency  $\omega$ , we can observe, from Fig. 7.27, that the rotation of the soliton is constantly decreasing with time. By plotting  $\omega$  using a log-log scale we reveal a power law scaling given by  $t^{-1}$  that is consistent with a self-similar growth of the vortex at late times. We can extract more information at this last stage of the dynamics by considering the variation of the parameters  $\tau$  and  $\nu$  with time as shown in Fig. 7.28. Even though it is difficult to make any exact prediction on the time evolution of  $\tau$  and  $\nu$  since they both experience large fluctuations, it is clear that during the early stage of the dynamics the two parameters have a very different dependence from one another, whereas at the end of the simulation they both seem to

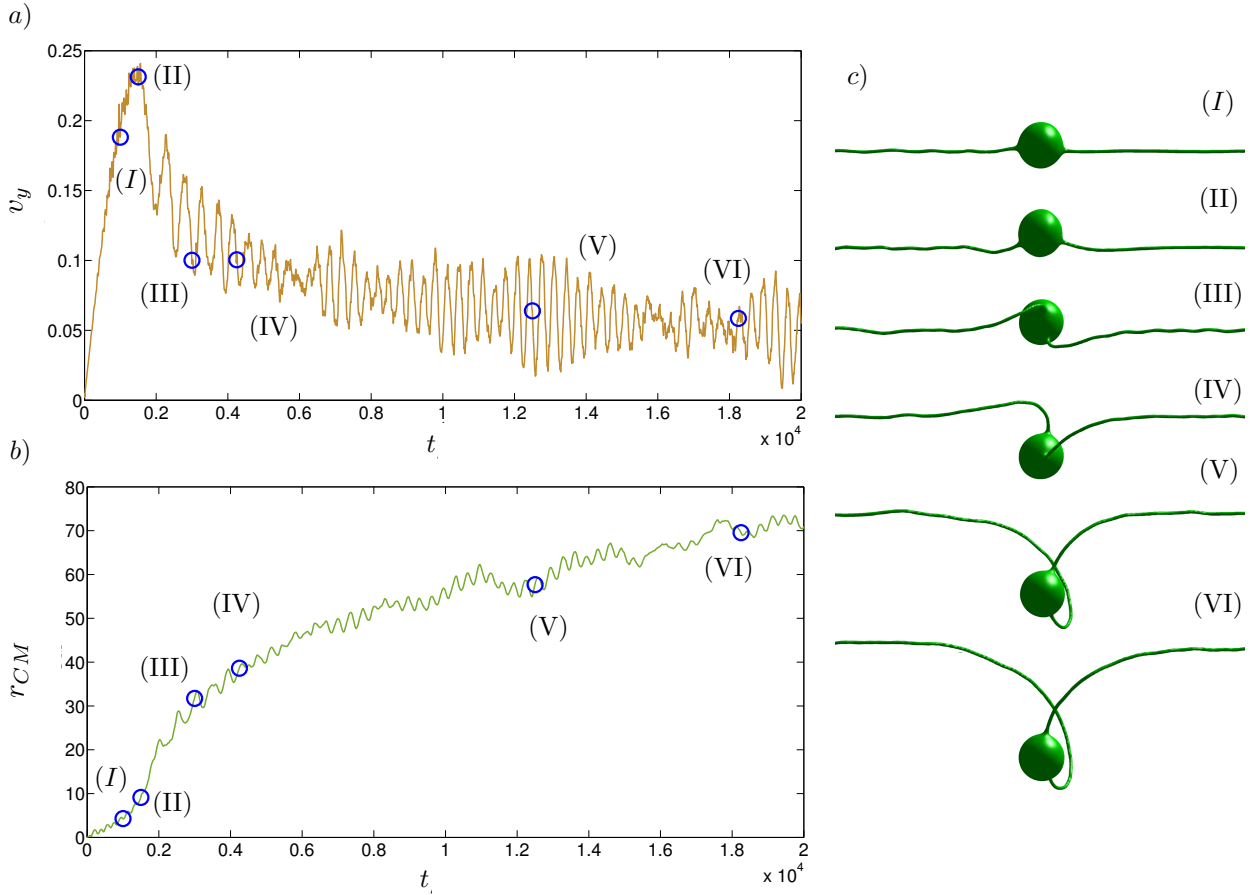


Figure 7.25: Dynamics of an electron bubble sliding along a vortex line under the influence of an applied electric field  $Q = 10^{-5}$ . a) time evolution of the component of the velocity of the bubble that is in the direction of the axis of the vortex; b) time evolution of the displacement of the bubble; c) isosurface plots corresponding to  $|\psi|^2 = 0.3$  at time  $t = 1000$ ,  $t = 1500$ ,  $t = 3000$ ,  $t = 4250$ ,  $t = 12500$  and  $t = 18250$ . The values of  $v_y$  and  $r_{CM}$  corresponding to the time of the isosurface plots are shown in a) and b) using blue circles.

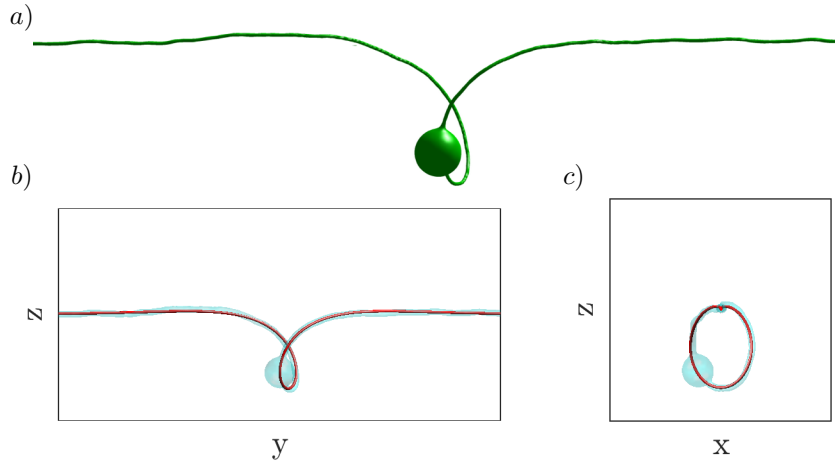


Figure 7.26: Plot of an electron bubble sliding along a vortex line for an electric field  $Q = 10^{-5}$ , at time  $t = 18250$ . The analytical solution corresponding to a Hasimoto loop-soliton having  $T = 0.65$  and  $\nu = 0.017$  is also shown. a) Isosurface plot, corresponding to  $|\psi|^2 = 0.3$ , of the bubble-vortex complex ; b) analytical solution for the Hasimoto soliton, rendered with a red tube, projected on the  $z$ - $y$ ; c)  $x$ - $z$  plane. The comparison between analytical and numerical solution projected into the isosurfaces, corresponding to  $|\psi|^2 = 0.9$ , shown in b) and c).

decrease slowly with a similar trend. This suggests that  $T$  tends to a constant value in time. Hence, assuming  $T = \text{const}$  and  $\omega \sim t^{-1}$  it is possible to estimate that the velocity of bubble will decrease according to the power law  $t^{-1/2}$  while  $r_{max}$  will increase according to  $t^{1/2}$ , see Fig. 7.29.

From the above discussion we can conclude that one possible scenario suggested by the evolution of our numerical results seems to support the idea that both the rotation and the velocity will decrease approaching zero in the long time dynamics.

For the seek of completeness we make a final observation concerning the dynamics of an electron under the electric field  $Q \geq 2 \times 10^{-5}$ . In this regime the rotation of the soliton is too fast to support a stable configuration with the bubble sat on the top of it and for that reason the electron can escape from the vortex line. After escaping from the line, the bubble nucleates a vortex ring and transits into a charged vortex ring, as described in the previous section. This charged ring can then leave the domain or be captured again by the vortex line generating highly unstable loop soliton configurations.

## 7.6 Conclusion

In this Chapter we studied the effect of a constant applied electric field on a free electron moving through a superfluid described with the GP model. Our findings reveal that, for sufficiently high electric fields, a bubble can avoid the transition into a

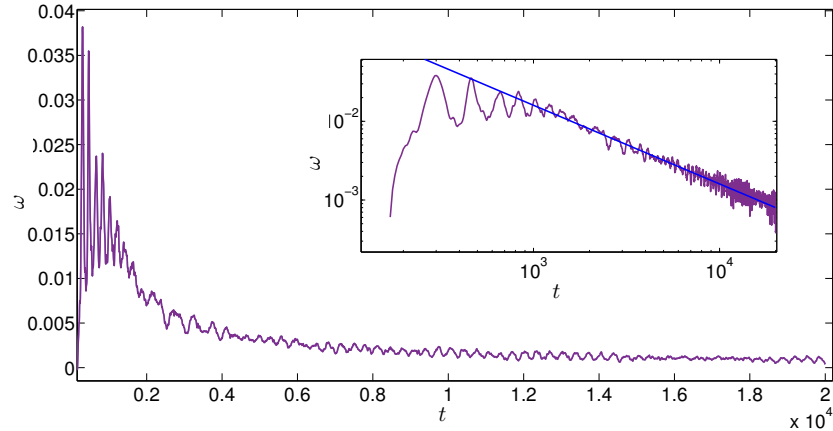


Figure 7.27: Plot of the angular velocity of an electronic bubble rotating during the motion along a vortex line under the influence of an applied electric field  $Q = 10^{-5}$ . A log-log plot is shown in the inset. The blue line superimposed on the data inside the inset represents a power law  $\propto t^{-1}$ .

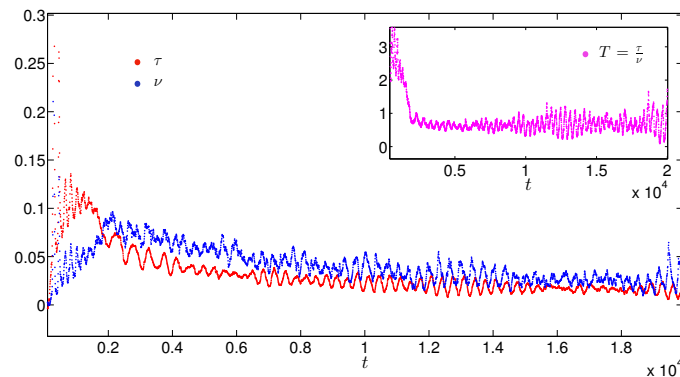


Figure 7.28: Time evolution of the coefficient  $\tau$ , red dots, and  $\nu$ , blue dots, evaluated from the dynamics of an electron bubble sliding along a vortex under the electric field  $Q = 10^{-5}$ . The inset shows the evolution of the parameter  $T = \tau/\nu$ .

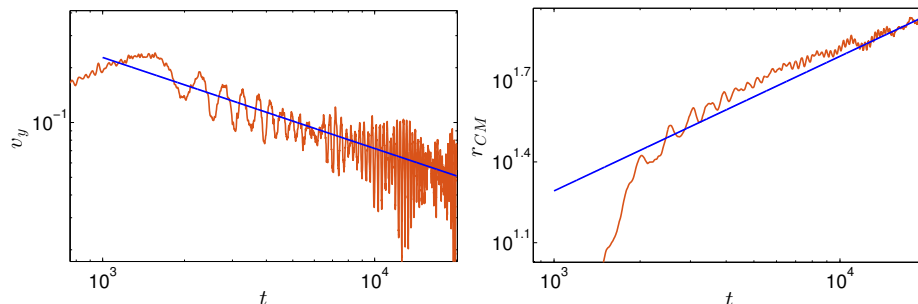


Figure 7.29: Log-log plot of the a) velocity  $v_y$  and b) transversal displacement  $r_{CM}$  of an electron bubble during the motion along a vortex line under the influence of an applied electric field  $Q = 10^{-5}$ . Blue lines superimposed on the data represents power laws a)  $\propto t^{-1/2}$  and b)  $\propto t^{1/2}$ .

charged vortex ring. Rather, the emission of a stream of vortex rings can lead to the formation of a small vortex tangle in the wake of the electron. By measuring the vortex nucleation limited mobility of the electron, we have demonstrated that, for low values of pressures and temperatures, the generation of such a vortex tangle can be considered as one of the main contributions that determines the value of the drift velocity attained by the electron. Our numerical values of mobility show excellent agreement with the previous experimental measurements of the vortex nucleation limited mobility obtained in [180]. This also provides further confirmation that the phenomenological model employed in our work can correctly describe the dynamics of electron bubbles in the considered range of temperatures and pressures where their motion is dominated by the presence of superfluid vortices. Moreover, this result allowed us to confirm the idea from Nancolas *et al.* [61] which considers the nucleation of a stream of vortex rings as a new form of drag that is required to explain the anomalous values of the drift velocities measured in [62].

In the second part of this Chapter, we focused on the motion of an electron bubble sliding along a vortex line under the effect of a constant applied electric field in the limit of zero temperature. On the one hand, for weak electric fields, we have confirmed that the generation of small amplitude KWs constitutes the main source of drag acting on the electron. In particular, we found remarkable agreement by comparing the frequency of the oscillation of the electron measured in our numerical simulations with the expected frequency predicted by the simple model presented in [163]. On the other hand, when high electric fields are considered, our findings reveal the presence of high amplitude KWs and also solitary waves propagating along the vortex line while the electron is moving. We have verified that such solitary waves correspond to a particular type of soliton predicted by Hasimoto [109] which was first observed in a rotating water tank by Maxworthy *et al* in [189]. Upon investigating the subsequent late time dynamics of these solitary waves, we identified a self-similar time evolution which is reflected in power-laws characterising the time dependence of both the amplitude of the velocity of the wave envelopes. This result could play a fundamental role in the understanding of the low temperature mobilities and limiting velocities measured by Galberson for an electron bubble sliding along a vortex line. In that work, a marked discrepancy was observed between the experimental measurements and the theoretical predictions [187, 190]. Since the current theories consider the scattering with low amplitude KWs as the only mechanism affecting the motion of the electron, we believe it would be of great interest to extend such theories to account for the role played by high amplitude KWs and Hasimoto soliton excitations.

# Chapter 8

## Conclusions and Future Perspectives

In this thesis, we have carried out a numerical study of a superfluid within a mean field approximation where the dynamics of the superfluid is governed by the GP model. One of the main results presented in this work is the development of a numerical tool that can be used to detect and analyse the presence of all the quantum vortices for a given complex GP field. This method has been thoroughly validated and used throughout this thesis to address several physical problems related to the understanding of the main mechanisms responsible for the transfer of energy in superfluid turbulence in the limit of zero temperature.

In Chapter 4, we applied this vortex tracking algorithm to study the interaction between a vortex line and a vortex ring. We focused on this type of vortex interaction since it represents a prototype of the dynamics occurring in the so called cross-over range of scales in quantum turbulence. The possibility of monitoring the length of vortex lines during the dynamics allowed us to estimate the amount of energy transferred from the vortex ring to the vortex line. Moreover, through knowledge of the position of the vortex filaments we were able to perform a direct comparison between the dynamics described by the GP equation and the one described by the Local Induction Approximation (LIA). We performed this comparison since LIA represents the most widely used model to formulate theoretical predictions concerning the energy transfer through different length scales in quantum turbulence.

In Chapter 5, we applied the vortex tracking method to investigate the evolution and the decay of a quantum vortex tangle. In particular, we measured the rate of decay of the total vortex line density of a tangle showing its agreement with Vinen's law given by Eq. (1.26) that is expected in the ultraquantum regime of turbulence. Our results provide the first realisation of this type of turbulence for a compressible superfluid characterised by the presence of sound waves. On the one hand, this observation extends previous results obtained in the study of liquid helium-4. On the other hand, it opens the possibility to experimentally observe this type of turbulence also in atomic Bose-Einstein condensates as was also suggested in [191]. We also studied the temporal

evolution of the Kelvin wave spectrum providing evidence of the development of a weak-wave turbulence cascade for transferring energy down to dissipative length scales. Our results are consistent with the universal exponent predicted by Lvov and Nazarenko although we have not quantified the influence of sound emission in our observed KW spectrum. We also investigated topological configuration and properties of quantum vortex tangles. Our results reveal that during the decay of turbulence, vortex rings can link.

Although Kelvin waves play a fundamental role in transferring energy to the smallest scales, a full understanding of the dissipative processes occurring in superfluids in the low-temperature limit must also take into account the reconnection events. In Chapter 6, we focused on properties of reconnections where we found that reconnections of quantized vortex filaments display both universal and nonuniversal phenomena. In particular, our results show that during a reconnection, the rate of approach and separation between vortices scales according to the power law  $t^{1/2}$ . This behaviour appears to be independent of the initial condition chosen. On the other hand, the dimensionless coefficients  $A_{\pm}$ , present in the rate of approach and the separation of the two filaments, exhibit a non-universal behaviour. From linear analysis, we showed that these coefficients are related to the local angle at which the vortices reconnect. Moreover, a strong discrepancy in the values of  $A^+$  and  $A^-$  seems to be associated with the emergence of shock-like structures in the value of the torsion measured along the filament. This behaviour might suggest a correlation between the strong emission of sound waves or a rarefaction pulse and the values of  $A^{\pm}$ . It would, therefore, be useful to conduct a statistical analysis of vortex reconnections in order to clarify which values of  $A^{\pm}$  are the most likely and whether a relation exists between  $A^{\pm}$  and the emission of sound waves.

In Chapter 7, we focused on modelling the dynamics of an electron bubble in superfluid liquid helium. This study is mainly motivated by the current experimental interest in detecting quantum turbulence by injecting electrons inside a turbulent vortex tangle. In this Chapter we demonstrated that the Gross-Clark (GC) equation, where the superfluid is modelled by the GP equation, represents a suitable mathematical model to describe the dynamics of an electron in regimes where its motion is dominated by the interaction with quantum vortices present in the system. In fact, the GC model does not in general represent an accurate model for liquid helium-4 since it neither describes the presence of rotons nor the correct equation of state. However, based on results of our numerical simulations, we showed that the value of the vortex nucleated limited mobility for the ion is in remarkable agreement with the experimental measurements. In the second part of the Chapter, we considered the interaction between an electron and quantum vortices: the motion of an ion sliding along the core of a straight vortex line under the influence of a constant applied electric field. This study revealed that during the motion of the electron, solitary wave structures can arise and propagate along the core of the vortex. We identified these structures as Hasimoto soliton like excitations.

The innovative method we have developed to track and study quantised vortex dy-

namics and the model used to study the interaction between electrons and superfluid liquid helium represent two of the main contributions presented in this thesis. In the future, it would be of interest to combine these two results in order to study the evolution of a turbulent vortex tangle where the presence of many electron bubbles is also considered. This scenario, together with inclusion of the Coulomb interaction between the ions, would allow us to directly visualise what is being measured nowadays in experiments in order to detect superfluid turbulence in the zero temperature limit. Moreover, it would be of great interest to compare the results obtained with the Gross-Clark model to other models where ions are treated as solid particles moving according to Newton's laws of motion. This could help establish under what circumstances a simpler and numerically less expensive description can be used to investigate the dynamics of electron bubbles in liquid helium.

As a final remark, since the GP equation is a model formally derived for a dilute gas of weakly interacting bosons, it would be ideal to extend this equation along the lines of a density-functional theory in order to provide a better description for liquid helium-4. In particular, by adding higher order non-linear terms to the GP equation, it is possible to obtain a more accurate description of the equation of state for liquid helium [166]. Moreover, by extending the model to account for non-local interactions between the helium atoms, it is possible to reproduce the roton part of the dispersion relation [49]. Including both of these features would allow us to extend our study presented in Chapter 7 on the motion of electron bubbles in a superfluid in order to perform a more systematic study on the mobility of free electron bubbles as a function of pressure. In addition, it would be of great interest to investigate more thoroughly under what conditions the adiabatic approximation for the evolution of the electron wave function may break down. In particular, relaxing this approximation can help in establishing the relevance of certain scenarios that have been proposed in order to explain the so-called exotic ions in liquid helium [192], whose nature remains unclear.

# Appendix A

## Taylor–Green Flow

In this work we use the so-called Taylor-Green initial condition introduced by Nore et al. [82]. We recall here for the sake of completeness how this initial condition is produced by making use of the Clebsch representation of a vector field. Let us assume that an incompressible velocity field  $\mathbf{u}_{\text{adv}}(x, y, z)$  admits a global Clebsch representation in terms of potentials  $\lambda(x, y, z)$ ,  $\mu(x, y, z)$  and  $\Phi(x, y, z)$  [78], such that  $\mathbf{u}_{\text{adv}} = \lambda \nabla \mu - \nabla \Phi$ . It follows that

$$\nabla \times \mathbf{u}_{\text{adv}} = \nabla \lambda \times \nabla \mu. \quad (\text{A.1})$$

The Clebsch representation has an interesting geometrical representation. A vortex line of the velocity flow  $\mathbf{u}_{\text{adv}}$  is mapped into a point in the  $(\lambda, \mu)$  plane. Indeed a vortex line  $\omega(\mathbf{s})$  is defined by  $\frac{d\omega}{ds} = \nabla \times \mathbf{u}_{\text{adv}}(\omega(\mathbf{s}))$ . A simple solution is given by  $\lambda(\omega(\mathbf{s})) = \lambda_v$  and  $\mu(\omega(\mathbf{s})) = \mu_v$ , with  $\lambda_v$  and  $\mu_v$  constants. It follows that, using a  $2D$  wavefunction  $\psi_{2D}$  of a vortex at the origin, it is straightforward to construct a  $3D$  wavefunction with a nodal line defined by  $\lambda(x, y, z) = \lambda_v$  and  $\mu(x, y, z) = \mu_v$ . This  $3D$  field simply reads

$$\psi(x, y, z) = \psi_{2D}(\lambda(x, y, z) - \lambda_v, \mu(x, y, z) - \mu_v) \quad (\text{A.2})$$

This idea is applied to the Taylor-Green velocity flow defined in the domain  $[0, 2\pi]^3$  as:

$$\mathbf{u}_{\text{adv}} = A(\sin(x) \cos(y) \cos(z), -\cos(x) \sin(y) \cos(z), 0). \quad (\text{A.3})$$

It is composed of 8 fundamental boxes that are obtained one from each other by mirror symmetric transformation of the sub-box  $[0, \pi]^3$ . It admits a decomposition in terms of the Clebsch potentials (see Eq. [82] for further details):

$$\begin{aligned} \lambda(x, y, z) &= \sqrt{A} \cos(x) \sqrt{2|\cos(z)|}, \\ \mu(x, y, z) &= \sqrt{A} \cos(y) \sqrt{2|\cos(z)|} \text{sign}[\cos(z)], \end{aligned} \quad (\text{A.4})$$

in the sense that  $\nabla \times \mathbf{u}_{\text{adv}} = \nabla \lambda \times \nabla \mu$ . Note that the circulation around the plane  $[0, \pi] \times [0, \pi]$  is  $8A$

A set of vortex lines can be defined in the wavefunction as

$$\begin{aligned} \psi_4(\lambda, \mu) &= \psi_{2D}\left(\lambda - \frac{1}{\sqrt{2}}, \mu\right) \psi_{2D}\left(\lambda + \frac{1}{\sqrt{2}}, \mu\right) \\ &\quad \times \psi_{2D}\left(\lambda, \mu - \frac{1}{\sqrt{2}}\right) \psi_{2D}\left(\lambda, \mu + \frac{1}{\sqrt{2}}\right) \end{aligned} \quad (\text{A.5})$$

Any 2D vortex profile approximation can be used as it will be later relaxed by using the Advective-Real-Ginzburg-Landau equation [82]. In order to match (as close as possible) the circulation to the Taylor-Green flow, the initial condition is defined as

$$\psi_{\text{TG}}(x, y, z) = \psi_4(x, y, z)^{n_c} \quad (\text{A.6})$$

where  $n_c = \lfloor (8A/\Gamma)/4 \rfloor$  and  $\Gamma$  represent the quantum of circulation. The wavefunction  $\psi_{\text{TG}}$  is then evolved under the Advective-Real-Ginzburg-Landau equation:

$$\hbar \frac{\partial \psi}{\partial t} = \frac{\hbar^2}{2m} \nabla^2 \psi - g|\psi|^2 \psi + \mu \psi - \hbar \left( i \mathbf{u}_{\text{adv}} \cdot \nabla \psi + \frac{u_{\text{adv}}^2}{2\hbar/m} \psi \right), \quad (\text{A.7})$$

subject to the chemical potential  $\mu$ . This equation is just the imaginary time evolution of the Gross-Pitaevskii equation after a Galilean transformation with a non-constant velocity field  $u_{\text{adv}}$ . The final states contains a clean (without sound) initial condition with a set of rings (of charge one) distributed along the vortical lines of the Taylor-Green velocity flow. A visualisation of the Taylor-Green flow is displayed in Fig.3.7a. The initial condition is then evolved using the Gross-Pitaevskii equation.

# Appendix B

## Conserved Quantities in the GP Model

In order to prove the conservation of the total mass, total momentum and total energy for a superfluid governed by the GP equation it is useful to explicitly rewrite the GP equation (2.15) and its complex conjugate as

$$\frac{\partial \psi}{\partial t} = i \frac{\hbar^2}{2m} \frac{\partial^2 \psi}{\partial x^2} - ig|\psi|^2 \psi \quad (\text{B.1})$$

and

$$\frac{\partial \psi^*}{\partial t} = -i \frac{\hbar^2}{2m} \frac{\partial^2 \psi^*}{\partial x^2} + ig|\psi|^2 \psi^* \quad (\text{B.2})$$

where for simplicity we reduced the calculation to a 1D wave function  $\psi(x, t)$  defined in the domain  $x \in (-X, X)$ . Motivated by the numerical scheme used throughout the thesis we also choose periodic boundary conditions. By using Eqs. (2.16), (B.1) and (B.2), we now begin investigating the conservation of the mass:

$$\begin{aligned} \frac{dM}{dt} &= m \int \frac{\partial}{\partial t} |\psi|^2 dx = m \int \left[ \psi^* \frac{\partial}{\partial t} \psi + \psi \frac{\partial}{\partial t} \psi^* \right] dx \\ &= i \frac{\hbar}{2} \int \left[ \psi^* \frac{\partial^2 \psi}{\partial x^2} - \psi \frac{\partial^2 \psi^*}{\partial x^2} \right] dx. \end{aligned} \quad (\text{B.3})$$

By integrating by parts we obtain

$$\frac{dM}{dt} = i \frac{\hbar}{2} \left[ \psi \frac{\partial \psi^*}{\partial x} - \psi^* \frac{\partial \psi}{\partial x} \right]_{-X}^{+X}. \quad (\text{B.4})$$

Hence, we can conclude that, for system where periodic boundary conditions are chosen, the total mass is conserved in time.

Similarly, we can study the conservation of the linear momentum (7.9):

$$\begin{aligned} \frac{dP}{dt} &= \frac{\hbar}{2i} \int \left( \frac{\partial \psi^*}{\partial t} \frac{\partial \psi}{\partial x} + \psi^* \frac{\partial^2 \psi}{\partial t \partial x} - \frac{\partial \psi}{\partial t} \frac{\partial \psi^*}{\partial x} - \psi \frac{\partial^2 \psi^*}{\partial t \partial x} \right) dx \\ &= -g \int \frac{\partial |\psi|^2}{\partial x} |\psi|^2 dx = -\frac{g}{2} \int \frac{\partial |\psi|^4}{\partial x} dx = -\frac{g}{2} |\psi|^4 \Big|_{-X}^{+X}. \end{aligned} \quad (\text{B.5})$$

Again, we can conclude that for system where periodic boundary conditions are chosen, the linear momentum is conserved in time. We now focus on the conservation of the last quantity: the energy of the system (2.17)”

$$\begin{aligned}
 \frac{dE}{dt} &= \frac{\hbar^2}{2m} \int \left( \frac{\partial^2 \psi}{\partial x \partial t} \frac{\partial \psi^*}{\partial x} + \frac{\partial^2 \psi^*}{\partial x \partial t} \frac{\partial \psi}{\partial x} \right) dx + \frac{g}{2} \int \frac{\partial |\psi|^4}{\partial t} dx \\
 &= i \frac{\hbar^3}{4m^2} \int \left[ \frac{\partial^3 \psi}{\partial x^3} \frac{\partial \psi^*}{\partial x} - \frac{\partial^3 \psi^*}{\partial x^3} \frac{\partial \psi}{\partial x} \right] dx + i \frac{g\hbar}{2m} \int \left[ \frac{\partial |\psi|^2 \psi^*}{\partial x} \frac{\partial \psi}{\partial x} - \frac{\partial |\psi|^2 \psi}{\partial x} \frac{\partial \psi^*}{\partial x} \right] dx + \\
 &+ i \frac{g\hbar}{2m} \int \left[ \psi^* |\psi|^2 \frac{\partial^2 \psi}{\partial x^2} - \psi |\psi|^2 \frac{\partial^2 \psi^*}{\partial x^2} \right] dx.
 \end{aligned} \tag{B.6}$$

Again, by using the integration by parts one can confirm the conservation in time of the system energy.

# Bibliography

- [1] J.F. Allen and A.D. Misener. Flow of Liquid Helium II. *Nature*, 141, Jan 1938.
- [2] P. Kapitza. Viscosity of Liquid Helium below the  $\lambda$ -Point. *Nature*, 141, Jan 1938.
- [3] Oliver Penrose and Lars Onsager. Bose-einstein condensation and liquid helium. *Phys. Rev.*, 104:576–584, Nov 1956.
- [4] M. H. Anderson, J. R. Ensher, M. R. Matthews, C. E. Wieman, and E. A. Cornell. Observation of bose-einstein condensation in a dilute atomic vapor. *Science*, 269(5221):198–201, 1995.
- [5] K. B. Davis, M. O. Mewes, M. R. Andrews, N. J. van Druten, D. S. Durfee, D. M. Kurn, and W. Ketterle. Bose-einstein condensation in a gas of sodium atoms. *Phys. Rev. Lett.*, 75:3969–3973, Nov 1995.
- [6] D. R. Allum, P. V. E. McClintock, and A. Phillips. The breakdown of superfluidity in liquid  $^4\text{He}$ : an experimental test of landau’s theory. *Philosophical Transactions of the Royal Society of London A: Mathematical, Physical and Engineering Sciences*, 284(1320):179–224, 1977.
- [7] R.J. Donnelly. *Quantized vortices in Helium II*, volume 3. Cambridge Univ Pr, 1991.
- [8] E.L. Adronikashvili and E.M. Lifshitz. *A Supplement to Helium*. Consultants Bureau, New York, 1959.
- [9] W. F. Vinen. The detection of single quanta of circulation in liquid helium ii. *Proceedings of the Royal Society of London A: Mathematical, Physical and Engineering Sciences*, 260(1301):218–236, 1961.
- [10] W. F. Vinen and J. J. Niemela. Quantum turbulence. *Journal of Low Temperature Physics*, 128(5):167–231, Sep 2002.
- [11] M. S. Paoletti, Michael E. Fisher, K. R. Sreenivasan, and D. P. Lathrop. Velocity statistics distinguish quantum turbulence from classical turbulence. *Phys. Rev. Lett.*, 101:154501, Oct 2008.
- [12] A. P. Finne, T. Araki, R. Blaauwgeers, V. B. Eltsov, N. B. Kopnin, M. Krusius, L. Skrbek, M. Tsubota, and G. E. Volovik. An intrinsic velocity-independent criterion for superfluid turbulence. *Nature*, 424(6952):1022–1025, 08 2003.

- [13] D. I. Bradley, D. O. Clubb, S. N. Fisher, A. M. Guénault, R. P. Haley, C. J. Matthews, G. R. Pickett, V. Tsepelin, and K. Zaki. Decay of pure quantum turbulence in superfluid  $^3\text{He}$ —B. *Phys. Rev. Lett.*, 96:035301, Jan 2006.
- [14] Simone Serafini, Luca Galantucci, Elena Iseni, Tom Bienaimé, Russell N. Bisset, Carlo F. Barenghi, Franco Dalfovo, Giacomo Lamporesi, and Gabriele Ferrari. Vortex reconnections and rebounds in trapped atomic bose-einstein condensates. *Phys. Rev. X*, 7:021031, May 2017.
- [15] R.P. Feynman. Chapter ii application of quantum mechanics to liquid helium. *Progress in Low Temperature Physics*, 1:17 – 53, 1955.
- [16] Uriel Frisch and A.N. Kolmogorov. *Turbulence: The Legacy of A. N. Kolmogorov*. Cambridge University Press, 1995.
- [17] Paul Walmsley, Dmitry Zmeev, Fatemeh Pakpour, and Andrei Golov. Dynamics of quantum turbulence of different spectra. *Proceedings of the National Academy of Sciences*, 111(Supplement 1):4691–4698, 2014.
- [18] Carlo F. Barenghi, Ladislav Skrbek, and Katepalli R. Sreenivasan. Introduction to quantum turbulence. *Proceedings of the National Academy of Sciences of the United States of America*, 111(SUPPL. 1):4647–4652, 3 2014.
- [19] J. Maurer and P. Tabeling. Local investigation of superfluid turbulence. *EPL (Europhysics Letters)*, 43(1):29, 1998.
- [20] J. Salort, C. Baudet, B. Castaing, B. Chabaud, F. Daviaud, T. Didelot, P. Diribarne, B. Dubrulle, Y. Gagne, F. Gauthier, A. Girard, B. Hbral, B. Rousset, P. Thibault, and P.-E. Roche. Turbulent velocity spectra in superfluid flows. *Physics of Fluids*, 22(12):125102, 2010.
- [21] L. Skrbek and Steven R. Stalp. On the decay of homogeneous isotropic turbulence. *Physics of Fluids*, 12(8):1997–2019, 2000.
- [22] L. Skrbek and K. R. Sreenivasan. Developed quantum turbulence and its decay. *Physics of Fluids*, 24(1):011301, 2012.
- [23] P. M. Walmsley, A. I. Golov, H. E. Hall, A. A. Levchenko, and W. F. Vinen. Dissipation of quantum turbulence in the zero temperature limit. *Phys. Rev. Lett.*, 99:265302, Dec 2007.
- [24] Tsunehiko Araki, Makoto Tsubota, and Sergey K. Nemirovskii. Energy spectrum of superfluid turbulence with no normal-fluid component. *Phys. Rev. Lett.*, 89:145301, Sep 2002.
- [25] Caroline Nore, Malek Abid, and ME Brachet. Decaying Kolmogorov turbulence in a model of superflow. *Physics of Fluids (1994-present)*, 9(9):2644–2669, 1997.

- [26] Andrew W. Baggaley, Jason Laurie, and Carlo F. Barenghi. Vortex-density fluctuations, energy spectra, and vortical regions in superfluid turbulence. *Phys. Rev. Lett.*, 109:205304, Nov 2012.
- [27] W. F. Vinen. Decay of superfluid turbulence at a very low temperature: The radiation of sound from a kelvin wave on a quantized vortex. *Phys. Rev. B*, 64:134520, Sep 2001.
- [28] Giorgio Krstulovic. Kelvin-wave cascade and dissipation in low-temperature superfluid vortices. *Phys. Rev. E*, 86:055301, Nov 2012.
- [29] W. F. Vinen, Makoto Tsubota, and Akira Mitani. Kelvin-wave cascade on a vortex in superfluid  $^4\text{He}$  at a very low temperature. *Phys. Rev. Lett.*, 91:135301, Sep 2003.
- [30] B.V. Svistunov. Superfluid turbulence in the low-temperature limit. *Phys. Rev. B*, 52:3647, 1995.
- [31] V.S. L'vov and S. Nazarenko. Spectrum of Kelvin-wave turbulence in superfluids. *JETP Letters*, 91:428–434, 2010. 10.1134/S002136401008014X.
- [32] Sonin, E. B. Dynamics of helical vortices and helical-vortex rings. *EPL*, 97(4):46002, 2012.
- [33] W. F. Vinen. Decay of superfluid turbulence at a very low temperature: The radiation of sound from a Kelvin wave on a quantized vortex. *Phys. Rev. B*, 64:134520, Sep 2001.
- [34] P. M. Walmsley and A. I. Golov. Quantum and quasiclassical types of superfluid turbulence. *Phys. Rev. Lett.*, 100:245301, Jun 2008.
- [35] A. W. Baggaley, C. F. Barenghi, and Y. A. Sergeev. Quasiclassical and ultra-quantum decay of superfluid turbulence. *Phys. Rev. B*, 85:060501, Feb 2012.
- [36] W. F. Vinen. Mutual friction in a heat current in liquid helium ii. i. experiments on steady heat currents. *Proceedings of the Royal Society of London A: Mathematical, Physical and Engineering Sciences*, 240(1220):114–127, 1957.
- [37] M. Walmsley, P. A. Tompsett, P. E. Zmeev, D. and I. Golov, A. Reconnections of quantized vortex rings in superfluid  $^4\text{He}$  at very low temperatures. *Phys. Rev. Lett.*, 113:125302, Sep 2014.
- [38] V.S. L'vov, S.V. Nazarenko, and O. Rudenko. Bottleneck crossover between classical and quantum superfluid turbulence. *Phys. Rev. B*, 76:024520, 2007.
- [39] Evgeny Kozik and Boris Svistunov. Kolmogorov and kelvin-wave cascades of superfluid turbulence at  $t = 0$ : What lies between. *Phys. Rev. B*, 77:060502, Feb 2008.

- [40] H. Salman. Breathers on Quantized Superfluid Vortices. *Phys. Rev. Lett.*, 111:165301, 2013.
- [41] S. K. Nemirovskii. Probing of quantum turbulence with the emitting vortex loops. *Low Temperature Physics*, 40(12):1116–1118, 2014.
- [42] W. Guo, J. D. Wright, S. B. Cahn, J. A. Nikkel, and D. N. McKinsey. Metastable helium molecules as tracers in superfluid  $^4\text{He}$ . *Phys. Rev. Lett.*, 102:235301, Jun 2009.
- [43] D.E. Zmeev, F. Pakpour, P.M. Walmsley, A.I. Golov, W. Guo, D.N. McKinsey, G.G. Ihas, P.V.E. McClintock, S.N. Fisher, and W.F. Vinen. Excimers  $\text{He}_2^*$  as Tracers of Quantum Turbulence in  $^4\text{He}$  in the  $T = 0$  Limit. *Phys. Rev. Lett.*, 110:175303, 2013.
- [44] Alberto Villois, Giorgio Krstulovic, Davide Proment, and Hayder Salman. A vortex filament tracking method for the grosspitaevskii model of a superfluid. *Journal of Physics A: Mathematical and Theoretical*, 49(41):415502, 2016.
- [45] A. F. Borghesani. *Ions and electrons in liquid helium*. Oxford University Press, USA, 2007.
- [46] E.P. Gross. *Quantum Fluids*. Amsterdam: North-Holland, 1966.
- [47] Natalia G Berloff and Paul H Roberts. Motion in a bose condensate: Viii. the electron bubble. *Journal of Physics A: Mathematical and General*, 34(1):81, 2001.
- [48] Nir Navon, Alexander L. Gaunt, Robert P. Smith, and Zoran Hadzibabic. Emergence of a turbulent cascade in a quantum gas. *Nature*, 539(7627):72–75, 11 2016.
- [49] PaulH. Roberts and NataliaG. Berloff. The Nonlinear Schrödinger Equation as a Model of Superfluidity. In C.F. Barenghi, R.J. Donnelly, and W.F. Vinen, editors, *Quantized Vortex Dynamics and Superfluid Turbulence*, volume 571 of *Lecture Notes in Physics*, pages 235–257. Springer Berlin Heidelberg, 2001.
- [50] David C. Samuels. *Vortex Filament Methods for Superfluids*, pages 97–113. Springer Berlin Heidelberg, Berlin, Heidelberg, 2001.
- [51] R. J. Arms and Francis R. Hama. Localized induction concept on a curved vortex and motion of an elliptic vortex ring. *Physics of Fluids (1958-1988)*, 8(4):553–559, 1965.
- [52] Alberto Villois, Hayder Salman, and Davide Proment. Scattering of line-ring vortices in a superfluid. *Journal of Low Temperature Physics*, 180(1-2):68–81, 2015.
- [53] Davide Proment, Miguel Onorato, and Carlo F. Barenghi. Vortex knots in a Bose-Einstein condensate. *Phys. Rev. E*, 85:036306, Mar 2012.

- [54] Alberto Villois, Davide Proment, and Giorgio Krstulovic. Evolution of a superfluid vortex filament tangle driven by the gross-pitaevskii equation. *Phys. Rev. E*, 93:061103, Jun 2016.
- [55] S. Zuccher, M. Caliari, A. W. Baggaley, and C. F. Barenghi. Quantum vortex reconnections. *Physics of Fluids*, 24(12), 2012.
- [56] C. Rorai, J. Skipper, R. M. Kerr, and K. R. Sreenivasan. Approach and separation of quantised vortices with balanced cores. *Journal of Fluid Mechanics*, 808:641?667, Dec 2016.
- [57] A. J. Allen, S. Zuccher, M. Caliari, N. P. Proukakis, N. G. Parker, and C. F. Barenghi. Vortex reconnections in atomic condensates at finite temperature. *Phys. Rev. A*, 90:013601, Jul 2014.
- [58] A. W. Baggaley, L. K. Sherwin, C. F. Barenghi, and Y. A. Sergeev. Thermally and mechanically driven quantum turbulence in helium ii. *Phys. Rev. B*, 86:104501, Sep 2012.
- [59] Alberto Villois, Davide Proment, and Giorgio Krstulovic. Universal and nonuniversal aspects of vortex reconnections in superfluids. *Phys. Rev. Fluids*, 2:044701, Apr 2017.
- [60] K. W. Schwarz. Interaction of quantized vortex rings with quantized vortex lines in rotating he ii. *Phys. Rev.*, 165:323–334, Jan 1968.
- [61] G. G. Nancolas, T. Ellis, P. V. E. McClintock, and R. M. Bowley. A new form of energy dissipation by a moving object in he ii. *Nature*, 316(6031):797–799, 08 1985.
- [62] T. Ellis, P. V. E. McClintock, R. M. Bowley, and D. R. Allum. The breakdown of superfluidity in liquid 4he. ii. an investigation of excitation emission from negative ions travelling at extreme supercritical velocities. *Philosophical Transactions of the Royal Society of London A: Mathematical, Physical and Engineering Sciences*, 296(1425):581–595, 1980.
- [63] R. M. Ostermeier and W. I. Glaberson. The mobility of ions trapped on vortex lines in pure 4he and 3he-4he solutions. *Journal of Low Temperature Physics*, 25(3):317–351, Nov 1976.
- [64] Alberto Villois and Hayder Salman. Vortex nucleation limited mobility of free electron bubbles in the gross-pitaevskii model of a superfluid. *Phys. Rev. B*, 97:094507, Mar 2018.
- [65] Miguel D. Bustamante and Sergey Nazarenko. Derivation of the biot-savart equation from the nonlinear schrödinger equation. *Phys. Rev. E*, 92:053019, Nov 2015.
- [66] D. R. Hartree. The wave mechanics of an atom with a non-coulomb central field. part i. theory and methods. *Mathematical Proceedings of the Cambridge Philosophical Society*, 24(1):89?110, 1928.

- [67] Pablo Echenique and J. L. Alonso. A mathematical and computational review of hartreefock scf methods in quantum chemistry. *Molecular Physics*, 105(23-24):3057–3098, 2007.
- [68] J. C. Slater. Note on hartree’s method. *Phys. Rev.*, 35:210–211, Jan 1930.
- [69] A.L. Fetter and J.D. Walecka. *Quantum Theory of Many-particle Systems*. Dover Books on Physics. Dover Publications, 2003.
- [70] L.P. Pitaevskii and S. Stringari. *Bose-Einstein Condensation*, volume 116. Oxford University Press, USA, 2003.
- [71] E. Madelung. Eine anschauliche Deutung der Gleichung von Schrödinger. *Naturwissenschaften*, 14:1004–1004, November 1926.
- [72] P.G. Saffman. *Vortex Dynamics*. Cambridge University Press, 1993. Cambridge Books Online.
- [73] Emil Lundh. Multiply quantized vortices in trapped bose-einstein condensates. *Phys. Rev. A*, 65:043604, Mar 2002.
- [74] Y. Shin, M. Saba, M. Vengalattore, T. A. Pasquini, C. Sanner, A. E. Leanhardt, M. Prentiss, D. E. Pritchard, and W. Ketterle. Dynamical instability of a doubly quantized vortex in a bose-einstein condensate. *Phys. Rev. Lett.*, 93:160406, Oct 2004.
- [75] V.L. Ginsburg and L.P. Pitaevskii. On the theory of superfluidity. *Journal of Experimental and Theoretical Physics*, 7(5):858, 1958.
- [76] G. K. Batchelor. *An introduction to fluid dynamics*. Cambridge University Press, 1967.
- [77] M. Rasetti and T. Regge. Vortices in he ii, current algebras and quantum knots. *Physica A: Statistical Mechanics and its Applications*, 80(3):217 – 233, 1975.
- [78] Horace Lamb. *Hydrodynamics*. Cambridge university press, 1932.
- [79] G. W. Rayfield and F. Reif. Quantized vortex rings in superfluid helium. *Phys. Rev.*, 136:A1194–A1208, Nov 1964.
- [80] J. Grant and P.H. Roberts. Motions in a bose condensate. III. the structure and effective masses of charged and uncharged impurities. *Journal of Physics A: Mathematical, Nuclear and General*, 7(2):260, 1974.
- [81] Carlo F. Barenghi, Renzo L. Ricca, and David C. Samuels. How tangled is a tangle? *Physica D: Nonlinear Phenomena*, 157(3):197 – 206, 2001.
- [82] Caroline Nore, Malek Abid, and ME Brachet. Decaying kolmogorov turbulence in a model of superflow. *Physics of Fluids (1994-present)*, 9(9):2644–2669, 1997.

- [83] J. Koplik and H. Levine. Vortex reconnection in superfluid helium. *Physical Review Letters*, 71(9):1375–1378, 1993.
- [84] Sergey Nazarenko and Robert West. Analytical Solution for Nonlinear Schrödinger Vortex Reconnection. *Journal of Low Temperature Physics*, 132(1):1–10, 2003.
- [85] S. Zuccher, M. Caliari, A. W. Baggaley, and C. F. Barenghi. Quantum vortex reconnections. *Physics of Fluids*, 24(12), 2012.
- [86] D. Proment, C. F. Barenghi, and M. Onorato. Interaction and decay of Kelvin waves in the Gross-Pitaevskii model. *ArXiv e-prints*, August 2013.
- [87] P. Clark di Leoni, P. D. Mininni, and M. E. Brachet. Spatiotemporal detection of Kelvin waves in quantum turbulence simulations. *Phys. Rev. A*, 92:063632, Dec 2015.
- [88] Martin W. Scheeler, Dustin Kleckner, Davide Proment, Gordon L. Kindlmann, and William T. M. Irvine. Helicity conservation by flow across scales in reconnecting vortex links and knots. *Proceedings of the National Academy of Sciences*, 111(43):15350–15355, 2014.
- [89] Simone Zuccher and Renzo L. Ricca. Helicity conservation under quantum reconnection of vortex rings. *Phys. Rev. E*, 92:061001, Dec 2015.
- [90] P. Clark di Leoni, P. D. Mininni, and M. E. Brachet. Helicity, Topology and Kelvin Waves in reconnecting quantum knots. *ArXiv e-prints*, February 2016.
- [91] N.G. Berloff and B.V. Svistunov. Scenario of strongly nonequilibrated Bose-Einstein condensation. *Physical Review A*, 66(1):13603, 2002.
- [92] Jeffrey Yopez, George Vahala, Linda Vahala, and Min Soe. Superfluid turbulence from quantum kelvin wave to classical kolmogorov cascades. *Physical Review Letters*, 103(8):084501, 2009.
- [93] Sergey Nazarenko and Miguel Onorato. Wave turbulence and vortices in bose-einstein condensation. *Physica D: Nonlinear Phenomena*, 219(1):1 – 12, 2006.
- [94] A J Taylor and M R Dennis. Geometry and scaling of tangled vortex lines in three-dimensional random wave fields. *Journal of Physics A: Mathematical and Theoretical*, 47(46):465101, 2014.
- [95] Natalia G. Berloff. Interactions of vortices with rarefaction solitary waves in a bose-einstein condensate and their role in the decay of superfluid turbulence. *Phys. Rev. A*, 69:053601, May 2004.
- [96] Christopher J. Foster, P. Blair Blakie, and Matthew J. Davis. Vortex pairing in two-dimensional bose gases. *Phys. Rev. A*, 81:023623, Feb 2010.

- [97] Angela C. White, Carlo F. Barenghi, and Nick P. Proukakis. Creation and characterization of vortex clusters in atomic bose-einstein condensates. *Phys. Rev. A*, 86:013635, Jul 2012.
- [98] G W Stagg, A J Allen, C F Barenghi, and N G Parker. Classical-like wakes past elliptical obstacles in atomic bose-einstein condensates. *Journal of Physics: Conference Series*, 594(1):012044, 2015.
- [99] William H. Press, Saul A. Teukolsky, William T. Vetterling, and Brian P. Flannery. *Numerical Recipes 3rd Edition: The Art of Scientific Computing*. Cambridge University Press, New York, NY, USA, 3 edition, 2007.
- [100] Giorgio Krstulovic, Marc Brachet, and Enrique Tirapegui. Radiation and vortex dynamics in the nonlinear Schrödinger equation. *Phys. Rev. E*, 78:026601, Aug 2008.
- [101] N.G. Berloff. Padé approximations of solitary wave solutions of the -Pitaevskii equation. *Journal of Physics A: Mathematical and General*, 37(5):1617, 2004.
- [102] Luiza Kondaurova, Victor L’vov, Anna Pomyalov, and Itamar Procaccia. Structure of a quantum vortex tangle in <sup>4</sup>He counterflow turbulence. *Phys. Rev. B*, 89:014502, Jan 2014.
- [103] F. Maggioni, S. Alamri, Carlo F. Barenghi, and Renzo L. Ricca. Velocity, energy, and helicity of vortex knots and unknots. *Physical Review E*, 82:026309, 2010.
- [104] D Proment, M Onorato, and C F Barenghi. Torus quantum vortex knots in the Gross-Pitaevskii model for Bose-Einstein condensates. *Journal of Physics: Conference Series*, 544(1):012022, 2014.
- [105] Dustin Kleckner, Louis H. Kauffman, and William T. M. Irvine. How superfluid vortex knots untie. *Nat Phys*, advance online publication:–, 03 2016.
- [106] E.V. Kozik and B.V. Svistunov. Theory of Decay of Superfluid Turbulence in the Low-Temperature Limit. *Journal of Low Temperature Physics*, 156(3-6):215–267, 2009.
- [107] Miguel D. Bustamante and Sergey Nazarenko. Derivation of the biot-savart equation from the nonlinear schrödinger equation. *Phys. Rev. E*, 92:053019, Nov 2015.
- [108] Sergey K. Nemirovskii. Energy spectrum of the 3d velocity field, induced by vortex tangle. *Journal of Low Temperature Physics*, 171(5):504–510, 2013.
- [109] Hidenori Hasimoto. A soliton on a vortex filament. *Journal of Fluid Mechanics*, 51:477–485, 2 1972.
- [110] R. L. Ricca and H.K. Moffatt. *Topological Aspects of the Dynamics of Fluids and Plasmas*, chapter The helicity of a knotted vortex filament. Springer, 1992.

- [111] N. Hietala, R. Hänninen, and H. Salman. Helicity and internal twist within the vortex filament model. *arXiv:1604.03350*, 2016.
- [112] Alexander L. Fetter. Quantum theory of superfluid vortices. i. liquid helium ii. *Phys. Rev.*, 162:143–153, Oct 1967.
- [113] Giorgio Krstulovic and Marc Brachet. Energy cascade with small-scale thermalization, counterflow metastability, and anomalous velocity of vortex rings in fourier-truncated gross-pitaevskii equation. *Physical Review E*, 83(6):066311, 2011.
- [114] C.A. Jones and P.H. Roberts. Motions in a Bose condensate: IV. Axisymmetric solitary waves. *J. Phys. A:Math. Gen.*, 15:2599–2619, 1982.
- [115] Evgeny Kozik and Boris Svistunov. Kelvin-wave cascade and decay of superfluid turbulence. *Phys. Rev. Lett.*, 92(3):035301, Jan 2004.
- [116] W. F. Vinen, Makoto Tsubota, and Akira Mitani. Kelvin-wave cascade on a vortex in superfluid  $^4\text{He}$  at a very low temperature. *Phys. Rev. Lett.*, 91:135301, Sep 2003.
- [117] E. B. Sonin. Symmetry of kelvin-wave dynamics and the kelvin-wave cascade in the  $t = 0$  superfluid turbulence. *Phys. Rev. B*, 85:104516, Mar 2012.
- [118] S. Fujiyama, A. Mitani, and M. Tsubota. Generation, evolution, and decay of pure quantum turbulence: A full biot-savart simulation. *Phys. Rev. B*, 81:180512(R), 2010.
- [119] D.I. Bradley, D.O. Clubb, S.N. Fisher, A.M. Guénault, R.P. Haley, C.J. Matthews, G.R. Pickett, V. Tsepelin, and K. Zaki. Emission of discrete vortex rings by a vibrating grid in superfluid  $^3\text{He-B}$ : A precursor to quantum turbulence. *Phys. Rev. Lett.*, 95:035302, 2005.
- [120] R.M. Caplan, J.D. Talley, R. Carretero-González, and P.G. Kevrekidis. Scattering and leapfrogging of vortex rings in a superfluid. *Phys. Fluids*, 26(9):097101, 2014.
- [121] Z.A. Sultan, A.J. Youd, and C.F. Barenghi. Reconnection of superfluid vortex bundles. *Phys. Rev. Lett.*, 101:215302, 2008.
- [122] A Griffin, G W Stagg, N P Proukakis, and C F Barenghi. Vortex scattering by impurities in a bose-einstein condensate. *Journal of Physics B: Atomic, Molecular and Optical Physics*, 50(11):115003, 2017.
- [123] R. Hänninen. Dissipation enhancement from a single vortex reconnection in superfluid helium. *Phys. Rev. B*, 88:054511, Aug 2013.
- [124] W. F. Vinen. Mutual friction in a heat current in liquid helium ii. iii. theory of the mutual friction. *Proceedings of the Royal Society of London A: Mathematical, Physical and Engineering Sciences*, 242(1231):493–515, 1957.

- [125] A. C. White, C. F. Barenghi, N. P. Proukakis, A. J. Youd, and D. H. Wacks. Nonclassical velocity statistics in a turbulent atomic bose-einstein condensate. *Phys. Rev. Lett.*, 104(7):075301, Feb 2010.
- [126] Steven R. Stalp, L. Skrbek, and Russell J. Donnelly. Decay of grid turbulence in a finite channel. *Phys. Rev. Lett.*, 82:4831–4834, Jun 1999.
- [127] Renzo L. Ricca. *Tropicity and Complexity Measures for Vortex Tangles*, pages 366–372. Springer Berlin Heidelberg, Berlin, Heidelberg, 2001.
- [128] Martin W. Scheeler, Dustin Kleckner, Davide Proment, Gordon L. Kindlmann, and William T. M. Irvine. Helicity conservation by flow across scales in reconnecting vortex links and knots. *Proceedings of the National Academy of Sciences*, 111(43):15350–15355, 2014.
- [129] P. Clark di Leoni, P. D. Mininni, and M. E. Brachet. Helicity, topology and kelvin waves in reconnecting quantum knots. *arXiv:1602.06880v1*, 2016.
- [130] A J Taylor and M R Dennis. Geometry and scaling of tangled vortex lines in three-dimensional random wave fields. *Journal of Physics A: Mathematical and Theoretical*, 47(46):465101, 2014.
- [131] D. Kivotides, J. C. Vassilicos, D. C. Samuels, and C. F. Barenghi. Kelvin waves cascade in superfluid turbulence. *Phys. Rev. Lett.*, 86:3080–3083, Apr 2001.
- [132] Giorgio Krstulovic. Kelvin-wave cascade and dissipation in low-temperature superfluid vortices. *Phys. Rev. E*, 86:055301, Nov 2012.
- [133] Andrew W. Baggaley and Jason Laurie. Kelvin-wave cascade in the vortex filament model. *Phys. Rev. B*, 89:014504, Jan 2014.
- [134] E. R. Priest. *Heating The Solar Corona By Magnetic Reconnection*, pages 77–100. Springer Netherlands, Dordrecht, 1999.
- [135] S. Kida and M. Takaoka. Vortex reconnection. *Annual Review of Fluid Mechanics*, 26(1):169–177, 1994.
- [136] Joel Koplik and Herbert Levine. Vortex reconnection in superfluid helium. *Phys. Rev. Lett.*, 71:1375–1378, Aug 1993.
- [137] Xue Zhike, Yan Xiaoli, Cheng Xin, Yang Liheng, Su Yingna, Kliem Bernhard, Zhang Jun, Liu Zhong, Bi Yi, Xiang Yongyuan, Yang Kai, and Zhao Li. Observing the release of twist by magnetic reconnection in a solar filament eruption. *Nat Commun*, 7, jun 2016.
- [138] Fazle Hussain and Karthik Duraisamy. Mechanics of viscous vortex reconnection. *Physics of Fluids*, 23(2), 2011.

- [139] Enrico Fonda, David P. Meichle, Nicholas T. Ouellette, Sahand Hormoz, and Daniel P. Lathrop. Direct observation of kelvin waves excited by quantized vortex reconnection. *Proceedings of the National Academy of Sciences*, 111(Supplement 1):4707–4710, 2014.
- [140] Peter Constantin, Charles Fefferman, and Andrew J Majda. Geometric constraints on potentially singular solutions for the 3-d euler equations. *Communications in Partial Differential Equations*, 21(3-4), 1996.
- [141] H. K. Moffatt. The interaction of skewed vortex pairs: a model for blow-up of the navier–stokes equations. *Journal of Fluid Mechanics*, 409:51–68, 04 2000.
- [142] K. W. Schwarz. Three-dimensional vortex dynamics in superfluid  $^4\text{He}$ : Homogeneous superfluid turbulence. *Phys. Rev. B*, 38:2398–2417, Aug 1988.
- [143] Gregory P. Bewley, Matthew S. Paoletti, Katepalli R. Sreenivasan, and Daniel P. Lathrop. Characterization of reconnecting vortices in superfluid helium. *Proceedings of the National Academy of Sciences*, 105(37):13707–13710, 2008.
- [144] B. P. Anderson, P. C. Haljan, C. A. Regal, D. L. Feder, L. A. Collins, C. W. Clark, and E. A. Cornell. Watching dark solitons decay into vortex rings in a bose-einstein condensate. *Phys. Rev. Lett.*, 86:2926–2929, Apr 2001.
- [145] S. Serafini, M. Barbiero, M. Debortoli, S. Donadello, F. Larcher, F. Dalfovo, G. Lamporesi, and G. Ferrari. Dynamics and interaction of vortex lines in an elongated bose-einstein condensate. *Phys. Rev. Lett.*, 115:170402, Oct 2015.
- [146] Sergey Nazarenko and Robert West. Analytical solution for nonlinear schrödinger vortex reconnection. *Journal of low temperature physics*, 132(1-2):1–10, 2003.
- [147] A. T. A. M. de Waele and R. G. K. M. Aarts. Route to vortex reconnection. *Phys. Rev. Lett.*, 72:482–485, Jan 1994.
- [148] Richard Tebbs, Anthony J Youd, and Carlo F Barenghi. The approach to vortex reconnection. *Journal of Low Temperature Physics*, 162(3-4):314–321, 2011.
- [149] S. Nazarenko. Kelvin wave turbulence generated by vortex reconnections. *JETP Letters*, 84(11):585–587, 2007.
- [150] R. Hänninen. Kelvin waves from vortex reconnection in superfluid helium at low temperatures. *Phys. Rev. B*, 92:184508, Nov 2015.
- [151] Martin W. Scheeler, Dustin Kleckner, Davide Proment, Gordon L. Kindlmann, and William T. M. Irvine. Helicity conservation by flow across scales in reconnecting vortex links and knots. *Proceedings of the National Academy of Sciences*, 111(43):15350–15355, 2014.
- [152] Y. Kimura and H. K. Moffatt. Reconnection of skewed vortices. *Journal of Fluid Mechanics*, 751:329–345, 007 2014.

- [153] Christian E Laing, Renzo L Ricca, and L Summers De Witt. Conservation of writhe helicity under anti-parallel reconnection. *Scientific reports*, 5, 2015.
- [154] Simone Zuccher and Renzo L. Ricca. Helicity conservation under quantum reconnection of vortex rings. *Phys. Rev. E*, 92:061001, Dec 2015.
- [155] Peter Constantin, Itamar Procaccia, and Daniel Segel. Creation and dynamics of vortex tubes in three-dimensional turbulence. *Phys. Rev. E*, 51:3207–3222, Apr 1995.
- [156] Simone Serafini, Luca Galantucci, Elena Iseni, Tom Bienaimé, Russell N Bisset, Carlo F Barenghi, Franco Dalfovo, Giacomo Lamporesi, and Gabriele Ferrari. Vortex reconnections and rebounds in trapped atomic bose–einstein condensates. *arXiv preprint arXiv:1611.01691*, 2016.
- [157] R. L. Williams. Ionic mobilities in argon and helium liquids. *Canadian Journal of Physics*, 35(2):134–146, 1957.
- [158] G. Careri, F. Scaramuzzi, and J. O. Thomson. Heat flush and mobility of electric charges in liquid helium. *Il Nuovo Cimento (1955-1965)*, 13(1):186–196, 1959.
- [159] F. Reif and Lothar Meyer. Study of superfluidity in liquid he by ion motion. *Phys. Rev.*, 119:1164–1173, Aug 1960.
- [160] Richard A. Ferrell. Long lifetime of positronium in liquid helium. *Phys. Rev.*, 108:167–168, Oct 1957.
- [161] C. G. Kuper. Theory of negative ions in liquid helium. *Phys. Rev.*, 122:1007–1011, May 1961.
- [162] J. Classen, C.-K. Su, M. Mohazzab, and H. J. Maris. Electrons and cavitation in liquid helium. *Phys. Rev. B*, 57:3000–3010, Feb 1998.
- [163] R. M. Ostermeier and W. I. Glaberson. Motion of ions trapped on vortices in he ii. *Phys. Rev. Lett.*, 35:241–244, Jul 1975.
- [164] R.C. Clark. Self-trapped electrons in liquid helium ii. *Physics Letters*, 16(1):42 – 43, 1965.
- [165] E.P Gross. Classical theory of boson wave fields. *Annals of Physics*, 4(1):57 – 74, 1958.
- [166] Dafei Jin and Wei Guo. Vortex nucleation induced phonon radiation from a moving electron bubble in superfluid  $^4\text{He}$ . *Phys. Rev. B*, 82:094524, Sep 2010.
- [167] P. Roche, G. Deville, N. J. Appleyard, and F. I. B. Williams. Measurement of the surface tension of superfluid  $^4\text{He}$  at low temperature by capillary wave resonances. *Journal of Low Temperature Physics*, 106(5):565–573, 1997.

- [168] A. Messiah. *Quantum Mechanics*. Dover books on physics. Dover Publications, 1961.
- [169] L. Lehtovaara, J. Toivanen, and J. Eloranta. Solution of time-independent schrödinger equation by the imaginary time propagation method. *J. Comput. Phys.*, 221(1):148–157, January 2007.
- [170] William H. Press, Saul A. Teukolsky, William T. Vetterling, and Brian P. Flannery. *Numerical Recipes 3rd Edition: The Art of Scientific Computing*. Cambridge University Press, New York, NY, USA, 3 edition, 2007.
- [171] Giorgio Krstulovic and Marc Brachet. Energy cascade with small-scale thermalization, counterflow metastability, and anomalous velocity of vortex rings in fourier-truncated gross-pitaevskii equation. *Phys. Rev. E*, 83:066311, Jun 2011.
- [172] L. Bruschi, B. Maraviglia, and P. Mazzoldi. Second-sound attenuation associated with hot ions in liquid he ii. *Phys. Rev.*, 143:84–90, Mar 1966.
- [173] D R Allum and P V E M McClintock. Observation of a second critical field for negative ions in he ii. *Journal of Physics C: Solid State Physics*, 9(14):L371, 1976.
- [174] G. G. Nancolas and P. V. E. McClintock. Quenching of the ion/vortex-ring transition in he ii by intense electric fields. *Phys. Rev. Lett.*, 48:1190–1192, Apr 1982.
- [175] T. Winiecki and C. S. Adams. Motion of an object through a quantum fluid. *EPL (Europhysics Letters)*, 52(3):257, 2000.
- [176] R. M. Bowley, P. V. E. McClintock, F. E. Moss, G. G. Nancolas, and P. C. E. Stamp. The breakdown of superfluidity in liquid  $^4\text{he}$ : Iii. nucleation of quantized vortex rings. *Philosophical Transactions of the Royal Society of London A: Mathematical, Physical and Engineering Sciences*, 307(1498):201–260, 1982.
- [177] C. M. Muirhead, W. F. Vinen, and R. J. Donnelly. The Nucleation of Vorticity by Ions in Superfluid  $^4\text{He}$ : I. Basic Theory. *Philosophical Transactions of the Royal Society of London Series A*, 311:433–467, June 1984.
- [178] Natalia G. Berloff. Vortex nucleation by a moving ion in a bose condensate. *Physics Letters A*, 277(45):240 – 244, 2000.
- [179] T. Frisch, Y. Pomeau, and S. Rica. Transition to dissipation in a model of superflow. *Phys. Rev. Lett.*, 69:1644–1647, Sep 1992.
- [180] A. Phillips and P. V. E. McClintock. Field emission and field ionisation in liquid  $^4\text{He}$ . *Phil. Trans. Roy. Soc. Lond. A*, 278:271, 1974.
- [181] T. Ellis and P. V. E. McClintock. The breakdown of superfluidity in liquid  $^4\text{he}$ . v. measurement of the landau critical velocity for roton creation. *Phil. Trans. R. Soc. Lond. A*, 315:259–300, 1985.

- [182] Richard E. Packard and T. M. Sanders. Observations on single vortex lines in rotating superfluid helium. *Phys. Rev. A*, 6:799–807, Aug 1972.
- [183] William I. Glaberson, Donald M. Strayer, and Russell J. Donnelly. Model for the core of a quantized vortex line in helium ii. *Phys. Rev. Lett.*, 21:1740–1744, Dec 1968.
- [184] R. A. Ashton and W. I. Glaberson. Vortex waves in superfluid  $^4\text{He}$ . *Phys. Rev. Lett.*, 42:1062–1064, Apr 1979.
- [185] Robert Betchov. On the curvature and torsion of an isolated vortex filament. *Journal of Fluid Mechanics*, 22(3):471–479, 1965.
- [186] Luigi Sante Da Rios. Sul moto d’un liquido indefinito con un filetto vorticoso di forma qualunque. *Rendiconti del Circolo Matematico di Palermo (1884-1940)*, 22(1):117–135, 1906.
- [187] Tetsuo Ohmi and Tunemaru Usui. Mobility of negative ions along superfluid vortices. *Progress of Theoretical Physics*, 45(6):1717, 1971.
- [188] Peter E. Parks and R. J. Donnelly. Radii of positive and negative ions in helium ii. *Phys. Rev. Lett.*, 16:45–48, Jan 1966.
- [189] T. Maxworthy, E. J. Hopfinger, and L. G. Redekopp. Wave motions on vortex cores. *Journal of Fluid Mechanics*, 151:141–165, 1985.
- [190] J. W. Halley and R. M. Ostermeier. A new calculation of the ion velocity shift in a vortex resonance experiment in he ii. *Journal of Low Temperature Physics*, 26(5):877–898, Mar 1977.
- [191] A. Cidrim, A. C. White, A. J. Allen, V. S. Bagnato, and C. F. Barenghi. Vinen turbulence via the decay of multicharged vortices in trapped atomic bose-einstein condensates. *Phys. Rev. A*, 96:023617, Aug 2017.
- [192] W Wei, Z-L Xie, Y Yang, G M Seidel, and H J Maris. Study of exotic ions in superfluid helium-4 using a carbon nanotube source. *Journal of Physics: Conference Series*, 568(1):012011, 2014.